THE UNIVERSITY OF QUEENSLAND

AUSTRALIA

Influence of hydrogen on some DP, Q&P and TWIP grades of advanced high strength steels for auto construction

Qinglong Liu

B. Sci., M. Eng.

A thesis submitted for the degree of Doctor of Philosophy at

The University of Queensland in 2017

The School of Mechanical and Mining Engineering

Abstract

Dual Phase (DP), Quenching and Partitioning (Q&P) and Twinning-Induced Plasticity (TWIP) advanced high-strength steels (AHSS) have demonstrated the capability to meet the demands of fuel efficiency and improved safety performance in auto industry, attributed to their excellent combination of strength and ductility, good formability and high energy absorption capability. However, hydrogen embrittlement (HE) is particularly under concern for the stressed AHSS, causing the deterioration of steel mechanical properties, especially ductility. For the lifetime of a car body, the sources of this hydrogen are extensive, such as steel making, auto construction processes, and corrosion processes in actual service. Therefore, in this doctoral dissertation, efforts have been made to gain a deeper understanding of hydrogen influence on the key DP, Q&P and TWIP steels produced for auto construction. The following issues have been covered:

1. Hydrogen influence on the mechanical properties of the DP, Q&P and TWIP steels.
2. Hydrogen diffusion and trapping in the key DP and Q&P steels.
3. Hydrogen concentration in some DP and Q&P steels.
4. Equivalent hydrogen fugacity during electrochemical charging of 980DP steels.

The following techniques were employed in this research: optical microscopy, scanning electron microscopy (SEM), energy dispersive X-ray spectroscopy (EDS), X-ray diffraction (XRD) analysis, transmission electron microscopy (TEM), electrochemical polarization, hydrogen permeation analysis, linearly increasing stress test (LIST), universal tensile machine (UTM), hot extraction analyser and thermal desorption spectroscopy (TDS).

The hydrogen influence on six different DP, Q&P and TWIP steels was studied using LIST with cathodic hydrogen charging. The steels were designated as 980DP, 980DP-650YS, 980DP-700YS, 1200DP, 980QP and 950TW. 980DP referred to a DP steel with tensile strength of 980 MPa. 980DP-650YS and 980DP-700YS referred to a DP steel with tensile strength of 980 MPa and increased yield strength of 650MPa and 700MPa, respectively. 1200DP referred to a DP steel with tensile strength of 1200 MPa. 980QP referred to a Q&P steel with tensile strength of 980 MPa. 950TW referred to a TWIP steel with tensile strength of 950 MPa. All steels exhibited HE susceptibility, manifested by (i) decreased strength, and (ii) reduced ductility and a change from ductile cup and cone fracture to brittle transgranular and/or intergranular fracture. There was no sub-critical crack growth at stresses below the ultimate tensile strength. The hydrogen influence increased with increasing strength, more

negative charging potential, and decreasing stress rate. Hydrogen brittle fracture was associated with the hard martensite phase for DP and Q&P steels.

The hydrogen influence was also studied using LIST and UTM (i) for immersion in 3 wt% NaCl, to simulate hydrogen picked in automobile service, and (ii) at substantial loading rates to simulate a crash. Simulated service corrosions caused minimal HE for 980DP and 1200DP, and some HE for 980DP-650YS, 980DP-700YS, 980QP and 950TW. Simulated crash situations caused HE for 980DP, 980QP and 950TW; their properties quickly reverted after the end of hydrogen charging. Two new HE mechanisms are proposed: (i) hydrogen enhanced macroscopic plasticity (HEMP) decreasing the yield stress, and (ii) hydrogen assisted micro-fracture (HAM) decreasing ductility at fracture at the ultimate tensile strength. The brittle features for 950TW were associated with mechanical twinning rather than martensitic transformation.

Hydrogen diffusion and trapping were studied by permeability experiments for DP and Q&P steels. The measured reversible hydrogen trap densities indicated that (i) trapping was less significant at a more negative potential, and (ii) the lattice diffusion coefficient of hydrogen could be measured from the partial transients at the most negative potentials. The reversible hydrogen trap densities evaluated from complete decays from −1.700 $V_{Hg/HgO}$ were ~ 2×10^{18} sites cm^{-3}, and were a factor of two higher than those from partial decay transients between −1.700 $V_{Hg/HgO}$ and −1.100 $V_{Hg/HgO}$.

The hydrogen concentration in DP and Q&P, under simulated service corrosion and cathodic charging conditions was investigated through permeability experiments and hot extraction analysis. The hydrogen concentration in the steels increased with a more negative potential under cathodic charging. The hydrogen concentration under simulated service corrosions in 3 wt% NaCl solution was lower than that at the least negative charging potential of −1.100 $V_{Hg/HgO}$ in 0.1M NaOH. Crevice corrosion introduces three times more hydrogen than the corrosion at the free corrosion potential.

The equivalent hydrogen fugacity during electrochemical charging was determined using a new TDS apparatus for 980DP steel. The hydrogen concentration increased with (i) more negative charging potential, and (ii) increasing hydrogen gas pressure. The equivalent hydrogen fugacity related to the electrochemical charging overpotential was determined. The detrapping activation energies were 40.5 kJ mol^{-1} and 50.2 kJ mol^{-1} for the two desorption peaks, considered as hydrogen traps at boundary defects.

Declaration by author

This thesis is composed of my original work, and contains no material previously published or written by another person except where due reference has been made in the text. I have clearly stated the contribution by others to jointly-authored works that I have included in my thesis.

I have clearly stated the contribution of others to my thesis as a whole, including statistical assistance, survey design, data analysis, significant technical procedures, professional editorial advice, and any other original research work used or reported in my thesis. The content of my thesis is the result of work I have carried out since the commencement of my research higher degree candidature and does not include a substantial part of work that has been submitted to qualify for the award of any other degree or diploma in any university or other tertiary institution. I have clearly stated which parts of my thesis, if any, have been submitted to qualify for another award.

I acknowledge that an electronic copy of my thesis must be lodged with the University Library and, subject to the policy and procedures of The University of Queensland, the thesis be made available for research and study in accordance with the Copyright Act 1968 unless a period of embargo has been approved by the Dean of the Graduate School.

I acknowledge that copyright of all material contained in my thesis resides with the copyright holder(s) of that material. Where appropriate I have obtained copyright permission from the copyright holder to reproduce material in this thesis.

Publications during candidature

Journal papers:

1. **Q Liu**, Q Zhou, J Venezuela, M Zhang, J Wang and A Atrens, A review of the influence of hydrogen on the mechanical properties of DP, TRIP, and TWIP advanced high-strength steels for auto construction, Corros Rev. 34 (2016) 127-152.
2. **Q Liu**, J Venezuela, M Zhang, Q Zhou and A Atrens, Hydrogen trapping in some advanced high strength steels, Corros Sci. 111 (2016) 770-785.
3. **Q Liu**, Q Zhou, J Venezuela, M Zhang and A Atrens, Hydrogen Concentration in Dual-Phase (DP) and Quenched and Partitioned (Q&P) Advanced High-Strength Steels (AHSS) under Simulated Service Conditions Compared with Cathodic Charging Conditions, Adv Eng Mater. 18 (2016) 1588-1599.
4. J Venezuela, **Q Liu**, M Zhang, Q Zhou and A Atrens, The influence of hydrogen on the mechanical and fracture properties of some martensitic advanced high strength steels studied using the linearly increasing stress test, Corros Sci. 99 (2015) 98-117.
5. J Venezuela, **Q Liu**, M Zhang, Q Zhou and A Atrens, A review of hydrogen embrittlement of martensitic advanced high-strength steels, Corros Rev. 34 (2016) 153-186.
6. J Venezuela, Q Zhou, **Q Liu**, M Zhang and A Atrens, Influence of hydrogen on the mechanical and fracture properties of some martensitic advanced high strength steels in simulated service conditions, Corros Sci. 111 (2016) 602-624.

Conference papers:

1. **Q Liu**, J Venezuela, M Zhang, Q Zhou and A Atrens, Study on hydrogen permeation in DP and Q&P grades of AHSS under cathodic charging and simulated service conditions, Proceedings of the 10th CSM Steel Congress and the 6th Baosteel Biennial Academic Conference, 21-23 October 2015, Shanghai, China.
2. **Q Liu**, J Venezuela, M Zhang, Q Zhou and A Atrens, Hydrogen permeation in dual phase (DP) and quenched and partitioned (Q&P) advanced high strength steels (AHSS) under cathodic charging and simulated service conditions, Proceedings of the 2016 European Corrosion Congress, 11-15 September 2016, Montpellier, France.
3. J. Venezuela, **Q. Liu**, M. Zhang, Q. Zhou, A. Atrens, Evaluation of hydrogen embrittlement susceptibility of four martensitic advanced high strength steels using

the Linearly Increasing Stress Test, Proceedings of CSM-Baoshan Steel Conference 2015, Oct 21-23, 2015 , Shanghai, China

4. J. Venezuela, **Q. Liu**, M. Zhang, Q. Zhou, A. Atrens, Hydrogen-influenced fracture of automotive martensitic advanced high strength steels in a linearly increasing stress test, Proceedings of 10th International Conference on Structural Integrity and Failure 2016, Jul 12-15, 2016, Adelaide, Australia
5. J. Venezuela, **Q. Liu**, M. Zhang, Q. Zhou, A. Atrens, Assessing hydrogen embrittlement susceptibility of automotive martensitic advanced high strength steels using the linearly increasing stress test , Proceedings of ACA Corrosion and Prevention 2016 Conference, Oct 4-6, 2016, Auckland, New Zealand

Publications included in this thesis

1. Q Liu, Q Zhou, J Venezuela, M Zhang, J Wang and A Atrens, A review of the influence of hydrogen on the mechanical properties of DP, TRIP, and TWIP advanced high-strength steels for auto construction, Corros Rev. 34 (2016) 127-152. Incorporated as Paper 1 in Chapter 1.

Contributor	Statement of contribution
Q Liu	Literature reading (95%) Conception design (80%) Paper writing (85%) Paper editing and review (70%)
Q Zhou	Paper editing and review (5%)
J Venezuela	Paper editing and review (5%)
M Zhang	Paper editing and review (5%)
J Wang	Conception design (5%) Paper editing and review (5%)
A Atrens	Literature reading (5%) Conception design (15%) Paper writing (15%)

	Paper editing and review (10%)

2. Q Liu, J Venezuela, M Zhang, Q Zhou and A Atrens, Hydrogen trapping in some advanced high strength steels, Corros Sci. 111 (2016) 770-785. Incorporated as Paper 2 in Chapter 4.

Contributor	Statement of contribution
Q Liu	Conception design (70%) Experimental (100%) Data analysis (95%) Paper writing (75%) Paper editing and review (80%)
J Venezuela	Paper editing and review (5%)
M Zhang	Paper editing and review (5%)
Q Zhou	Paper editing and review (5%)
A Atrens	Conception design (30%) Data analysis (5%) Paper writing (25%) Paper editing and review (5%)

3. Q Liu, Q Zhou, J Venezuela, M Zhang and A Atrens, Hydrogen Concentration in Dual-Phase (DP) and Quenched and Partitioned (Q&P) Advanced High-Strength Steels (AHSS) under Simulated Service Conditions Compared with Cathodic Charging Conditions, Adv Eng Mater. 18 (2016) 1588-1599. Incorporated as Paper 3 in Chapter 5.

Contributor	Statement of contribution
Q Liu	Conception design (70%) Experimental (100%) Data analysis (95%) Paper writing (75%) Paper editing and review (80%)

Q Zhou	Paper editing and review (5%)
J Venezuela	Paper editing and review (5%)
M Zhang	Paper editing and review (5%)
A Atrens	Conception design (30%) Data analysis (5%) Paper writing (25%) Paper editing and review (5%)

Contributions by others to the thesis

No contributions by others.

Statement of parts of the thesis submitted to qualify for the award of another degree

None.

Acknowledgements

To become a qualified PhD has never been easy. The past three years of PhD study is a bitter sweet, yet, precious chapter in my life. Now when I look back, I can proudly say, I am almost there. But nothing would be accomplished without the support and company of the following people.

First, I would like to thank my principle supervisor Prof. Andrejs Atrens, for the opportunities, advice and great support you have been given me. It is a great honour to work under your supervision. I sincerely appreciate all you provided to help me become a better researcher.

I would also like to thank my co-supervisor, Prof. Mingxing Zhang for the valuable advice and support.

To my colleague, Jeffrey Jones de Guzman Venezuela, thank you for being there throughout the PhD study, as a colleague, a teacher, a big brother and a great friend. I am privileged to get to know you and to work with you. I will always remember all the fun time singing, playing and travelling. As we said, we had good life.

In addition, I would like to thank these people:

Dr. Zhiming Shi, Dr. Qian Liu and Dr. Fuyong Cao for the generous help with the permeability experiment, electrochemical analysis, and the LIST test during my PhD study.

Dr. Qingjun Zhou, for the warm hospitality during my stay at Baosteel in Shanghai.

Professor Evan Gray and Dr. Clotario Tapia-Bastidas from the Griffith University, for the training on thermal desorption spectroscopy apparatus, and the valuable discussion and advice on the experiments and papers.

Prof. Krzysztof Wolski and Dr. Frédéric Christien, for the valuable discussion and warm hospitality during my visit to the Ecole Nationale Supérieure de Mines de Saint-Etienne, Saint-Étienne, France.

Dr. Ron Rasch, Ms. Eunice Grinan, A/Prof. Kevin Jack, Ms. Anya Yago, Dr. Graeme Auchterlonie, Dr. Hui Diao, Ms. Mun Teng Soo, and other CMM staff at the University of Queensland, for their patient training and assistance with the SEM, XRD and TEM analysis.

Ms. Glenda Zemanek, Mr. Doug Malcolm and Mr. Jonathan Read, for the training and help with the apparatus in the labs of material testing and metallography.

My colleagues and friends, Sean Johnston, Akif Soltan, Dr. Yamasaki, Jiewei Cao, Yongmei Zhao, Jian Xi, Dr. Chengwei Kang, Dr. Qiu Dong, Dr. Ming Li, Jianmin Li, Qiyang Tan,

Ning Mo, Xuan Quy Tran, and Yahia Ali Hassan Mohamed Ali, for their pleasant company and advice during my stay in UQ.

The financial supports provided throughout the research are gratefully acknowledged: the University of Queensland International Scholarship (UQI), and the Baosteel-Australia Joint Research & Development Centre (BAJC) Grant, BA13037, with linkage to Baoshan Iron and Steel Co., Ltd of China.

Finally, I would like to express my gratitude to my parents in China, for their unquestioning support through my ups and downs in Australia. Special thanks to my fiancée, Xiaohong Zhang, for her patience, support and love. Being able to manage through the long distance relationship and get into marriage is another proud achievement I have had during the PhD study.

Keywords

Hydrogen embrittlement, advanced high strength steels, permeability test, linearly increasing stress test, universal tensile test, hot extraction analysis, TDS, SEM, XRD.

Australian and New Zealand Standard Research Classifications (ANZSRC)

ANZSRC code: 091207, Metals and Alloy Materials, 100%

Fields of Research (FoR) Classification

FoR code: 0912, Materials Engineering, 100%

Table of Contents

List of Figures

List of Tables

List of Abbreviations

AC	Analytical chamber
AHSS	Advanced high strength steels
AIDE	Adsorption-induced dislocation emission
AR	As-received
CP	Complex-phase
CSL	Coincidence site lattice
DCPD	Direct current potential drop
DP	Dual phase
EDS	Energy-dispersive X-ray spectroscopy
EHE	External hydrogen embrittlement
FB	Ferritic-bainitic
HAM	Hydrogen assisted micro-fracture
HE	Hydrogen embrittlement
HEDE	Hydrogen enhanced decohesion
HELP	Hydrogen enhanced localized plasticity
HEMP	Hydrogen enhanced macroscopic plasticity
HER	Hydrogen evolution reaction
HF	Hot-formed
IHE	Internal Hydrogen Embrittlement
LC	Loading chamber
LIST	Linearly increasing stress test
MS	Martensitic
MVC	Micro-void coalescence
OCP	Open circuit potential
PDF	Powder diffraction file
Q&P	Quenching and partitioning
RGA	Residual gas analyser

RPH	Revolutions per hour
SEM	Scanning electron microscopy
SFE	Stacking fault energy
SSRT	Slow strain rate tests
TDS	Thermal desorption spectroscopy
TEM	Transmission electron microscopy
TMP	Turbo molecular pump
TRIP	Transformation-induced plasticity
TWIP	Twinning-induced plasticity
UHP	Ultra-high purity
UTM	Universal testing machine
XRD	X-ray diffraction

Introduction

In recent years, there has been escalating concern of environmental friendliness and improved safety performance in the auto industry, leading to the research and development of steels, as steels are the main choice of auto body materials. Thus, the advanced high strength steels (AHSS) have been developed and are being adopted. The AHSS permit less fuel consumption and concomitantly less greenhouse gas emission by weight reduction, yet, without sacrifice safety performance. Among the AHSS, Dual Phase (DP), Quenching and Partitioning (Q&P) and Twinning-Induced Plasticity (TWIP) steels are promising candidates, due to their high strength, good ductility, good formability, and good energy absorption ability. Their good mechanical properties make these steels suitable for automobile parts that are structural, safety-critical, and with complex shape.

However, hydrogen embrittlement (HE) is particularly a concern for high strength steels. HE is the consequence of hydrogen interacting with the stressed steel. For automotive steel components, hydrogen can be introduced into the steels, during steel making, or during auto construction processes such as painting, or during corrosion processes in practical service. HE can reduce the strengths and ductility of the steel components, or may trigger catastrophic failures, suddenly, without warning, upon the application of a sufficiently large stress.

In the past few decades, a great amount of work has been conducted to study the HE susceptibility of DP, Q&P and TWIP grades of AHSS, however, yielding inconsistent results, especially for Q&P and TWIP steels. Indeed, the occurrence of HE depends on various factors, such as the steel strength, the steel microstructure, the steel chemical composition, and the severity of hydrogen environment. Thus, it is necessary to understand the HE susceptibility of the DP, Q&P and TWIP grades of AHSS from commercial productions, for the safe applications in auto construction.

In this study, linearly increasing stress tests (LIST) and universal tensile tests were used to study the hydrogen influence on the mechanical properties of the DP, Q&P and TWIP steels subjected to cathodic hydrogen charging and simulated service conditions. Electrochemical permeability experiments, hot extraction analysis, and thermal desorption spectroscopy (TDS) analysis were conducted to determine the (i) hydrogen diffusion, (ii) hydrogen concentration, (iii) reversible hydrogen trap density, (iv) hydrogen trap activation energy, and (v) relationship of hydrogen fugacity during electrochemical charging and the charging overpotential. Moreover, the light microscopy (LM), scanning electron microscopy (SEM), and the X-ray diffraction (XRD) were used to examine the microstructure features

associated with the hydrogen influence on the steels. The expected results would permit understanding the interactions of hydrogen and steel microstructures, and consequently the influence on the steel mechanical properties. Furthermore, the results would allow estimating the safety of the steel applications and improving HE resistance of the steels, for auto construction.

This thesis contains the following published journal papers (incorporated in Chapters 1, 4 and 5), and manuscripts (incorporated in Chapters 2, 3 and 6) submitted to journals or industrial partner for publication approvals, as individual chapters, which contribute to the whole PhD programme. As mentioned above, three experiments, including LIST experiments, electrochemical permeability experiments, and TDS analysis, were mainly focused on in this PhD study. The LIST results were presented in Chapters 2 and 3. Chapters 4 and 5 incorporated the results from permeability experiments to characterize the hydrogen, such as hydrogen trapping and hydrogen concentration in the steels. The TDS results were introduced in Chapter 6. Therefore, the structure of this PhD thesis is as following. Chapter 1 presents a review of the hydrogen influence on the mechanical properties of the key AHSS for auto construction. Chapter 2 studies the hydrogen influence on our DP, Q&P and TWIP grades of AHSS under cathodic charging conditions. Chapter 3 investigates the influence of hydrogen on these steels under simulated service conditions. Chapter 4 explores the hydrogen trapping in these key steels. Chapter 5 compares the hydrogen concentration in the key DP and Q&P steels under simulated service conditions with that under cathodic charging conditions. Chapter 6 determines the equivalent hydrogen fugacity during electrochemical charging and identifies the hydrogen trap types in DP steels. The final section presents the summary and conclusions, and suggestions for future work.

Chapter 1

A review of the influence of hydrogen on the mechanical properties of DP, TRIP and TWIP advanced high-strength steels for auto construction

(published in *Corrosion Reviews*)

In this chapter, the hydrogen influence on the mechanical properties of DP, TRIP and TWIP advanced high-strength steels for auto construction was critically reviewed to get an understanding of how hydrogen influenced the steels similar to our key steels. In addition, the microstructures, properties and applications of the DP, TRIP and TWIP were also studied. Moreover, to better understand the hydrogen influence on the steels, it is also necessary to understand (i) the hydrogen evolution at the steel surface, (ii) the hydrogen adsorption, absorption, and transportation through the steel bulk, and (iii) the mechanisms of embrittlement by hydrogen. Therefore, a review of the hydrogen behaviours has also been included.

It should be mentioned that the quenching and partitioning (Q&P) was considered a new method to produce TRIP steel, and the good properties of the Q&P steel also benefited from the TRIP effect. Thus, the hydrogen influence on TRIP and Q&P steels was reviewed and incorporated together in this work.

A review of the influence of hydrogen on the mechanical properties of DP, TRIP and TWIP advanced high-strength steels for auto construction

Qinglong Liu [a], Qingjun Zhou [b,*], Jeffrey Venezuela [a], Mingxing Zhang [a], Jianqiu Wang [c], Andrej Atrens [a,*]

[a] The University of Queensland, Division of Materials, School of Mining and Mechanical Engineering, St. Lucia, 4072 Australia

[*] Corresponding author, andrejs.atrens@uq.edu.au, andrejs.atrens@uq.edu.au, +61 7 3365 3748, zhouqingjun@baosteel.com, +86 21 26641807

[b] Baoshan Iron & Steel Co., Ltd, Research Institute, Shanghai, 201900, China

[c] Institute of Materials Research, Chinese Academy of Sciences, Shenyang 110016, China

Abstract

The literature is reviewed regarding the influence of hydrogen on DP, TRIP and TWIP steels. Hydrogen influences DP steels by decreasing ductility whilst strengths are largely unaffected. TRIP steels may be susceptible to HE, indicated by loss of ductility and some brittle fracture features. The literature on the influence of hydrogen on TWIP steels was inconsistent. Some researchers found no significant influence of hydrogen on TWIP steel properties and fully ductile fractures, whilst others found significant loss of ductility and strength due to hydrogen, and some brittle features. Possible countermeasures for HE are tempering for DP and TRIP steels, and aluminium alloying for TWIP steels.

Keywords: hydrogen embrittlement; mechanical properties; DP steel; TRIP steel; TWIP steel

1. Introduction

For automotive components, hydrogen can be introduced into the steels, (i) during steel making, (ii) during such auto construction processes such as painting, or (iii) during corrosion in service. This hydrogen present in steels can cause catastrophic failures, suddenly, without warning, upon the application of a stress. The failures can occur at stresses at which failures do not occur for steels in the absence of hydrogen. This phenomenon, of hydrogen causing failures of engineering materials, is called hydrogen embrittlement (HE) (Liu &

Atrens, 2013; Ramamurthy & Atrens, 2013). Hydrogen embrittlement can also cause a decrease of ductility, with little or no decrease in yield strength or tensile strength.

Advanced high-strength steels (AHSS) have been created and adopted for auto construction during the last few decades. AHSS have higher strengths allowing weight savings by the use of thinner sections. AHSS have enhanced formability compared with the conventional steels used for automobile construction, and allow designs with enhanced crashwothiness. However, high-strength steels are susceptible to hydrogen embrittlement (HE), so HE may be of concern for the advanced high-strength steels (AHSS) used in the auto construction.

Quenching and partitioning (Q&P) is a new heat treatment to produce TRIP steel with better strength and ductility (Chen et al., 2012). The steel is quenched below the martensite start temperature, and above the martensite finish temperature, to form a controlled amount of martensite. The subsequent partitioning treatment, at the same or higher temperature than the initial quenching, completes the enrichment of carbon from the martensite to the remaining austenite, and thus stabilizes the retained austenite at room temperature (Edmonds et al., 2006; Santofimia, Zhao & Sietsma, 2011). Because of the TRIP effect, quenching and partitioning (Q&P) steels show a quite-high strain-hardening capacity, and higher ductility and formability than other steels with the same strength, making them promising third generation AHSS, with a combination of higher strength and ductility (Matlock & Speer, 2009). However, since there is limited research on the HE of Q&P steels, these steels are not considered in this review.

This review focuses on (i) the influence of hydrogen on the mechanical and fracture properties of DP, TWIP and TRIP AHSS, and (ii) the metallurgical features responsible for this influence of hydrogen.

2. Advanced high-strength steels

2.1 Importance

Advanced high-strength steels (AHSS) were created for the automotive industry, due to escalating concerns of fuel consumption and emissions of greenhouse gases, and the increasing focus on safety (Bhattacharya, 2005; Bracke, Verbeken, Kestens & Penning, 2009; WorldAutoSteel, 2014; Zhu, Ma & Wang, 2007).

A range of strength, toughness and ductility values have been achieved by (i) selection of appropriate AHSS compositions and microstructures, (ii) controlling the heat treatments, and (iii) applying various strengthening methods. The strength of AHSS is often between 500 to 1500 MPa.

The principal difference between AHSS and conventional steels is their microstructure. Conventional steels are typically ferritic. In contrast, AHSS have a microstructure containing a phase other than ferrite: such as martensite, bainite, austenite, or retained austenite. In addition, typical AHSS have a combination of strength and ductility better than those of conventional steels, as illustrated in Fig. 1. AHSS include dual phase (DP), complex-phase (CP), ferritic-bainitic (FB), martensitic (MS), transformation-induced plasticity (TRIP), hot-formed (HF), and twinning-induced plasticity (TWIP) steels. The TWIP steels are different to the other steels in having an austenite matrix which ensures quite different hydrogen embrittlement properties because of the much lower hydrogen diffusivities.

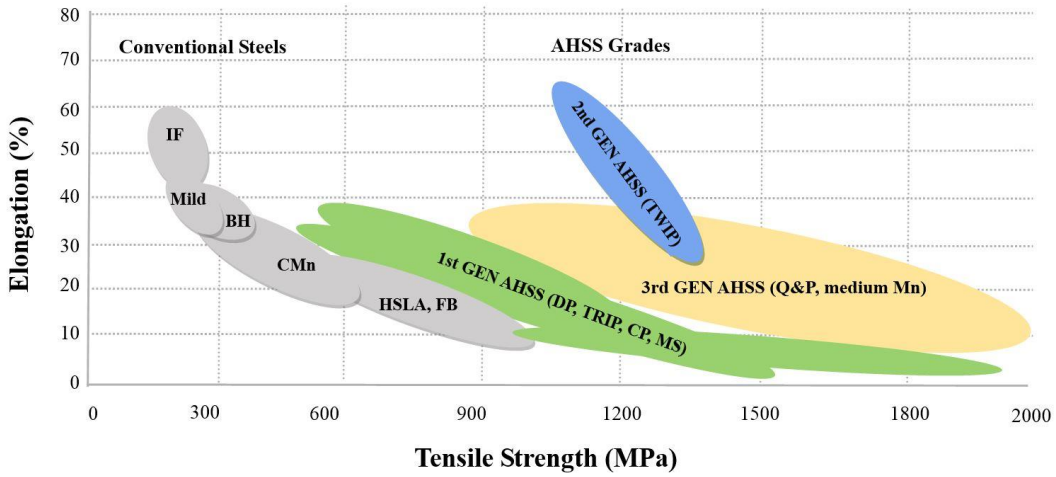

Fig. 1 Comparison of ductility and strength of AHSS and conventional steels. IF, interstitial-free steel; BH, bake hardenable steel; CMn, carbon manganese steel; HSLA, high-strength low-alloy steely; FB: ferritic-bainitic steel; 1st GEN AHSS, first generation AHSS; DP, dual phase steel; TRIP, transformation-induced plasticity steel; CP, complex-phase steel; MS, martensitic steel; 2nd GEN AHSS, second generation AHSS; TWIP, twinning-induced plasticity steel; 3rd GEN AHSS, third generation AHSS; Q&P, quenching and partitioning steel.

The ultra-light steel auto body (ULSAB) advanced vehicle concept indicates that utilizing ~85% AHSS for an automotive body would achieve ~25% weight reduction compared with an average base model, and without any increase of the manufacturing cost. AHSS have been widely used by the auto industry since their first production (AutoSteel, 2002), because of their high-strength/weight ratio, and good energy absorption.

2.2 Dual phase (DP) steels

Dual phase (DP) steel is a first generation AHSS. DP steel has a ferrite and martensite microstructure. DP steel development for the auto industry began in the 1980's (Galán et al., 2012) and the demand for DP steel continues to be strong. DP steels are widely used due to their good combination of strength and ductility, and their relatively ease of production.

2.2.1 Microstructure

DP steels have a two-phase microstructure. A hard martensitic second phase, in the form of islands, is located along the grain boundaries of the soft ferrite matrix. DP steels are commonly produced by cold rolling, followed by continuous annealing and quenching (Granbom, 2010; Oliver, Jones & Fourlaris, 2007). The annealing is in the intercritical region, which is the two-phase field of austenite and ferrite. On quenching, the austenite transforms to martensite. A higher annealing temperature produces a higher volume fraction of austenite, which transforms to martensite during quenching, and a higher strength, because the strength of DP steels is usually proportional to the volume fraction of martensite (Khan, Kuntz, Biro & Zhou, 2008).

Fig. 2 shows a typical microstructure of DP steel. The darker areas are the ferrite matrix. The embossed martensite islands appear light-coloured and are located along the grain boundaries. There is less martensite than ferrite.

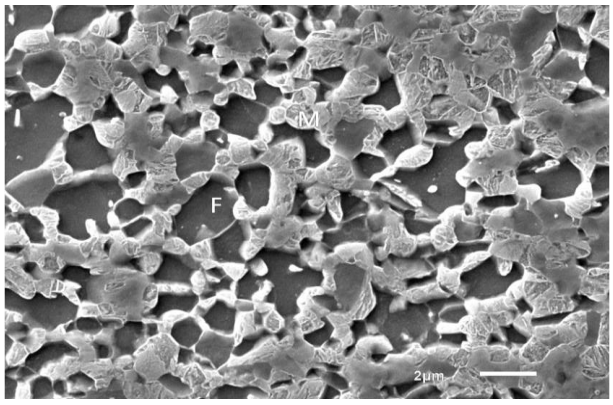

Fig. 2 SEM image showing a typical microstructure of a DP steel. The darker and smooth areas are ferrite (F). The light-coloured and embossed islands are martensite (M).

2.2.2 Properties and applications

DP steel microstructure consists of a soft ferrite matrix in which is dispered a hard martensite phase. The soft, continuous ferrite phase provides good formability, whilst the hard martensite contributes to their high-strength. DP steels also exhibit cost efficiency and high deformation hardening, which means high-energy absorption ability. DP steels with

different tensile strengths and formabilities have been produced for different design requirements. This variation of mechanical properties can be achieved (i) by controlling the carbon content and the content of other alloying elements individually and in combination, and by (ii) controlling the martensite volume fraction through the annealing temperature.

Due to their good formability, high-strength, high-deformation hardening and relatively low cost, DP steels are widely used in automotive body components (AutoSteel, 2002), especially structural components, and reinforcement and anti-collision components, such as under-body cross-members, bumpers, B-pillars, etc. (Baosteel, 2013).

In some cases, DP steels may be galvanised, which applies a zinc coating to the steel surface to protect against corrosion. Galvanisation is often through a continuous hot-dip galvanizing line (Liu et al., 2012). The dual phase steel is annealed in the inter-critical region, slowly cooled, and passed through a bath of molten zinc at 460 °C. For galvanized DP steel, the thermal processing variables, such as cooling rate and soaking time at 460 °C, influence the mechanical properties. For example, Liu et al. (2012) found that, for a Mn-Si dual phase steel, the ultimate tensile strength and elongation to fracture increased about 3% and 10%, respectively, when the cooling rate was increased from 10 °C s^{-1} to 50 °C s^{-1}. When the soaking time was increased from 3 s to 20 s, the ultimate tensile strength decreased about 5%, while there was negligible change of elongation to fracture. However, they further proposed that, adding Cr and Mo to DP steels stabilized the mechanical properties during hot-dip galvanizing. A galvanizing company (IndustrialGalvanizersCorporation, 2013) showed that, for immersion times less than 15 minutes in the molten zinc at 455 °C, the hot-dip galvanization did not affect the mechanical properties of steels with yield strength up to 500 MPa.

2.3 Transformation-induced plasticity (TRIP) steels

Transformation induced plasticity (TRIP) steel is a first generation AHSS. TRIP steel has a multi-phase microstructure of ferrite, retained austenite, bainite and possibly martensite. TRIP steels have attracted much attention since their first development in the 1990's for the automobile industry (Galán et al., 2012), because of a good combination of strength and formability.

2.3.1 Microstructure

TRIP steel has a microstructure consisting of typically three phases, a ferrite matrix, islands of retained austenite, and dispersed bainite regions. Martensite is also commonly

present (Oliver, Jones & Fourlaris, 2007). There are two processing routes for TRIP steel: hot rolling and cold rolling.

Hot rolling starts from the fully austenitic region. After finishing rolling, the sheet goes through a run-out table and controlled cooling. During cooling, ferrite forms, the carbon concentration in the remained austenite increases, due to the carbon solubility lower in ferrite than in austenite, and pearlite formation is avoided. During the following coiling, the sheet is coiled in the bainitic region, and the austenite transforms to bainite. The transformation from austenite to bainite further enriches small islands of austenite with carbon, making this untransformed austenite stable at room temperature.

In contrast, cold rolled TRIP steel is transformed from an initial microstructure consisting of ferrite and pearlite in two stages: intercritical annealing and isothermal bainitic transformation. The steel is (i) heated into the ferrite and austenite intercritical region to form a two-phase microstructure of ferrite and austenite, and (ii) rapidly cooled to avoid formation of intercritical ferrite or pearlite, and quenched to a lower temperature, the isothermal bainitic transformation region, where there occurs the partial transformation of austenite to bainite, and the enrichment of the remaining austenite with carbon, resulting in the remaining austenite being stable at room temperature. The higher carbon, silicon or aluminium content of TRIP steel plays a significant role of the retention of austenite, and austenite stabilization (WorldAutoSteel, 2014).

Hot rolling can be used to produce steel sheets with a minimum gauge of 3 mm. In comparison, cold rolling can produce thinner gauge steel sheets. In addition, cold rolling produces steel with smaller grain size because ferrite recrystallization occurs during annealing, which decreases the grain size (Huang, Poole & Militzer, 2004).

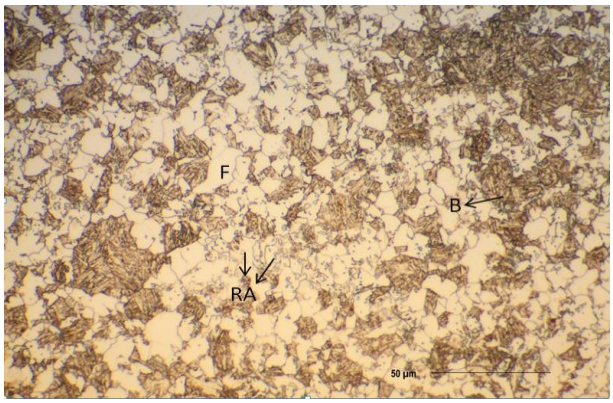

Fig. 3 Light optical micrograph showing a typical microstructure of a TRIP steel. F is for ferrite, B is for bainite and RA refers to retained austenite.

Fig. 3 presents an optical micrograph of a typical TRIP steel, etched using 2% nital. The ferrite appears yellow and is marked with “F”. The bainite appears brown. The retained austenite appears as the small white blocks dispersed in the ferrite and the bainite.

2.3.2 Properties and applications

TRIP steels have a microstructure of a ferrite matrix, with about 5~20 v% retained austenite, and hard phases of bainite or martensite. During deformation of TRIP steels, (i) the hard second-phase martensite, dispersed in the soft ferrite matrix, creates a high strain-hardening rate, and (ii) the transformation of retained austenite to martensite increases the strain-hardening rate at higher strain levels (Zackay, Parker, Fahr & Busch, 1967). Thus, t strain hardening rates of TRIP steels are substantially higher than for conventional steels. High strain-hardening rates, high mechanical strength and a strong bake hardening effect, provide TRIP steels with excellent energy absorption ability, making TRIP steel a good choice for crash performance compared with dual phase steel, bainitic steel, low carbon steel, and structural steel (Galán et al., 2012).

The high energy absorption capacity and the combination of high-strength and high-ductility makes TRIP steels particularly suitable for structural and reinforcement parts of complex shape, such as B-pillar reinforcement panels, cross members, longitudinal beams, sills and bumper reinforcements (Baosteel, 2013).

2.4 Twinning-induced plasticity (TWIP) steels

Twinning induced plasticity (TWIP) steel is a second-generation advanced high-strength steel. TWIP steel exhibits a combination of high-strength and good formability, and thus has attracted a lot of attention in recent decade in the auto industry.

2.4.1 Microstructure

TWIP steel has a microstructure consisting entirely of austenite at room temperature, caused by the high manganese content (typically more than 15%), as shown in Fig. 4. TWIP steel also typically contains alloying elements such as a relatively high content of C, Si and Al. C assists in the stabilization of austenite at room temperature, and strengthens the austenite by solid solution strengthening. Si also increases the strength by solid solution strengthening (Chen, Zhao & Qin, 2013). The high Al content increases the stacking fault energy (SFE) of the austenite, and stabilizes the austenite against transformation to ε-

martensite. Al also helps strengthen the austenite by solid solution strengthening (Wan, Chen & Hsu, 2001).

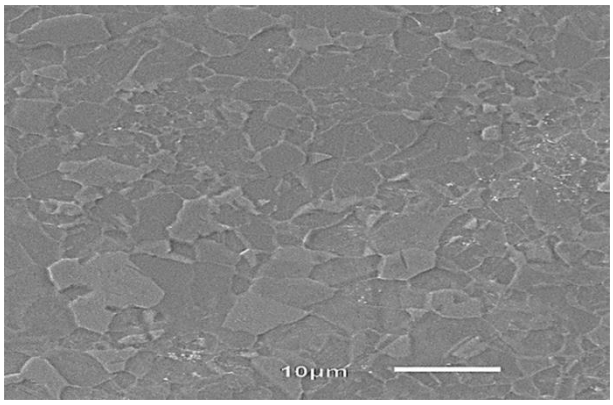

Fig. 4 SEM image showing the typical microstructure of a TWIP steel.

TWIP steels can be produced by the same manufacturing methods as the other grades of steels, and are compatible with processes, such as rolling, pressing and continuous casting. But technical difficulties can occur in the production of TWIP steel, such as: (i) the high manganese partial pressure during melting and casting, (ii) cracking during hot rolling resulting from the tendency to form strong oxide scales, and (iii) the requirement of stronger rolling equipment due to their high-strength during rolling (Kliber et al., 2012).

2.4.2 Properties and applications

TWIP steels have a face-centred cubic (fcc) crystal structure, with a low stacking fault energy (SFE). Their low stacking fault energy facilitates deformation twinning, which allows production of steels with high-strength, through strain hardening, and increases ductility (Neu, 2013). Thus, TWIP steels have higher strength and ductility than other steel grades used in the automotive industry.

The mechanism of strain hardening for TWIP steels involves both dislocation glide, and deformation twinning (Chung et al., 2011; De Cooman et al., 2009; EuropeanCommission, 2012). During straining, twins are continuously formed in the microstructure. These twins subdivide grains with twin boundaries, which act as barriers to dislocation movement, and decrease the effective glide distance or mean free path of dislocations (De Cooman, Kwon & Chin, 2012). This is the dynamic Hall-Petch effect, and leads to the high strain hardening, which results in the good combination of strength and ductility of TWIP steels. Upon straining, the twins keep being formed, and refine the grain size, so that the strength increases continuously via the Hall-Petch effect, resulting in a high strain-hardening rate. Twinning deformation is thus a crucial aspect of the high strain

hardening, and occurs when the stacking fault energy (SFE) ranges from 18 mJ m^{-2} to 50 mJ m^{-2} (De Cooman, Kwon & Chin, 2012; Lee, 2012).

The good combination of high-strength and ductility, makes TWIP steels suitable for manufacturing structural frame and safety parts with complex shapes, such as bumpers and B-pillars (Baosteel, 2013). However, TWIP steels have not been widely used in the auto industry (Neu, 2013).

3. Hydrogen in steels

3.1 Introduction

In order to understand the influence of hydrogen on the mechanical properties of AHSS for auto construction, it is necessary to understand (i) hydrogen evolution at the steel surface, (ii) hydrogen adsorption, absorption, and transportation through the steel bulk, and (iii) the mechanisms of embrittlement by hydrogen. This includes (i) how hydrogen is formed on the steel surface, (ii) how much hydrogen enters in to the steels, (iii) how far the hydrogen can diffuse in a certain period, and (iv) how the hydrogen interacts with the defects of the steels.

3.2 Hydrogen evolution and entry

Hydrogen can be introduced into steels by two main methods, (i) exposure to hydrogen gas and (ii) exposure to electrolytic hydrogen produced either by cathodic polarization or by a corrosion reaction.

In a hydrogen gaseous environment, the interaction of hydrogen with the steel surface involves the steps of physisorption, chemisorption and adsorption (Liu & Atrens, 2013). Physisorption is the result of the van der Waals force between a surface and an absorbent. Physisorption is reversible, and generally occurs quickly. Physisorption has a low adsorption energy, and it is relatively easy to reach equilibrium at room temperature. For chemisorption, a chemical reaction occurs between the surface atoms and absorbent molecules. Chemisorption dominates the hydrogen uptake at higher temperatures. Chemisorption is limited to a monolayer since short-range chemical forces are involved. Chemisorption is usually slow, and either slowly reversible or irreversible. The physisorbed hydrogen usually transfers into chemisorbed hydrogen before the hydrogen enters into the metal. The final step of the gas-solid interaction is adsorption, which involves the incorporation of the

chemisorption products into the metal lattice. The amount of hydrogen entering into the steel is controlled by the hydrogen pressure and temperature (Perng & Wu, 2003).

Another source of hydrogen is cathodic polarization or corrosion. The hydrogen evolution reaction (HER) can proceed in acid, neutral or alkaline conditions through the following steps (Lasia & Grégoire, 1995):

$H_3O^+ + M + e \leftrightarrow MH_{ads} + H_2O$ Volmer (acid) (1)

$H_2O + M + e \leftrightarrow MH_{ads} + OH^-$ Volmer (neutral, alkaline) (2)

$MH_{ads} + H_3O^+ + e \leftrightarrow H_2 + H_2O + M$ Heyrovsky (acid) (3)

$MH_{ads} + H_2O + e \leftrightarrow H_2 + OH^- + M$ Heyrovsky (neutral, alkaline) (4)

$2MH_{ads} \leftrightarrow H_2 + 2M$ Tafel (5)

$MH_{ads} \leftrightarrow MH_{abs}$ (6)

where M represents the metal surface and MH_{ads} represents the adsorbed hydrogen on the metal surface. Reactions (1-2) form atomic hydrogen adsorbed on the surface. The adsorbed hydrogen can be desorbed by the electrochemical (Heyrovsky reaction, 3 or 4) or the chemical (Tafel reaction, 5) desorption reaction to form molecular hydrogen, and leave the steel surface. Alternatively, part of the adsorbed hydrogen enters into the metal, through the hydrogen absorption reaction (reaction 6).

Two models have been proposed (Bockris, McBreen & Nanis, 1965; Crolet & Bonis, 2001; Flitt & Bockris, 1981) for the hydrogen entrance into the metal. Model A considers that the adsorbed atomic hydrogen enters into the metal substrate. The hydrogen absorption reaction and hydrogen recombination processes are competing. The passage of atomic hydrogen into metal depends on the surface coverage (θ) and on the number of available sites for the hydrogen to occupy. The absorption of hydrogen leads to accumulation to a concentration (C_0) under the surface. As the surface coverage, θ, is determined by the charging conditions (surface coverage increases with decreasingly negative applied potential and current) and temperature, the subsurface concentration of hydrogen, C_0, depends on the charging conditions (applied potential and current), temperature and state of the surface, such as presence of poisons or oxides, and the adsorption of species other than hydrogen on the surface.

In the other model, model B, a discharged hydrogen proton proceeds directly through the interface into the metal substrate without passing through the intermediate adsorbed state and thus, the hydrogen absorption reaction is competing with the hydrogen evolution processes for the same discharged protons. The transfer of a discharged hydrogen proton H^+ could occur from water as well as by deprotonation of other complexes adsorbed on the surface, such as H_2S becomes HS^-.

3.3 Hydrogen diffusion

Diffusion is the movement of a substance from a high concentration to a low concentration. The driving force for the diffusion of hydrogen is a gradient of chemical potential, typically due to a variation in concentration, c, mol cm^{-3}. The diffusion flux of hydrogen, J, mol cm^{-2} s^{-1}, can be represented with Fick's first law:

$$J = -D\frac{\partial C}{\partial x} \tag{7}$$

where D, cm^2 s^{-1}, is the diffusion coefficient. The diffusion flux is proportional to the concentration gradient. Eq. 7 applies to an isotropic medium. The diffusion coefficient D is exponentially dependent on temperature T, as given by:

$$D = D_0 \exp\left(-\frac{Q}{RT}\right) \tag{8}$$

where Q , kJ mol^{-1}, is the activation energy, D_0, cm^2 s^{-1}, is the constant, pre-exponential term, and R, J mol^{-1} K^{-1}, is the gas constant.

To understand hydrogen transportation in the bulk steel, it is important to know the hydrogen diffusion coefficient D (apparent and intrinsic), and the subsurface hydrogen concentration C_0, which allows evaluation of the amount and diffusion speed of hydrogen in the steels. These two crucial parameters can be measured using permeation experiments.

In 1962, Devanathan and Stachurski (1962) established a sensitive electrochemical technique that permitted the recording of the instantaneous permeation rate of electrolytic hydrogen through palladium membranes by using a simple double–cell arrangement. Fig. 5 presents a schematic drawing of an electrolytic permeation apparatus (Atrens, Mezzanotte, Fiore & Genshaw, 1980; Liu & Atrens, 2015; Liu et al., 2014).

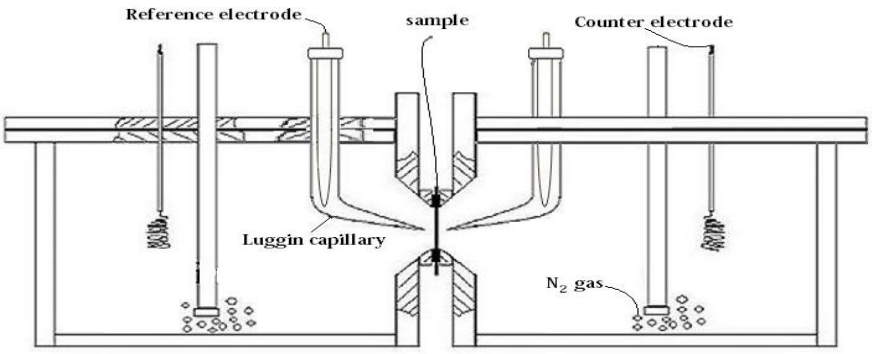

Fig. 5 Schematic of the permeability cell.

The two cells are separated by a thin metal membrane electrode of the test material. One side (typically the left side) of the membrane acts as the cathodic side, and the opposite side acts as the anodic side. The cathodic polarization of one side and anodic polarization of the opposite side ensure that the coverage of hydrogen on the membrane is maintained at a certain fixed concentration on one side, and on the opposite side the hydrogen concentration is zero. As viewed from the hydrogen evolution and entry reactions, hydrated protons are reduced from the aqueous solution under cathodic polarization at one side of the cell mostly by combining to form hydrogen gas bubbling away from the electrode surface, and a small fraction absorbed at the membrane surface diffusing through the membrane to the opposite side, which is under anodic polarization. The anodic polarization oxidises the emerging hydrogen atoms, and removes them from the membrane. Thus an increase of current as a function of time is recorded on the anode side. This current increases and reaches a steady value. The recorded current is a direct measure of the instantaneous permeation rate of hydrogen. The sensitivity of this method reveals details in the permeation. Subsequently, much research (Addach, Berçot, Rezrazi & Takadoum, 2009; Atrens, Mezzanotte, Fiore & Genshaw, 1980; Devanathan & Stachurski, 1964; Liu et al., 2014; Manolatos et al., 1995a,b,c; Wang et al., 2013; Zakroczymski, 2006) on hydrogen diffusion and permeability has been conducted based on this method of Devanathan and Stachurski.

When using the technique of Devanathan and Stachurski to study the diffusion and permeation of steels, a palladium coating is typically applied on the anodic side (Atrens, Mezzanotte, Fiore & Genshaw, 1980; Devanathan & Stachurski, 1964; Liu et al., 2014; Manolatos & Jerome, 1996; Zakroczymski, 2006). Without a palladium coating, a passive layer could be formed on the detection side and acts as a barrier to hydrogen permeation (Addach, Berçot, Rezrazi & Takadoum, 2009; Manolatos et al., 1995a,b,c). Atrens et al. (1980) introduced a palladium layer on the detection side of their Ni specimen to avoid Ni

oxidation during their study of hydrogen diffusion and permeability in Ni. Devanathan and Stachurski (1964) also adopted a palladium coating on the detection side to reduce the possibility of passivation when they studied the hydrogen diffusion in iron. In contrast, the studies of Manolatos et al. (1995a,b) did not use the palladium coating on the hydrogen exit side. They found that a passive layer was formed and was a barrier to hydrogen permeation, depending on the time and the applied potential on the exit side. They further suggested that this barrier might cause hydrogen accumulation, and thus result in unreliable hydrogen diffusion parameters. Moreover, they proposed that these phenomena did not occur with a palladium layer on the detection side, since the oxidation of hydrogen occurs fast and completely at a palladium coated surface. Similarly, Addach et al. (2009) studied hydrogen permeation in iron without a palladium layer on the detection side, and also found a lower hydrogen permeation flux with a longer passivation time. They attributed this difference of the permeation curves to the passive layer formed on the detection side of the specimen acting as a barrier to the hydrogen permeation.

Permeation experiments allow determination of the diffusion coefficient D (apparent and intrinsic) and the subsurface hydrogen concentration C_H, via the following methods.

3.3.1 Time lag method

The time lag method for calculating D (Boes & Züchner, 1976; Daynes, 1920; Devanathan & Stachurski, 1962) can be understood by considering Fick's second law:

$$\frac{\partial C}{\partial t} = D\frac{\partial^2 c}{\partial x^2} \tag{9}$$

The initial and boundary conditions are assumed to be:

$$t = 0,\ C = 0 \text{ for } 0 < x < L \tag{10}$$

$$t > 0,\ C = C_0 \text{ for } x = 0;\ C = 0 \text{ for } x = L \tag{11}$$

and a permeation transient is measured on the exit side of the steel membrane.

In time-lag method, the diffusion coefficient D is related to time lag as follows:

$$D = \frac{L^2}{6\, t_L} \tag{12}$$

where L, cm, is the thickness of the sample, and t_L, s, is the time lag, given by the intercept on the t-axis of the extrapolation of the straight line in the current-time curve. Usually, t_L is the corresponding time at which the permeation rate is 0.63 times the steady-state value.

The time-lag method is widely used because of its simplicity. However, the time-lag method has drawbacks. A serious shortcoming is that the values of D obtained at low temperatures scattered widely (Kiuchi & McLellan, 1983).

3.3.2 The breakthrough method

The breakthrough time method (Boes & Züchner, 1976; Devanathan & Stachurski, 1962) evaluates the breakthrough time, t_b, as the time for the first hydrogen to arrive at the detection side of the sample after the boundary conditions at the anodic side have been changed. The diffusion coefficient is evaluated using:

$$D = \frac{L^2}{15.3\ t_b} \tag{13}$$

3.3.3 Successive transient method

In the successive transient method (Atrens, Mezzanotte, Fiore & Genshaw, 1980; Hadam & Zakroczymski, 2009; Liu et al., 2014; McBreen, Nonis & Beck, 1966; Zakroczymski, 2006), rise or decay permeation transients are measured after the prior transient has achieved steady state conditions. The formation of a rise or decay transient is the result of changing cathodic polarization potential by either an increase or a decrease, respectively. Atrens et al. (1980) and McBreen et al. (1966) (i) defined a generalized transient in terms of a normalized current parameter, $\frac{i_\tau - i_\infty^0}{i_\infty^1 - i_\infty^0}$, and a dimensionless time parameter, $\tau = \frac{Dt}{L^2}$, (ii) showed that a normalised experimental permeation transient plotted against time t, could be compared with the generalised transient to yield a value of B from:

$$\log \tau = \log B \tag{14}$$

where $B = \frac{D}{L^2}$ is the distance of displacement, which enabled evaluation of D. Alternatively, once the experimental and master curves are brought into coincidence, each t value fixes a value of τ, and thus, D may be determined by:

$$D = L^2\ \log^{-1}\left[\log(\tau/t)\right] \tag{15}$$

3.3.4 Refined successive transient method

A refined successive transient method was developed by Liu et al. (2014). Based on McBreen et al. (1966), Zakroczymski (2006) expressed the permeation transient by the following equations:

$$\frac{i_p - i_p^0}{i_p^\infty - i_p^0} = \frac{2L}{\sqrt{\pi Dt}} \sum_{n=0}^{\infty} \exp\left(-\frac{(2n+1)^2 L^2}{4Dt}\right) \quad \text{(Rise transients)} \quad (16)$$

$$\frac{i_p - i_p^\infty}{i_p^0 - i_p^\infty} = 1 - \frac{2L}{\sqrt{\pi Dt}} \sum_{n=0}^{\infty} \exp\left(-\frac{(2n+1)^2 L^2}{4Dt}\right) \quad \text{(Decay transients)} \quad (17)$$

where i_p, μA cm^{-2}, is the measured permeation rate at time t, i_p^0 is the initial steady-state permeation rate at time t = 0, i_p^∞ is the new steady-state permeation rate, L is the thickness of the membrane. In particular, for the first charging $i_p^0 = 0$, and for the complete decay $i_p^\infty = 0$. For the partial rise, $0 < i_p^0 < i_p^\infty$, and for the partial decay, $0 < i_p^\infty < i_p^0$.

Liu et al. (2014) fitted the pertinent permeation equation to the experimental permeation transient to determine the diffusion coefficient D.

3.3.5 Other methods

There are additional methods for determining the diffusion coefficient D (Boes & Züchner, 1976; Devanathan & Stachurski, 1962; Zhang & Zheng, 1998).

3.3.6 Hydrogen concentration

The hydrogen concentration of the entrance side of the membrane, C_H, mol cm^{-3}, can be evaluated from the diffusion coefficient, D, using:

$$C_H = \frac{i_p^\infty L}{F D} \quad (18)$$

where F = 96485 s A mol^{-1}, is the Faraday constant, L, cm, is the thickness of the membrane, and i_p^∞, μA cm^{-2}, is the steady-state permeation rate.

3.4 Hydrogen diffusion measurements

Atrens et al. (1980) studied hydrogen diffusion and permeability in annealed Ni from 25 to 90 °C. In a typical permeability experiment, after a potential was applied to the input side of the permeability membrane, the current increased from zero to a steady state value. Various potentials were applied in succession after steady state had been attained at the prior

potential. Depending on whether the potential was increased or decreased, rise or decay transients were obtained, respectively. Individual rise and decay transients, and successive rise transients were recorded at each temperature. Analysis of these transients using the aforementioned successive transient method gave values of the diffusion coefficient D. Fig. 6 presents a plot of D vs T^{-1} of the authors' data as compared with the data designated KGB of Katz, Guinan, and Borg (Katz, Guinan & Borg, 1971). The dashed line designated KGB represents D values determined from outgassing of high purity (99.999%) Ni single crystals at higher temperatures. The solid line was for permeation experiments with rise transients. There was a small, but significant, decrease in D from the KGB line to the D_{rise} data, and to the D_{decay} data. These differences can be explained in terms of differences in H trapping. Due to the use of high purity Ni, the trapping effect was small.

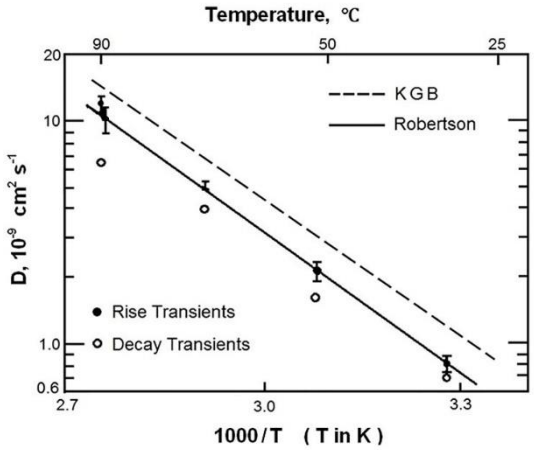

Fig. 6 Variation of the diffusivity D with T^{-1} (Atrens et al. 1980).

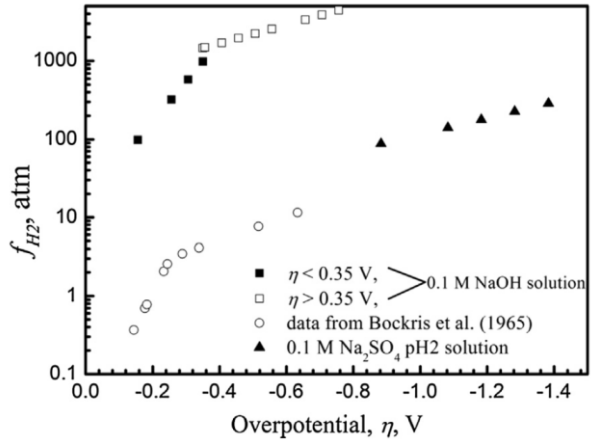

Fig. 7 Hydrogen fugacity versus overpotential for a low interstitial steel from the work of Liu et al. (2014) charged in (i) 0.1 M NaOH (squares and circles) and (ii) acidified (pH2) 0.1 M Na_2SO_4 solution (triangles).

Liu et al. (2014) determined the relationship between electrolytic charging conditions and hydrogen fugacity of low interstitial steel, see Fig. 7, using the permeation technique

based on the method of Devanathan and Stachurski. Palladium was plated on the detection side of the specimen to prevent oxidation. 0.1M NaOH solution was used in the hydrogen detection cell, while the charging cell contained either acidified pH 2 0.1M Na_2SO_4 solution, or 0.1M NaOH solution. The successive transient method was used for evaluating the diffusion coefficient D. A series of successive partial rise and decay transients were recorded both in acid and alkaline charging solutions. The average D values obtained from acid and alkaline charging solutions were $6.4 \pm 0.7 \times 10^{-5}$ and $4.4 \pm 0.4 \times 10^{-5}$ cm^2 s^{-1}, respectively.

Begić Hadžipašić et al. (2011) studied the influence of microstructure on hydrogen diffusion and embrittlement of multiphase structural steels with increased plasticity and strength. The diffusion of hydrogen was studied using Devanathan and Stachurski's method, with 2 mol L^{-1} H_2SO_4 as the charging solution, and 1 mol L^{-1} NaOH on the anodic side. The anodic side of the metal membrane was coated with nickel to ensure the membrane was passivated and corrosion resistant. The effective diffusion coefficient D_{eff} values, calculated by the time-lag method, for DP and TRIP steels were 7.5×10^{-7} and 5.7×10^{-7} cm^2 s^{-1}, respectively. The effective diffusion coefficient D_{eff} referred to the diffusion coefficient obtained with the influence of trapping effects, and thus was lower than the diffusion coefficient obtained from low interstitial steels by Liu et al. (2014).

3.5 Hydrogen trapping

3.5.1 Influence of traps

During hydrogen diffusion in steels, the hydrogen atoms are located in the interstitial sites and also attractively interact with microstructure features, such as voids, crack tips, dislocations, grain boundaries, carbide interfaces and impurities. These microstructure features are characterized as hydrogen traps (Araújo, Vilar & Palma Carrasco, 2014; Castaño Rivera, Ramunni & Bruzzoni, 2012; Lee & Lee, 1986). Hydrogen atoms are bound by these traps. Consequently, a hydrogen atom spends more time in such a trap site than in a normal interstitial lattice site. Hydrogen trapping influences the hydrogen distribution in the microstructure, the hydrogen diffusion coefficient, the hydrogen solubility, and the hydrogen embrittlement susceptibility of a material. Hydrogen trapping increases hydrogen solubility.

Hydrogen trapping also decreases the hydrogen transportation rate by decreasing the effective diffusion coefficient. The magnitude of this decrease depends on (i) the strength of the traps, which can be represented by the hydrogen-trap binding energy E_b, and (ii) the density of trap sites N_T, which is the number of trap sites per unit volume (Castaño Rivera,

Ramunni & Bruzzoni, 2012). Both these parameters can be obtained by experimental techniques, such as permeation measurements (Dong, Liu, Li & Cheng, 2009; Liu & Atrens, 2015) and hydrogen thermal desportion spectroscopy (Lee & Lee, 1986; Pérez Escobar et al., 2013a,b).

A number of mathematical models have been proposed for hydrogen trapping effects. McNabb and Foster (1963) developed a kinetic model based on trapping. Oriani (1970) reformulated this model by assuming the existence of a local equilibrium between trapped hydrogen atoms and mobile hydrogen. They suggested that solid-solid interfaces are the more important microstructural feature for hydrogen trapping in non-cold-worked steels, though dislocations are also trapping sites.

3.5.2 Trap density

Yen and Huang (2003) studied the effects of cold work on hydrogen diffusivity, hydrogen concentration and hydrogen trap density in AISI 430 stainless steel via permeation experiments. Based on the approach of Oriani (1970), they proposed that the density of trapping sites, N, per unit volume, was determined by:

$$N = \frac{C_0}{3}\left(\frac{D_L}{D_{eff}} - 1\right) \tag{19}$$

where C_0, mol cm^{-3}, is the hydrogen concentration just inside the metal surface and in equilibrium with the hydrogen source, D_L, cm^2 s^{-1}, is the lattice diffusion coefficient of hydrogen in α-Fe, and D_{eff}, cm^2 s^{-1}, is the effective hydrogen diffusion coefficient. However, Araújo et al. (2014) argued that the calculated value of the trapping site density, using Eq. 19, was so small that the hydrogen trapping effect could be neglected, and was inconsistent with the scale unit of the parameter N. Thus, they proposed to add Avogadro's constant N_A to Eq. 19.

Dong et al. (2009) and Haq et al. (2013), considering the hydrogen trap binding energy, proposed that the number of hydrogen trap sites per unit volume, N_T, is given:

$$\ln\left(\frac{D_L}{D_{eff}} - 1\right) = \ln\frac{N_T}{N_L} + \frac{E_b}{R}\times\frac{1}{T} \tag{20}$$

where, D_L, cm^2 s^{-1}, is the lattice diffusion coefficient of hydrogen, N_L, sites cm^{-3}, is the density of the interstitial sites in the steel, E_b, kJ mol^{-1}, is the hydrogen trap binding energy, R is the gas constant, which equals to 8.314 J mol^{-1} K^{-1} and T, K, is the absolute temperature.

When applying the model of Dong et al. (2009), the relevant parameters such as D_L, E_b and N_L may be unavailable for the studied steel. In that case, parameters of α-Fe have been applied as per Dong et al. (2009), however, this can lead to incorrect values of trapping site density by more than one order of magnitude (Araújo, Vilar & Palma Carrasco, 2014).

Zakroczymski (2006) proposed an alternative method to determine the hydrogen trap density using the electrochemical permeation and desorption techniques. The lattice diffusivity of hydrogen, and the amounts and distribution of diffusible and trapped hydrogen, were determined by analysing the partial permeation transients and the desorption rate of hydrogen from both sides of the membrane, respectively. It was suggested that the complete decay was sensitive to hydrogen de-trapping and thus could be used for the characterisation of the reversibly trapped hydrogen. The area under the experimental obtained desorption curve corresponded to the total amount of lattice diffused and trapped hydrogen. The area under the theoretical permeation decay curve, constructed with D_L and steady state current density, corresponded to the lattice diffused hydrogen. By integration of these two curves, one could determine the area difference, which represented the amount of reversible trapped hydrogen.

3.5.3 Trapping sites

A hydrogen trap can be any metallurgical defect, such as a void, crack tip, dislocation, carbide interface, or impurity. Traps are characterized as reversible and irreversible (Krom & Bakker, 2000; Luppo & Ovejero-Garcia, 1991). Irreversible sites are sites with a high trap activation energy, and thus the saddle point energy is much higher than the activation energy of lattice diffusion, making the de-trapping of hydrogen quite difficult. In other words, for an irreversible trap site, the trap activation energy E_{aT} is much higher, more than 60 kJ mol^{-1}, than the trap binding energy, which represents the strength of the trap. Examples of irreversible trap sites are inclusions and carbide interfaces. In contrast, hydrogen de-trapping is easier from trap sites with a lower saddle energy. These are characterized as reversible traps. Examples are dislocations, grain boundaries and micro-voids. The trap activation energy E_{aT} of reversible trap site is usually less than 60 kJ mol^{-1}. Hydrogen atoms have a limited residence time in reversible trap sites. Pressouyre (1979) stated that the irreversible hydrogen traps would always function as sinks, which were hard for hydrogen to jump out from. In contrast, reversible hydrogen traps influenced the hydrogen embrittlement susceptibility, since those traps might be detrimental hydrogen sources.

3.5.4 Trapping and HE

Ryu et al. (2012) indicated that austenite serves as a reversible trapping site more potent than grain boundaries or dislocations in ferrite. This was based on a study of hydrogen trapping in multiphase TRIP steels using thermal desorption spectroscopy. They suggested that the partial transformation from austenite to martensite resulted in an alteration in the trapping condition of hydrogen, and suggested that this phase transformation caused a reduction in the trap binding energy, leading to easier hydrogen diffusion, resulting in an enhanced deterioration in ductility of TRIP steels containing austenite. Laureys et al. (2016) found similar results that, after deformation, the newly formed martensite was supersaturated with hydrogen, which came from the original austenite acting as a hydrogen trap, and this explained the fact that they found most of the cracks initiated in or along martensitic regions. In addition, they also proposed other hydrogen traps, such as dislocations in ferrite and bainite, introduced by stresses in these regions due to phase transformation.

So et al. (2009) studied the hydrogen delayed fracture (HDF) and internal hydrogen behaviour in TWIP steels, using (i) slow strain rate tests (SSRT) to evaluate the effects of diffusible hydrogen on hydrogen delayed fracture, and (ii) thermal desorption analysis (TDA) to identify the major trapping sites of diffusible hydrogen, and to determine the activation energies for hydrogen desorption at the trapping sites. They found that the major hydrogen trap sites in TWIP steels were dislocations, grain boundaries and twins, with activation energies for hydrogen de-trapping of around 35 kJ mol^{-1} for dislocations or grain boundaries, and 62 kJ mol^{-1} for twins. They proposed that TWIP steels exhibited good immunity to hydrogen delayed fracture, compared with other high-strength steels. This was partially due to the absence of strain or hydrogen charging induced transformation of austenite to either α- or ε-martensite. In contrast, Lee et al. (2016) found hydrogen trapped by mechanical twins and in the ε-martensite formed during transformation, and further observed some brittle features caused in these hydrogen trapped regions.

In addition, for TWIP steels, which are fully fcc austenitic, the hydrogen diffusion coefficient is at least three orders of magnitude lower than for bcc steels (So et al., 2009). The coincidence site lattice (CSL) boundaries are preferential deep hydrogen traps (Oudriss et al., 2014), where trapped hydrogen is not diffusible, and contribute to a better resistance to HE (Chun, Park & Lee, 2012; Oudriss et al., 2014). In the coincidence site lattice (CSL) theory, Σ represents the degree of fit between the structures of two grains, equal the reciprocal of the ratio of the coincidence sites to the total sites. The coherent Σ3 twin boundaries are usually

considered as coincidence site lattice (CSL) boundaries. Some boundaries with low Σ, such as coherent Σ3 twin boundaries, have special properties. In a study of stainless steels, the coherent Σ3 twin boundaries were reported to be the only crack resistant boundaries (Gertsman & Bruemmer, 2001). However, in other studies (Koyama et al., 2012a,b; Müllner, 1997), cracking on twin boundaries was reported, even on coherent Σ3 twin boundaries. An explanation for this inconsistancy is addressed in section 7.2.

4. Hydrogen embrittlement

4.1 Introduction

Hydrogen embrittlement, first described in 1874 (Johnson, 1874), is the designation of the phenomenon in which hydrogen decreases of mechanical properties of a metal. This degradation can range from (i) subcritical crack growth leading to fracture at a low applied stress, to (ii) some decrease in ductility with no decrease in yield stress, no decrease in the tensile strength and no sub-critical crack growth. Hydrogen embrittlement is of concern for high-strength steels (Hardie, Charles & Lopez, 2006). Hydrogen may be unintentionally introduced into the steel by finishing and forming processes (Lovicu et al., 2012), such as electroplating, forging and welding, and by corrosion and cathodic protection (Robinson & Kilgallon, 1994). The degree of hydrogen embrittlement is dependent on many variables such as hydrogen concentration, temperature, level and type of applied or residual stress, microstructure and surface condition of the steel (Lovicu et al., 2012; Michalska, Chmiela, Łabanowski & Simka, 2014). Susceptibility to hydrogen embrittlement has been found to increase successively for lower bainite, quenched and tempered martensite or bainite, pearlite or spheroidized structures and un-tempered martensite. In addition, steels with finer grain size and carbide size are more resistant to hydrogen embrittlement (Hirth, 1980; Lovicu et al., 2012).

Many mechanisms of hydrogen embrittlement have been proposed. The three most likely mechanisms of HE in steel, which is a non-hydride forming material, are outlined below.

4.2 Hydrogen enhanced decohesion (HEDE)

The decohesion theory, proposed by Troiano (1960) and developed by Oriani et al. (1970, 1974), is based on the idea that hydrogen accumulated within the lattice reduces the interatomic cohesive forces. The reduction of interatomic cohesive forces results from the

increased interatomic distance due to the electron transfer from the 1s band of hydrogen to the 3d and 4s bands of iron.

Oriani and Josephic (1974) postulated that the highly elastically-stressed region at the crack front lowered sufficiently the chemical potential of dissolved hydrogen, which attained a concentration several orders of magnitude larger than in normal lattice sites and lowered the cohesive energy. Cracks propagated when the local crack tip tensile stress exceeded the atomic cohesive energy. This fracture initiated at a distance ahead of the crack tip where the tensile stress was a maximum.

The hydrogen enhanced decohesion (HEDE) mechanism is supported by the facts (Oriani, 1987) that (i) large concentration of hydrogen should accumulate at crack tips where there are high stresses, and (ii) atomistic simulations reveal that hydrogen can reduce atomic cohesion. The hydrogen enhanced decohesion (HEDE) mechanism considers that there is a critical concentration of hydrogen which causes brittle fracture. HEDE could also cause intergranular fracture, in which a high concentration of hydrogen accumulates at grain boundaries and thus reaches the critical concentration for brittle fracture.

4.3 Hydrogen enhanced localized plasticity (HELP)

This mechanism, first formulated by Beachem (1972), proposes that hydrogen enhances dislocation motion so that the localized plastic deformation is large enough to cause subcritical crack growth with macroscopically brittle characteristics. The presence of hydrogen in solid solution increases dislocation mobility and creates localised high deformation regions. The increase of dislocation mobility is attributed to the reduction in the interactions between dislocations or between dislocations and other obstacles. The dislocations thus move closer to each other and to obstacles, forming more compact pile-ups and less ductile zones. These dislocation pile-up zones are surrounded by high deformation regions, and the applied stress is concentrated on these zones which macroscopically occupy a small portion of the cross section. Failure occurs when the tensile stress in these zones is higher than the ultimate tensile strength of the material. This fracture process leads to cracking by microvoid coalescence along preferred crystallographic glide planes (Abraham & Altstetter, 1995; Liang et al., 2008).

Robertson (2001) conducted deformation studies in a hydrogen environment in situ in a TEM equipped with an environmental cell to elucidate the mechanisms of hydrogen embrittlement. The hydrogen enhanced localized plasticity (HELP) mechanism was supported by observations revealing increased number of dislocations in a pile-up, and

decreased stacking-fault energy, as well as the increased crack propagation rate caused by solute hydrogen.

4.4 Adsorption-induced dislocation emission (AIDE)

The AIDE mechanism was developed by Lynch (1988, 2012). The AIDE model involves both dislocation nucleation and subsequent movement away from the crack tip. The nucleation of dislocations is facilitated by the adsorbed hydrogen at the surface of the crack tip. During the nucleation, the adsorbed hydrogen weakens the interatomic bond, facilitating the simultaneous formation of a dislocation core and a surface step by the breaking and reforming of interatomic bonds. Once the nucleation is accomplished, dislocations can readily move away from the crack tip under the applied stress, contributing to the crack growth.

In the AIDE model, in addition to dislocation emission, crack growth involves the nucleation and growth of microvoids at the crack tip. The nucleation and growth of voids occurs because the stresses for dislocation emission are so high that some dislocation activity occurs ahead of the crack. Although the void formation can contribute to the crack growth, the crack growth primarily occurs by the dislocation emission from crack tips.

4.5 Other mechanisms

Other mechanisms, such as the internal pressure theory (Zapffe & Sims, 1941) and hydride induced embrittlement (HIE) (Petch & Stables, 1952; Westlake, 1969), have been proposed. There have also suggestions (Gangloff, 2003; Koyama et al., 2014) of mixed mechanisms.

5. HE in DP steels

5.1 Mechanical degradation

The influence of hydrogen on the mechanical properties is often studied using slow tensile tests, which enable the measurements of the yield strength, ultimate tensile strength, total elongation and reduction in cross section. A smooth cylindrical, a notched cylindrical or a plane sample is subjected to a slow, continuously-increasing tensile strain in air or in various hydrogen environments until failure. Two widely used methods are the slow strain rate test (SSRT) (Koyama, Akiyama & Tsuzaki, 2012a,b; Lovicu et al., 2012; Ryu et al., 2012; So et al., 2009; Zhu et al., 2014) and the linearly increasing stress test (LIST) (Atrens

et al., 1993; Gamboa & Atrens, 2005; Liu, Irwanto & Atrens, 2013; Ramamurthy, Lau & Atrens, 2011; Ramamurthy & Atrens, 2010; Venezuela et al., 2015; Villalba & Atrens, 2008a,b, 2009; Winzer et al., 2008).

The LIST allows direct measurement of the stress at which hydrogen induced cracking begins. For SSRT, the strain is increased until fracture. Embrittlement can be characterised using (i) the threshold stress for the initiation of subcritical hydrogen cracking, (ii) the change of ductility, and (iii) the hydrogen embrittlement index. The change of ductility is measured either as a total elongation (e) or as the reduction in area at fracture (R_A %).

$$e = \frac{l_f - l_i}{l_i} \times 100\% \quad (21)$$

$$R_A\,\% = \frac{A_i - A_f}{A_i} \times 100\% \quad (22)$$

where l_f , mm, is the final gauge length, li , mm, is the initial gauge length, A_i , mm^2, is the initial area, A_f , mm^2, is the final fracture area.

The hydrogen embrittlement index I can be evaluated using (Begić Hadžipašić, Malina & Malina, 2011; Loidl, Kolk, Veith & Göbel, 2011):

$$I = \frac{R_{A,air} - R_{A,H}}{R_{A,air}} \times 100\% \quad (23)$$

where the $R_{A,air}$ is the reduction in area in air, and $R_{A,H}$ is the reduction in area in the hydrogen charging environment. The index can range from 0 to 100%, where 0% indicates no hydrogen embrittlement and 100% indicates zero ductility in hydrogen.

Loidl et al. (2011) studied the hydrogen embrittlement of automotive advanced high-strength steels. Slow strain rate tests (SSRT) were conducted in helium and a gaseous hydrogen environment to investigate the effect of hydrogen on the mechanical properties of various AHSS, including DP 1000 and DP 1200. Changes of strength, total elongation, and hydrogen embrittlement index were used to characterise the effect of hydrogen on the steels. For the DP steels, neither the yield strength nor the ultimate tensile strength changed significantly in the presence of hydrogen, meaning that there was no noteworthy effect of hydrogen on the strength of the steels. However, there was considerable loss of ductility for the DP steels. The DP 1000 and DP 1200 experienced decreases of total elongation from 12% to 7% and from 9% to 5%, respectively, resulting in a hydrogen embrittlement index of 40% and 47%, respectively, which were higher than those of complex phase (CP) and martensitic

steels with similar strengths, tested under the same conditions. But the authors claimed that the slow strain rate testing was just one possible method to judge hydrogen embrittlement in steels. They suggested that other methods, such as hydrogen induced delayed fracture with static loading, also needed to be investigated in order to gain a more comprehensive understanding of the behaviour of different steel grades under the influence of hydrogen.

Begić Hadžipašić et al. (2011) obtained similar results in their investigation of the influence of microstructure on hydrogen embrittlement of DP and TRIP steels. Tensile testing was carried out to evaluate changes of mechanical properties of hydrogen charged specimens. The hydrogen charging was conducted by cathodic polarization at –700 mV_{SCE} for four hours at 19 ± 2 °C. The tensile tests were started within 30 minutes after the cathodic polarization. Hydrogen did not significantly influence the yield strength and ultimate tensile strength, but decreased total elongation and reduction of area. The reduction of area of DP steel decreased from 64% to 26%, resulting in a hydrogen embrittlement index of 59%, indicating that the DP steels had low resistance to hydrogen embrittlement, which they ascribed to the presence of martensite.

Davies (1981) also studied the influence of hydrogen on DP steels, using two DP steels with tensile strength of 690 MPa. Hydrogen charging did not significantly decrease the tensile strength, but the total elongation decreased considerably from 23% to 6% and from 21% to 5%, respectively. SEM observations and delayed fracture tests reinforced the conclusion that the DP steels were susceptible to hydrogen embrittlement, and this susceptibility was due to the presence of high-carbon, high-strength matensite islands in the microstructure.

Koyama et al. (2014) studied hydrogen embrittlement of DP steels. Neither the yield nor the tensile strength changed significantly after hydrogen charging, whereas the ductility decreased by 52%, indicating that the DP steel was influenced by hydrogen embrittlement.

Depover et al. (2014) studied the effect of hydrogen charging on the mechanical properties of several advanced high strength steels, including DP steel, by tensile tests using two different speeds. The ductility loss was 54% for DP steel tested at the faster speed and was 73% at the lower test speed. Similar results were obtained when they investigated the role of hydrogen diffusion on hydrogen embrittlement susceptibility of DP steels (Depover, Wallaert & Verbeken, 2016). They determined the hydrogen uptake as a function of electrochemical pre-charging time and the corresponding influence of different charging time on the hydrogen embrittlement resistance. They found increased loss of ductility and brittle features with longer pre-charging time, up to 50% loss of ductility for samples saturated with hydrogen. They further proposed that the hydrogen embrittlement sensitivity increased with

decreasing test speed, providing hydrogen with enough time to diffuse to the stressed region ahead of the crack tip and facilitate the crack propagation.

5.2 Fractography

Davies (1981) observed a fracture change during hydrogen embrittlement from ductile dimpling to transgranular cleavage in their study of the hydrogen embrittlement of DP steels. The steel failed by ductile shear with considerable local necking without hydrogen. However, after hydrogen charging, the steel failed in a brittle manner, which was at right angles to the tensile axis, with no necking. Furthermore, Davies indicated that the fracture involved cleavage of both martensite and ferrite phases in the DP steels, and these cleavage cracks probably initiated in the stronger martensite, or at the interfaces between martensite and ferrite, and then propagated through the softer ferrite. The crack initiation might result from stress concentration caused by the different strain hardening rates of ferrite and martensite. The presence of hydrogen assisted crack initiation was caused either by lowering the lattice cohesive energy resulting in transgranular fractures, or by changing the ferrite slip character resulting in increasing stress concentration at the head of a dislocation pile up, or by a combination of both.

Sun et al. (1989) also found that cracks initiated along the interfaces between martensite and ferrite, and along the martensite lath boundaries when they investigated the hydrogen influence on martensite and ferrite dual phase steels. They cathodically charged the specimens with hydrogen in a 5% sulphuric acid solution containing a small amount of arsenic trioxide at different current densities for 30 minutes. They found that the martensite lath boundaries widened with hydrogen charging. When the steel was cathodically charged at a high current density, a microcrack was nucleated along the boundary of lath martensite. The widening was also occurred at the interfaces between martensite and ferrite. The interfaces widened and changed from a smooth form, into a tortuous form with increasing cathodic charging current density, resulting in a significant local stress at these interfaces, and crack initiation.

Koyama et al. (2014) studied the hydrogen influence on DP steels using a high-resolution scanning electron microscopy-based damage quantification technique, post-mortem electron channelling contrast imaging, electron backscatter diffraction analyses and in situ deformation experiments. They found that the cracks were initiated in martensite, and propagated along martensite and ferrite interfaces, or through ferrite. Furthermore, in the crack incubation period, hydrogen reduced the critical strain for decohesion in martensite by

the HEDE mechanism. When this critical strain was reached, decohesion associated martensite cracking initiated. Upon further straining, hydrogen facilitated cracks propagated along martensite and ferrite interfaces or through ferrite, associated with HEDE and HELP mechanisms, respectively.

Depover et al. (2014, 2016) found a change of fracture surface from ductile dimples to brittle transgranular cleavage after hydrogen charging. They observed a clear distinction between a brittle hydrogen affected region and a ductile non-affected zone. In their study (Depover, Wallaert & Verbeken, 2016), hydrogen charging started at the moment the tensile test started, so that the hydrogen diffusion distance and hydrogen effect could be studied at various cross-head displacement speed. At cross-head displacement speeds of 5 mm min^{-1} and 0.5 mm min^{-1}, a brittle zone was observed on both sides of the sample, whereas the fracture surface at the centre was still ductile. At the lower test speed, a larger hydrogen influenced zone was observed. However, at 0.05 mm min^{-1}, the distinction between the hydrogen affected zone and the non-affected zone became less obvious, with even some brittle features in the central region. They further claimed that their DP steel contained a Mn-rich segregation line in the centre, providing more MnS precipitates and thus attributing to hydrogen induced cracking, as also reported by others (Pérez Escobar et al., 2011). In addition, they suggested that the more significantly increased dislocation densities at the slowest speed attributed to an increase in hydrogen diffusion coefficient, so that hydrogen might be able to diffuse to the central part of the sample and embrittle the segregation line.

5.3 Microstructure

Martensite has been identified as the cause of hydrogen embrittlement in DP steels (Begić Hadžipašić, Malina & Malina, 2011; Davies, 1981; Sun, Gu & Chen, 1989) as cracks initiated in the martensite, or at the interface between martensite and ferrite.

The influence of the martensite content on hydrogen embrittlement in DP steels (Davies, 1983) was studied using a series of specimens quenched into brine from a salt bath at different temperatures, so as to produce ferritic and martensite structures, containing from 5 to 45% martensite, situated along the ferrite grain boundaries. With increasing martensite content, the ferrite grain size decreased, and the tensile strength linearly increased. However, the susceptibility to hydrogen embrittlement did not linearly increase with increasing tensile strength and martensite content. The ratio of uniform elongation after hydrogen charging to that without hydrogen was taken as a measure of hydrogen embrittlement. This ratio was plotted as a function of the martensite content for all the tested DP steels. For all the five

experimental steels, the embrittlement could be divided into three regions: (i) there was no hydrogen embrittlement in the first region up to 10% martensite; (ii) there was increasing hydrogen embrittlement in the second region as the martensite content increased from 10% to about 30%; and (iii) the embrittlent was constant for a martensite content greater than 30%.

This change of hydrogen embrittlement with martensite content was attributed to the variation in ferrite and martensite morphology. The grain size of the ferrite decreased and the size of martensite islands increased in the steels with martensite content up to 10%, which did not encounter hydrogen embrittlement. The size of martensite islands was not large enough to enable the cracks formed in the martensite to grow through the large volume of soft ferrite and cause failure. When the martensite content was in the range of 10 to 30%, the decreased ferrite grain size and increased size of the martensite islands along the ferrite grain boundaries allowed an easy path for crack propagation, and thus the susceptibility to hydrogen embrittlement increased. For steels containing more than 30% martensite, the regions of martensite almost linked together forming a continuous network, resulting in a constant degree of hydrogen embrittlement.

Davies (1981) studied the influence of martensite tempering at temperatures from 200 to 500 °C for DP steels that suffered hydrogen embrittlement caused by the martensite. He postulated that tempering to soften high-carbon martensite should reduce hydrogen embrittlement. The total elongation of hydrogen charged specimens increased with tempering temperature and at 500 °C approached that of the specimen without hydrogen charging. At the same time, the yield strength increased with increasing tempering temperature while the tensile strength decreased up to the tempering temperature of 350 °C. Thus, the tensile strength was unchanged by hydrogen charging for tempering temperatures of 350 °C and above.

Inclusions may influence hydrogen induced crack initiation (Begić Hadžipašić, Malina & Malina, 2011; Pérez Escobar et al., 2011). Begić Hadžipašić et al. (2011) used SEM to show that their dual phase steel contained many globular and elongated inclusions, identified by EDS to be (Ca, Al)-oxides, (Al, Mn)-oxisulphides and (Al, Mn)-oxicarbides. These inclusions acted as irreversible traps contributing to the susceptibility to hydrogen embrittlement of the DP steel. Elongated inclusions were also identified by Pérez Escobar et al. (2011). They found elongated MnS inclusions in the middle of the crack for their DP 600 steel, and suggested these particles play a role in the initiation of hydrogen-induced cracks.

In conclusion, hydrogen in DP steels may not decrease strength but may reduce ductility, and induce more brittle features on the fracture surface. The hydrogen associated

cracks might initiate in the martensite or at the interface between martensite and ferrite, and then propagate along the interfaces or through ferrite. The cracking mechanism was suggested to be HEDE and HELP. Inclusions might also play a role in the crack initiation. Hydrogen resistance could be improved by tempering.

6. HE in TRIP steels

6.1 Mechanical degradation

The hard martensite is the microstructure most susceptible to hydrogen embrittlement (Hirth, 1980). Furthermore, hydrogen has a higher diffusivity in martensite than in austenite, but a higher solubility in austenite. Mine et al. (2009) indicated that when austenite transforms to martensite, the excess hydrogen is released from the austenite, and can rapidly diffuse through the martensite. Since the crack propagation needs continuous hydrogen transport and accumulation at the crack tip, the crack advance was controlled by the hydrogen transport (Oriani & Josephic, 1974). Thus the increased diffusivity of hydrogen assisted crack propagation. Consequently, there is concern that TRIP steels, which have transformation induced plasticity, are susceptible to hydrogen embrittlement.

Ronevich et al. (2010) studied hydrogen embrittlement of commercial TRIP steels, and showed that increasing hydrogen content caused an increase of ductility loss without significant change in the deformation behaviour.

Lovicu et al. (2012) also observed similar changes in stress-strain curves in slow strain rate tests (SSRT) on TRIP 800 with different hydrogen contents. There was a significant increased ductility loss with increased hydrogen content. Furthermore, a critical hydrogen concentration was needed to cause hydrogen embrittlement. The critical hydrogen concentration of TRIP 800 steel was about 2.5 wtppm, which caused a hydrogen embrittlement index of about 27%. Combined with fractographic analysis, it was concluded that the TRIP 800 steel had some susceptibility to hydrogen embrittlement, attributed to the high hydrogen uptake of the austenite, and the tendency of this austenite to transform into embrittled martensite. Similarly, Ryu et al. (2012) showed a decrease in ductility with increasing hydrogen content for TRIP steels.

In a comparative study of hydrogen embrittlement of different multiphase ferritic steels (Loidl, Kolk, Veith & Göbel, 2011), TRIP 700 showed the highest tendency for hydrogen embrittlement. Slow strain rate tests (SSRT) indicated that the total elongation of TRIP 700 decreased from 30% to 10% resulting in hydrogen embrittlement index of 66%,

which was higher than other complex phase, dual phase and martensitic steels tested under the same conditions. In the TRIP steels, the deformation from austenite to martensite was the critical factor for hydrogen embrittlement, which was different from the mechanisms of other steels.

6.2 Fractography

TRIP steels experience a significant degradation of mechanical properties with increasing hydrogen content. Furthermore, the fracture surfaces exhibit a change from ductile dimples to brittle features, with an increasing brittle percentage with increasing hydrogen content (Loidl, Kolk, Veith & Göbel, 2011; Lovicu et al., 2012; Sojka et al., 2011; Zhu et al., 2014).

Lovicu at al. (2012) observed that fracture surfaces became increasingly brittle with increasing hydrogen content. The uncharged specimen exhibited a completely ductile fracture. With increasing hydrogen content, above the critical concentration of 2.5 wtppm, brittle features took up an increasing area of the fracture surface.

Sojka et al. (2011) investigated the influence of hydrogen on the fracture characteristics of two TRIP 800 C-Mn-Si steels at different hydrogen charging current densities of 15 mA cm^{-2} and 30 mA cm^{-2}, and with hydrogen absorption promoters. Charging lasted for 8 h at ambient temperature. The fractographic analysis showed that, without hydrogen charging, the failure characteristics of both steels were ductile failure characterised by a dimple morphology. After hydrogen charging, the fracture surfaces showed a change in the failure mechanism. For the lower charging current density of 15 mA cm^{-2} without a hydrogen absorption promoter, the fracture surfaces consisted of a mixture of transgranular ductile and transgranular cleavage fracture. For the higher current density of 30 mA cm^{-2}, or with a hydrogen absorption promoter in the solution, transgranular cleavage fracture became dominant for the fracture surfaces.

Lovicu et al. (2012) indicated that the cracks initiated near the regions of hard particles based on the transformation from austenite to martensite. In TRIP steels, the hydrogen behaviour was influenced by the presence of austenite. Due to the high solubility and low diffusivity of hydrogen in austenite, austenite was enriched in hydrogen with a higher concentration than the other phases. When the transformation from austenite to martensite occurred, because martensite has the highest susceptibility to hydrogen embrittlement, the hydrogen enriched transformed martensite cracked immediately, causing failure of the specimen. During this deformation, the unstable austenite was made less stable

by the presence of hydrogen, which induced further martensite transformation, and failure. This crack initiation mechanism was supported by other researches. Imlau et al. (2009) suggested that the crack forming region was highly correlated with the martensite transformation regions. Ronevich et al. (2010) found that some cracks initiated from hard martensite islands and propagated into ferrite grains. Laureys et al. (2016) highlighted similar crack initiation mechanisms in their study of hydrogen induced cracking in TRIP steel using EBSD. They found that cracks initiated mostly in or between two martensitic regions by decohesion and then propagated in the ferrite or the martensite and the matrix interface. Zhu et al. (2013) also used EBSD to study hydrogen induced cracking in TRIP steels and revealed that cracks initiated in martensite, which was freshly transformed from the unstable austenite, and propagated into the adjacent ferrite.

6.3 Microstructure

The microstructure, alloying elements, deformation and manufacture processes, can affect the influence of hydrogen on steels.

Many researches (Loidl, Kolk, Veith & Göbel, 2011; Lovicu et al., 2012; McCoy & Gerberich, 1973; Ronevich et al., 2010, 2012) attribute hydrogen embrittlement of TRIP steels to the transformation of austenite into martensite on straining. McCoy et al. (1973), stated that the TRIP steel was relatively immune to hydrogen embrittlement in the austenitic state but when the austenite transformed into martensite induced by straining, the transformed martensite was brittle, and led to premature failures of TRIP steels.

Ryu et al. (2012) studied the effect of deformation on the hydrogen influence on TRIP steels in respect to hydrogen trapping and effusion, characterized using thermal desorption spectroscopy (TDS). Plastic deformation caused the transformation from austenite to martensite and led to an alternation of the inherited trapped hydrogen. The austenite in TRIP steels had a relatively larger solubility for hydrogen than that of generic traps in ferrite and martensite, so the austenite could be regarded as a more potent trapping site than dislocations or grain boundaries in ferrite. In this case, the deformation induced martensitic transformation led to the reduction of trap binding energy, leaving the inherited hydrogen with enhanced mobility, likely resulting in a more damaging effect on mechanical properties than in a steels without the presence of deformation induced transformation from austenite to martensite.

Ronevich et al. (2012) studied the effect of dislocations on the distribution on hydrogen embrittlement of TRIP steels. The TRIP steels were prestrained 5% at the different temperatures of 253 K, 296 K and 375 K to introduce various amounts of transformed

martensite, and then cathodically charged to a hydrogen content of 1 to 2 ppm. Thermal desorption spectroscopy (TDS) indicated that the dislocations in TRIP steels were the main trapping sites for hydrogen, and the density of these trapping sites increased during deformation. Furthermore, dislocations in TRIP steels prestrained 5% at the lower temperatures of 253 K and 296 K were clustering adjacent to transformed martensite, while in TRIP steels prestrained 5% at higher temperatures of 375 K, dislocations were less localized and distributed more uniformly, dispersing hydrogen and providing better resistance to hydrogen embrittlement.

Hojo et al. (2010) investigated the influence of the alloying elements Al, Nb, and Mo on hydrogen embrittlement of ultra-high-strength TRIP steels developed for automotive structural application. The addition of Al, Nb, and Mo, increased the amount of stable retained austenite, mainly resulting from the addition of aluminium. The total hydrogen concentration in the steels after charging increased with increasing volume fraction of retained austenite, since hydrogen was preferentially trapped in the retained austenite or at the interface between retained austenite and matrix. The normal trapping at grain boundaries, at dislocations and at carbide-matrix interfaces, which made it easier for crack propagation, was suppressed, resulting in less effect of hydrogen on the properties of those steels with Al, Nb, and Mo addition.

Zhu et al. (2013) explored the effect of a cryogenic tempering (CT) treatment, on hydrogen embrittlement of TRIP steels using slow strain-rate tensile (SSRT) tests, EBSD observations of microstructure evolution and crack initiation, and SEM examination of fractured surfaces. They found that with the CT treatment, the TRIP steel exhibited better resistance to hydrogen embrittlement, characterized by lower loss of total elongation and less brittle “flat” features compared with the untreated counterparts. The reduced susceptibility to hydrogen embrittlement after the cryogenic tempering treatments was attributed to the CT treatment contributing to the enhanced stability of the retained austenite and the reduced the amount of fresh untempered martensite after straining, and thus lowering the local stress intensity and hydrogen concentration, reducing the possibility of occurrence of crack initiation caused by hydrogen. Furthermore, from a comparison between specimens with CT treatment and without CT treatment, the specimens with CT treatment had a better dislocation distribution avoiding dislocations clustering adjacent to retained austenite. This dislocation distribution may lower the hydrogen concentration in local regions near retained austenite, which were sensitive to hydrogen embrittlement. This dispersion of dislocations, caused by the CT treatment, may be another reason for the higher resistance to hydrogen embrittlement.

Sojka et al. (2011) attributed the poor resistance of their steels to hydrogen embrittlement partially to the non-metallic inclusions in the TRIP steels, around which high hydrogen content was expected. These non-metallic inclusions were preferential initiation sites for hydrogen embrittlement. A similar concept relating to inclusions for the easier crack initiation in TRIP steels was also stated by Begić Hadžipašić et al. (2011).

In conclusion, TRIP steel is influenced by hydrogen, in that the ductility is reduced, whereas the strength is not affected. Different critical hydrogen concentrations were proposed. The various hydrogen concentrations were due to the different microstructure of the TRIP steels. The hydrogen influence on TRIP steels was attributed to the transformation of retained austenite to martensite during straining. The retained austenite, which has a higher solubility of hydrogen, acted as a detrimental hydrogen source, releasing hydrogen to the freshly formed hard martensite, which was susceptible to HE. The susceptibility of TRIP steels to HE can be improved by a cryogenic tempering (CT) treatment.

7. HE in TWIP steels

7.1 Mechanical degradation

The research results are not consistent with regard to hydrogen-delayed fracture (HDF). There are reports that the TWIP steel is prone to delayed fracture after forming, attributed to hydrogen embrittlement (Chin et al., 2011; Chun, Park & Lee, 2012). There are also reports stating that some grades of TWIP steels are immune to hydrogen delayed fracture (Chin et al., 2011; So et al., 2009). Furthermore, it was also reported that by adding Al as an alloying element, the hydrogen delayed fracture susceptibility can be decreased or even avoided (Park et al., 2012). Investigations concerning mechanical degradation after introducing hydrogen are also not consistent.

Some researches have observed negligible mechanical degradation using tensile tests with hydrogen pre-charged specimens (Jung et al., 2008; Ronevich, Kim, Speer & Matlock, 2012; Ronevich, Speer & Matlock, 2010; So et al., 2009). Similarly, So et al. (2009) found there was little difference of the mechanical properties of Fe–18Mn–1.5Al–0.6C TWIP steel charged with different hydrogen contents and those without hydrogen charging. Similarly, Ronevich et al. (2010, 2012) studied the influence on TWIP steels of different hydrogen contents, introduced by cathodic charging the steels at the same current density for different durations before the tensile tests. The tensile properties, including yield stress, ultimate tensile stress, strain to failure and strain hardening behaviour, of the TWIP steels without

hydrogen, and with different hydrogen contents, were essentially the same. It was concluded that the TWIP steels in their studies were not affected by hydrogen, attributed to the low hydrogen diffusion coefficient in austenite, introducing basically no hydrogen into the bulk steel, and leading to the steels unaffected by hydrogen.

Suh (2014) critically reviewed hydrogen induced fracture in TWIP steels and concluded that because of the low diffusion coefficient of hydrogen in austenite, there was limited penetration of hydrogen into the bulk of the steels, resulting in the little change of the mechanical properties of TWIP steels.

In contrast, Koyama et al. (2012a,b,c) found a significant decrease of mechanical properties, caused by the presence of hydrogen, of the Fe–18Mn–0.6C and Fe–18Mn–1.2C TWIP steels. Tensile tests measured the change of mechanical properties. The specimens were cathodically charged in a 3% NaCl aqueous solution containing 3 g/L NH_4SCN at current density of 10 A/m^2 during the tensile tests to introduce hydrogen. Koyama et al. (2012b) found that, their hydrogen charged Fe–18Mn–0.6C TWIP steels had values of average total elongation and ultimate tensile strength of 32% and 1010 MPa, respectively, compared with 70% and 1200 MPa without hydrogen. For Fe–18Mn–1.2C TWIP steel (Koyama et al., 2012c), there was a similar reduction of elongation and ultimate tensile strength by hydrogen, which was about a 20% reduction of ultimate tensile strength, and about 40% reduced elongation from about 80% to 42%.

7.2 Fractography

Researchers who measured a negligible decrease of mechanical properties caused by hydrogen observed a fully ductile fracture surface morphology (Ronevich, Kim, Speer & Matlock, 2012; Ronevich, Speer & Matlock, 2010; So et al., 2009), whilst those who measured a significant decrease of mechanical properties after hydrogen charging observed brittle fracture surfaces (Chun, Park & Lee, 2012; Koyama et al., 2012a,b,c).

For those TWIP steels which experienced negligible degradation of mechanical properties with hydrogen charging, the fracture surface after the slow strain rate tests of specimens both without and with hydrogen charging contents showed fully ductile fractures, characterized by dimples, resulting from micro-void nucleation and coalescence.

In contrast, Koyama et al. (2012b) reported that the hydrogen introduced into the TWIP steels influenced the characteristics of the fracture surface along with the total elongation. The fracture surfaces of the charged specimens exhibited intergranular features in the parts near the surface of the specimen, whilst in the central part of the specimen, there

were ductile dimples which resembled those of the uncharged specimen. The intergranular fractures were only located near the surface. This was attributed to the hydrogen concentration difference from the surface to the interior. Near the surface, the hydrogen concentration was high, and this high concentration of hydrogen induced the intergranular fracture. However, the hydrogen concentration in the interior was low and not high enough to induce intergranular fracture. They attributed the causes of the intergranular fracture to the reduction of grain boundary cohesion, deformation twinning and martensite transformation, influenced by hydrogen. In another of their research concerning hydrogen in TWIP steels (Koyama et al., 2012c), there were also brittle features in the vicinity of the surface and ductile dimples in the interior. However, the brittle features were different, as the fracture mode was not all intergranular, but also included some transgranular fracture. This transgranular fracture propagated along the primary deformation twin boundaries, and parallel to the secondary twinning plane. The intergranular fracture resulted from the interception of grain boundaries at primary deformation twin boundaries. The following twin-twin interaction, in which the primary deformation twins were intercepted by the secondary deformation twin boundaries, caused the transgranular fracture.

As previously mentioned, crack initiation and propagation were observed on even coherent Σ3 twin boundaries. This was in contradiction to some studies (Chun, Park & Lee, 2012; Oudriss et al., 2014), suggesting that coherent Σ3 twin boundaries as coincidence site lattice (CSL) boundaries were crack arrest sites, as introduced in section 3.3.3. Koyama et al. (2013) further explained this contradiction in four aspects: (i) very high stress concentration existed at the tip of a moving deformation twin contributed to crack initiation, (ii) the dislocation - twin interaction influenced the coherency of the twin boundaries, (iii) the change in the position of interstitial carbon atoms from an octahedral to a tetrahedral site lead to lattice distortions in the deformation twins, producing a local elastic strain, and (iv) large amount of lattice defects, such as dislocations and nanotwins, existed in and around deformation twins, acting as reversible hydrogen trapping sites.

7.3 Stacking fault energy

During austenite plastic deformation, the following three mechanisms could occur: martensite transformation, twinning and dislocation glide. The stacking fault energy (SFE) is a critical factor that determines which transformation occurs. The SFE depends on the temperature and the chemical composition of the TWIP steel, in particular concentrations of manganese, aluminium and silicon. The effect of stacking fault energy on the deformation

mechanism (Remy & Pineau, 1977) is that twinning occurs when the stacking fault energy (SFE) is within the range of 18-50 mJ/m^2. If the SFE is lower, the martensite transformation is more likely. If the SFE is higher, dislocation glide is the only possible mechanism (De Cooman, Kwon & Chin, 2012). However, different ranges have been reported for the value of stacking fault energy for mechanical twinning, such as 18–45 mJ/m^2 (Curtze & Kuokkala, 2010), 20–40 mJ/m^2 (Lee, 2012) and 12–35 mJ/m^2 (Allain et al., 2004). These differences result from the difficulty in experimentally determining the value of stacking fault energy (Lee, 2012).

It has been reported that, hydrogen, under cathodic charging conditions, can cause the austenite phase of austenitic stainless steels to transform to α- or ε-martensite (Mine, Horita & Murakami, 2009; Rozenak & Bergman, 2006; Yang, Qiao, Chiovelli & Luo, 1999; Yang & Luo, 2000). These studies indicate that hydrogen can decrease austenite stability. Furthermore, Yang et al. (1999) found that there was surface cracking only in specimens, in which there was hydrogen induced martensitic transformation, indicating that hydrogen could reduce austenite stability, induce austenite to transform into martensite, and cause mechanical propoerty degradation. This could be explained based on (i) the assumption that the hydrogen lowers the SFE of austenite, and (ii) the increased stress gradients. Pontini et al. (1997) measured the reduction of SFE caused by hydrogen in an AISI 304 steel by XRD with the aid of TEM, and found that the SFE was reduced about 40% by 274 ppm hydrogen.

For TWIP steels, Ryu et al. (2013) found a reduction of the stacking fault energy in Fe–0.6C–18Mn TWIP steel charged with hydrogen. This reduction of SFE led to the transformation from austenite to ε-martensite, which was susceptible to hydrogen embrittlement, resulting in transgranular cracking parallel to interfaces between ε-martensite and austenite. Similarly Nue (2013) reported that a decrease of SFE could cause the transformation of α-martensite. McCoy (1973) stated that with decreasing the Mn content in Fe–(15–25)Mn–0.3C steels, α-martensite was formed, resulting in the decreased hydrogen embrittlement resistance.

One possible explanation for the reduction of stacking fault energy is the decrease in energy associated with the formation of H–H pairs during faulting (Moro et al., 1998).

7.4 Grain boundaries

Since there are reports of significant degradation of mechanical properties of TWIP steels by hydrogen (Koyama et al., 2012b,c; Ryu et al., 2013), it is important to investigate the influence of hydrogen content on embrittlement behaviour on TWIP steels.

Koyama et al. (2012a) studied the effect of hydrogen content on the hydrogen embrittlement in Fe–18Mn–0.6C TWIP steels through tensile tests with hydrogen charging at different current densities to introduce various hydrogen contents. The hydrogen concentration in the steels increased significantly with increasing hydrogen charging current density. There was a critical diffusible hydrogen content, which divided the effect of hydrogen on embrittlement behaviour. At a relatively low diffusible hydrogen content, 0.33 wtppm corresponding to a charging current density of 1 A/m^2, there was no significant change of tensile properties compared with those without hydrogen charging, and the fracture surface was ductile and consisted of dimples, which was similar to the fractures without hydrogen. For the samples with higher hydrogen contents, corresponding to charging current densities within the range of 3 A/m^2 to 10 A/m^2, the true stress and elongation decreased significantly with increased charging current density, premature fracture occurred, and there was intergranular fracture. The strain hardening behaviour was not affected by hydrogen charging even when hydrogen embrittlement occurred. This lack of change in the strain hardening behaviour was assumed to indicate that dislocation slip, martensitic transformation and deformation twinning was not affected by hydrogen, since the behaviour of those deformation mechanisms would be changed if the strain hardening behaviour altered. The possible cause of hydrogen embrittlement behaviour under the relatively high charging current densities was attributed to the reduction of the cohesion of grain boundaries, not twin boundaries, which explained the lack of change in strain hardening behaviour, the occurrence of premature fracture and the intergranular fracture. This lack of change in strain hardening behaviour seems to contradict the references (Pontini & Hermida, 1997; Ryu et al., 2013), which indicated a change of stacking fault energy by hydrogen, as mentioned in section 7.3. In the study of Ryu et al. (2013), the transformation of ε-martensite contributed to hydrogen embrittlement, and was attributed to the reduced SFE by hydrogen. In contrast, in this study of the effect of hydrogen content on hydrogen embrittlement in TWIP steels, hydrogen embrittlement occurred without the transformation of ε-martensite and without hydrogen affecting the strain hardening behaviour of the steel, indicating that the main reason for hydrogen embrittlement in this case was the reduction in the cohesion of grain boundaries, which could lead to the hydrogen assisted cracking without changing stress-strain behaviour of the steel, instead of hydrogen-dislocation interactions (Koyama, Akiyama, Tsuzaki & Raabe, 2013).

7.5 Al concentration

As mentioned in Sections 2.4 and 7.3, aluminium influences the stacking fault energy (SFE), which is a relevant parameter for determining the deformation mechanism in austenitic steels, and the deformation mechanism in TWIP steels, resulting in a change of resistance of TWIP steels to hydrogen embrittlement. As a consequence, it is important to investigate the effect of aluminium on hydrogen embrittlement in TWIP steels.

Chin et al. (2011) found that the addition of aluminium in TWIP steels decreased the tensile elongation, and the deformation twinning was more homogenous and less intense than those in TWIP steels without aluminium. This led to a lower stress concentration during cup forming than that without aluminium, which exhibited crack formation.

Ryu et al. (2013) investigated the effect of aluminium on hydrogen-induced embrittlement in TWIP steels. The addition of aluminium reduced the loss in both elongation and ultimate tensile strength. The fracture surface had regions near the surface of brittle features that were both intergranular and transgranular, and those in the centre were ductile with dimples. The depth of the brittle zones increased with the increasing hydrogen charging current density, but was reduced by the addition of aluminium, consistent with the results that the mechanical properties of TWIP steel with aluminium were less sensitive to hydrogen. This effect of aluminium was attributed to the fact that aluminium could increase the stacking fault energy of austenite, reducing the possibility of mechanical twinning and suppressing the transformation of ε-martensite during deformation, both of which would contribute to the hydrogen trapping and promote transgranular fracture, and thus lead to a lower susceptibility of the steel to hydrogen embrittlement.

Park et al. (2012) investigated the effect of different aluminium contents on hydrogen-induced embrittlement in TWIP steels using slow strain rate tensile tests with hydrogen charging in aqueous solution, and obtained results that were consistent with those of Ryu et al. (2013). Park et al. found that the addition of aluminium retarded the loss of mechanical properties of TWIP steels, and the area of the brittle zone in the vicinity of the surface was decreased with the increased aluminium content. For the 2Al TWIP steel, which contained higher amount of aluminium than the others, there was almost no brittle fracture after the tensile test with hydrogen charging. A different explanation of the aluminium effect on hydrogen embrittlement was given that during hydrogen charging in aqueous solution an aluminium-oxide layer was formed on the surface and hindered the absorption of hydrogen into the steel. Thus the amount of diffusible hydrogen inside the sample, which could cause

hydrogen-induced embrittlement, was reduced and the resistance to hydrogen embrittlement was improved.

Consistent results showing that the hydrogen embrittlement susceptibility decreased with increasing aluminium content was also provided by Koyama et al. (2013). Moreover, they further proposed that the strain rate of pre-deformed steels also affected the hydrogen embrittlement susceptibility in a way that the hydrogen embrittlement susceptibility decreased with increasing strain rate. They explained the improved resistance to hydrogen embrittlement from the viewpoint of strengthening by strain aging. It was proposed that the addition of aluminium contributed to the suppression of static strain aging under loading, and the increased Al content and strain rate led to the suppression of dynamic strain aging during pre-deformation. Since dynamic and static strain aging influenced the hydrogen embrittlement, the increased aluminium content and strain rate could affect the susceptibility to hydrogen embrittlement.

7.6 Influence of Ti

Park et al. (2014) also investigated the influence of Ti on the hydrogen embrittlement of TWIP steel. There was a significant reduction in elongation and quasi-cleavage brittle features in the hydrogen-charged sample containing Ti, indicating the low resistance of this steel to hydrogen embrittlement. Moreover, without Ti, the sample charged with hydrogen exhibited no reduction in elongation and fully ductile fracture. The reduction in total elongation was attributed to the transition from ductile fracture to brittle fracture at the hydrogen-concentrated edge part of the samples. There were TiN particles near the quasi-cleavage brittle features, revealing that the TiN particles acted as strong hydrogen traps and contributing to the low resistance of Ti-bearing TWIP steels to hydrogen embrittlement.

7.7 Summary

In summary, the results of the influence of hydrogen on TWIP steels were not consistent from the researches as introduced above. Some researchers found no significant influence of hydrogen on TWIP steels and fully ductile fracture features, and they attributed the lack of influence to the low diffusivity of hydrogen in austenite. In contrast, some other researchers found significant loss of ductility and strength due to the presence of hydrogen and some brittle features. They attributed the hydrogen influence to the reduction of cohesion between grain boundaries, deformation twinning and ε-martensite transformation, which resulted from the decreased stacking fault energy caused by hydrogen. In addition, aluminium

alloying and increased strain rate were found to decrease HE susceptibility, whereas titanium alloying was found to be detrimental.

8. Conclusions

1. DP, TRIP and TWIP grades of advanced high-strength steels (AHSS) are important and promising materials for auto construction and may suffer hydrogen embrittlement. Hydrogen influences DP and TRIP steels in that ductility is reduced whereas the strengths are not changed. Furthermore, hydrogen caused the fracture features to become more brittle.
2. The influence of hydrogen on TWIP steels was inconsistent. Some researchers found no significant influence of hydrogen on TWIP steels and fully ductile fracture features. Others fould significant loss of ductility and strength due to the presence of hydrogen and some brittle features.
3. The susceptibility of steels to hydrogen embrittlement (HE) was influenced by the steel strength, microstructure and hydrogen concentration.

Acknowledgements

This research is supported by the Baosteel-Australia Joint Research & Development Centre (BAJC) Grant, BA13037, with linkage to Baoshan Iron and Steel Co., Ltd of China.

References

Abraham DP, Altstetter CJ. Hydrogen-enhanced localization of plasticity in an austenitic stainless steel. Metall Mater Trans A 1995; 26: 2859-2871.

Addach H, Berçot P, Rezrazi M, Takadoum J. Study of the electrochemical permeation of hydrogen in iron. Corros Sci 2009; 51: 263-267.

Allain S, Chateau J-P, Bouaziz O, Migot S, Guelton N. Correlations between the calculated stacking fault energy and the plasticity mechanisms in Fe–Mn–C alloys. Mater Sci Eng A 2004; 387: 158-162.

Araújo DF, Vilar EO, Palma Carrasco J. A critical review of mathematical models used to determine the density of hydrogen trapping sites in steels and alloys. Int J Hydrogen Energy 2014; 39: 12194-12200.

Atrens A, Brosnan CC, Ramamurthy S, Oehlert A, Smith IO. Linearly increasing stress test (LIST) for SCC research. Meas Sci Technol 1993; 4: 1281.

Atrens A, Mezzanotte D, Fiore N, Genshaw M. Electrochemical studies of hydrogen diffusion and permeability in Ni. Corros Sci 1980; 20: 673-684.

AutoSteel. Ulsab-avc (advacend vehicle concetp) overview report. Retrieved July 22, 2014 from http://www.autosteel.org/.

Baosteel. Baosteel automotive advanced high strength steels. Retrieved January 07, 2015 from http://www.baosteel.com/.

Beachem C. A new model for hydrogen-assisted cracking (hydrogen "embrittlement"). Metall Trans 1972; 3: 441-455.

Begić Hadžipašić A, Malina J, Malina M. The influence of microstructure on hydrogen diffusion and embrittlement of multiphase fine-grained steels with increased plasticity and strength. Chem Biochem Eng Q 2011; 25: 159-169.

Bockris JM, McBreen J, Nanis L. The hydrogen evolution kinetics and hydrogen entry into [alpha]-iron. J Electrochem Soc 1965; 112: 1025-1031.

Boes N, Züchner H. Electrochemical methods for studying diffusion, permeation and solubility of hydrogen in metals. J Less Common Met 1976; 49: 223-240.

Bracke L, Verbeken K, Kestens L, Penning J. Microstructure and texture evolution during cold rolling and annealing of a high Mn TWIP steel. Acta Mater 2009; 57: 1512-1524.

Castaño Rivera P, Ramunni VP, Bruzzoni P. Hydrogen trapping in an AOI 5L X60 steel. Corros Sci 2012; 54: 106-118.

Chen L, Zhao Y, Qin X. Some aspects of high manganese twinning-induced plasticity (TWIP) steel, a review. Acta Metall Sin (Engl Lett) 2013; 26: 1-15.

Chen M, Wu R, Liu H, Wang L, Shi J, Dong H, Jin X. An ultrahigh strength steel produced through deformation-induced ferrite transformation and Q&P process. Sci China Technol Sci 2012; 55: 1827-1832.

Chin KG, Kang CY, Shin SY, Hong S, Lee S, Kim HS, Kim KH, Kim NJ. Effects of Al addition on deformation and fracture mechanisms in two high manganese TWIP steels. Mater Sci Eng A 2011; 528: 2922-2928.

Chun YS, Park KT, Lee CS. Delayed static failure of twinning-induced plasticity steels. Scripta Materialia 2012; 66: 960-965.

Chung K, Ma N, Park T, Kim D, Yoo D, Kim C. A modified damage model for advanced high strength steel sheets. Int J Plast 2011; 27: 1485-1511.

Crolet J, Bonis M. Revisiting hydrogen in steel, part I: Theoretical aspects of charging, stress cracking and permeation. CORR NACE 2001; 2001: 11-16.

Curtze S, Kuokkala VT. Dependence of tensile deformation behavior of TWIP steels on stacking fault energy, temperature and strain rate. Acta Mater 2010; 58: 5129-5141.

Davies R. Hydrogen embrittlement of dual-phase steels. Metall Trans A 1981; 12: 1667-1672.

Davies R. Influence of martensite content on the hydrogen embrittlement of dual-phase steels. Scripta metallurgica 1983; 17: 889-892.

Daynes H. The process of diffusion through a rubber membrane. Proc R Soc Lond A 1920; 97: 286-307.

De Cooman BC, Kwon O, Chin KG. State-of-the-knowledge on TWIP steel. Mater Sci Technol 2012; 28: 513-527.

Depover T, Pérez Escobar D, Wallaert E, Zermout Z, Verbeken K. Effect of hydrogen charging on the mechanical properties of advanced high strength steels. Int J Hydrogen Energy 2014; 39: 4647-4656.

Depover T, Wallaert E, Verbeken K. Fractographic analysis of the role of hydrogen diffusion on the hydrogen embrittlement susceptibility of DP steel. Mater Sci Eng A 2016; 649: 201-208.

Devanathan M, Stachurski Z. The mechanism of hydrogen evolution on iron in acid solutions by determination of permeation rates. J Electrochem Soc 1964; 111: 619-623.

Devanathan M, Stachurski Z. The adsorption and diffusion of electrolytic hydrogen in palladium. Proc Roy Soc of Lond A Mat 1962; 270: 90-102.

Dong CF, Liu ZY, Li XG, Cheng YF. Effects of hydrogen-charging on the susceptibility of X100 pipeline steel to hydrogen-induced cracking. Int J Hydrogen Energy 2009; 34: 9879-9884.

Edmonds DV, He K, Rizzo FC, De Cooman BC, Matlock DK, Speer JG. Quenching and partitioning martensite—a novel steel heat treatment. Mater Sci Eng A 2006; 438-440: 25-34.

European Commission. Metallurgical design of high-strength austenitic Fe-C-Mn steels with excellent formability (metaldesign). Retrieved November 28, 2014 from http://europa.eu/.

Flitt H, Bockris JM. Hydrogen/metal interactions with special reference to electrochemical approaches. Int J Hydrogen Energy 1981; 6: 119-138.

Galán J, Samek L, Verleysen P, Verbeken K, Houbaert Y. Advanced high strength steels for automotive industry. Rev Metal Madrid 2012; 48: 118-131.

Gamboa E, Atrens A. Material influence on the stress corrosion cracking of rock bolts. Eng Fail Anal 2005; 12: 201-235.

Gertsman VY, Bruemmer SM. Study of grain boundary character along intergranular stress corrosion crack paths in austenitic alloys. Acta Mater 2001; 49: 1589-1598.

Hadam U, Zakroczymski T. Absorption of hydrogen in tensile strained iron and high-carbon steel studied by electrochemical permeation and desorption techniques. Int J Hydrogen Energy 2009; 34: 2449-2459.

Haq AJ, Muzaka K, Dunne DP, Calka A, Pereloma EV. Effect of microstructure and composition on hydrogen permeation in X70 pipeline steels. Int J Hydrogen Energy 2013; 38: 2544-2556.

Hardie D, Charles EA, Lopez AH. Hydrogen embrittlement of high strength pipeline steels. Corros Sci 2006; 48: 4378-4385.

Hirth J. Effects of hydrogen on the properties of iron and steel. Metall Trans A 1980; 11: 861-890.

Hojo T, Kobayashi J, Kajiyama T, Sugimoto K. Effects of alloying elements on impact properties of ultra high-strength TRIP-aided bainitic ferrite steels. Res Rep Tsuyama Technical College 2010; 52: 9-16.

Huang J, Poole W, Militzer M. Austenite formation during intercritical annealing. Metall Mater Trans A 2004; 35: 3363-3375.

Imlau J, Bleck W, Zaefferer S. Comparison of damage development depending on the local microstructure in low alloyed Al-TRIP-steels, IF steel and a DP steel. Int J Mater Res 2009; 100: 584-593.

Industrial Galvanizers Corporation. How does hot-dip galvanizing affect steel strength. Retrieved February 15, 2015 from http://www.valmont.com/

Johnson WH. On some remarkable changes produced in iron and steel by the action of hydrogen and acids. Proc R Soc London 1874; 23: 168-179.

Jung J, Lee O, Park Y, Kim D, Jin K. Hydrogen embrittlement behavior of high Mn TRIP/TWIP steels. Korean J Mater Res 2008; 18: 394-399.

Katz L, Guinan M, Borg R. Diffusion of H_2, D_2, and T_2 in single-crystal Ni and Cu. Phys Rev B 1971; 4: 330.

Khan MI, Kuntz ML, Biro E, Zhou Y. Microstructure and mechanical properties of resistance spot welded advanced high strength steels. Mater Trans 2008; 49: 1629-1637.

Kiuchi K, McLellan R. The solubility and diffusivity of hydrogen in well-annealed and deformed iron. Acta Metall 1983; 31: 961-984.

Kliber J, Kursa T, Drozd K, Hajduchová L, Peslova F. Metallographic exploration of TWIP steel. In: Proc 24th Intl Con Metall Mater METAL, Brno, 2012: 23-25

Koyama M, Akiyama E, Tsuzaki K. Hydrogen embrittlement in a Fe–Mn–C ternary twinning-induced plasticity steel. Corros Sci 2012; 54: 1-4.

Koyama M, Akiyama E, Tsuzaki K. Effects of static and dynamic strain aging on hydrogen embrittlement in TWIP steels containing Al. ISIJ Int 2013; 53: 1268-1274.

Koyama M, Akiyama E, Tsuzaki K. Effect of hydrogen content on the embrittlement in a Fe–Mn–C twinning-induced plasticity steel. Corros Sci 2012; 59: 277-281.

Koyama M, Akiyama E, Sawaguchi T, Raabe D, Tsuzaki K. Hydrogen-induced cracking at grain and twin boundaries in an Fe–Mn–C austenitic steel. Scripta Mater 2012; 66: 459-462.

Koyama M, Akiyama E, Tsuzaki K, Raabe D. Hydrogen-assisted failure in a twinning-induced plasticity steel studied under in situ hydrogen charging by electron channeling contrast imaging. Acta Mater 2013; 61: 4607-4618.

Koyama M, Tasan CC, Akiyama E, Tsuzaki K, Raabe D. Hydrogen-assisted decohesion and localized plasticity in dual-phase steel. Acta Materialia 2014; 70: 174-187.

Krom AH, Bakker A. Hydrogen trapping models in steel. Metall Mater Trans 2000; 31: 1475-1482.

Lasia A, Grégoire D. General model of electrochemical hydrogen absorption into metals. J Electrochem Soc 1995; 142: 3393-3399.

Laureys A, Depover T, Petrov R, Verbeken K. Microstructural characterization of hydrogen induced cracking in TRIP-assisted steel by EBSD. Mater Charact 2016; 112: 169-179.

Lee J, Lee S. Hydrogen trapping phenomena in metals with bcc and fcc crystals structures by the desorption thermal analysis technique. Surf Coat Technol 1986; 28: 301-314.

Lee SM, Park IJ, Jung JG, Lee YK. The effect of Si on hydrogen embrittlement of Fe-18Mn-0.6C-xSi twinning-induced plasticity steels. Acta Mater 2016; 103: 264-272.

Lee YK. Microstructural evolution during plastic deformation of twinning-induced plasticity steels. Scripta Mater 2012; 66: 1002-1006.

Liang Y, Ahn D, Sofronis P, Dodds Jr R, Bammann D. Effect of hydrogen trapping on void growth and coalescence in metals and alloys. Mech Mater 2008; 40: 115-132.

Liu H, Li F, Shi W, Swaminathan S, He Y, Rohwerder M, Li L. Challenges in hot-dip galvanizing of high strength dual phase steel: Surface selective oxidation and mechanical property degradation. Surf Coat Technol 2012; 206: 3428-3436.

Liu Q, Atrens A. Reversible hydrogen trapping in a 3.5NiCrMoV medium strength steel. Corros Sci 2015; 96: 112-120.

Liu Q, Atrens A. A critical review of the influence of hydrogen on the mechanical properties of medium-strength steels. Corros Rev 2013; 31:

Liu Q, Atrens AD, Shi Z, Verbeken K, Atrens A. Determination of the hydrogen fugacity during electrolytic charging of steel. Corros Sci 2014; 87: 239-258.

Liu Q, Irwanto B, Atrens A. The influence of hydrogen on 3.5NiCrMoV steel studied using the linearly increasing stress test. Corros Sci 2013; 67: 193-203.

Loidl M, Kolk O, Veith S, Göbel T. Characterization of hydrogen embrittlement in automotive advanced high strength steels. Materialwiss Werkstofftech 2011; 42: 1105-1110.

Lovicu G, Bottazzi M, D'Aiuto F, De Sanctis M, Dimatteo A, Santus C, Valentini R. Hydrogen embrittlement of automotive advanced high-strength steels. Metall Mater Trans A 2012; 43: 4075-4087.

Luppo M, Ovejero-Garcia J. The influence of microstructure on the trapping and diffusion of hydrogen in a low carbon steel. Corros Sci 1991; 32: 1125-1136.

Lynch S. Environmentally assisted cracking: Overview of evidence for an adsorption-induced localised-slip process. Acta Metall 1988; 36: 2639-2661.

Lynch S. Hydrogen embrittlement phenomena and mechanisms. Corros Rev 2012; 30: 105-123.

Manolatos P, Jerome M. A thin palladium coating on iron for hydrogen permeation studies. Electrochimica Acta 1996; 41: 359-365.

Manolatos P, Jerome M, Duret-Thual C, Le Coze J. The electrochemical permeation of hydrogen in steels without palladium coating. Part I: Interpretation difficulties. Corros Sci 1995; 37: 1773-1783.

Manolatos P, Duret-Thual C, Le Coze J, Jerome M, Bollinger E. The electrochemical permeation of hydrogen in steels without palladium coating. Part II: Study of the influence of microstructure on hydrogen diffusion. Corrosion science 1995; 37: 1785-1796.

Manolatos P, Jerome M, Galland J. Necessity of a palladium coating to ensure hydrogen oxidation during electrochemical permeation measurements on iron. Electrochim Acta 1995; 40: 867-871.

McBreen J, Nonis L, Beck W. A method for determination of the permeation rate of hydrogen through metal membranes. J Electrochem Soc 1966; 113: 1218-1222.

McCoy R, Gerberich W. Hydrogen embrittlement studies of a TRIP steel. Metall Trans 1973; 4: 539-547.

McCoy RA. Development of a high-strength manganese steel resistant to hydrogen embrittlement. In: Proc Int Conference on the Effects of Hydrogen on Materials Properties and Selection and Structural Design, ASM, 1973: 169-178

McNabb A, Foster P. A new analysis of the diffusion of hydrogen in iron and ferritic steels. Trans Aime 1963; 227: 618.

Michalska J, Chmiela B, Łabanowski J, Simka W. Hydrogen damage in superaustenitic 904l stainless steels. J Mater Eng Perform 2014; 23: 2760-2765.

Mine Y, Horita Z, Murakami Y. Effect of hydrogen on martensite formation in austenitic stainless steels in high-pressure torsion. Acta Mater 2009; 57: 2993-3002.

Moro L, Obiol E, Roviglione A, Hermida D, Juan A. A theory of hydrogen trapping in a faulted zone of fcc iron. J Phys D: Appl Phys 1998; 31: 893.

Müllner P. On the ductile to brittle transition in austenitic steel. Mater Sci Eng A 1997; 234: 94-97.

Neu R. Performance and characterization of TWIP steels for automotive applications. Mater Performance Charact 2013; 2: 244-284.

Oliver S, Jones TB, Fourlaris G. Dual phase versus TRIP strip steels: Microstructural changes as a consequence of quasi-static and dynamic tensile testing. Mater Charact 2007; 58: 390-400.

Oriani R. Hydrogen-the versatile embrittler. Corrosion 1987; 43: 390-397.

Oriani RA, Josephic PH. Equilibrium aspects of hydrogen-induced cracking of steels. Acta Metall 1974; 22: 1065-1074.

Oriani RA. The diffusion and trapping of hydrogen in steel. Acta Metall 1970; 18: 147-157.

Oudriss A, Bouhattate J, Savall C, Creus J, Feaugas X, Martin F, Laghoutaris P, Chêne J. On the implication of hydrogen on inter-granular fracture. Procedia Mater Sci 2014; 3: 2030-2034.

Park I-J, Jeong K-H, Jung J-G, Lee CS, Lee Y-K. The mechanism of enhanced resistance to the hydrogen delayed fracture in Al-added Fe–18Mn–0.6C twinning-induced plasticity steels. Int J Hydrogen Energy 2012; 37: 9925-9932.

Park IJ, Jo SY, Kang M, Lee SM, Lee YK. The effect of ti precipitates on hydrogen embrittlement of Fe–18Mn–0.6C–2Al–xTi twinning-induced plasticity steel. Corros Sci 2014; 89: 38-45.

Pérez Escobar D, Miñambres C, Duprez L, Verbeken K, Verhaege M. Internal and surface damage of multiphase steels and pure iron after electrochemical hydrogen charging. Corros Sci 2011; 53: 3166-3176.

Pérez Escobar D, Wallaert E, Duprez L, Atrens A, Verbeken K. Thermal desorption spectroscopy study of the interaction of hydrogen with TiC precipitates. Met Mater Int 2013; 19: 741-748.

Pérez Escobar D, Duprez L, Atrens A, Verbeken K. Thermal desorption spectroscopy study of experimental Ti/S containing steels. Mater Sci Technol 2013; 29: 261-267.

Perng TP, Wu JK. A brief review note on mechanisms of hydrogen entry into metals. Mater Lett 2003; 57: 3437-3438.

Petch N, Stables P. Delayed fracture of metals under static load. Nature 1952; 169: 842-843.

Pontini AE, Hermida JD. X-ray diffraction measurement of the stacking fault energy reduction induced by hydrogen in an AISI 304 steel. Scripta Mater 1997; 37: 1831-1837.

Pressouyre GM. A classification of hydrogen traps in steel. Metall Trans A 1979; 10: 1571-1573.

Ramamurthy S, Lau W, Atrens A. Influence of the applied stress rate on the stress corrosion cracking of 4340 and 3.5NiCrMoV steels under conditions of cathodic hydrogen charging. Corros Sci 2011; 53: 2419-2429.

Ramamurthy S, Atrens A. Stress corrosion cracking of high-strength steels. Corros Rev 2013; 31: 1-31.

Ramamurthy S, Atrens A. The influence of applied stress rate on the stress corrosion cracking of 4340 and 3.5NiCrMoV steels in distilled water at 30 ℃. Corros Sci 2010; 52: 1042-1051.

Remy L, Pineau A. Twinning and strain-induced fcc→ hcp transformation in the Fe-Mn-Cr-C system. Mater Sci Eng 1977; 28: 99-107.

Robertson I. The effect of hydrogen on dislocation dynamics. Eng Fract Mech 2001; 68: 671-692.

Robinson M, Kilgallon P. Hydrogen embrittlement of cathodically protected high-strength, low-alloy steels exposed to sulfate-reducing bacteria. Corrosion 1994; 50: 626-635.

Ronevich J, De Cooman B, Speer J, De Moor E, Matlock D. Hydrogen effects in prestrained transformation induced plasticity steel. Metall Mater Trans A 2012; 43: 2293-2301.

Ronevich J, Kim S, Speer J, Matlock D. Hydrogen effects on cathodically charged twinning-induced plasticity steel. Scripta Mater 2012; 66: 956-959.

Ronevich JA, Speer JG, Matlock DK. Hydrogen embrittlement of commercially produced advanced high strength sheet steels. SAE Int J Mater Manuf 2010; 3(1): 255-267.

Rozenak P, Bergman R. X-ray phase analysis of martensitic transformations in austenitic stainless steels electrochemically charged with hydrogen. Mater Sci Eng A 2006; 437: 366-378.

Ryu JH, Chun YS, Lee CS, Bhadeshia HKDH, Suh DW. Effect of deformation on hydrogen trapping and effusion in TRIP-assisted steel. Acta Mater 2012; 60: 4085-4092.

Ryu JH, Kim SK, Lee CS, Suh D-W, Bhadeshia H. Effect of aluminium on hydrogen-induced fracture behaviour in austenitic Fe–Mn–C steel. Proc R Soc A 2013; 469: 20120458.

Santofimia MJ, Zhao L, Sietsma J. Overview of mechanisms involved during the quenching and partitioning process in steels. Metall Mater Trans A 2011; 42: 3620-3626.

So KH, Kim JS, Chun YS, Park KT, Lee YK, Lee CS. Hydrogen delayed fracture properties and internal hydrogen behavior of a Fe-18Mn-1.5Al-0.6C TWIP steel. ISIJ Int 2009; 49: 1952-1959.

Sojka J, Vodárek V, Schindler I, Ly C, Jérôme M, Váňová P, Ruscassier N, Wenglorzová A. Effect of hydrogen on the properties and fracture characteristics of TRIP 800 steels. Corros Sci 2011; 53: 2575-2581.

Suh D-W. Critical assessment 2: Hydrogen induced fracture in austenitic, high-manganese TWIP steel. Mater Sci Technol 2014; 30: 1131-1134.

Sun S, Gu J, Chen N. The influence of hydrogen on the sub-structure of the martensite and ferrite dual-phase steel. Scripta metallurgica 1989; 23: 1735-1737.

Troiano AR. The role of hydrogen and other interstitials in the mechanical behavior of metals. Trans ASM 1960; 52: 54-80.

Venezuela J, Liu Q, Zhang M, Zhou Q, Atrens A. The influence of hydrogen on the mechanical and fracture properties of some martensitic advanced high strength steels studied using the linearly increasing stress test. Corros Sci 2015; 99: 98-117.

Villalba E, Atrens A. Hydrogen embrittlement and rock bolt stress corrosion cracking. Eng Fail Anal 2009; 16: 164-175.

Villalba E, Atrens A. SCC of commercial steels exposed to high hydrogen fugacity. Eng Fail Anal 2008; 15: 617-641.

Villalba E, Atrens A. Metallurgical aspects of rock bolt stress corrosion cracking. Mater Sci Eng A 2008; 491: 8-18.

Wan J, Chen S, Hsu TY. The stability of transition phases in Fe-Mn-Si based alloys. Calphad 2001; 25: 355-362.

Wang G, Yan Y, Li J, Huang J, Su Y, Qiao L. Hydrogen embrittlement assessment of ultra-high strength steel 30CrMnSiNi2. Corros Sci 2013; 77: 273-280.

Westlake D. Generalized model for hydrogen embrittlement. Transactions 1969; 62: 1000-1006.

Winzer N, Atrens A, Dietzel W, Song G, Kainer KU. Comparison of the linearly increasing stress test and the constant extension rate test in the evaluation of transgranular stress corrosion cracking of magnesium. Mater Sci Eng A 2008; 472: 97-106.

WorldAutoSteel. Advanced high-strength steels application guidelines version 5.0. Retrieved November 17, 2014 from http://www.worldautosteel.org/.

Wriedt HA, Oriani RA. Effect of tensile and compressive elastic stress on equilibrium hydrogen solubility in a solid. Acta Metall 1970; 18: 753-760.

Yang Q, Qiao LJ, Chiovelli S, Luo JL. Critical hydrogen charging conditions for martensite transformation and surface cracking in type 304 stainless steel. Scripta Mater 1999; 40: 1209-1214.

Yang Q, Luo J. Martensite transformation and surface cracking of hydrogen charged and outgassed type 304 stainless steel. Mater Sci Eng A 2000; 288: 75-83.

Yen SK, Huang IB. Critical hydrogen concentration for hydrogen-induced blistering on AISI 430 stainless steel. Mater Chem Phys 2003; 80: 662-666.

Zackay VF, Parker ER, Fahr D, Busch R. The enhancement of ductility in high-strength steels. ASM TRANS QUART 1967; 60: 252-259.

Zakroczymski T. Adaptation of the electrochemical permeation technique for studying entry, transport and trapping of hydrogen in metals. Electrochim Acta 2006; 51: 2261-2266.

Zapffe C, Sims C. Hydrogen embrittlement, internal stress and defects in steel. Trans AIME 1941; 145: 225-271.

Zhang TY, Zheng YP. Effects of absorption and desorption on hydrogen permeation—I. Theoretical modeling and room temperature verification. Acta Mater 1998; 46: 5023-5033.

Zhu X, Ma Z, Wang L. Current status of advanced high strength steel for auto-making and its development in baosteel. Rep Baosteel Research Institute 2007; 201900: 1-8.

Zhu X, Li W, Zhao H, Jin X. Effects of cryogenic and tempered treatment on the hydrogen embrittlement susceptibility of TRIP-780 steels. Int J Hydrogen Energy 2013; 38: 10694-10703.

Zhu X, Li W, Zhao H, Wang L, Jin X. Hydrogen trapping sites and hydrogen-induced cracking in high strength quenching & partitioning (Q&P) treated steel. Int J Hydrogen Energy 2014; 39: 13031-13040.

Chapter 2

Hydrogen influence on some advanced high strength steels

(submitted to *Corrosion Science*)

In Chapter 1, a review was conducted to study the hydrogen influence on DP, TRIP, and TWIP steels, which were similar to the key steels in this PhD research. Inconsistent results were obtained, especially for the TWIP steel. It was also indicated that the influence of hydrogen on the key steels depended on various factors, such as the steel strength, the steel microstructure, the steel chemical composition and the hydrogen concentration.

Therefore, it is necessary to conduct specific study on our key DP, Q&P and TWIP steels to determine whether there would be hydrogen influence on these steels, and further, if there was hydrogen influence, examination of the microstructural features associated with the hydrogen influence was performed. The results were included in the following Chapter 2.

Hydrogen influence on some advanced high strength steels

Qinglong Liu[a], Qingjun Zhou[b,*], Jeffrey Venezuela[a], Mingxing Zhang[a], Andrej Atrens[a,*]

[a] The University of Queensland, Division of Materials, School of Mining and Mechanical Engineering, St. Lucia, 4072 Australia

[*] Corresponding author, andrejs.atrens@uq.edu.au, +61 7 3365 3748,

zhouqingjun@baosteel.com,+86 21 26641807

[b] Baoshan Iron & Steel Co., Ltd, Research Institute, Shanghai, 201900, China

Abstract

The hydrogen influence on DP, Q&P and TWIP advanced high strength steels was studied using the linearly increasing stress test with concomitant cathodic hydrogen charging. All steels exhibited hydrogen sensitivity, manifested by (i) decreased strength attributed to solid solution softening by hydrogen, and (ii) reduced ductility and a change from ductile cup and cone fracture to brittle transgranular and/or intergranular fracture, caused by hydrogen assisted fracture processes after the onset of necking. There was no sub-critical crack growth at stresses below the ultimate tensile strength. The hydrogen influence increased with increasing strength, more negative charging potential, and decreasing stress rate.

Key words: advanced high strength steel; SEM; hydrogen embrittlement

1. Introduction

1.1. Advanced high strength steels (AHSS)

In the auto industry, the trend in recent years has been towards weight reduction and improved safety performance, leading to the research and development of steels, as steels are the main choice of auto body materials. Consequently, the advanced high strength steels (AHSS) have been developed and are being adopted. The AHSS permit increases in both strength and formability, enhancing weight savings and crashworthiness [1-6].

The AHSS include Dual Phase (DP), Transformation-Induced Plasticity (TRIP), Complex-Phase (CP), Martensitic (MS), Hot-Formed (HF), and Twinning-Induced Plasticity (TWIP) steels [2].

DP steels are among the first-generation AHSS. DP steels have a microstructure of a soft ferrite matrix and hard martensite islands dispersed in the matrix. DP steels exhibit high

strength, high strain hardening and good formability [2]. Thus, DP steels find applications in the 'crumple zone' at the front and rear of the vehicle, where a high energy absorption capacity is required [7].

Twinning induced plasticity (TWIP) steels belong to the second-generation of AHSS. TWIP steels possess a fully austenitic microstructure. TWIP steels exhibit high strength and good formability, and thus are suitable for manufacturing structural safety-critical parts with complex shape [8]. However, TWIP steels may face technical challenges in processing, and may be expensive due to the high alloying required for the austenitic microstructure [9].

Quenching and partitioning (Q&P) is a novel heat treatment to produce TRIP steels, with enhanced properties compared with the first-generation TRIP steels. Q&P steels have a microstructure of ferrite, controlled amounts of retained austenite, and martensite [10, 11]. Benefitting from the TRIP effect, Q&P steels possess quite a high strain-hardening rate, and a greater ductility and formability than first-generation AHSS with comparable strength. Thus, Q&P steels are third-generation AHSS, with enhanced properties compared with the first-generation AHSS, and lower costs than that required for the alloying additions in the second-generation AHSS [9]. Q&P steels are suited for structural and safety automotive parts with complex shape, such as B-pillar reinforcement [8].

1.2. Hydrogen embrittlement (HE)

Hydrogen present in steels, even as a small amount, can cause the steels to undergo mechanical property degradation, or sudden catastrophic failures, upon the application of a stress, which the steels would have withstood in the absence of hydrogen. This phenomenon is called hydrogen embrittlement (HE).

The three most likely mechanisms of HE in steel [12], which is a non-hydride-forming material, are as follows. (i) Hydrogen-enhanced decohesion (HEDE) postulates that hydrogen accumulated within the lattice reduces the interatomic cohesive forces, and cracks propagate when the local stress exceeds a critical value [13]. (ii) The hydrogen-enhanced localized plasticity (HELP) mechanism proposes that hydrogen facilitates dislocation mobility and facilitates localized high deformation regions, where the applied stress is concentrated. Failures occur when the local stress is higher than the local ultimate tensile stress of the steel [14-16]. (iii) Adsorption-induced dislocation emission (AIDE) is a mechanism similar but more complex than the HELP mechanism. Dislocation emission involves both dislocation nucleation and subsequent movement away from the crack tips. Hydrogen adsorbs on and within several atomic distances from the steel surfaces, where

stress concentrates, such as at crack tips. This adsorbed hydrogen facilitates the nucleation of dislocations. Once nucleation is accomplished, dislocations can readily move away from crack tips under the applied stress, contributing to crack growth [12, 17].

The degree of HE depends on many variables, such as temperature, hydrogen concentration, level and type of applied or residual stress, microstructure, and surface condition of the steel [18, 19]. Increased steel strength correlates with increased HE susceptibility. Thus, HE is of concern for advanced high strength steels [5, 18, 20]. HE susceptibility has been reported to increase successively for lower bainite, quenched and tempered martensite or bainite, pearlite or spheroidized structures, and untempered martensite [21]. Although studies have been conducted on the hydrogen influence of AHSS, predictions of AHSS resistance to HE, based on the type, strength level, microstructure and processing of the steels, are difficult due to the aforementioned complicated variables influencing HE. Therefore, the issue of HE susceptibility of AHSS is still open and further studies are needed.

1.3. Testing methods

The hydrogen influence on steels has been widely studied using two methods: (i) the slow strain rate test (SSRT) [18, 22-26], and (ii) the linearly increasing stress test (LIST) [27-31]. SSRT is strain controlled, and LIST is stress controlled. Winzer et al. [32] compared these two methods and showed that both methods are identical up until yielding, or the onset of subcritical crack growth. LIST produced faster testing, whereas SSRT took a longer time to complete. However, both methods could provide comparable results.

The SSRT has been used to study HE of DP, Q&P and TWIP steels. DP steels, studied by SSRT, were reported to show some susceptibility to hydrogen embrittlement, manifested by significant loss of ductility and the presence of brittle features [20, 22-24, 33]. In addition to ductility loss and brittle features, Lovicu et al. [5] found that DP steels also had decreased ultimate tensile strength, whereas other studies [20, 24, 33] documented no significant influence on ultimate tensile strength and yield strength by hydrogen. Some studies on Q&P steels [34-37] found susceptibility to HE with decreased ultimate tensile strength and ductility. Inclusions present in DP and Q&P steels were suggested to be detrimental to HE resistance by causing brittle fisheye features [34, 38]. In recent years, hydrogen influence on TWIP steels has also attracted a lot of attention. However, investigations concerning hydrogen influenced mechanical degradation have not been consistent. Ronevich et al. [25] found that the ductility and tensile properties of TWIP steels were not influenced by hydrogen with contents up to 9.5 ppm. In contrast, Ryu et al. [39]

found significant decreases of elongation and ultimate tensile strength caused by hydrogen concentrations of about 0.5 ppm. Koyama et al. [26] also found a similar negative influence of hydrogen on TWIP steels. They studied the influence of diffusible hydrogen content on the tensile strength and fracture modes, and proposed two cases: (i) a ductile fracture and no deterioration of tensile properties with a low diffusible hydrogen content, and (ii) inter-granular brittle fracture and decreased fracture stress with a relatively high hydrogen content [40]. In brief, inconsistent results have been reported concerning (i) the existence of a hydrogen influence on some key AHSS, and (ii) which properties are influenced by hydrogen.

The linearly increasing stress test (LIST) was proposed by Atrens and co-workers [27] to study parts and structures in service which are subjected to load-controlled conditions. LIST has been utilized to study HE and stress corrosion cracking (SCC) of materials such as medium strength steels [28, 29], high strength steels [41-43] and martensitic advanced high strength steels for auto constructions [30, 31]. Venezuela et al. [30] studied the hydrogen influence on four commercial martensitic advanced high strength steels using LIST with various hydrogen charging conditions and stress rates. They found that the hydrogen influence became more significant with increasingly negative hydrogen charging potential and decreased stress rate.

There has yet no study of hydrogen influence on DP, Q&P and TWIP grades of AHSS using LIST. Such a study will therefore add to the knowledge base of HE of AHSS.

1.4. Scope of study

The current work (i) studied the HE behaviour of commercial DP, Q&P and TWIP steels using LIST on specimens subjected to (a) increasingly negative hydrogen charging potentials and (b) decreasing stress rates, (ii) identified HE mechanisms associated with the fracture processes, and (iii) correlated microstructures with the hydrogen influence on the steels.

2. Experimental details

2.1. Materials

The HE susceptibility was studied for six commercial DP, Q&P and TWIP, designated as follows: 980DP, 980DP-650YS, 980DP-700YS, 1200DP, 980QP and 950TW. These steels were supplied from commercial production as rolled sheets. 980DP-650YS, 980DP-700YS and 1200DP steels were galvanized and the thicknesses of the zinc coatings

were in the range of 10-30 µm based on observation using scanning electron microscopy (SEM). Table 1 shows the chemical compositions and mechanical properties as provided by the steel supplier.

2.2. Microstructural characterization

Table 1 also includes the microstructures of the studied steels. All the steels were mechanically ground and polished to 1 µm. DP and Q&P steels were etched with a 2% nital solution. TWIP steel was electro-etched with a solution consisted of 10% perchloric acid and 90% methanol. The microstructures were examined after etching, using a JEOL 6610 scanning electron microscope (SEM). The volume fraction of each phase in DP and Q&P steels was estimated by the point counting method [44]. The mean grain size of DP and TWIP steels were evaluated using the linear intercept method [45, 46], and that of Q&P steel was measured using the microscope calibration bar.

2.3. LIST and hydrogen charging

LIST specimens were cut from the steel sheets with as received thickness. Fig. 1 shows the dimensions of a LIST specimen. The longitudinal dimension was parallel to the rolling direction of the sheet. The surfaces of the specimens were mechanically ground and polished with SiC papers in the following order: 320 grit, 600 grit and 1200 grit. This removed (i) the zinc coating of the galvanized steels and (ii) the surface rust and contamination of the non-galvanized steels. The mean thickness of the specimens after polishing was 1.75 mm for 980 DP, 0.95 mm for 980DP-650YS, 0.89 mm for 980DP-700YS, 1.32 mm for 1200DP, 1.14 mm for 980QP and 1.33 mm for 950TW.

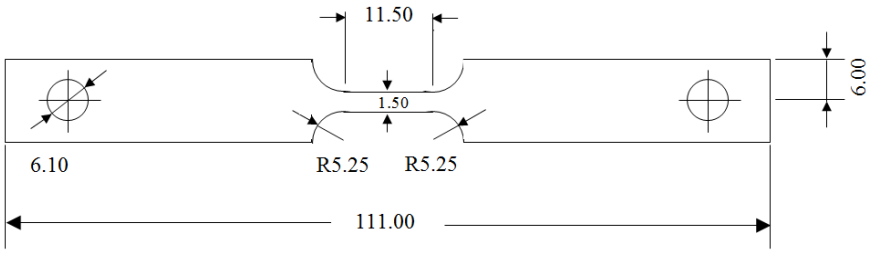

Fig.1. Dimensions of a LIST specimen (in mm).

Table 1 Chemical composition (in wt %), mechanical properties, and microstructures of the AHSS. The chemical composition and mechanical properties were provided by the steel supplier. The volume fractions and the grain sizes of the phases were experimentally determined by the authors of this work. The grain sizes of marteniste referred to the sizes of prior austenite grains. 950 TW was full austenite. All other steels contained ferrite and martensite. 980 QP also contained some retained austenite.

Steel designation	C	Si	Mn	Al	Nb	Ti	Yield stress (MPa)	Tensile stress (MPa)	Elongation at fracture (e_f, %)	Ferrite		Martensite		Austenite	
										Fraction (%)	Grain size (μm)	Fraction (%)	Grain size (μm)	Fraction (%)	Grain size (μm)
980DP	0.09	0.28	2.4	<0.03	<0.04	<0.02	592	930	8.3	40%	6.8 ± 2.4	60%	5.5 ± 2.1	0	-
980DP-650YS	0.09	0.29	2.4	<0.03	<0.04	<0.03	645	1057	7.9	37%	2.1 ± 0.5	63%	1.5 ± 0.2	0	-
980DP-700YS	0.08	0.41	2.4	<0.03	<0.04	<0.05	697	1039	6.9	36%	1.1 ± 0.2	64%	1.4 ± 0.2	0	-
1200DP	0.12	0.30	2.4	<0.03	<0.04	<0.03	896	1198	4.7	26%	5.0 ± 1.5	74%	4.8 ± 0.7	0	-
980QP	0.20	1.50	2.0	<0.03	<0.04	<0.01	682	1020	11.3	39%	9.8 ± 2.7	53%	9.4 ± 2.0	8%	1.3 ± 0.6
950TW	0.60	0.09	15.2	1.46	—	—	497	981	45	0	-	0	-	100%	3.9 ± 0.5

Table 2 Values of the applied motor speed (revolutions per hour, rph) and the corresponded stress and strain rates.

Steel designation	Average thickness, (mm)	Motor speed, (rph)	Corresponded stress rate, (MPa s^{-1})	Corresponded strain rate in the initial elastic region, (s^{-1})
980DP	1.75	300	0.54	2.7×10^{-6}
		30	0.054	2.7×10^{-7}
		3	0.0054	2.7×10^{-8}
980DP-650YS	0.95	300	1.00	5.0×10^{-6}
		30	0.100	5.0×10^{-7}
		3	0.0100	5.0×10^{-8}
980DP-700YS	0.89	300	1.07	5.4×10^{-6}
		30	0.107	5.4×10^{-7}
		3	0.0107	5.4×10^{-8}
1200DP	1.32	300	0.72	3.6×10^{-6}
		30	0.072	3.6×10^{-7}
		3	0.0072	3.6×10^{-8}
980QP	1.14	300	0.84	4.2×10^{-6}
		30	0.084	4.2×10^{-7}
		3	0.0084	4.2×10^{-8}
950TW	1.33	300	0.72	3.6×10^{-6}
		30	0.072	3.6×10^{-7}
		3	0.0072	3.6×10^{-8}

Fig. 2 shows a schematic of the LIST apparatus. The LIST was based on the principle of a lever beam. One side of the beam was connected to a specimen, which was subjected to various experimental environments, whilst the other side was loaded with a known weight (14 kg). A synchronous motor drove the weight away from the fulcrum, resulting in a linearly increasing engineering stress applied to the specimen. The applied stress, S (MPa), was calculated using:

$$S = \frac{(13720)d}{A} \quad (1)$$

where d (m) is the distance between the position of the weight and the zero load condition, measured by the metric scale attached to the beam, and A (mm^2) is the original cross-section area of the gauge part of the specimen. The numerical factor of 13720 in Eq. (1) depends on the mechanical advantage, the mass of the weight (14 kg), and the acceleration of gravity.

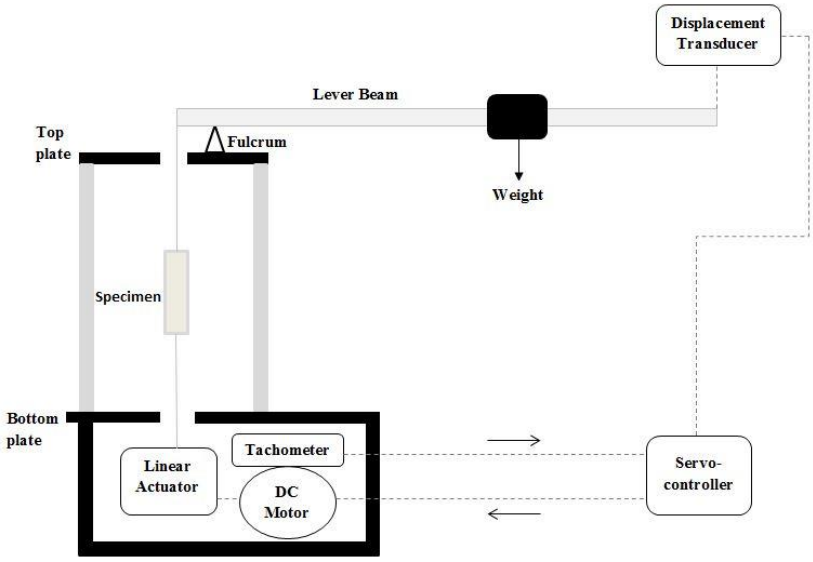

Fig.2. Schematic of the LIST apparatus.

The applied stress rate depended on (i) the speed of the synchronous motor and (ii) the specimen cross-section area. Three motor speeds, 3, 30 and 300 revolutions per hour (rph), were used to apply various stress rates to the specimens. 3 rph provided the slowest stress rate. 30 rph provided the medium stress rate. 300 rph produced the fastest stress rate. Based on the two aforementioned dependent factors and Eq. (1), the stress rate could be calculated. For example, for 980DP, the stress rate using the 300, 30 and 3 rph motors corresponded to 0.54, 0.054 and 0.0054 MPa s^{-1}, respectively. Various cross-section areas, resulted from the various thicknesses, led to the differences in the stress rates at the same motor speed for the different types of steel. For example, at the same motor speed of 30 rph, the applied stress rate for

980DP, 980DP-650YS, 980DP-700YS, 1200DP, 980QP and 950TW was 0.054, 0.100, 0.107, 0.072, 0.084 and 0.072 MPa s^{-1}, respectively. Table 2 shows the values of the applied motor speed and the corresponded stress rates for all the steels. The strain rate corresponding to each applied stress rate in the initial elastic region of the LIST test can also be estimated by taking into account of the Young's modulus of the steels. For example, an applied stress rate of 0.107 MPa s^{-1} in the initial elastic region of the LIST corresponded to a strain rate of 5.4×10^{-7} s^{-1}. Table 2 includes the strain rate values that corresponded to each stress rate in the initial elastic region in LISTs, for the ease of comparison with other studies using strain controlled tensile tests. For tests in air, three motor speeds were used, whereas the medium and slowest motor speeds were used for tests in the 0.1 M NaOH solution.

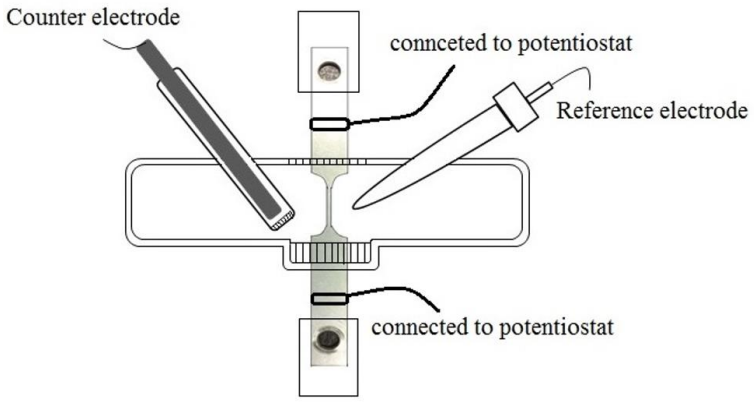

Fig.3. Schematic of the hydrogen charging set-up.

Experimental environments for LIST tests in this work were ambient air, and electrochemical cathodic hydrogen charging at – 1.100 $V_{Hg/HgO}$, – 1.400 $V_{Hg/HgO}$, and – 1.700 $V_{Hg/HgO}$ in a 0.1 M NaOH solution. Liu et al. [47] reported an increased hydrogen fugacity with increasingly negative charging potential. Thus, a more negative cathodic charging potential herein was expected to provide a higher hydrogen fugacity and thereby a higher possibility of a hydrogen influence on the studied steels. For LIST tests in the 0.1M NaOH solution, hydrogen charging was conducted in a three-electrode charging cell, as shown in Fig. 3. Only the gauge part of the specimen was subjected to the solution, with other specimen surfaces covered with a Teflon tape. The working electrode was the specimen. The reference electrode was an Hg/HgO, KOH (20%) electrode. The counter electrode was a graphite rod with an isolation chamber collecting the shedding carbon powders, as suggested by Venezuela et al. [31]. A 24-hour pre-charging was carried out at the applied potential, with a static stress of 20% yield strength applied to the specimen, to ensure a constant hydrogen content throughout the specimen gauge part before each LIST test for the DP and Q&P steels.

It should be noted that a 24-hour pre-charging would not permit an uniform hydrogen concentration across the TWIP specimen, due to a much lower hydrogen diffusion coefficient in the austenitic TWIP steel, at least three orders of magnitude lower than in the ferritic DP or Q&P steels [5]. However, the influence of hydrogen with 24-hour pre-charging on TWIP steels was still of interest and was studied in this work. After the 24-hour pre-charging, the LIST test was started, and the hydrogen charging was maintained until final fracture of the steel.

LIST specimens were designated with the following format: 'steel type-testing environment-motor speed', as shown in Table 3. For testing in air, 'A' was used to designate the testing environment, whilst for tests in the 0.1M NaOH solution, the absolute value of the applied potential was used. For example, '980DP-650YS-A-300' indicated 980DP-650YS was tested in air using a 300 rph motor, and '1200DP-1.7-3' indicated 1200DP, tested in the 0.1 M NaOH solution with an applied hydrogen charging potential of $-1.700\ V_{Hg/HgO}$, using a motor speed of 3 rph. Table 3 also includes designations as 'steel type-A-S', with the applied stress rate designated as 'UTM'. These tests were in air using a universal tensile machine and were carried out by the steel supplier. The strain rate approximately corresponded to a stress rate of 50 MPa s^{-1} in the initial elastic region, and was considerably faster than that corresponding to the fastest motor speed of 300 rph in LISTs in this work.

A direct current potential drop (DCPD) method was used to determine the apparent threshold stress for the initiation of subcritical cracking for specimens tested in the solution, σ_{th}, or the yield stress for specimens tested in air, σ_y. A constant 3-ampere current was applied to the specimen. The potential drop across the specimen was recorded. The increase of resistance led to an increased potential drop. With the increased applied stress, the specimen cross-section area slightly decreased and the specimen length increased, leading to a slightly increased resistance, and concomitantly a slowly increasing potential drop. At the onset of subcritical cracking or plastic yielding, the decrease of specimen cross-section area became more significant, resulting in a greater increase of potential drop. Therefore, the plot of the recorded potential drop as a function of the applied stress showed a change in slope. The stress at this change corresponded to the threshold stress, σ_{th}, or the yield stress, σ_y.

The fracture stress, σ_f, could be determined using Eq. (1) with values of d at fracture and the original cross-section area, A, in each test. The reduction in area, R_A, was evaluated using the original cross-section area and that after testing in air or with hydrogen charging. The degree of hydrogen influence, expressed by the hydrogen embrittlement index (EI), was

quantified using the R_A values after testing under various environments, as following [20, 30, 33]:

$$EI = \frac{R_{A,air} - R_{A,H}}{R_{A,air}} \times 100\% \quad (2)$$

where $R_{A,air}$ is the reduction in area tested in air, and $R_{A,H}$ is the reduction in area under hydrogen charging conditions. The values of EI range from 0 to 100%, with EI = 0 indicating no HE susceptibility, and EI = 100% indicating full susceptibility to HE.

2.4. Fracture surface observation

After fracture, the specimen was cleaned by ultrasonic cleaning in a hot Alconox solution for 30 min [30], and each fracture surface was examined using the JEOL 6610 SEM attached with an EDS. Thereafter, typical fractured DP and Q&P specimens were mounted in resin, ground and polished to 1 μm, etched with a 2% nital solution, and SEM examination was carried out of the hydrogen induced surface cracks on the transverse surface.

3. Results

3.1. Microstructure

Fig. 4 and Table 1 present the typical microstructures and phase fractions of the studied steels as in our previous studies [4, 48, 49].

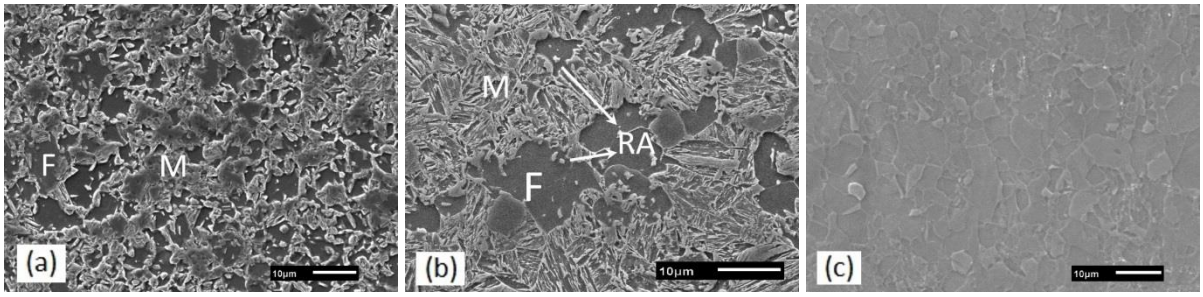

Fig.4. Microstructures of (a) 980DP, (b) 980QP and (c) 950TW steels observed under SEM. F stands for ferrite, M is for martensite and RA refers to retained austenite.

Fig. 4(a) shows that the typical microstructure of DP steels consisted of a soft ferrite matrix and hard martensite islands embedded along ferrite grain boundaries. For the four DP steels, the ferrite fraction decreased and the martensite fraction increased in the following order 980 DP, 980DP-650YS, 980DP-700YS and 1200DP, correlating with the increasing yield strength. Due to the relatively high volume fraction of martensite in the four DP steels, some of the martensite islands linked into a semi-continuous network, as presented in Fig. 4(a) and was also described in [50]. The ferrite and martensite grain sizes were comparable in

each of the DP steels, and were larger in 980 DP and 1200DP than in 980DP-650YS and 980DP-700YS.

Fig. 4(b) shows that the microstructure of the Q&P steel consisted of about 39% ferrite, 53% martensite and 8% retained austenite. The retained austenite was in the shape of a block, dispersed in ferrite or adjacent to martensite constituents. The grain size of the retained austenite was significantly smaller than that of ferrite and martensite.

TWIP steel was fully austenitic, as shown in Fig. 4(c). The average grain size was around 3.9 μm.

3.2. Mechanical properties

Fig. 5 presents typical plots of potential drop versus engineering stress for DP, Q&P and TWIP steels. These plots allowed determination of the values of σ_{th} or σ_y, corresponding to the stress at which a significant increase in slope occurred.

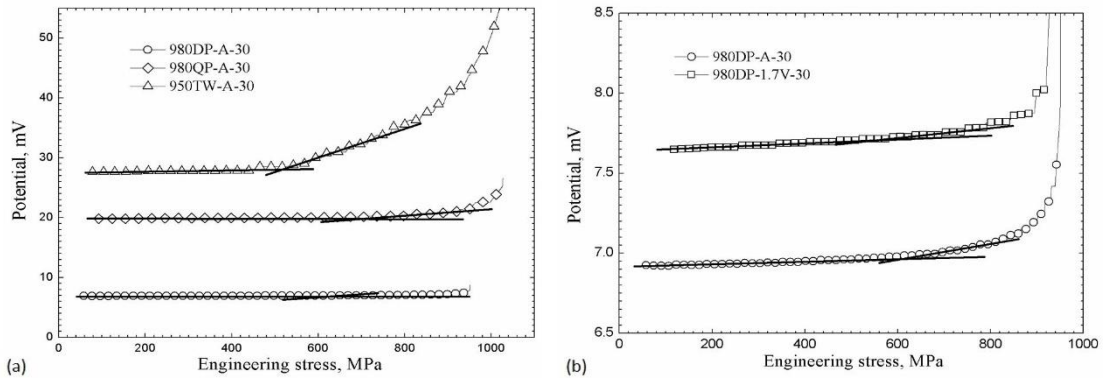

Fig.5. Typical plots of potential drop (mV) vs. engineering stress (MPa) (a) for DP, Q&P and TWIP steels and (b) magnified plots for 980DP steels tested in air and with hydrogen charging.

Fig. 5(a) shows potential drop plots of 980DP, 980QP and 950TW steels tested in air at the medium stress rates corresponding to a motor speed of 30 rph. The different type of steels exhibited significantly different potential drop ranges, correlating to the intrinsic difference in steel elongations, as presented in Fig. 1. 950TW possessed an elongation of 45% and showed the largest potential drop range. In contrast, the lower potential drop range of the DP steel was so low that it was hard to distinguish the transition of the plot. Typical potential drop plots of 980DP tested in air and with hydrogen charging were included in Fig. 5(b). Similar plots were obtained for all the other LIST tests, permitting evaluating the σ_{th} or σ_y for each test. The precision for measurement of σ_{th} or σ_y was ±5 MPa. The precision for evaluation of σ_f was ±2 MPa. Table 3 and Fig. 6 present the values for σ_f, σ_{th} or σ_y, R_A, EI and a summary of the fractography.

3.2.1. In air

Table 3 indicated that, for LIST tests in air, the values of tensile strength, σ_f, and yield strength, σ_y, were consistent with the corresponding values obtained by the steel supplier from conventional tensile tests as presented in Table 1. The values of σ_f, σ_y and R_A for each steel tested at the three stress rates were similar to each other for the DP, Q&P and TWIP steels. For example, the values of reduction in area, R_A, were 62%, 61% and 62% for 980DP-700YS-A-300, 980DP-700YS-A-30 and 980DP-700YS-A-3, respectively.

However, for 1200DP, there appeared to be a slight decrease in tensile strength with decreasing stress rate. For 1200DP the tensile strength in air at 0.72, 0.072 and 0.0072 MPa s^{-1} was 1182, 1175, 1150 MPa, respectively. Such a decrease was less than 3% and was not present in all cases. This may be attributed to the fact that the experimental error, resulting from steel variation, was larger than the precision of the LIST.

In addition, for 950TW, R_A was lower at the lower stress rates. At the highest stress rate of 0.72 MPa s^{-1}, the reduction in area was 65% for 950TW tested in air, which decreased by 12% to 57% for the tests at the two slower stress rates. Such a decrease suggested that the ductility of 950TW steel was somewhat decreased at the slower stress rates.

3.2.2. Hydrogen charged DP steels

Table 3 and Fig. 6 indicate that the four DP steels showed susceptibility to hydrogen under cathodic hydrogen charging for all the charging potentials at the medium and slowest applied stress rates. The hydrogen influence was manifest by the decreased values of reduction in area, R_A, and thereby the increased hydrogen embrittlement index, EI. For example, the R_A of 980DP steel in air at 0.0054 MPa s^{-1} was 78%, whereas the R_A was 29% with the hydrogen charging potential of -1.700 $V_{Hg/HgO}$ tested at the same stress rate, giving an EI value of 63%. In addition, the decrease in R_A and increase in EI increased with a more negative charging potential, evidenced for example by comparing 980DP-650YS-1.1-30, 980DP-650YS-1.4-30 and 980DP-650YS-1.7-30. There was the same trend of the change in R_A and EI as the applied stress rate became slower. For instance, when charged at -1.700 $V_{Hg/HgO}$, the respective R_A and EI values of 1200DP at 0.072 MPa s^{-1} were 32% and 56%, and changed to 21% and 70% at a slower applied stress rate of 0.0072 MPa s^{-1}. Table 3 and Fig. 6 also show that 980DP had the lowest hydrogen embrittlement index, EI, of the four DP steels, followed by 1200DP. The EI values of 980DP-650YS and 980DP-700YS were similar and were higher than those of 980DP and 1200DP.

Table 3 Results from LIST experiments in air and in NaOH solutions. (σ_{th}, apparent threshold stress. σ_y, yield stress. σ_f , fracture stress, UTS. R_A, reduction in area. EI, hydrogen embrittlement index)

Specimen designation	Environment	Potential ($V_{Hg/HgO}$)	Applied stress rate (MPa s^{-1})	σ_{th} or σ_y ±5 (MPa)	σ_f ±2 (MPa)	R_A (%)	EI (%)	Fractography
980DP-A-S	Air	n/a	UTM	592	930			
980DP-A-300	Air	n/a	0.54	579	988	79		cup and cone, necking
980DP-A-30	Air	n/a	0.054	603	949	79		cup and cone, necking
980DP-A-3	Air	n/a	0.0054	600	957	78		cup and cone, necking
980DP -1.1-30	S (NaOH)	-1.100	0.054	578	955	51	35	shearing, necking
980DP -1.4-30	S (NaOH)	-1.400	0.054	555	949	41	48	shearing, necking
980DP -1.7-30	S (NaOH)	-1.700	0.054	540	932	39	51	shearing, necking
980DP -1.7-3	S (NaOH)	-1.700	0.0054	524	957	29	63	shearing, necking
980DP-650YS-A-S	Air	n/a	UTM	645	1057			
980DP-650YS-A-300	Air	n/a	1.00	650	1105	65		cup and cone, necking
980DP-650YS-A-30	Air	n/a	0.100	647	1052	61		cup and cone, necking
980DP-650YS-A-3	Air	n/a	0.0100	655	1073	63		cup and cone, necking
980DP-650YS -1.1-30	S (NaOH)	-1.100	0.100	634	1038	19	69	shearing, necking visible
980DP-650YS -1.4-30	S (NaOH)	-1.400	0.100	607	1028	15	75	shearing, necking visible
980DP-650YS -1.7-30	S (NaOH)	-1.700	0.100	582	1102	14	77	shearing, necking visible
980DP-650YS -1.7-3	S (NaOH)	-1.700	0.0100	553	1004	9	86	shearing, little necking visible
980DP-700YS-A-S	Air	n/a	UTM	697	1039			
980DP-700YS-A-300	Air	n/a	1.07	681	1045	62		cup and cone, necking
980DP-700YS-A-30	Air	n/a	0.107	679	1010	61		cup and cone, necking
980DP-700YS-A-3	Air	n/a	0.0107	680	1003	62		cup and cone, necking
980DP-700YS -1.1-30	S (NaOH)	-1.100	0.107	671	1025	20	67	shearing, necking visible
980DP-700YS -1.4-30	S (NaOH)	-1.400	0.107	649	937	17	72	shearing, necking visible
980DP-700YS -1.7-30	S (NaOH)	-1.700	0.107	640	998	16	74	shearing, necking visible
980DP-700YS -1.7-3	S (NaOH)	-1.700	0.0107	622	906	12	81	shearing, little necking visible
1200DP-A-S	Air	n/a	UTM	896	1198			
1200DP-A-300	Air	n/a	0.72	883	1182	73		cup and cone, necking
1200DP-A-30	Air	n/a	0.072	877	1175	72		cup and cone, necking
1200DP-A-3	Air	n/a	0.0072	880	1150	70		cup and cone, necking
1200DP -1.1-30	S (NaOH)	-1.100	0.072	868	1149	42	42	shearing, necking
1200DP -1.4-30	S (NaOH)	-1.400	0.072	846	1139	37	49	shearing, necking
1200DP -1.7-30	S (NaOH)	-1.700	0.072	831	1176	32	56	shearing, necking
1200DP -1.1-3	S (NaOH)	-1.100	0.0072	846	1169	29	59	shearing, necking visible
1200DP -1.4-3	S (NaOH)	-1.400	0.0072	836	1123	27	61	shearing, necking visible
1200DP -1.7-3	S (NaOH)	-1.700	0.0072	812	1119	21	70	shearing, necking visible

980QP-A-S	Air	n/a	UTM	682	1020			
980QP-A-300	Air	n/a	0.84	683	1074	62		cup and cone, necking
980QP-A-30	Air	n/a	0.084	677	1025	63		cup and cone, necking
980QP-A-3	Air	n/a	0.0084	687	1029	63		cup and cone, necking
980QP -1.1-30	S (NaOH)	-1.100	0.084	669	949	21	67	shearing, necking visible
980QP -1.4-30	S (NaOH)	-1.400	0.084	651	923	19	70	shearing, necking visible
980QP -1.7-30	S (NaOH)	-1.700	0.084	639	933	13	79	shearing, necking visible
980QP -1.1-3	S (NaOH)	-1.100	0.0084	658	919	13	79	shearing, necking visible
980QP -1.4-3	S (NaOH)	-1.400	0.0084	573	929	10	84	shearing, little necking visible
980QP -1.7-3	S (NaOH)	-1.700	0.0084	596	866	9	86	shearing, little necking visible
950TW-A-S	Air	n/a	UTM	497	981			
950TW-A-300	Air	n/a	0.72	513	1023	65		cup and cone, necking
950TW-A-30	Air	n/a	0.072	479	1005	57		shearing, necking
950TW-A-3	Air	n/a	0.0072	483	990	57		shearing, necking
950TW-1.1-30	S (NaOH)	-1.100	0.072	473	982	43	25	shearing, necking visible
950TW-1.4-30	S (NaOH)	-1.400	0.072	464	954	40	30	shearing, necking visible
950TW-1.7-30	S (NaOH)	-1.700	0.072	457	955	39	32	shearing, necking visible
950TW-1.1-3	S (NaOH)	-1.100	0.0072	464	936	39	32	shearing, necking visible
950TW-1.4-3	S (NaOH)	-1.400	0.0072	460	916	38	33	shearing, necking visible
950TW-1.7-3	S (NaOH)	-1.700	0.0072	451	922	33	42	shearing, necking visible

Moreover, σ_f and σ_{th} were also somewhat decreased under hydrogen charging conditions compared with the values in air for each of the DP steels. There was a small decease in σ_f and σ_{th} with a more negative charging potential, as is clear for example by comparing those values for 980DP-1.1-30, 980DP-1.4-30 and 980DP-1.7-30. However, there was not such a decrease in every case. There were also similar decreases in σ_f and σ_{th} with a lower stress rate. For example, a comparison between 980DP-650YS-1.7-30 and 980DP-650YS-1.7-3 indicated a decrease of 5% in σ_{th} from 582 MPa to 553 MPa and a decrease of 9% in σ_f from 1102 MPa to 1004 MPa.

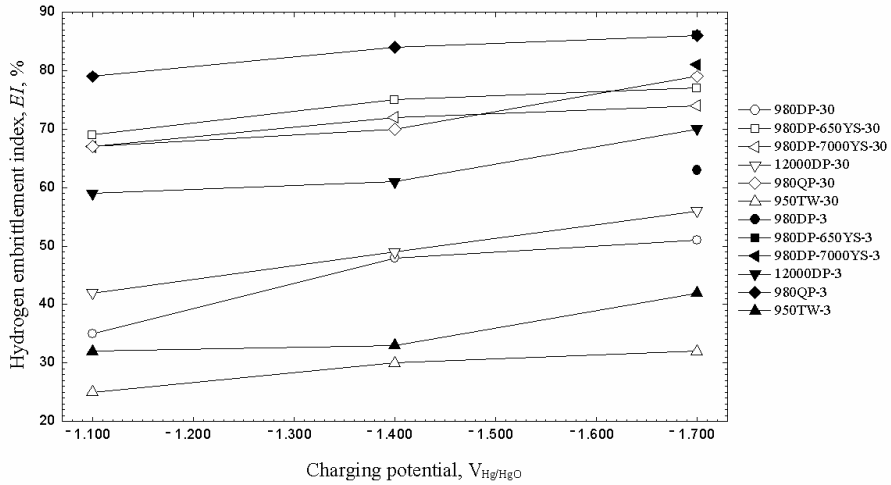

Fig.6. Hydrogen embrittlement index, EI, versus charging potential for all the studied steels.

3.2.3. Hydrogen charged Q&P steel

Table 3 and Fig. 6 also include the LIST results for 980QP. Similar to the DP steels, 980QP, when subjected to hydrogen charging conditions, experienced some hydrogen influence as indicated by decreased values of σ_f, σ_{th} and R_A and an increased hydrogen embrittlement index, EI. This change of σ_f, σ_{th}, R_A and EI was enhanced with an increasingly negative hydrogen charging potential and a slower stress rate. Thus, 980QP-1.7-3, tested at –1.700 $V_{Hg/HgO}$ at 0.0084 MPa s^{-1}, was considered the severest testing condition and exhibited a 16% decrease in σ_f and a 13% decrease in σ_{th}, compared with those values in air, and the highest EI value of 86%. This indicated that 980QP was embrittled at this testing condition. 980QP showed a higher hydrogen embrittlement index, EI, than all the DP steels under hydrogen charging, even higher than 1200DP with a higher strength. This was consistent with results from the literature [20, 22, 33] and was considered due to the high solubility of hydrogen in the retained austenite. During deformation, austenite could transform into martensite, which was quite susceptible to the hydrogen influence. Thus, when the stress was

applied, the retained austenite transformed to the hydrogen enriched susceptible martensite, whereupon the martensite cracked.

3.2.4. Hydrogen charged TWIP steel

950TW steel also exhibited susceptibility to hydrogen, as shown in Table 3 and Fig. 6. The values of σ_f, σ_{th} and R_A decreased with hydrogen charging compared with the uncharged specimens. With an increasingly negative charging potential and a lower stress rate, σ_f, σ_{th} and R_A decreased further, and EI increased accordingly. 950TW-1.7-3, the severest testing condition, resulted in the respective decrease of σ_f and σ_{th} by 7% and 9%, and the highest EI of 42%.

950TW steels showed the lowest hydrogen embrittlement susceptibility compared with other AHSS in this study. This may be attributed to their fully austenitic microstructure, which has a hydrogen diffusion coefficient at least three orders of magnitude lower than that of ferrite phase [5]. Therefore, a direct comparison between TWIP steel with other ferritic DP and Q&P steels should be undertaken carefully.

3.3. Fracture surfaces

3.3.1. In air

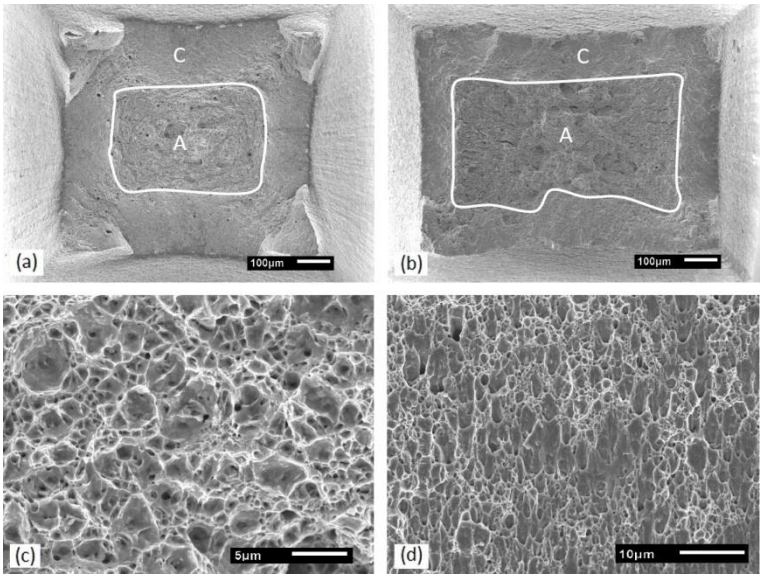

Fig.7. Micrographs showing the top view of typical fracture surface of (a) 980DP-A-3 and (b) 980QP-A-30 tested in air, and magnified view of (c) the outlined cone part and (d) its surrounding cup regions in (a).

Fig. 7 presents the fracture surface of 980DP-A-3 and 980QP-A-30 tested in air. Fig. 7(a) and (b) show typical cup and cone fractures, where there was (i) the outlined centre cone part A and (ii) its adjacent shear lip regions C. Figs. 7(c) and (d) illustrate the magnified view of the centre cone part and the surrounding shear lips, respectively, as outlined in Fig. 7(a) for

980DP. The centre cone part was relatively flat, normal to the tensile direction, and possessed round ductile dimples due to micro-void coalescence, as shown in Fig. 7(c). There were secondary cracks occasionally in the centre cone part, e.g. in Fig. 7(b). The shear lips, surrounding the centre cone part, were not flat and were typically at an angle of 45 degree to the tensile direction. Fig. 7(d) presents the magnified view of the shear lips. These shear fractures also possessed dimples, but the dimples were different from those in the cone part as in Fig. 7(c) in that these dimples were shallower and were sheared to a parabolic shape. The cup and cone fracture indicated that fractures formed in the centre cone region and grew to initiate the final shear fracture in the surrounding shear regions. The shear dimples in the shear lips provided indications of the shear stress direction.

All the DP and the Q&P steels exhibited the cup and cone features tested in air at the three stress rates in this study. This cup and cone fracture indicated good ductility, which was in agreement with the high values of reduction in area, all higher than 60% for these steels, as shown in Table 3.

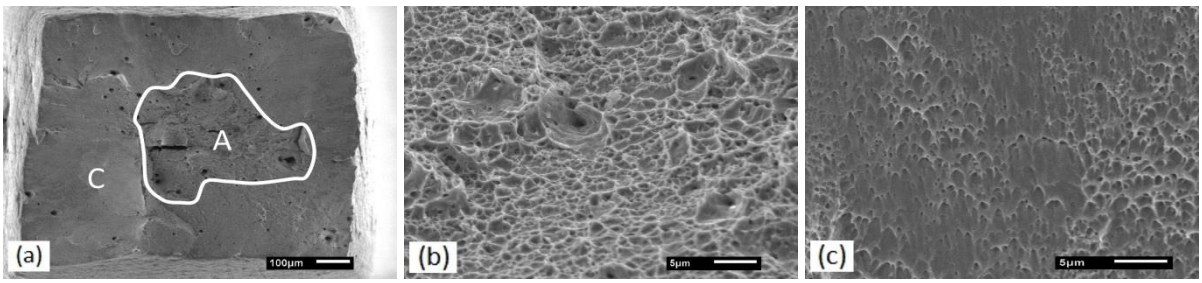

Fig. 8. Fracture appearance of 950TW-A-300: (a) a top overview, magnified views of (b) the centre region A and (c) region C near the edge.

Fig. 8 shows images of the fractured 950TW steels tested in air at the fastest stress rate. Fig. 8(a) presents the top overview of the fracture appearance of 950TW-A-300, which was similar to the cup and cone fracture of DP and Q&P steels tested in air. Region A corresponded to the cone part and the surrounding C regions were shear lips. Fig. 8(b) illustrates the detailed fracture fractography of region A, where ductile dimples dominated, along with some secondary cracks. In the shear lips (region C), there were shallower, parabolic shear dimples, as presented in Fig. 8(c). The fracture initiated at the centre region A and grew to cause final shear fracture.

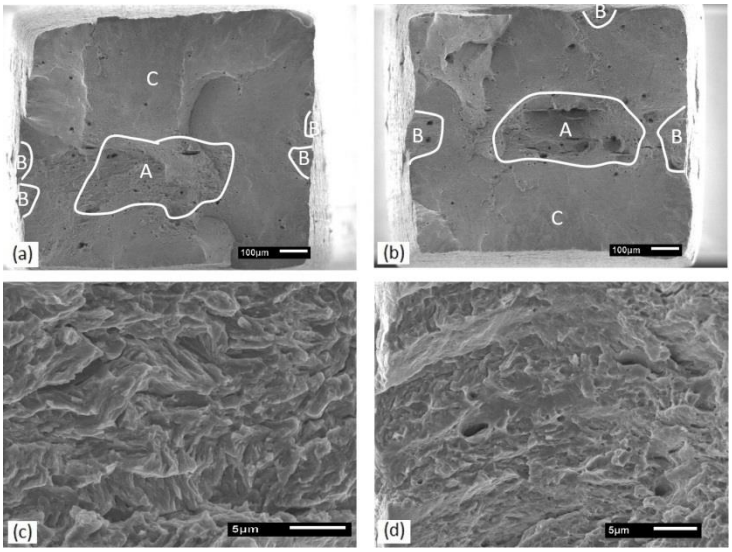

Fig. 9. Respective SEM images of 950TW-A-30 and 950TW-A-3 : (a) and (b) top views, (c) and (d) magnified images of region B.

Figs. 9 (a) and (b) present the top overview of fractured 950TW-A-30 and 950TW-A-3, respectively. There were similar regions A and C. There were small region B areas near the edge of the surface, where there were noticeable brittle features. Magnified images of region B in 950TW-A-30 and 950TW-A-3 are presented in Fig. 9(c) and (d), respectively. The characteristics of region B were transgranular quasi-cleavage with some secondary cracks. In addition, there were separated inclusions occasionally in region B, as shown in Figs. 10.

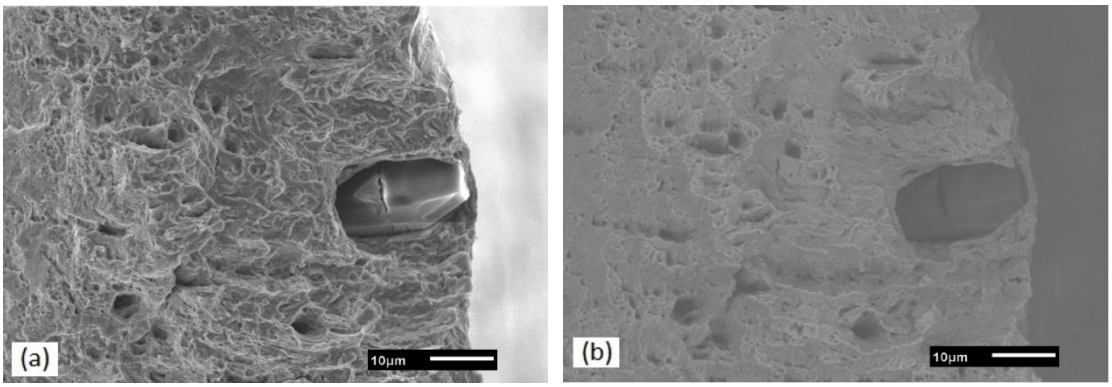

Fig. 10. SEM Images showing an inclusion observed with (a) secondary electron and (b) backscattered electron.

The inclusion had a shape like a prism, a length of about 20 μm, and was surrounded by transgranular quasi-cleavage features. EDS analysis of the inclusion revealed that the inclusion might be AlN. Such AlN inclusion in TWIP steels was also reported in other research [51, 52]. The presence of AlN was attributed to the relatively high Al concentration for stabilizing the austenite against transforming to ε-martensite [4, 53]. The brittle region B on the fracture surface was also considered as an initiation site contributing to the final fracture of 950TW-A-30 and 950TW-A-3.

3.3.2. Hydrogen charged DP steel

Fig. 11 presents the fracture appearance of the four DP steels tested with the hydrogen charging potential of – 1.100 $V_{Hg/HgO}$ at the medium stress rate. This testing condition was the mildest hydrogen charging conditions used in this study.

The fracture appearance was significantly different from the cup and cone fratures for testing in air (e.g. see Fig. 7). Fig. 11 indicates two types of fracture regions: (i) a shear fracture region indicated by 'S' and (ii) brittle fracture regions indicated by 'B'. Each brittle B region was located near the edges of the fracture surface and normally had an arched shape. The appearance of region B indicated that these fractures initiated from the edge and grew towards the inner part of the specimen. The brittle region B was relatively flat compared with other regions of the fracture surface, whereas the shear fracture region S was not flat and had an angle to the tensile direction. The shearing could occur in one direction, as in Figs. 11(a) and (d), or along different planar surfaces, see Figs. 11(b) and (c). The white arrows in Fig. 11 indicate the directions of shear fracture propagation. In each case, the fracture initiated from the B regions or from a lower edge of the S region. For example, Fig. 11(b) shows fracture initiated from region B on the right edge and grew towards the inner part of the specimen, where the fracture met the shear fracture originating from another lower edge on the left of the specimen.

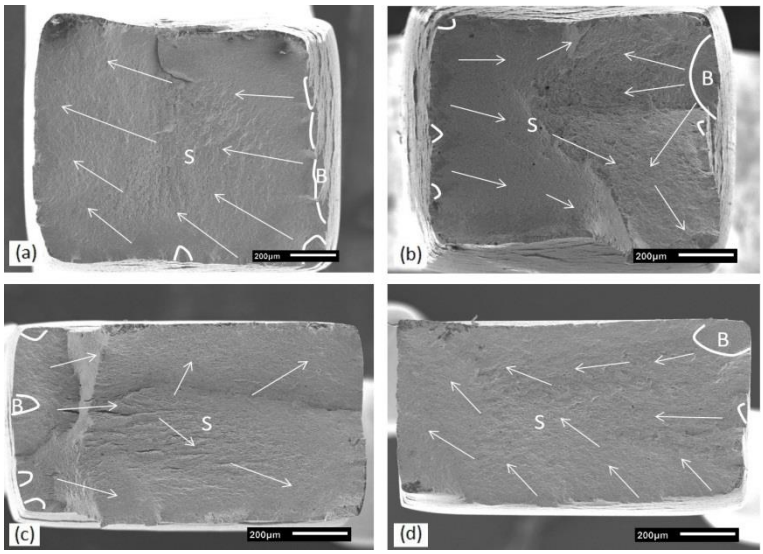

Fig. 11. Fracture appearance of (a) 980DP-1.1-30, (b) 1200DP-1.1-30, (c) 980DP-650YS-1.1-30 and (d) 980DP-700YS-1.1-30.

Fig. 12 shows the shear dimples in region S of 980DP-1.1-30 and 980DP-700YS-1.1-30. These shear dimples were throughout the whole region S. Most of the dimples had a bowl-shaped depression to a deep extent, as illustrated in Figs. 12(a) and (c). In contrast, the dimples near the fracture edges were much shallower due to the ductile tearing.

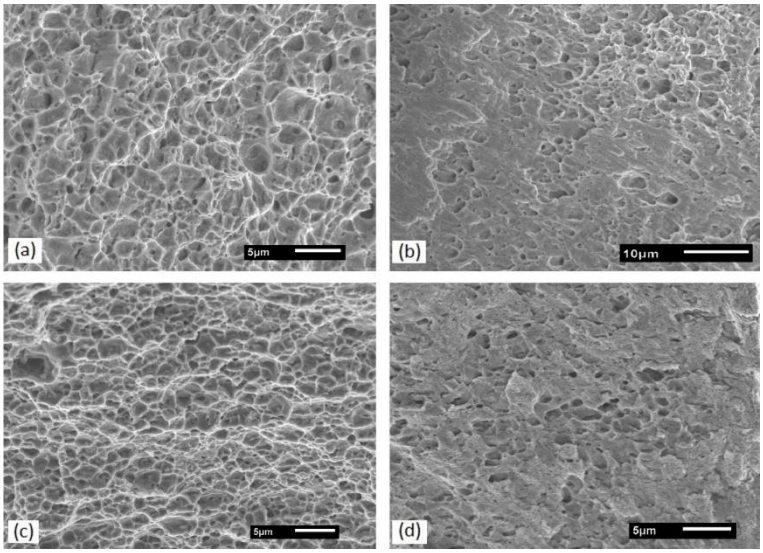

Fig. 12. Shear dimples of (a, b) 980DP-1.1-30 and (c, d) 980DP-700YS-1.1-30.

Fig. 13 presents the magnified images of the brittle features in region B as presented in Fig. 11. The features were significantly different from the dimples and were flatter, indicating brittle behaviour. These flat brittle features were identified as transgranular quasi-cleavage and were similar in Figs. 13(a) to (d), showing that all these four DP steels fractured in a similar manner despite their variations in composition and microstructure. There were also secondary cracks in region B.

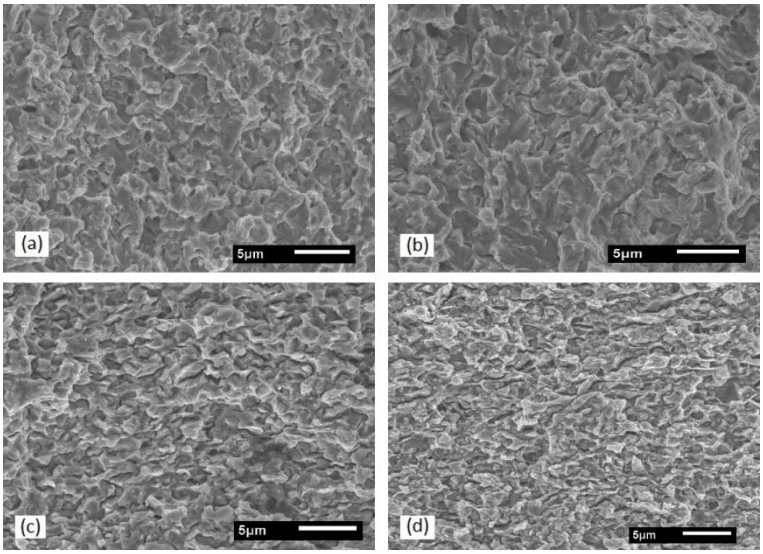

Fig. 13. Details of brittle fractures of (a) 980DP-1.1-30, (b) 1200DP-1.1-30, (c) 980DP-650YS-1.1-30 and (d) 980DP-700YS-1.1-30.

Table 3 and Fig. 6 indicate that an increasingly negative charging potential and a lower stress rate caused an increased loss of strength and ductility. Thus, the hydrogen charging potential of – 1.700 $V_{Hg/HgO}$ at the slowest stress rate was the severest testing condition in this study, and caused the largest property loss. Fig. 14 presents the corresponded fratography for the four DP steels. There were brittle regions B and ductile

shearing regions S. The characteristic features of region S were identical to those tested with less severe conditions. Fig. 15 shows images of the brittle region B in 1200DP-1.7-3 as an example. The patterns of brittle region B in Fig. 15(a) indicated that the brittle fracture initiated from a sharp edge, radiated to a distance in the inner area of the specimen and then transited to ductile shearing manner. The magnified image in Fig. 15(b) demonstrated that there was also transgranular quasi-cleavage features identical to those under less severe conditions, as compared with Fig. 13(b). However, comparing Fig. 11 and 14, indicated a larger area of brittle B region at the severer condition, indicating a more brittle character. This was consistent with the more significant deterioration of properties for this condition.

In addition, there was a new region M on the fracture surface at the severest testing condition, as shown in Fig. 14. This region M consisted of ductile dimples, as those in Fig. 12, small brittle regions and fisheyes. Region M seemed as a transition zone situated between the brittle region B and the ductile shearing region S.

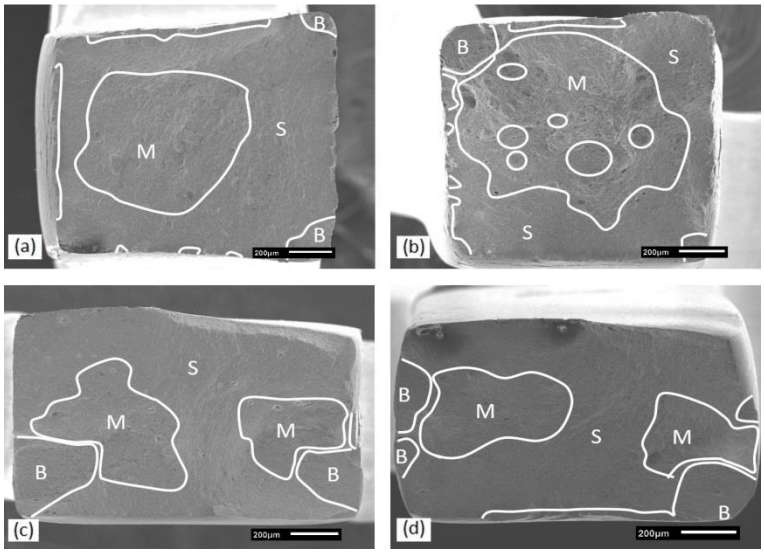

Fig. 14. Fracture appearance of (a) 980DP-1.7-3, (b) 1200DP-1.7-3, (c) 980DP-650YS-1.7-3 and (d) 980DP-700YS-1.7-3.

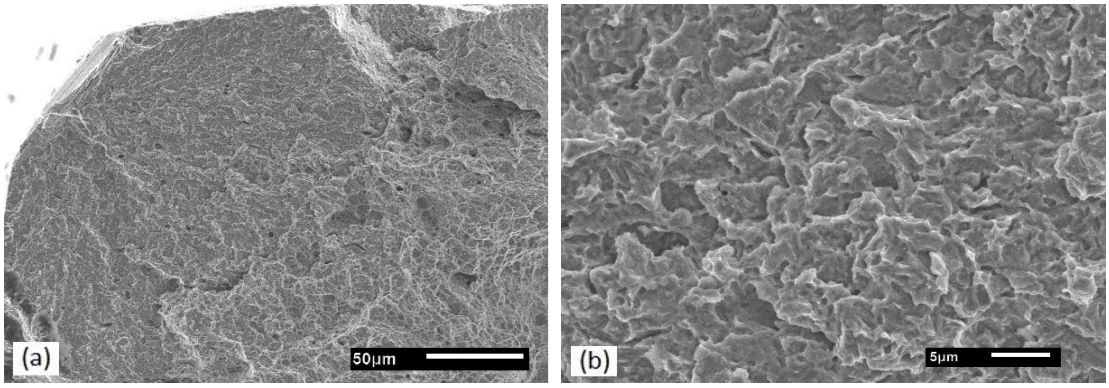

Fig. 15. Details of a brittle region of 1200DP-1.7-3 viewed in (a) low and (b) high magnifications.

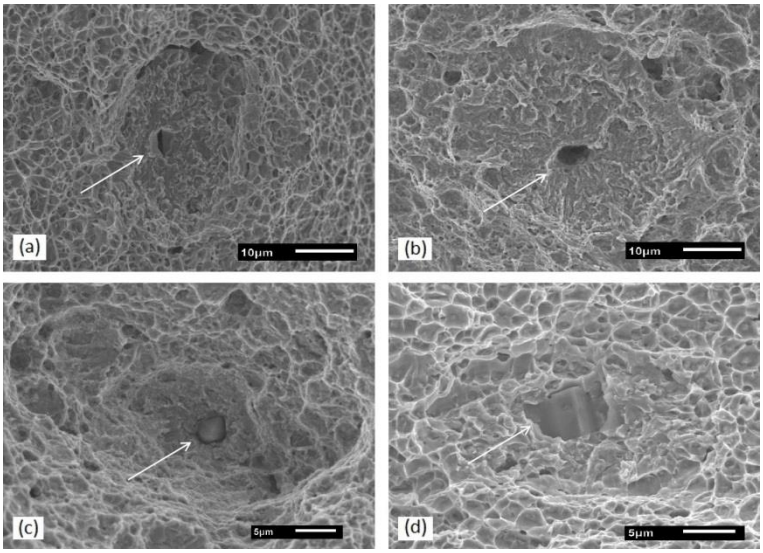

Fig. 16. SEM images showing fisheyes initiated from (a) elongated hole, (b) oval hole, (c) Al_2O_3 inclusion, and (d) TiN inclusion.

Fig. 16 demonstrates typical fisheyes presented in region M of the four DP steels. The fisheyes consisted of a nucleus in the center surrounded by a small facet fracture structure. Judging from the orientation of the ridges, fracture initiated from the center point and radiated outward, forming a circular pattern. The fisheyes were surrounded by ductile dimples. The fracture initiation nucleus, as indicated by the arrow, generally corresponded to a hole or an inclusion. Figs. 16(a) and (b) illustrate that the fractures of a fisheye initiated from an elongated and oval pore, respectively, whereas Figs. 16(c) and (d) show an inclusion in the center of a fisheye. The inclusion in Fig. 16(c) possessed a shape like a roundish particle with a diameter of about 5 μm. EDS analysis identified the composition of this inclusion corresponded probably to alumina. Fig. 16(d) shows an inclusion with a different shape. This inclusion had an approximate shape of a cube with a length of 5-10 μm, and corresponded to a TiN inclusion, according to the EDS analysis.

There was region M with fisheyes at (i) the severest condition for 980DP (980DP-1.7-3) and (ii) all the conditions except for the mildest one (-1.100 $V_{Hg/HgO}$, medium stress rate) in 980DP-650YS, 980DP-700YS and 1200DP.

3.3.3. Hydrogen charged Q&P steel

Fig. 17 compares the fracture surfaces of 980QP tested at the medium stress rate under hydrogen charging potential of -1.100 $V_{Hg/HgO}$ with that tested at the slowest stress rate with the charging potential of -1.700 $V_{Hg/HgO}$. The characters were similar to those of the DP steels.

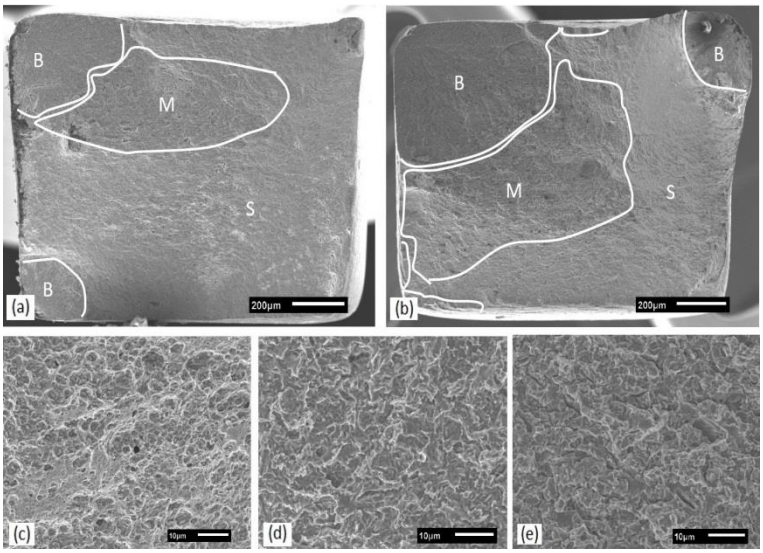

Fig. 17. Images showing fracture appearance of (a) 980QP-1.1-30, (b) 980QP-1.7-3, (c) dimples, and (d, e) brittle features in (a) and (b), respectively.

There were three regions. Fractures initiated from brittle regions B, a lower edge or a sharp corner of the specimen surface; propagated to form a region M where there were shear dimples and brittle fisheyes; and then grew in a shear manner (region S) until the specimen ruptured. Region S contained shear dimples as shown in Fig. 17(c). Region B possessed transgranular quasi-cleavage brittle features, the details of which did not change with a severer charging testing condition, as evidenced by comparing Figs. 17 (d) and (e). There were secondary cracks in region B. When the testing condition became severer, indicated by the more negative charging potential and lower stress rate, the area of brittle regions was increased, as evidenced by comparing Figs. 17 (a) and (b). This was consistent with the more significant loss of properties influenced by hydrogen, as shown in Table 3 and Fig. 6.

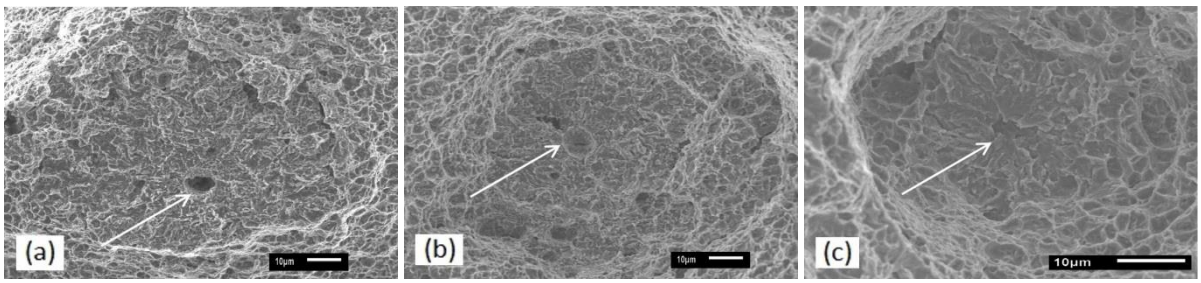

Fig. 18. SEM images of 980QP showing typical fisheyes initiated from (a) oval hole, (b) brittle phase with elongated void, and (c) brittle phase with sharp edges.

Fisheyes were present in region M for 980QP tested at all conditions, from 980QP-1.1-30 to 980QP-1.7-3. Fig. 18 shows some typical fisheyes. A fisheye in 980QP also initiated from a centre nucleus and radiated to a certain distance forming a roundish shape. The initiation core, as pointed by the arrow, corresponded to an oval hole, brittle phase with elongated void and brittle phase with sharp edges, as illustrated in Figs. 18(a), (b) and (c),

respectively. EDS analysis indicated that the brittle phases in the initiation point were not alien inclusions, which was different from the case with DP steels.

3.3.4. Hydrogen charged TWIP steel

Fig. 19 illustrates three regions of the fracture surface. These regions were essentially similar to those in the DP and Q&P steels. Figs. 19(a) and (b) indicate that the fracture characteristics under different charging conditions resembled each other. The fracture initiated from both of the surfaces at the short transverse sides and grew towards each other into the inner part of the specimen, forming two arch-shaped brittle regions B. There were also regions M and shear regions S. Region M also consisted of shear dimples, a small brittle area and fisheyes. Region S contained shear dimples. Figs. 19(c) to (e) demonstrated that the fracture under hydrogen charging in solution contained (i) brittle region B possessing transgranular quasi-cleavage features, which were the same as in the small brittle regions after testing in air (see Fig. 9), and (ii) some secondary cracks. In addition, Figs. 19(d) and (e) illustrate another different feature, which was some intergranular smooth facets, as marked with white squares. These smooth facets only occurred near the surface edge in region B in the specimen tested at the severest condition (-1.700 $V_{Hg/HgO}$, slowest stress rate), such as as the one in Fig. 19(b).

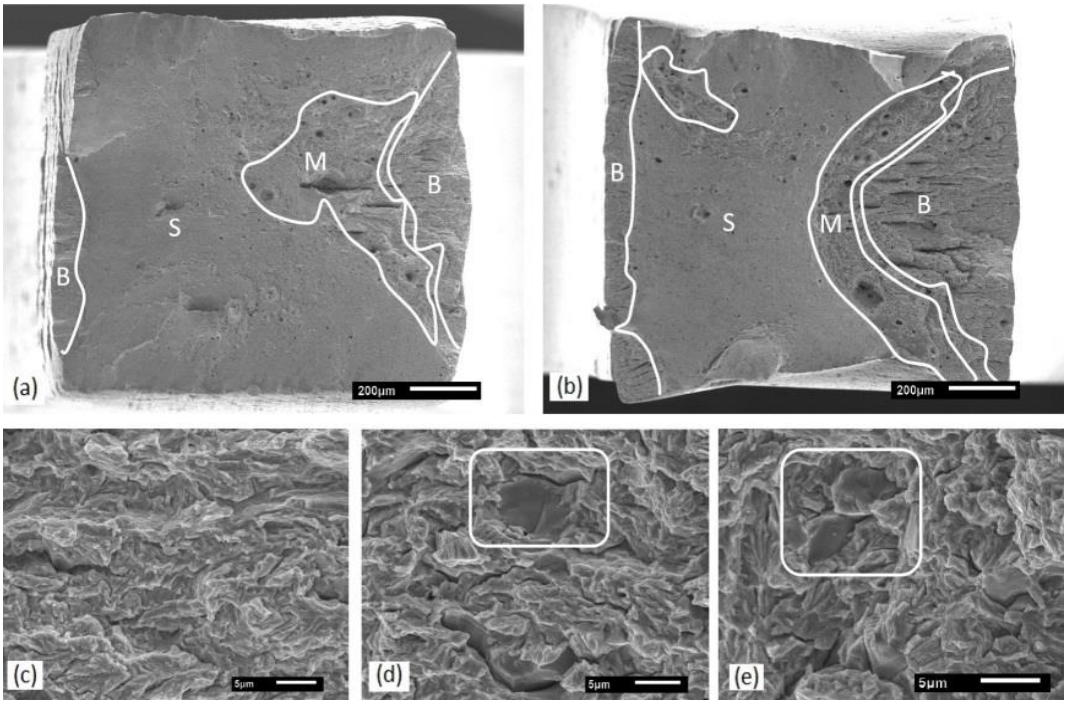

Fig. 19. Images showing fracture appearance of (a) 950TW-1.1-30, (b) 950TW-1.7-3, (c) brittle features in (a), and (d, e) brittle features in (b).

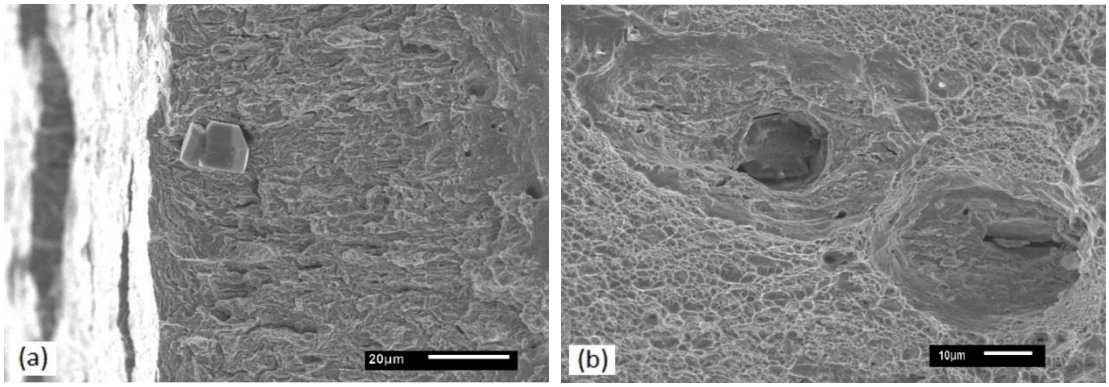

Fig. 20. SEM images of 950TW showing (a) an inclusion near edge and (b) fisheye features initiated from an inclusion and brittle phase.

950TW steels tested in air at the medium and the slowest stress rate exhibited small brittle regions, as shown in Fig. 9, and a lower value of reduction in area than that of the test in air at the fastest stress rate, see Table 3, indicating there was some decease of ductility in air at lower stress rates. As aforementioned, when 950TW steels were tested under hydrogen charging at both the medium and the slowest stress rates, there was also a brittle region B and this region became larger in area, indicating a more significant influence of hydrogen on the steels, as was evidenced by the higher degree of properties loss (see Table 3). Comparing Figs. 19(a) and (b) indicated that the area of brittle region B increased as the charging potential became more negative and the stress rate decreased.

There were inclusions occasionally dispersed in the small brittle region B in specimens tested in air, as the one shown in Fig. 10. There were similar inclusions in the brittle region B in specimens tested with hydrogen charging, as shown in Fig. 20(a). The inclusion in Fig. 20(a) seemed to have randomly located in region B near the edge of the surface, whereas the one in Fig. 10 appeared to be near the edge. Nevertheless, EDS analysis indicated the inclusions in region B with hydrogen charging conditions were also AlN. These AlN inclusions also acted as the initiation nucleus of fisheye features in the mixed region M, such as the one for the fisheye on the left-hand-side illustrated in Fig. 20(b). The fisheyes in region M could also initiate from a brittle phase, which was not alien based on the EDS results. The right-hand-side fisheye in Fig. 20(b) was an example of such a fisheye. There was such a region M with these fisheyes in each of the 950TW specimens tested with hydrogen charging.

3.4. Transverse specimen appearance

Fig. 21 presents the appearance of the transverse specimen surfaces of the uncharged 980DP, 980QP and 950TW steels after testing in air at the medium stress rate. 980DP and

980QP exhibited similar appearance as shown in Figs. 21(a) and (b), where there was significant necking. The characteristics were consistent with the cup and cone fracture, and with the relatively high values of reduction in area, as listed in Table 3. There were some crossed shear bands and these were magnified in Figs. 21(d) and (e). These shear bands were all in the necking part of the specimen and were nucleated under conditions of a large plastic deformation. There were these necking and shallow shearing banding crack features in all the DP and Q&P steels tested in air. In addition, there were no horizontal cracks on the transverse surfaces of these DP and Q&P steels. 950TW also showed significant necking, as shown in the transverse side view in Fig. 21(c). However, there was a lower region in the centre of the surface edge, corresponding to the brittle region B as shown in Fig. 9(a). There were also small cracks along the shear bands, 45 degree to the tensile stress direction. For 950TW steels tested in air at the two slower stress rates, there was another type of secondary crack, perpendicular to the tensile stress direction, as indicated by the arrows in Fig. 21(f). These cracks seemed to have propagated along the horizontal direction with some grown large enough to interconnect, forming a stepwise cracking pattern. This stepwise crack propagation was stated to be associated with the presence of hydrogen [54]. However, these 950TW steels were not pre-charged with hydrogen and were tested in air. Some unintentionally introduced hydrogen might be a possible source of hydrogen associated with the aforementioned cracking in the uncharged 950TW steels. This is discussed later in the following sections. All the surface cracks were in the necked region, and their size and amount decreased with a longer distance from the fracture surface.

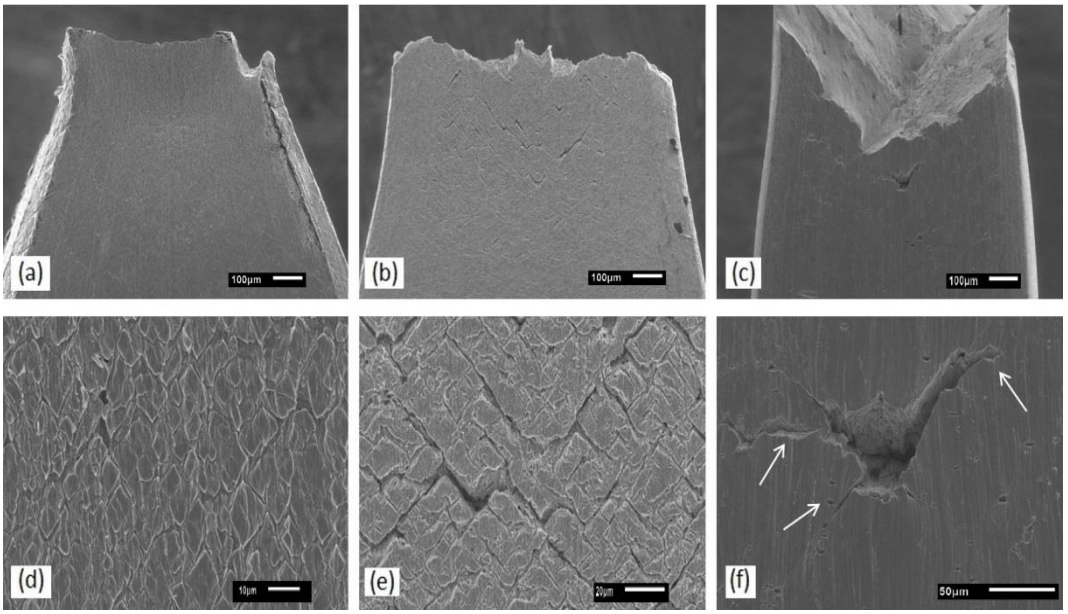

Fig. 21. Transverse surface appearance of (a, d) 980DP, (b, e) 980QP and (c, f) 950TW tested in air at the medium stress rate, viewed in low and high magnification, respectively.

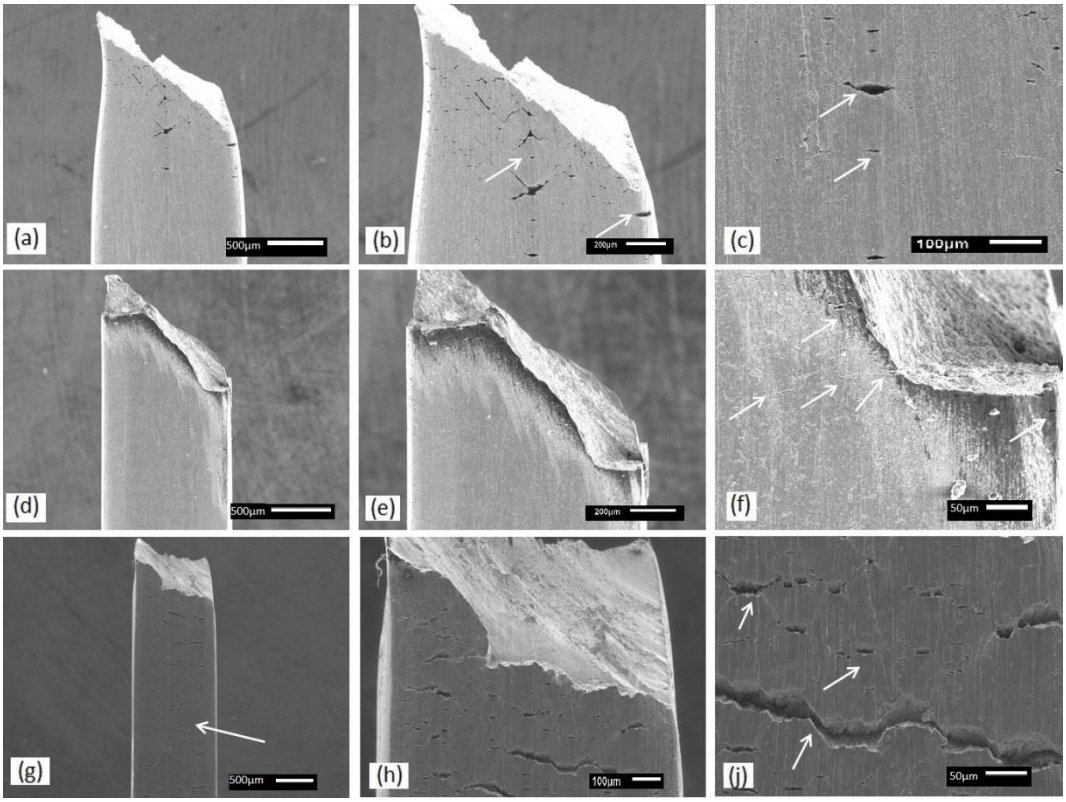

Fig. 22. SEM images in increased magnifications showing the transverse surface appearance of (a-c) 980DP, (d-f) 980QP and (g-j) 950TW with hydrogen charging at – 1.100 $V_{Hg/HgO}$ at the medium stress rate.

Fig. 22 shows the transverse views of steel specimens tested under hydrogen charging conditions at significant magnifications. Figs. 22(a-c) show 980DP tested under the mildest hydrogen charging condition (– 1.100 $V_{Hg/HgO}$, medium stress rate), as an example of all the four DP steels in this study tested under the same condition. The hydrogen charged 980DP exhibited extensive necking, as evident in Figs. 22(a) and (b). There were many horizontal cracks near the edge and in the centre of the transverse surface of the specimen, as indicated by the arrows in Figs. 22(b) and (c). These cracks were perpendicular to the tensile direction with some of them connected to each other propagating in a stepwise manner. There were no such horizontal cracks for uncharged DP steels tested in air. Therefore, the formation of these small horizontal cracks was induced by the presence of hydrogen. Furthermore, the stepwise crack propagation was also associated with the presence of hydrogen [54]. The lower corner with some cracks nearby, as shown in Figs. 22(b), corresponded to the brittle region B in the right lower corner in Fig. 11(a). In addition, there were several cracks at 45 degree to the tensile stress direction. All the cracks were in the necked region, and decreased in incidence with increasing distance from the fracture surface.

Figs. 22(d-f) present the transverse views of 980QP tested at the same condition (– 1.100 $V_{Hg/HgO}$, medium stress rate). The necking was not as significant but still evident, as shown in Figs. 22(d) and (e). Two horizontal platforms at the edges of the specimens were

clearly recognized. These platforms were perpendicular to the tensile direction and corresponded to the two brittle regions at the left corners in Fig. 17(a). There were substantial small horizontal cracks near the platforms, as indicated by the arrows in Fig. 22(f). These platforms and horizontal cracks were not present in the uncharged 980QP steels and thus were also considered to be induced by hydrogen. The cracks were also in the necking region.

Figs. 22(g-j) present the transverse micrographs of 950TW tested at the mildest condition (-1.100 $V_{Hg/HgO}$, medium stress rate). Necking was also present, as shown in Figs. 22(g) and (h). The lower region of the fracture surface, which was relatively flat, corresponded to the brittle region B at the left edge in Fig. 19(a). There were numerous cracks on the surface. These cracks were essentially all horizontal, as demonstrated in Fig. 22(j). Similar to those 950TW steels tested in air at the two slower stress rates, as shown in Figs. 22(c) and (f), some of the horizontal cracks interconnected resulting in the stepwise crack propagation. Furthermore, the cracks were also only in the necked region with the size and amount decreasing as a function of the distance from the fracture surface. Unlike DP and Q&P steels, there were some cracks in 950TW at a distance from the surface, as indicated by the arrow in Fig. 22(g). This was attributed to the substantial elongation of 950TW steels, as evidenced by values listed in Table 1 and by the comparison of potential drop curves in Fig. 5.

3.5. Hydrogen influenced microstructure

As mentioned above, the horizontal cracks, for DP and Q&P steels, occurred for hydrogen charged specimens and not for uncharged ones, and thus were induced by hydrogen. The initiation and propagation of these hydrogen-induced cracks was further explored after polishing and etching the transverse surfaces, in order to reveal the microstructures associated with the hydrogen influence. This investigation of hydrogen-induced surface cracks was conducted ex situ after the LIST tests rather than in situ during the tests. The cracks occurred near the edge and the top flat brittle region.

3.5.1. DP

Fig. 23 presents the micrographs of transverse surfaces after etching of 980DP and 1200DP steels. The cracks were horizontal, perpendicular to the tensile direction, and were in the vicinity of the edge of the transverse surface. Fig. 23(a) shows that a large crack had propagated to a distance and through martensite and ferrite in 980DP. There were several smaller sub-cracks near the large crack, as pointed by the arrows. These small cracks had initiated at martensite islands or at the interface of martensite and ferrite. Fig. 23(b) presents a

magnified image of the cracks in another area. Similarly, the cracks also initiated at martensite or at the interface of martensite and ferrite. One crack then propagated through the martensite, whilst another crack opened and propagated into the ferrite. There was the same manner of crack initiation and propagation in hydrogen charged 1200DP steels, as shown in Figs. 23(c) and (d). Therefore, the four DP steels possessed similar cracking manners.

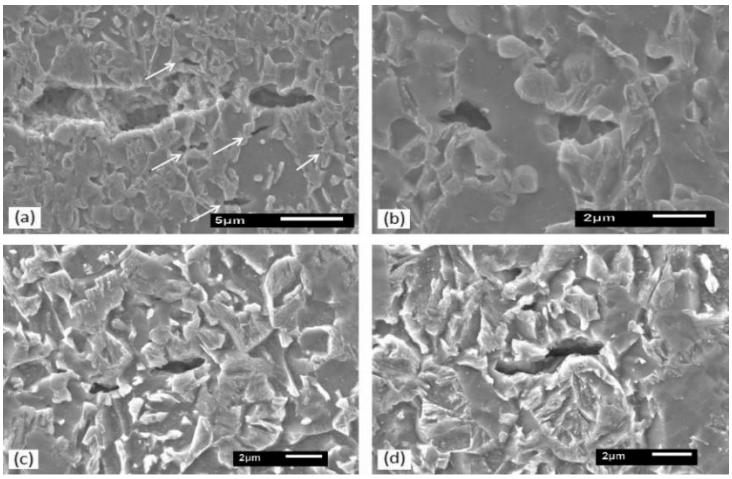

Fig. 23. SEM micrographs illustrating the transverse fracture surface cracks of (a, b) 980DP and (c, d) 1200DP steels polished and etched after LIST tests under hydrogen charging.

3.5.2. Q&P

Fig. 24 presents the micrographs of the etched transverse surface of 980QP steel. There was successive crack propagating through all the phases, as shown in Fig. 24(a). There were substantial smaller cracks nearby. Examples of the hydrogen induced small cracks were illustrated in Figs. 24(b) to (d). The initiation of the cracks was likely associated with the hard martensite constituents, as was indicated by the white arrows in Figs. 24(b) to (d). The cracks then opened and propagated into adjacent ferrite or through martensite.

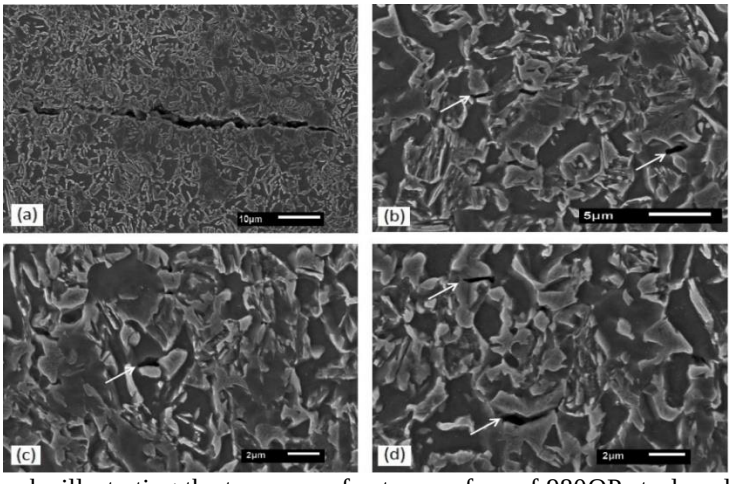

Fig. 24. SEM micrographs illustrating the transverse fracture surface of 980QP steels polished and etched after LIST tests under hydrogen charging.

4. Discussion

4.1. Hydrogen charging

This work investigated the hydrogen influence on steels using LIST tests conducted in solutions with hydrogen charging at a constant potential. Atrens et al. [55] and Liu et al. [47] related the hydrogen fugacity, f, and the hydrogen concentration, C_H, in the steel, to the cathodic charging overpotential, η, by the following equations:

$$f = A \exp\left(\frac{-\eta F}{zRT}\right) \quad (3)$$

$$C_H = K\sqrt{f} \quad (4)$$

where F is the Faraday constant, R is the gas constant, T the absolute temperature, A and z are constants related to the mechanism of the hydrogen evolution reaction, and K is the solubility constant.

Eq.(3) indicates that a more negative charging potential causes an increased overpotential and an exponentially increased hydrogen fugacity, and hydrogen concentration in the steel. This is consistent with the results of our previous study [49], where we charged the steels in 0.1 M NaOH at various cathodic potentials for 24 hour and measured the concentration of diffusible hydrogen by permeation and hot extraction methods. The hydrogen concentration increased with increasingly negative charging potential, and was 0.107, 0.120 and 0.197 ppm for 980DP, 1200DP and 980QP, respectively, charged at the least negative potential of – 1.2480 V_{SCE} (corresponded to – 1.100 $V_{Hg/HgO}$ in this study). Since the DP and Q&P steels were influenced by HE when charged at – 1.100 $V_{Hg/HgO}$ as shown above, the lowest hydrogen concentration corresponding to this potential from our previous was sufficient to cause HE of these steels. However, there was a time interval of about 10 min between the end of hydrogen charging and the start of hydrogen analysis. This period of time could lead to some egress of hydrogen. Venezuela et al. [31] showed that 8 min after charging could result in 15% of the hydrogen diffusing out of the martensitic high strength steels. Furthermore, the amount of hydrogen diffusing out of the steel increases with a higher hydrogen diffusion coefficient [49]. Nevertheless, the increase in hydrogen concentration with a more negative charging potential, as measured in our previous study, is consistent with Eqs. (3) and (4). Thus, an increasingly negative charging potential in this work increased the hydrogen concentration, and thereby increased the hydrogen embrittlement. Similar results were also obtained in other studies [18, 28, 30, 31, 35, 56, 57].

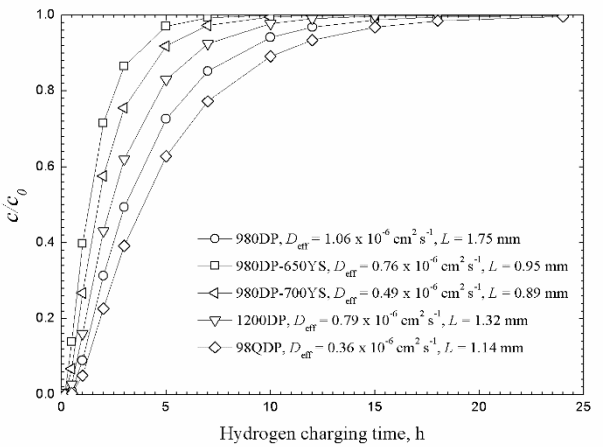

Fig. 25. c/c_0 at the centre of DP and Q&P steels vs hydrogen charging time. D_{eff} values were for the steels charged at – 1.100 $V_{Hg/HgO}$.

A 24-hour pre-charging was conducted for each of the steels in this work to ensure constant hydrogen content throughout the DP and Q&P steels and a certain amount of hydrogen into 950TW. The saturation time of hydrogen in DP and Q&P steels under hydrogen charging at – 1.100 $V_{Hg/HgO}$ is illustrated in Fig. 25. The method was adopted from the work of Venezuela et al. [31] considering Fick's second law, where the steels were charged from both sides of a thin specimen, essentially the same as in this work. The boundary conditions were:

$$t = 0,\ C = 0 \text{ for } x = -L/2 = L/2 \tag{5}$$

$$t > 0,\ C = C_0 \text{ for } x = -L/2 = L/2;\ \frac{\partial C}{\partial x} = 0 \text{ for } x = 0 \tag{6}$$

where L is the thickness of the specimen, C is the hydrogen concentration at the inside of the specimen, C_0 is the hydrogen concentration at both of the specimen surfaces when subjected to hydrogen charging, x = – L/2 = L/2 is at the specimen surfaces, x = 0 is for the centre of the specimen.

The hydrogen diffusion was considered to be the same from both surfaces. The hydrogen concentration as a function of charging time is given by [31, 58]:

$$\frac{C}{C_0} = 1 - \frac{4}{\pi}\sum_{n=0}^{\infty}\frac{(-1)^n}{2n+1}\left\{\frac{-D_{eff}\,(2n+1)^2\,\pi^2\,t}{4\,L^2}\right\}\cos\frac{(2n+1)\pi\,x}{2\,L} \tag{7}$$

where at the specimen centre, x = 0, D_{eff} is the hydrogen diffusion coefficient, C/C_0 is the ratio of hydrogen concentration at the centre to that at the surface. Therefore, the plots of C/C_0 as a function of charging time, as shown in Fig. 25, illustrate the amount of time needed for the hydrogen concentration at the centre of the specimen to reach the same concentration as that at the specimen surface when subjected to cathodic charging. There are studies [48, 59,

60] suggesting hydrogen diffusion coefficient was higher at a more negative charging potential or a higher hydrogen activity. As was indicated in Eq. (7), for the hydrogen concentration at the centre to reach the same level (same value of C/C_0), a higher diffusion coefficient then contributes to a less required time. Thereby, for Fig. 25, the D_{eff} values were adopted for steels charged at the least negative charging potential of – 1.100 $V_{Hg/HgO}$ from our previous work, so that the longest time for hydrogen saturation in the steels was shown. Any potential that is more negative than – 1.100 $V_{Hg/HgO}$ would ensure a shorter period of time for the hydrogen concentration at the centre to become equal to that at the surface. Fig. 25 indicates that the time duration, for hydrogen concentration at the centre to reach 99.9% of that at the surface, was about 8, 12, 15, 18 and 22 h for 980DP-650YS, 980DP-700YS, 1200DP, 980DP and 980QP, respectively. The hydrogen saturation time for each of the DP and Q&P steels charged at – 1.400 and – 1.700 $V_{Hg/HgO}$ would be shorter than the corresponded value at – 1.100 $V_{Hg/HgO}$. Therefore, 24-hour of pre-charging was enough for ensuring constant hydrogen content throughout the whole specimen for DP and Q&P steels. This is consistent with the observation of some hydrogen induced brittle facets and fisheyes in region M at the centre of the fracture surface of charged specimens, as shown in Figs. 14 and 17.

950TW steels also underwent 24-hour pre-charging. The boundary conditions were the same as in Eqs. (5) and (6), consequently, Eq. (7) is also applicable to 950TW. The D_{eff} value was reported to be 1.29×10^{-9} cm^2 s^{-1} for hydrogen in austenitic TWIP steel at room temperature [61]. This value was used for 950TW and applied to Eq. (7) in this study. As a result of this significantly lower value of D_{eff}, the 24-hour pre-charging was estimated to saturate only about 30 μm inside the specimen from both surfaces rather than the whole specimen. This distance is somewhat smaller than the extent of the brittle region B, which reached at least 100 μm inside the specimen, as shown in Fig. 19. This is attributed to the interaction between hydrogen and deformation during a tensile test. Since hydrogen has a low diffusion coefficient in austenitic TWIP steel, hydrogen absorption is enhanced by the transport of the hydrogen-carrying dislocations newly formed during deformation [62]. In this study, hydrogen charging was continued during the LIST tests. Thus, the kinetics for such transport is larger and thereby explains the larger extent of hydrogen influenced region B. In addition, as aforementioned, an increasingly negative charging potential gives a higher diffusion coefficient, and consequently a larger extent of hydrogen saturation region based on Eq. (7). This is consistent with the larger area of brittle region B at a more negative charging potential, as by comparing Figs. 19(a) and (b).

4.2. LIST in air

As illustrated in Table 3 and mentioned in section 3.2, the LIST tests in air provided values of tensile strength, σ_f, and yield strength, σ_y, comparable to the corresponded values obtained by the steel supplier from conventional tensile tests as provided in Table 1. The values of R_A for the same steel tested at three stress rates were all substantial, indicating significant ductility, and also were close to each other.

The change in slopes of the potential drop plots (see Fig. 5) allowed direct determination of the yield stress in LISTs. The conventional tensile test is strain controlled. There is slow extension between necking and final fracture, associated with a decreasing applied engineering stress. The period for necking until fracture takes up a significant portion of the total testing time, whereas LIST is associated with increasing load, and necking occurs at the maximum load, whereupon the specimen becomes mechanically unstable, necks and fractures in a short period of time. Nevertheless, there was obvious necking for all the LIST tests in air, as demonstrated by Figs. (7-9) and (21), and the fracture stress in LISTs corresponded to the ultimate tensile stress in the strain-controlled tensile tests. Therefore, the LIST could accurately measure the values of tensile strength, σ_f, and yield strength, σ_y.

The four DP steels exhibited R_A values ranging from 61% to 79%. These high values indicated significant ductility, as was also evidenced by the cup and cone fractures and the obvious necked region. Comparing 980DP and 1200DP with similar grain sizes, the stronger 1200DP possessed lower values of R_A, attributed to the higher amounts of carbon and martensite. For the three 980DP steels with increasing yield strength in the following order: 980DP, 980DP-650YS and 980DP-700YS, there was a decrease of R_A values from 980DP to 980DP-650YS, followed by a slightly further decrease to 980DP-700YS. The increased yield strength therefore is considered to account for the R_A decrease. In addition, the increasing content of martensite from 980DP to 980DP-700YS, as shown in Table 1, is also considered to be associated with the R_A decrease. Table 2 illustrates the mean thickness was 1.75, 0.95 and 0.89 mm for 980DP, 980DP-650YS and 980DP-700YS, respectively. This manner of a sharp decrease followed by a slight decrease in thickness is somewhat the same as that of R_A decrease. The study [63] suggested that the elongation of steels decreased with reduced specimen thickness. Thus, the difference in thickness may play a role in the decrease in R_A, however, further study is still needed for better elucidation.

Table 3 also indicates that R_A value of 980QP were quite high, around 63%, indicating good ductility, yet lower than that of 980DP, which was about 79%. 980QP and

980DP have similar microstructures, except that 980QP possess some retained austenite. During deformation, the retained austenite transforms to martensite, leading to volume change and concomitantly, increased plastic deformation of the ferrite nearby [20, 64, 65]. As a result, there is local strengthening during transformation, hindering further deformation in this local region, and consequently reducing the necking and reduction in area, R_A.

The R_A values for the DP and Q&P steels tested at all three stress rates were close to each other, indicating that the influence of different stress rates on the deformation behaviour was not significant.

For 950TW, however, there was a significant drop of R_A for tests at the two slower stress rates, even though in all cases the R_A values were substantial. The fractographic images in Fig. 9 show the presence of region B with some brittle features, which resemble those brittle features caused by hydrogen as in other studies on TWIP steels [26, 62]. There were no such brittle regions in DP and Q&P steels tested in air at the slower stress rates in this study. The amount of diffusible hydrogen in uncharged DP and Q&P steels was negligible (less than 0.01 wtppm), according to our previous measurements [49]. Consequently, there was no hydrogen influence on these steels. The fully austenitic 950TW steel, on the other hand, has a significantly greater solubility of hydrogen [37]. Dieudonné et al. [62] stated that there was around 0.7 wtppm of hydrogen introduced in their TWIP steels after processing. However, they further found that this amount of hydrogen was non diffusible and as their results after tensile testing in air showed fully ductile features. In contrast, Ryu et al. [66] indicated that austenite served as a reversible trap for hydrogen. Therefore, significant residual hydrogen could be present in the uncharged 950TW, due to the relatively high solubility of hydrogen in austenite, and this hydrogen content could induce some transgranular brittle features, as shown in Fig. 9 in this work. During deformation, mechanical twinning occurs. Hydrogen interacts with dislocations associated with the twinning mechanism, favouring hydrogen accumulation at the twin boundaries and the consequent hydrogen induced transgranular cracking. The fact that 950TW steels exhibited these brittle features at the two slower stress rates in air could be interpreted in a way that the decrease in stress rate is anticipated to accelerate hydrogen diffusion by moving dislocations and thereby increase the susceptibility to hydrogen influence [62, 67, 68]. In addition, inclusions were reported to be associated with hydrogen embrittlement [29, 34]. Therefore, the existed inclusions in 950TW (see Fig. 10) could also act as hydrogen traps, promoting sensitivity to hydrogen embrittlement.

4.3. LIST with hydrogen charging

Table 3 and Fig. 6 indicated that all the hydrogen-charged DP, Q&P and TWIP steels exhibited some susceptibility to hydrogen, evidenced by the significant values of the hydrogen embrittlement index, EI, resulting from decreased R_A, and the slightly decreased σ_f and σ_{th}. There are also previous studies reporting hydrogen influence on DP [22-24, 50, 56], Q&P [34, 36, 37, 69], and TWIP [26, 39, 40, 52, 70] steels. The fractography, in Figs. 11 to 20, supported the hydrogen influence by demonstrating a change of fracture surface from ductile dimples in air to brittle features when subjected to hydrogen charging. Fig. 22 shows some necking of the hydrogen-charged specimen, indicating that the fracture occurred at the ultimate tensile stress whereupon the specimen became mechanically unstable, rather than caused by subcritical crack growth at the threshold stress. Thus the decreased in σ_{TH} is considered as the decrease in yield strength, as was also interpreted in other work [30]. The hydrogen influence on yield strength and fracture strength was slight, and that on the ductility was significant, in this work. These results are consistent with various works [22, 24, 29], that indicated the hydrogen influence was manifested by the loss of ductility rather than by decreased strengths of the steels. Venezuela et al. [30] studied HE susceptibility of martensitic AHSS and measured a decrease of yield strength and tensile strength influenced by hydrogen. They further elucidated that the decrease in yield strength was due to hydrogen solid solution softening, and the decrease in fracture stress was attributed to the interaction between hydrogen and dislocations leading to enhanced localized plasticity.

LIST tests have been carried out on martensitic high-strength steels with increasing strengths under similar hydrogen environments [30]. A comparison of those results with the results from this work indicates that the martensitic steels showed less sensitivity to hydrogen embrittlement than the DP steels of comparable strength in this study. For example, for the same tensile strength level of 980 MPa, the martensitic steels were not subjected to any hydrogen influence when charged with all the potentials at medium stress rate, whereas the 980DP demonstrated significant susceptibility to HE (see Table 3) under the same conditions of charging potentials and stress rate. This contradicts our expectation at a first approximation, which was that martensitic advanced high strength steels are less resistant to HE than DP steels, since the martensite phase is considered to be quite susceptible to HE [21]. Davies [24] mentioned that for a DP steel, with a tensile strength of about 655 MPa and containing about 20% of martensite, the tensile strength of the martensite phase exceeded 2000 MPa, whereas that of ferrite was less than 300 MPa. By simple calculations based on the properties and

phase volume fractions of our 980DP steels, the tensile strength of the martensite phase in our 980DP steels was around 1500 MPa, significantly higher than that of the soft ferrite. Koyama et al. [23] pointed out that the high mechanical contrast in ferrite-martensite microstructure put DP steels under potential risk of cracking. Therefore, DP steels are more susceptible to HE in this paper. Consistent results have been found. For instance, Loidl et al. [22] indicated that their martensitic steel experienced less elongation loss and a smaller hydrogen embrittlement index than DP steels of the same or even lower tensile strength level.

Table 3 and Fig. 6 also indicate that the susceptibility to HE of DP steels could be related to their strength, as is evidenced by the increasing hydrogen embrittlement index values with increased strength from 980DP to 1200DP. The increased steel strength in this study is consistent with (i) increased amount of martensite, (ii) decreased ferrite content and (iii) increased strength of martensite due to a higher carbon content. The higher HE susceptibility of 1200DP than 980DP could also be attributed to more reversible hydrogen traps with the increased martensite content. The influence of reversible traps on hydrogen embrittlement is discussed in detail in the following section. A similar trend of increased HE sensitivity with increasing steel strength of DP steels was also documented in other research [5, 22]. However, differences in microstructure, chemical composition, processing history and electrochemistry properties, should also be taken into account when assessing the HE susceptibility of steels.

For the three 980DP steels with increased yield strength, the hydrogen embrittlement index increased in the following order: 980DP, 980DP-700YS and 980DP-650YS (see Table 3 and Fig. 6). HE susceptibility for the two 980DP steels with higher yield strength was similar, and was significantly higher than that of 980DP. Decrease of ductility and increase of likelihood to HE with increasing yield strength have also been stated in other research [56, 71]. This trend of change in HE index could be correlated to the decrease in the fraction and grain size of the ferrite, as shown in Table 1, enhancing the possibility of an easy path for crack propagation [50]. In addition, the increased amount of Si alloying element may also lead to ferrite with higher brittleness and thereby higher embrittlement of the steel [50]. Furthermore, the difference in the thickness of these three 980DP steels may also play a role in the HE resistance. As indicated by Eq. (7) and in section 4.1, the time needed for the hydrogen content at a certain place in the specimen to reach the same level as that at the surface, depends on hydrogen diffusion coefficient and specimen thickness. Therefore, as presented in Fig. 25, 8, 12, and 18 h was needed for 980DP-650YS, 980DP-700YS, and 980DP, respectively, to reach the same amount of hydrogen at the centre as that at the surface

of the specimen when subjected to cathodic charging at – 1.100 $V_{Hg/HgO}$. In other words, given the same amount of time, there would be more hydrogen diffusing to a certain region (e.g. a potential flaw), in the following order: 980DP, 980DP-700YS and 980DP-650YS, consistent with increased HE susceptibility. Similarly, the aforementioned higher HE susceptibility of 1200DP than 980DP could also be explained in this perspective.

980QP in this work showed susceptibility to hydrogen embrittlement, as was also reported in other works [34, 37, 69, 72]. Compared with 980DP, 980QP exhibited a higher hydrogen embrittlement index, as was also consistent with the literature [5, 18, 20, 22]. The greater HE susceptibility is attributed to the TRIP effect [34, 73], in which the retained austenite transforms to martensite. The freshly formed martensite, which is susceptible to HE, is then enriched with hydrogen, due to the high solubility of hydrogen in the retained austenite, leading to high HE susceptibility of Q&P steels. On the other hand, if the retained austenite could stay stable under straining, it would act as an innocuous hydrogen sink reducing hydrogen embrittlement, as stated in other studies [33, 36, 74]. Nevertheless, since 980QP in our work exhibited higher HE susceptibility, martensitic transformation could have occurred during straining. Moreover, the higher carbon content of 980QP may also influence the hydrogen embrittlement by providing transformed martensite with significant carbon content and by increasing hydrogen saturation in the steels [20]. Furthermore, inclusions were also reported to account for poor HE resistance [33, 34, 75]. However, there were no such inclusions in our 980QP steels. It should also be noted that Loidl et al. [22] stated that differences in driving force for hydrogen embrittlement, such as martensitic transformation from retained austenite during a TRIP effect, made the TRIP steels not comparable to others (e.g. DP) steels.

For 950TW steels, there was an influence of (residual) hydrogen when tested in air at the two slower stress rates, leading to a decrease in R_A, σ_f and σ_y, compared with that of the hydrogen-immune one tested at the fastest stress rate. For 950TW tested at these two stress rates after 24-hour pre-charging, there was a further deterioration of properties, due to higher hydrogen content, as illustrated in Table 3 and Fig. 6. Thus, the properties of uncharged 950TW were also taken as reference for the pre-charged ones. Such influence of hydrogen on TWIP steels was also observed by other researchers [26, 39, 61, 62, 70, 76]. Possible causes for hydrogen influence are mechanical twinning during deformation and hydrogen induced martensitic transformation [26, 39, 76]. Furthermore, Al and Cu alloying elements enhanced HE resistance of TWIP steels [39, 62, 77, 78]. Ryu et al. [39] compared the HE resistance of TWIP steels with 1.5wt% aluminium and without aluminium, and found that aluminium

significantly reduced the hydrogen influence. However, TWIP steels with 1.5wt% aluminium were still subjected to HE in their study. Similarly, 950TW in our study also contains around 1.5wt% aluminium, as given in Table 1, and there was some influence by hydrogen. The result that the hydrogen embrittlement index of 950TW was lower than that of other AHSS in this work could be attributed to much lower hydrogen diffusion coefficient in the fully austenitic microstructure [5]. Again, as above mentioned, due to the difference in driving force for hydrogen embrittlement, direct comparison of 950TW with other steels in this study may not be appropriate.

All the DP, Q&P and TWIP steels in this study showed susceptibility to HE when subjected to cathodic hydrogen charging. The charging conditions at -1.100 $V_{Hg/HgO}$, -1.400 $V_{Hg/HgO}$ and -1.700 $V_{Hg/HgO}$ in 0.1 M NaOH were significantly more severe than any environment that the steel compartments may encounter during actual service, yet allow observation of hydrogen influence in a relatively short period of time. Study of hydrogen influence on these AHSSs under simulated service conditions is underway.

4.4. LIST with decreased stress rates

Table 3 and Fig. 6 indicate that hydrogen influence increased with a decreased stress rate. For example, there was a decrease in σ_{TH}, σ_f, and R_A and an increase in EI between 1200DP-1.7-30 and 1200DP-1.7-3. The fractography supported the increased hydrogen influence, as is clear by comparing Figs. 11, 14, 17 and 19. The transgranular quasi-cleavage fracture features at the slowest stress rate were similar to that at the medium stress rate, the area of brittle regions was increased, along with some reduction in necking. Another observation is that, for 950TW tested in air at 0.72, 0.072 and 0.0072 MPa s^{-1} without hydrogen pre-charging, there was an influence of (residual) hydrogen at the two slower stress rates and was absent for the fastest one.

These observations indicate that a decreased stress rate facilitates the loss of ductility, yet fracture occurs in the same manner at the ultimate tensile strength when the steel becomes mechanically unstable. It has been concluded that stress-controlled LIST and strain-controlled SSRT testing methods could provide comparable results and were both capable to evaluate the hydrogen influence on materials [32]. Furthermore, correspondence between stress rate and strain rate in the initial elastic region can be established [30], as illustrated in Table 2. Therefore, the influence of stress rates on HE resistance is anticipated to be in the same manner as that of strain rates. Such an increase of HE with decreased stress or strain

rates have been documented in other research [20, 30, 31, 79, 80]. In some cases [30, 80], HE was only observed for stress or strain rate lower than a critical rate.

In this work, hydrogen charging was continued after 24-hour pre-charging, and after the start of LIST test until the fracture of the specimen. The difference in stress rate caused the time duration of LIST test and exposure to hydrogen charging at the slowest stress rate to be an order of magnitude higher than those at the medium stress rate. For the influence of the extra hydrogen charging after 24 hours, Venezuela et al. [30] found that there was no influence on HE, since the 24-hour pre-charging had already caused a constant hydrogen content throughout the specimen. The calculations in this work (see Fig. 25) and from our previous permeation experiments, are consistent with their findings. Thus, in this work, the longer exposure time to hydrogen charging, at a lower stress rate, is not considered to account for the more pronounced hydrogen influence.

Depover et al. [20, 79] attributed the increased HE sensitivity with decreasing strain rate to hydrogen diffusion, as hydrogen had more time to diffuse to the critical stressed regions. Moreover, HE dependence on strain rate could also be interpreted by the dynamic trapping effect [80, 81]. During plastic deformation, a great number of dislocations are created. These newly created dislocations are essentially free of hydrogen and therefore obtain hydrogen by diffusion or by interacting with hydrogen enriched reversible traps to meet equilibrium [81, 82]. Thus if the stress or strain rate is high, the multiplication of dislocations are too high to be supplied with enough hydrogen for cracking, whereas, at a slower stress or strain rate, the diffusion or interaction with reversible traps are sufficient, so that dislocations will be filled with hydrogen and these mobile dislocations can also reach further in the specimen, causing a more profound embrittlement effect.

4.5. Fractography

4.5.1. Without hydrogen influence

Figs. 7, 8 and 21 present the fractography of ductile cup and cone fracture, accompanied with considerable necking, indicating there was little influence of hydrogen on the steels in air. There was such ductile cup and cone fracture for all the DP and Q&P steels tested in air, and for 950TW tested in air at the fastest stress rate.

Magnified images of the cone part on the fracture surface demonstrated spherical dimples, due to microvoid coalescence (MVC). The ductile microvoid nucleation and coalescence was considered to be responsible for the fracture initiation and propagation of the

specimen [83]. In the centre cone part, microvoids nucleated, grew and coalesced, contributing to fracture growth to the outer cup region, where the final fracture occurred due to shear stress. In the outer cup region with shear fracture, there were shallower and parabolic dimples and these supported the final rupture by shearing [84], along with the shear bands and the orientation of the cup region at 45 degree to the tensile direction.

In addition, there were secondary cracks in the centre cone part surrounded by ductile dimples, as presented in Figs. 7(b) and 8(a). These secondary cracks were probably caused by a decohesion phenomenon [83]. Such secondary cracks, with some having considerable length of around 100 μm, were present in 980DP-650YS, 980DP-700YS, 980QP and 950TW, but were absent in 980DP and 1200DP, when tested in air at all stress rates. This observation coincides with the indication in Table 3 that 980DP and 1200DP exhibited higher ductility, evidenced by more than 70% R_A values, than the other four steels, which had R_A values less than 65%. However, these secondary cracks were ductile and occurred at the final fracture due to substantial tensile stresses. Another observation of the fracture surfaces for steels tested in air, coincided with the higher ductility of 980DP and 1200DP than the other steels, was the deeper spherical dimples in their centre cone regions than those in the other four steels. This was consistent with that deeper dimples reflect a higher ductility [30].

4.5.2. With hydrogen influence

All the DP, Q&P and TWIP steels in this study were subjected to HE when charged with hydrogen, as is evident from Table 3 and Fig. 6. Fractography, in Figs. 11, 14, 17 and 19, indicated brittle features supporting the hydrogen influence, since such features were not present without hydrogen charging. The brittle features were characterized as transgranular quasi-cleavage in all the hydrogen-charged steels (e.g. see Figs. 13 and 15), except for 950TW at the severest testing condition (-1.700 $V_{Hg/HgO}$ and the slowest stress rate), where there were intergranular features, as indicated in Figs. 19(d) and (e). Furthermore, a comparison of Fig. 11 with Fig. 14, Fig. 17(a) with Fig. 17 (b), and Fig. 19(a) with Fig. 19 (b), indicates that the increased hydrogen influence did not affect the morphology of the brittle features, instead, it increased the extent of the brittle regions B and M. Such an increase in brittle area was consistent with (i) increased tensile strength, (ii) increased yield strength, (iii) more negative charging potential, and (iv) slower stress rate. In addition, necking was present in each case under hydrogen charging, as shown in Fig. 22 and concluded in Table 3, indicating brittle fracture and ductile fracture occurred competitively. This is also indicated by the ductile dimple-contained regions along with the brittle regions on the fracture surfaces.

Hydrogen needs time to diffuse to the crack tip, contributing to brittle fracture and enhancing crack propagation. Such hydrogen diffusion may take longer time than crack propagation induced by applied load, leading to ductile cracking in the remaining surface [54].

As mentioned above, the fracture features were cup and cone without hydrogen influence, and fracture initiated in the centre cone part, whereas, under hydrogen influence, fracture occurred in a shearing manner along single or multiple planes. Fractures initiated at the specimen surface from both brittle region B (containing dominantly transgranular and a few intergranular features) and shearing region S (containing shear dimples), as indicated in Figs. 11, 14, 17 and 19. This observation of higher hydrogen influence near the surface is consistent with the facts that (i) hydrogen is introduced through external charging, (ii) there is higher hydrogen concentration at the specimen surfaces, and (iii) surface cracks are much more effective in producing fracture, because a surface crack has a stress intensity factor twice that of an identical sized interior crack [85].

Crack initiation from shearing region S at the surface can be associated with both the hydrogen-enhanced local plasticity (HELP) and adsorption-induced dislocation emission (AIDE) mechanisms, since there is intense localized plastic deformation during final fracture accompanied with necking. Hydrogen entering by adsorption from external charging favours the AIDE mechanism. In addition, (i) the presence of necking, which indicates that brittle fracture competed with ductile fracture, and (ii) the fact that fracture occurs fast when the specimen became mechanically unstable at the ultimate tensile strength, both also favour AIDE. However, 24-hour pre-charging ensured there was enough solute hydrogen throughout the specimen, meeting the requirement of HELP. The shear fracture is thus considered attributed to a combination of AIDE and HELP. For instance, the shear fracture could start by AIDE, in a way that adsorbed hydrogen at the external surface facilitates the nucleation and subsequent emission of dislocations under the applied stress. Then the emitted dislocations may move away from the crack tips more rapidly due to the effect of HELP, reducing the back-stress on the following dislocation emission and enhancing fracture propagation [12]. The transgranular and intergranular brittle features in this work could be explained by hydrogen-enhanced decohesion (HEDE) occurring at grain interior and grain boundaries, respectively.

DP steels exhibited transgranular features in the brittle region B, as shown in Fig. 13. Fig. 23 demonstrate micrographs of the etched transverse surfaces of DP steels after LIST tests to reveal the microstructures associated with hydrogen induced fractures. The fractures were situated inside martensite region or at the interface of martensite and ferrite. These

microstructures are preferential hydrogen traps. Thus, hydrogen is considered to diffuse to such sites, reduce cohesive energy and cause fracture initiation upon the stress reaching a critical stress. This process is described as HEDE. Moreover, the fractures were also situated in ferrite or transverse martensite. Therefore, it is presumed that fracture initiates in martensite regions or/and at martensite and ferrite interface via the HEDE mechanism, thereafter propagates into ferrite or transverse martensite, causing transgranular brittle features. This is consistent with other research [23, 24, 56]. Sun et al. [56] observed the widening of martensite lath boundary substructures and microcracks appearing long the lath boundaries, as well as widening and fracture at the martensite and ferrite interface, in the hydrogen-charged DP steels. Koyama and co-workers [23] further attributed crack propagation in ferrite to the enhanced dislocation movement, which was associated with the HELP mechanism.

Q&P steels also showed brittle regions containing exclusively transgranular features, as illustrated in Fig. 17. Figs. 24 presents the hydrogen induced small fractures in association with microstructures, demonstrating fractures were situated somewhere near or at interior martensitic M regions, as indicated by the arrows in Figs. 24(b) to (d). In addition, the fractures propagated into adjacent ferrite or transverse martensite. The presence of lath martensite, accommodated with a high dislocation density, favours high hydrogen concentrations in such martensite. Moreover, during deformation, phase transformation from retained austenite to martensite [35] and concomitant volume expansion occur [37], increasing the local stress intensity in the transformed regions. Thus, hydrogen assembles near the retained austenite/martensite interfaces. In addition, the high hydrogen solubility in austenite could enrich the freshly formed martensite with hydrogen [66]. The high hydrogen concentration, in the original or freshly formed martensite and near the interfaces of such martensite and untransformed retained austenite, thus results in the reduced cohesive energy and fracture initiation via HEDE. Thereafter, fractures transverse martensite by the HEDE mechanism, or propagate into ferrite due to the decreased fracture arresting capability of ferrite by hydrogen enhanced dislocation mobility, e.g. HELP mechanism, as aforementioned for DP steels. Consequently, the corresponded macroscopic transgranular features were formed. This observation of hydrogen induced fractures initiating from hard phase and then propagating into soft ferrite is consistent with results from other works [18, 35, 37, 54, 72].

TWIP steels contained transgranular features in brittle regions B for all the hydrogen influenced steels, except for the one tested with severest conditions of $-1.700\ V_{Hg/HgO}$ and the slowest stress rate, which possessed the additional intergranular facets, as presented in Fig. 19.

For TWIP steels undergoing deformation, mechanical twins can be produced and act as hydrogen traps [39], as also reported by Park et al. [52] that hydrogen transported to freshly formed twin boundaries under deformation. Such hydrogen segregation at twin boundaries or twin-twin intersections within a grain would reduce the cohesion of the twin boundaries and result in fracture initiation upon a critical stress. Thereafter, fractures would propagate along the twin boundaries causing macroscopic transgranular brittle features [61, 62]. This process is within the framework of HEDE. Similarly, grain boundaries are also preferential hydrogen trap sites due to their possible role as short circuit for hydrogen diffusion, and movement of dislocation-carried hydrogen to such a high stressed site. Thus, possible fracture initiation sites could be the grain boundary triple junction [86], or the intercept of the grain boundary and the deformation twins [61], which are both highly hydrogen accumulated and highly stress concentrated. It was further stated that the high stress, at the grain boundaries intercepted by the expanding deformation twins, could cause intergranular cracking even in the absence of hydrogen [61]. Fractures then would propagate along the grain boundaries and generate the corresponded intergranular brittle features, also by the HEDE mechanism. Such intergranular fracture was also documented in other works [26, 40]. The presence of such intergranular facets among the transgranular features is consistent with the severer hydrogen influence at the slowest stress rate with hydrogen charging potential of $-1.700\ V_{Hg/HgO}$. In addition, the formation of ε- or α- martensite and fracture at the interface of this martensite and austenite was also a possible cause of transgranular features [39, 62, 87]. Such fracture initiation and propagation processes are also considered associated with the HEDE mechanisms. However, further investigations, such as XRD and TEM, on the formation of any ε- or α- martensite are required to help elucidate the transgranular features in this work.

There were fisheyes in all the DP, Q&P and TWIP steels subjected to hydrogen charging. They were reported to be indications of hydrogen embrittlement [34]. For 980DP steels, fisheyes were only present at the most negative charging potential ($-1.700\ V_{Hg/HgO}$) and the slowest stress rate, whereas for other stronger DP steels, there were fisheyes at the less negative potential of $-1.400\ V_{Hg/HgO}$ and the medium stress rate, and at any severer condition (e.g. more negative potential and slower stress rate). For 980QP and 950TW, there were fisheyes in all the specimens tested with hydrogen charging. Thus, no clear dependence of such fisheye formation could be concluded. Venezuela et al. [30] ruled out the dependence of fisheye formation on stress rate by experiments on martensitic steels, but they found that martensite was associated with the fisheye formation. The formation of fisheyes involves the accumulation of hydrogen at a defect, such as an inclusion or microvoid, and the locally

critical deformation due to loading [88]. In this work, pores, brittle phases and inclusions were associated with fisheye initiation. The hydrogen may first accumulate in the voids at a martensite and ferrite interface, or around the edges of an inclusion, producing internal pressure. When the deformation associated with external loading reaches a critical level, a fracture could then nucleate. This process could be explained within the scope of the HEDE mechanism. Non-metallic inclusions were nuclei for fisheyes in this work, such as Al_2O_3 and TiN in DP steels, and AlN for 950TW. These inclusions most likely come from the steelmaking process. Details involved in the formation of such inclusions are not discussed here since those are beyond the scope of this study. However, the role of these non-metallic inclusions as nuclei for brittle fisheyes is detrimental to HE resistance. Moreover, the observation that fisheye occurred at the centre of DP and Q&P specimens and near the edge of TWIP, is consistent with the hydrogen saturation region, which is the whole specimen for DP and Q&P and a certain extent from the surface edge for 950TW, as mentioned above. Furthermore, the brittle features of fisheyes all radiated to a distance and thereafter were surrounded by ductile dimples features (e.g. see Fig. 16). This observation implies that the brittle fracturing of fisheyes competed with ductile fracturing during the final fracture process.

4.5.3. Surface cracks

As aforementioned, there were shallow shear cracks in the neck part on the transverse surfaces of all the steels tested in air. These cracks were along a direction at 45 degree to the tensile stress, due to the maximum shear stress in this direction during plastic deformation.

For those under hydrogen charging, there were also such cracks at 45 degree to the tensile stress direction. Moreover, there were also small horizontal cracks. These small cracks were either separated or interconnected to form larger ones in a stepwise manner. All the cracks were mostly close to the final fracture surface. These cracks were considered as induced by hydrogen. The occurrence of surface cracks as a manifestation of a hydrogen influence was also reported in other literature [5, 30, 54]. All these cracks were in the necked region and were absent in the uniform plastic deformation regions. The crack size and amount decreased as a function of distance from the fracture surface. These observations indicated that the hydrogen induced cracks only took place after the onset of necking and competed with ductile fracture during the final fracture process. In should be mentioned that these hydrogen induced cracks were also demonstrated for the non-pre-charged 950TW tested in air at the medium and slowest stress rates, indicating a hydrogen influence. Such a hydrogen influence was attributed to the residual hydrogen after processing and the

favourable slower stress rates, as explained above in sections 4.1 and 4.4. There were similar cracks for hydrogen pre-charged 950TW tested at corresponding stress rates. Moreover, the size and amount of such cracks for hydrogen charged specimens were much more significant than those without hydrogen charging, indicating a severer influence of hydrogen. However, with further increasingly negative potential or lower stress rate, there was little increase in crack size and amount, despite the severer hydrogen influence manifested by the larger brittle fracture area and more deteriorated properties. This might be partly attributed to the relatively rapid fracture process after the onset of necking during a LIST test. Furthermore, the hydrogen induced surface cracks can occur via HELP or AIDE for the shear-induced fracture or through HEDE for the brittle fracture, as mentioned above in section 4.5.3.

4.6. Effect of hydrogen traps on HE

In DP, Q&P, and TWIP steels, microstructure features such as grain boundaries, dislocations, impurities, twins, can act as traps for hydrogen. Hydrogen traps can decrease hydrogen permeation by reducing the effective diffusion coefficient [4]. Thus, the hydrogen influence could be related to hydrogen trapping. Traps can be characterized as reversible and irreversible. Accepting the concept that a critical hydrogen concentration needs to be reached for crack initiation, these traps can have the following two influences in hydrogen embrittlement. (i) Some of the traps are potential flaws, meaning they may nucleate fractures. A fracture is expected to nucleate if the critical amount of hydrogen is reached at such a trap during the tensile test. (ii) Many traps do not nucleate cracks. They either hinder hydrogen from reaching the flaws or assist the flaws in gaining more hydrogen [81].

Irreversible traps have high trapping activation energy and always function as hydrogen sinks, preventing hydrogen from moving to flaws. During a tensile test introducing plastic deformation, the interface grows and enhances the trapping capacity, so that irreversible traps do not saturate and maintain their character as hydrogen sinks for the length of the test at room temperature, and therefore are beneficial to HE resistance, whereas, reversible traps can function in completely opposite roles, either innocuous sinks or detrimental source for hydrogen in terms of embrittlement, depending on the test conditions [89]. Pressouyre et al. [81, 82, 90, 91] comprehensively discussed the role of reversible traps in hydrogen embrittlement during a tensile test and concluded that the prevailing role would depended on two main factors: (i) the location of hydrogen before testing (internal or external) and (ii) by what means hydrogen moved into the specimen (e.g. interstitial diffusion, dislocation atmosphere). Pre-charging was considered to introduce internal hydrogen prior to

the test (Internal Hydrogen Embrittlement, IHE), whist no hydrogen was expected prior to testing in the situation of external hydrogen embrittlement (EHE). Presuming that hydrogen moved by a dislocation atmosphere, reversible traps and movable dislocations interacted in two manners. For external hydrogen embrittlement, dislocations, nucleated at the specimen surface during plastic deformation, carried external hydrogen into the specimen, and lost hydrogen to both the hydrogen-free irreversible and reversible traps on their way to potential flaws that could nucleate fractures. Therefore, the dislocations, when met with flaws, possessed less hydrogen to reach the critical hydrogen concentration, and consequently, the possibility of fractures nucleating at the flaws decreased. For internal hydrogen embrittlement, on the other hand, the intrinsic irreversible and reversible traps already contained some hydrogen. The moving dislocations would also give hydrogen to irreversible traps, due to the aforementioned hydrogen-sink function of irreversible traps, however, they might possess less hydrogen than the reversible traps, and thus gain some hydrogen from the reversible traps. As a result, the moving dislocations can carry more hydrogen when they arrive at potential flaws. Fracture nucleation then had a better chance to occur.

In this present study, a 24-hour pre-charging of hydrogen was conducted prior to LIST testing. The aforementioned internal hydrogen situation, where reversible hydrogen acted as hydrogen source and was detrimental to HE resistance, is therefore applicable to the current case. More reversibly trapped hydrogen can be interpreted as associated with increased susceptibility to hydrogen embrittlement. Thus, the reduced resistance to HE of the three 980DP steels can also be explained with their increased amount of reversibly trapped hydrogen, and similarly, the higher susceptibility to HE of 1200DP than 980DP can also be related to the higher reversibly trapped hydrogen content, as evaluated by the complete decay of permeation tests in our previous work [48].

However, hydrogen transport and interaction with traps are complex processes. The abovementioned theory assumes that hydrogen moves by dislocation atmospheres. Hydrogen movement by other cases, such as interstitial diffusion and diffusion along short circuit paths (e.g. grain boundaries parallel to hydrogen flux), may occur and interact with traps at the same time. Moreover, during tensile tests accompanied with plastic deformation, phase transformation may also occur, producing a concomitant new phase with different influence on HE resistance. For example, about 8% retained austenite was present in the 980QP steel. The reversibly trapped hydrogen content was estimated to be significant lower by a factor of 3-4 than that for 980DP steels in the previous permeation study [48]. The HE resistance of 980QP would therefore be expected to be higher than for 980DP, based on the

aforementioned theory of reversible traps. In contrast, as mentioned in section 4.3, 980QP showed significantly higher susceptibility to HE than 980DP. This contradiction could be explained by the fact that the retained austenite transformed to martensite and acted as detrimental source of hydrogen (similar to aforementioned reversible traps) during tensile tests [66, 73], whereas there was no such phase transformation in permeation experiments in our previous work. Indeed, if the retained austenite can remain stable, suppressing transformation to martensite during tensile tests, it will act as a beneficial hydrogen sink due to its high solubility of hydrogen [37, 75], similar to the aforementioned irreversible traps.

5. Conclusions

The hydrogen influence on some DP, Q&P and TWIP grades of advanced high strength steels was studied by using the linearly increasing stress test (LIST) with simultaneous cathodic hydrogen charging. This research led to the following conclusions:

1. The hydrogen influence was manifested by decreased strength, reduced ductility and fracture mode change from ductile cup and cone fracture to brittle transgranular and/or intergranular fracture.
2. The decrease in yield strength was attributed to solid solution softening by hydrogen.
3. The hydrogen influence was greater with increased strength, more negative charging potential and decreased stress rate.
4. For 950TW steels, there was some hydrogen influence for non-pre-charged specimens tested in air at the two slower stress rates, and the influence was greater with hydrogen pre-charging.
5. Hydrogen assisted fracture occurred after the onset of necking.
6. There was no hydrogen assistant sub-critical crack growth at stresses below the ultimate tensile strength.
7. Hydrogen assisted fracture competed with ductile fracture in the final fracture process.
8. Hydrogen brittle fracture was associated with the hard martensite phase for DP, Q&P steels via HEDE and HELP mechanisms.

Acknowledgements

This research was supported by the Baosteel-Australia Joint Research & Development Centre (BAJC) Grant, BA13037, with linkage to Baoshan Iron and Steel Co., Ltd of China. The

authors also wish to thank the staff at the Centre for Microscopy and Microanalysis at the University of Queensland for their assistance.

References

[1] D Bhattacharya, Developments in advanced high strength steels, Proceedings of Proceedings of the Joint International Conference of HSLA Steels, Sanya, 2005, 70-73.
[2] WorldAutoSteel, Advanced high-strength steels application guidelines version 5.0, Available from http://www.worldautosteel.org/, Access on 2014.
[3] X Zhu, Z Ma and L Wang, Current status of advanced high strength steel for auto-making and its development in Baosteel, Rep Baosteel Research Institute. 201900 (2007) 1-8.
[4] Q Liu, Q Zhou, J Venezuela, M Zhang, J Wang and A Atrens, A review of the influence of hydrogen on the mechanical properties of DP, TRIP, and TWIP advanced high-strength steels for auto construction, Corros Rev. 34 (2016) 127-152.
[5] G Lovicu, M Barloscio, M De Sanctis, A Dimatteo, C Santus, R Valentini, M Bottazzi, F D'Aiuto, C Federici and S Maggi, Hydrogen embrittlement of advanced high strength steels for automotive use, Proceedings of 2nd International Conference ''Super High Strength Steels'', Italie, 2010,
[6] BC De Cooman, L Chen, HS Kim, Y Estrin, SK Kim and H Voswinckel, State-of-the-Science of High Manganese TWIP Steels for Automotive Applications, Microstructure and Texture in Steels, Charpter 10, p. 165-183, Springer, London, 2009.
[7] BaoSteel, BaoSteel automotive advanced high strength steels, Avaliable from www.baosteel.com, Access on November 12, 2014 (2013).
[8] Baosteel, Baosteel automotive advanced high strength steels, Available from http://www.baosteel.com/, Access on 2013.
[9] DK Matlock and JG Speer, Third Generation of AHSS: Microstructure Design Concepts, Microstructure and Texture in Steels, Charpter 11, p. 185-205, Springer London, 2009.
[10] DV Edmonds, K He, FC Rizzo, BC De Cooman, DK Matlock and JG Speer, Quenching and partitioning martensite—A novel steel heat treatment, Mater Sci Eng A. 438-440 (2006) 25-34.
[11] MJ Santofimia, L Zhao and J Sietsma, Overview of Mechanisms Involved During the Quenching and Partitioning Process in Steels, Metall Mater Trans A. 42 (2011) 3620-3626.

[12] S Lynch, Hydrogen embrittlement phenomena and mechanisms, Corros Rev. 30 (2012) 105-123.
[13] RA Oriani and PH Josephic, Equilibrium aspects of hydrogen-induced cracking of steels, Acta Metall. 22 (1974) 1065-1074.
[14] C Beachem, A new model for hydrogen-assisted cracking (hydrogen "embrittlement"), Metall Trans. 3 (1972) 441-455.
[15] DP Abraham and CJ Altstetter, Hydrogen-enhanced localization of plasticity in an austenitic stainless steel, Metall Mater Trans A. 26 (1995) 2859-2871.
[16] HK Birnbaum and P Sofronis, Hydrogen-enhanced localized plasticity—a mechanism for hydrogen-related fracture, Mater Sci Eng A. 176 (1994) 191-202.
[17] S Lynch, Environmentally assisted cracking: overview of evidence for an adsorption-induced localised-slip process, Acta Metall. 36 (1988) 2639-2661.
[18] G Lovicu, M Bottazzi, F D'Aiuto, M De Sanctis, A Dimatteo, C Santus and R Valentini, Hydrogen Embrittlement of Automotive Advanced High-Strength Steels, Metall Mater Trans A. 43 (2012) 4075-4087.
[19] J Michalska, B Chmiela, J Łabanowski and W Simka, Hydrogen Damage in Superaustenitic 904L Stainless Steels, J Mater Eng Perform. 23 (2014) 2760-2765.
[20] T Depover, D Pérez Escobar, E Wallaert, Z Zermout and K Verbeken, Effect of hydrogen charging on the mechanical properties of advanced high strength steels, Int J Hydrogen Energy. 39 (2014) 4647-4656.
[21] J Hirth, Effects of hydrogen on the properties of iron and steel, Metall Trans A. 11 (1980) 861-890.
[22] M Loidl, O Kolk, S Veith and T Göbel, Characterization of hydrogen embrittlement in automotive advanced high strength steels, Materialwiss Werkstofftech. 42 (2011) 1105-1110.
[23] M Koyama, CC Tasan, E Akiyama, K Tsuzaki and D Raabe, Hydrogen-assisted decohesion and localized plasticity in dual-phase steel, Acta Mater. 70 (2014) 174-187.
[24] R Davies, Hydrogen embrittlement of dual-phase steels, Metall Trans A. 12 (1981) 1667-1672.
[25] J Ronevich, S Kim, J Speer and D Matlock, Hydrogen effects on cathodically charged twinning-induced plasticity steel, Scripta Mater. 66 (2012) 956-959.
[26] M Koyama, E Akiyama and K Tsuzaki, Hydrogen embrittlement in a Fe–Mn–C ternary twinning-induced plasticity steel, Corros Sci. 54 (2012) 1-4.
[27] A Atrens, CC Brosnan, S Ramamurthy, A Oehlert and IO Smith, Linearly increasing stress test (LIST) for SCC research, Meas Sci Technol. 4 (1993) 1281.

[28] Q Liu, B Irwanto and A Atrens, The influence of hydrogen on 3.5NiCrMoV steel studied using the linearly increasing stress test, Corros Sci. 67 (2013) 193-203.
[29] Q Liu, B Irwanto and A Atrens, Influence of hydrogen on the mechanical properties of some medium-strength Ni–Cr–Mo steels, Mater Sci Eng A. 617 (2014) 200-210.
[30] J Venezuela, Q Liu, M Zhang, Q Zhou and A Atrens, The influence of hydrogen on the mechanical and fracture properties of some martensitic advanced high strength steels studied using the linearly increasing stress test, Corros Sci. 99 (2015) 98-117.
[31] J Venezuela, Q Zhou, Q Liu, M Zhang and A Atrens, Influence of hydrogen on the mechanical and fracture properties of some martensitic advanced high strength steels in simulated service conditions, Corros Sci. 111 (2016) 602-624.
[32] N Winzer, A Atrens, W Dietzel, G Song and KU Kainer, Comparison of the linearly increasing stress test and the constant extension rate test in the evaluation of transgranular stress corrosion cracking of magnesium, Mater Sci Eng A. 472 (2008) 97-106.
[33] A Begić Hadžipašić, J Malina and M Malina, The influence of microstructure on hydrogen diffusion and embrittlement of multiphase fine-grained steels with increased plasticity and strength, Chem Biochem Eng Q. 25 (2011) 159-169.
[34] G Lovicu, EP Bagliani, M De Sanctis, A Dimatteo, R Ishak and R Valentini, Hydrogen embrittlement of a medium carbon Q&P steel, Metallurgical Italiana. 6 (2013) 3-10.
[35] X Zhu, K Zhang, W Li and X Jin, Effect of retained austenite stability and morphology on the hydrogen embrittlement susceptibility in quenching and partitioning treated steels, Mater Sci Eng A. 658 (2016) 400-408.
[36] J Yang, F Huang, Z Guo, Y Rong and N Chen, Effect of retained austenite on the hydrogen embrittlement of a medium carbon quenching and partitioning steel with refined microstructure, Mater Sci Eng A. 665 (2016) 76-85.
[37] X Zhu, W Li, H Zhao, L Wang and X Jin, Hydrogen trapping sites and hydrogen-induced cracking in high strength quenching & partitioning (Q&P) treated steel, Int J Hydrogen Energy. 39 (2014) 13031-13040.
[38] J Malina, A Begić Hadžipašić and Š Nižnik, Electrochemical corrosion and hydrogen diffusivity in dual-phase steel, Proceedings of 2nd International Conference Corrosion and Material Protection, EFC Event, 2010,
[39] JH Ryu, SK Kim, CS Lee, D-W Suh and H Bhadeshia, Effect of aluminium on hydrogen-induced fracture behaviour in austenitic Fe–Mn–C steel, Proc R Soc A. 469 (2013) 20120458.

[40] M Koyama, E Akiyama and K Tsuzaki, Effect of hydrogen content on the embrittlement in a Fe–Mn–C twinning-induced plasticity steel, Corros Sci. 59 (2012) 277-281.
[41] S Ramamurthy and A Atrens, Stress corrosion cracking of high-strength steels, Corros Rev. 31 (2013) 1-31.
[42] E Villalba and A Atrens, Metallurgical aspects of rock bolt stress corrosion cracking, Mater Sci Eng A. 491 (2008) 8-18.
[43] E Villalba and A Atrens, Hydrogen embrittlement and rock bolt stress corrosion cracking, Eng Fail Anal. 16 (2009) 164-175.
[44]E562-08, Standard test method for determining volume fraction by systematic manual point count, 2008.
[45]E-112, Standard test methods for determining average grain size, 2010.
[46] GF Vander Voort, Metallography, principles and practice, ASM International, 1984.
[47] Q Liu, AD Atrens, Z Shi, K Verbeken and A Atrens, Determination of the hydrogen fugacity during electrolytic charging of steel, Corros Sci. 87 (2014) 239-258.
[48] Q Liu, J Venezuela, M Zhang, Q Zhou and A Atrens, Hydrogen trapping in some advanced high strength steels, Corros Sci. 111 (2016) 770-785.
[49] Q Liu, Q Zhou, J Venezuela, M Zhang and A Atrens, Hydrogen Concentration in Dual-Phase (DP) and Quenched and Partitioned (Q&P) Advanced High-Strength Steels (AHSS) under Simulated Service Conditions Compared with Cathodic Charging Conditions, Adv Eng Mater. 18 (2016) 1588-1599.
[50] R Davies, Influence of martensite content on the hydrogen embrittlement of dual-phase steels, Scripta metallurgica. 17 (1983) 889-892.
[51] C Zhuang, J Liu, Z Mi, H Jiang, D Tang and G Wang, Non-Metallic Inclusions in TWIP Steel, steel research international. 85 (2014) 1432-1439.
[52] IJ Park, SY Jo, M Kang, SM Lee and YK Lee, The effect of Ti precipitates on hydrogen embrittlement of Fe–18Mn–0.6 C–2Al–xTi twinning-induced plasticity steel, Corros Sci. 89 (2014) 38-45.
[53] L Chen, Y Zhao and X Qin, Some aspects of high manganese twinning-induced plasticity (TWIP) steel, a review, Acta Metall Sin (Engl Lett). 26 (2013) 1-15.
[54] A Laureys, T Depover, R Petrov and K Verbeken, Characterization of hydrogen induced cracking in TRIP-assisted steels, Int J Hydrogen Energy. 40 (2015) 16901-16912.
[55] A Atrens, D Mezzanotte, N Fiore and M Genshaw, Electrochemical studies of hydrogen diffusion and permeability in Ni, Corros Sci. 20 (1980) 673-684.

[56] S Sun, J Gu and N Chen, The influence of hydrogen on the sub-structure of the martensite and ferrite dual-phase steel, Scripta metallurgica. 23 (1989) 1735-1737.
[57] P Vanova, J Sojka, K Konecna and A Wenglorzova, Study of hydrogen embrittlement of the TRIP 980 steels by means of tensile tests at simultaneous hydrogen charging, 23rd International Conference on Metallurgy and Materials METAL 2014 (2012)
[58] J Crank, The mathematics of diffusion, Oxford university press, 1979.
[59] Q Liu and A Atrens, Reversible hydrogen trapping in a 3.5NiCrMoV medium strength steel, Corros Sci. 96 (2015) 112-120.
[60] L Marchetti, E Herms, P Laghoutaris and J Chêne, Hydrogen embrittlement susceptibility of tempered 9%Cr–1%Mo steel, Int J Hydrogen Energy. 36 (2011) 15880-15887.
[61] M Koyama, E Akiyama, K Tsuzaki and D Raabe, Hydrogen-assisted failure in a twinning-induced plasticity steel studied under in situ hydrogen charging by electron channeling contrast imaging, Acta Mater. 61 (2013) 4607-4618.
[62] T Dieudonné, L Marchetti, M Wery, J Chêne, C Allely, P Cugy and C Scott, Role of copper and aluminum additions on the hydrogen embrittlement susceptibility of austenitic Fe–Mn–C TWIP steels, Corros Sci. 82 (2014) 218-226.
[63] K Wang, D Wang and F Han, Effect of sample thickness on the tensile behaviors of Fe–30Mn–3Si–3Al twinning-induced plasticity steel, Mater Sci Eng A. 642 (2015) 249-252.
[64] PJ Jacques, Q Furnémont, F Lani, T Pardoen and F Delannay, Multiscale mechanics of TRIP-assisted multiphase steels: I. Characterization and mechanical testing, Acta Mater. 55 (2007) 3681-3693.
[65] F Lani, Q Furnémont, T Van Rompaey, F Delannay, PJ Jacques and T Pardoen, Multiscale mechanics of TRIP-assisted multiphase steels: II. Micromechanical modelling, Acta Mater. 55 (2007) 3695-3705.
[66] JH Ryu, YS Chun, CS Lee, HKDH Bhadeshia and DW Suh, Effect of deformation on hydrogen trapping and effusion in TRIP-assisted steel, Acta Mater. 60 (2012) 4085-4092.
[67] YS Chun, K-T Park and CS Lee, Delayed static failure of twinning-induced plasticity steels, Scripta Mater. 66 (2012) 960-965.
[68] J Tien, AW Thompson, IM Bernstein and RJ Richards, Hydrogen transport by dislocations, Metall Trans A. 7 (1976) 821-829.
[69] X Zhu, W Li, TY Hsu, S Zhou, L Wang and X Jin, Improved resistance to hydrogen embrittlement in a high-strength steel by quenching–partitioning–tempering treatment, Scripta Mater. 97 (2015) 21-24.

[70] M Koyama, E Akiyama, T Sawaguchi, D Raabe and K Tsuzaki, Hydrogen-induced cracking at grain and twin boundaries in an Fe–Mn–C austenitic steel, Scripta Mater. 66 (2012) 459-462.
[71] Y Tomita, Effect of morphology of second-phase martensite on tensile properties of Fe-0.1 C dual phase steels, Journal of Materials science. 25 (1990) 5179-5184.
[72] X Zhu, W Li, H Zhao and X Jin, Effects of cryogenic and tempered treatment on the hydrogen embrittlement susceptibility of TRIP-780 steels, Int J Hydrogen Energy. 38 (2013) 10694-10703.
[73] J Ronevich, B De Cooman, J Speer, E De Moor and D Matlock, Hydrogen effects in prestrained transformation induced plasticity steel, Metall Mater Trans A. 43 (2012) 2293-2301.
[74] R McCoy and W Gerberich, Hydrogen embrittlement studies of a trip steel, Metall Trans. 4 (1973) 539-547.
[75] J Sojka, V Vodárek, I Schindler, C Ly, M Jérôme, P Váňová, N Ruscassier and A Wenglorzová, Effect of hydrogen on the properties and fracture characteristics of TRIP 800 steels, Corros Sci. 53 (2011) 2575-2581.
[76] S-M Lee, I-J Park, J-G Jung and Y-K Lee, The effect of Si on hydrogen embrittlement of Fe-18Mn-0.6C-xSi twinning-induced plasticity steels, Acta Mater. 103 (2016) 264-272.
[77] M Koyama, E Akiyama and K Tsuzaki, Effects of static and dynamic strain aging on hydrogen embrittlement in TWIP steels containing Al, ISIJ Int. 53 (2013) 1268-1274.
[78] I-J Park, K-H Jeong, J-G Jung, CS Lee and Y-K Lee, The mechanism of enhanced resistance to the hydrogen delayed fracture in Al-added Fe–18Mn–0.6 C twinning-induced plasticity steels, Int J Hydrogen Energy. 37 (2012) 9925-9932.
[79] T Depover, E Wallaert and K Verbeken, Fractographic analysis of the role of hydrogen diffusion on the hydrogen embrittlement susceptibility of DP steel, Mater Sci Eng A. 649 (2016) 201-208.
[80] M Hashimoto and RM Latanision, The role of dislocations during transport of hydrogen in hydrogen embrittlement of iron, Metall Trans A. 19 (1988) 2799-2803.
[81] GM Pressouyre, Trap theory of Hydrogen embrittlement, Acta Metall. 28 (1980) 895-911.
[82] GM Pressouyre and IM Bernstein, An example of the effect of hydrogen trapping on hydrogen embrittlement, Metall Trans A. 12 (1981) 835-844.
[83] M Faccoli, G Cornacchia, M Gelfi, A Panvini and R Roberti, Notch ductility of steels for automotive components, Eng Fract Mech. 127 (2014) 181-193.

[84] S Huang, Y-x Zhao and C-f He, Shear Fracture of Advanced High Strength Steels, Journal of Iron and Steel Research, International. 21 (2014) 938-944.
[85] M Nagumo, Hydrogen embrittlement of steels turning of the research direction, Tetsu-To-Hagane/Journal of the Iron and Steel Institute of Japan. 95 (2009) 222-227.
[86] M Koyama, H Springer, SV Merzlikin, K Tsuzaki, E Akiyama and D Raabe, Hydrogen embrittlement associated with strain localization in a precipitation-hardened Fe–Mn–Al–C light weight austenitic steel, Int J Hydrogen Energy. 39 (2014) 4634-4646.
[87] KH So, JS Kim, YS Chun, K-T Park, Y-K Lee and CS Lee, Hydrogen delayed fracture properties and internal hydrogen behavior of a Fe-18Mn-1.5 Al-0.6 C TWIP steel, ISIJ Int. 49 (2009) 1952-1959.
[88] M Moeser, Fractography with the SEM (Failure Analysis), Avaliable from http://martin-moeser.de/, Access on May 01, 2016.
[89] GM Pressouyre, A classification of hydrogen traps in steel, Metall Trans A. 10 (1979) 1571-1573.
[90] GM Pressouyre, Hydrogen traps, repellers, and obstacles in steel; Consequences on hydrogen diffusion, solubility, and embrittlement, Metall Trans A. 14 (1983) 2189-2193.
[91] GM Pressouyre and IM Bernstein, A quantitative analysis of hydrogen trapping, Metall Trans A. 9 (1978) 1571-1580.

Chapter 3

Influence of hydrogen on some commercial DP, Q&P and TWIP advanced high-strength steels under simulated automobile service conditions

(submitted to industrial partner for approval of publication)

In Chapter 2, the hydrogen influence on some DP, Q&P and TWIP grades of AHSS was studied using the linearly increasing stress test (LIST) under cathodic charging in a 0.1 M NaOH solution. It was found that all the steels exhibited HE susceptibility, manifested by (a) reduced strength and ductility, and (b) a change of fracture mode from ductile cup and cone fracture to a macroscopically brittle transgranular and/or intergranular fracture, caused by some hydrogen assisted fracture processes after the onset of necking competing with ductile fracture. The hydrogen influence increased with increasing strength, increasing hydrogen fugacity, and decreasing stress rate. The hydrogen influence was also identified associated with hard martensite phase for DP and Q&P steels.

It was then considered whether the hydrogen influence would occur to the key steels regarding to a hydrogen environment that was similar to the actual service condition, which was much less severe than the cathodic charging conditions as used in the study in Chapter 2. Therefore, Chapter 3 aims to answer this question.

Influence of hydrogen on some commercial DP, Q&P and TWIP advanced high-strength steels under simulated automobile service conditions

Qinglong Liu[a], Qingjun Zhou[b,*], Jeffrey Venezuela[a], Mingxing Zhang[a], Andrej Atrens[a,*]

[a]The University of Queensland, Division of Materials, School of Mining and Mechanical Engineering, St. Lucia, 4072 Australia

[*]Corresponding author, andrejs.atrens@uq.edu.au, +61 7 3365 3748,

zhouqingjun@baosteel.com, +86 21 26641807

[b]Baoshan Iron & Steel Co., Ltd, Research Institute, Shanghai, 201900, China

Abstract

HE susceptibility was studied (i) for immersion in 3 wt% NaCl, to simulate hydrogen picked in automobile service, and (ii) at substantial loading rates to simulate a crash. Simulated service conditions caused minimal HE for 980DP and 1200DP, and some HE for 980DP-650YS, 980DP-700YS, 980QP and 950TW. Simulated crash situations caused HE for 980DP, 980QP and 950TW; their properties quickly reverted after the end of hydrogen charging. Two new HE mechanisms are proposed: (i) hydrogen enhanced macroscopic plasticity (HEMP) decreasing the yield stress, and (ii) hydrogen assisted micro-fracture (HAM) decreasing ductility at fracture at the ultimate tensile strength.

Key words: advanced high strength steel; SEM; hydrogen embrittlement

1. Introduction

Dual Phase (DP), Quenching and Partitioning (Q&P) and Twinning-Induced Plasticity (TWIP) advanced high-strength steels (AHSS) have been studied for auto construction applications that fulfil the demands of lightweight and improved safety performance [1-5]. DP, Q&P and TWIP steels exhibit high strength, good ductility, and good formability, which is attributed to a high strain hardening capacity [6, 7]. Their good mechanical properties make these steels suitable for automobile parts that are structural, safety-critical, and with complex shape, such as bumper reinforcements, A-pillars and B-pillars [4, 6, 8, 9]. During a crash, the stress in such parts can be substantial, and the loading rate can be high, even though the stress is low during normal auto service.

Hydrogen embrittlement (HE) can reduce the mechanical properties of the DP, Q&P and TWIP advanced high-strength steels, especially the ductility [10-28]. This could restrict their applications for auto construction. HE occurs by hydrogen interacting with the stressed steel. The hydrogen can come from general corrosion of the car body during auto service [29-32]. This was demonstrated by Ootsuka et al. [32], who related the amount of absorbed hydrogen to the corrosion mass loss of the steel, in an in-situ study using a monitoring system attached onto a moving car. They found that the amount of absorbed hydrogen was influenced by the moving states of a vehicle, and the conditions of the road surface. Therefore, HE is of concern for DP, Q&P and TWIP advanced high-strength steel auto compartments during auto service conditions. It is important to understand the steel performance during these service conditions.

Venezuela et al. [33] simulated auto service conditions in a study into the hydrogen influence on some martensitic advanced high-strength steels (MS-AHSS). They found that there was little influence of hydrogen on the MS-AHSS under such conditions, attributed to the relatively low hydrogen concentrations under these conditions. Furthermore, Zhou et al. [34] studied delayed fracture of TS 980 MPa advanced high-strength steels using a 0.1 M HCl solution, and found that the susceptibility of martensitic steels was higher than that of DP and Q&P steels. Thus, one would expect that there would be also minimal hydrogen influence on the less susceptible DP or Q&P steels under simulated auto service conditions similar to those in the study of Venezuela et al. [33]. However, it is important to verify this prediction, since the susceptibility to HE depends on many variables, such as microstructure and surface condition of the steel, level and type of applied or residual stress, and hydrogen concentration [13]. There are also studies showing the opposite conclusion; that martensitic steels were less susceptible than DP and Q&P steels [10, 13]. Thus, it is necessary to conduct research simulating auto service conditions to study the hydrogen influence on DP, Q&P and TWIP steels.

Previously, we studied the hydrogen influence on some DP, Q&P and TWIP advanced high-strength steels using the linearly increasing stress test (LIST) under cathodic charging in a 0.1 M NaOH solution [35]. All the steels exhibited HE susceptibility, manifested by (a) reduced ductility, and (b) a change of fracture mode from ductile cup and cone fracture to a macroscopically brittle transgranular and/or intergranular fracture, caused by some hydrogen assisted fracture processes after the onset of necking competing with ductile fracture. The strengths of the steels also somewhat decreased. The decrease in yield strength was attributed to solid solution softening by hydrogen. The hydrogen influence

increased with increasing strength, increasing hydrogen fugacity, and decreasing stress rate. There was no sub-critical crack growth at stresses below the ultimate tensile strength.

Moreover, the hydrogen content introduced into steels by cathodic charging in a 0.1 M NaOH solution in our previous study [35] was significantly higher than that which could occur in service conditions [36, 37]. HE does not occur for a hydrogen content lower than a critical value under the same applied stress [19, 26].

Thus, the current work builds on our previous study of the hydrogen influence on AHSS using LIST [35]. The current work studied the auto service HE susceptibility of some DP, Q&P and TWIP steels. The specific aims were (i) to study auto service HE susceptibility of some commercial DP, Q&P and TWIP steels, using specimens immersed in a 3 wt% NaCl solution at the free potential and at the zinc potential, simulating hydrogen charging from the corrosion conditions in actual auto service, (ii) to understand the influence of hydrogen under fast loading rates to simulate crash situations, and (iii) to correlate the steel microstructures with the hydrogen influence on the TWIP steels.

2. Experimental section

2.1. Materials and microstructure

The DP, Q&P and TWIP steels were commercial steels supplied from commercial production in the form of rolled sheets. Their designations were as follows: 980DP, 980DP-650YS, 980DP-700YS, 1200DP, 980QP and 950TW. These designations include the steel type as DP, QP or TWIP. 980DP-650YS, 980DP-700YS and 1200DP were galvanized. Before each test, each specimen was mechanically ground with SiC papers to remove (i) the zinc coating of the galvanized steels, or (ii) the surface rust and contamination of the non-galvanized steels. The average thickness of the specimens after grinding was 1.75 mm for 980 DP, 1.00 mm for 980DP-650YS, 0.97 mm for 980DP-700YS, 1.37 mm for 1200DP, 1.15 mm for 980QP and 1.35 mm for 950TW.

Table 1 presents the chemical compositions and mechanical properties for each steel, provided by the steel supplier in the first line, and, in the second line, the chemical compositions measured by Spectrometer Service Pty. Ltd, Coburg, Vic. The microstructures of these DP, Q&P and TWIP steels were presented in our previous works [35-37]. DP steels had a dual-phase microstructure consisted of a soft ferrite matrix and hard martensite islands. The fraction of martensite increased from 60% to 63%, 64% and 74% for DP steels in the following order: 980DP, 980DP-650YS, 980DP-700YS and 1200DP. This increase in

fraction martensite correlated with the yield strength. 980QP possessed a microstructure consisting of 39% ferrite, 53% martensite and about 8% retained austenite. 950TW had a fully austenitic microstructure.

Table 1 Chemical compositions (in wt %) and mechanical properties of the AHSS. Chemical compositions were determined by two independent institutes.

Steel designation	Compositions (wt%)							Mechanical properties		
	C	Si	Mn	Al	Nb	Ti	Cr	Yield strength (MPa)	Tensile strength (MPa)	Elongation at fracture (e_f, %)
980DP	0.09	0.28	2.26	0.03	<0.01	0.02	0.54	592	930	8.3
	0.08	0.27	2.31	0.02	0.01	0.03	0.55			
980DP-650YS	0.09	0.29	2.19	0.03	0.04	0.03	0.43	645	1057	7.9
	0.09	0.30	2.17	0.03	0.03	0.03	0.37			
980DP-700YS	0.08	0.41	2.18	0.03	0.04	0.05	0.02	697	1039	6.9
	0.09	0.44	2.22	0.05	0.05	0.04	0.02			
1200DP	0.12	0.24	2.43	0.03	0.02	0.03	0.56	896	1198	4.7
	0.11	0.25	2.49	0.03	0.03	0.03	0.58			
980QP	0.21	1.39	1.88	0.04	0.03	0.01	0.03	682	1020	11.3
	0.19	1.30	1.87	0.04	<0.01	0.03	0.02			
950TW	0.60	0.09	15.2	1.46	—	—	—	497	981	45
	0.59	0.14	15.2	1.16	0.01	0.03	0.07			

2.2. LIST method

The linearly increasing stress test (LIST) was proposed by Atrens and co-workers [38], as a stress-controlled test similar to the strain-controlled slow strain rate test (SSRT). Winzer et al. [39] compared these two tests and concluded that both could provide comparable results. Both tests were identical up until yielding, or the onset of subcritical crack growth, after which LIST test is completed in a shorter period of time.

Fig. 1 shows a schematic of the LIST apparatus. The LIST was based on the principle of a lever beam. One side of the beam was connected to a specimen, whilst the other side was loaded with a known weight (14 kg), which could be moved away from the fulcrum, driven by a synchronous motor, resulting in a linearly increasing (engineering) stress applied to the specimen. The stress rate was depended on (i) the speed of the synchronous motor, and (ii) the specimen cross-section area. The applied stress, S (MPa), can be calculated by:

$$S = \frac{(13720)d}{A} \quad (1)$$

where d (m) is the distance between the position of the weight and the zero load position, measured by the metric scale attached to the beam, and A (mm^2) is the original cross-section

area of the gauge part of the specimen. The numerical factor of 13720 in Eq. (1) depends on the mechanical advantage, the mass of the weight (14 kg), and the acceleration of gravity.

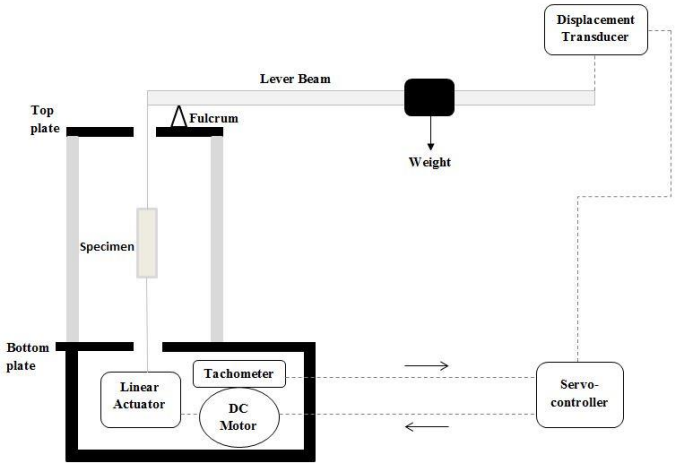

Fig. 1. Schematic of the LIST apparatus.

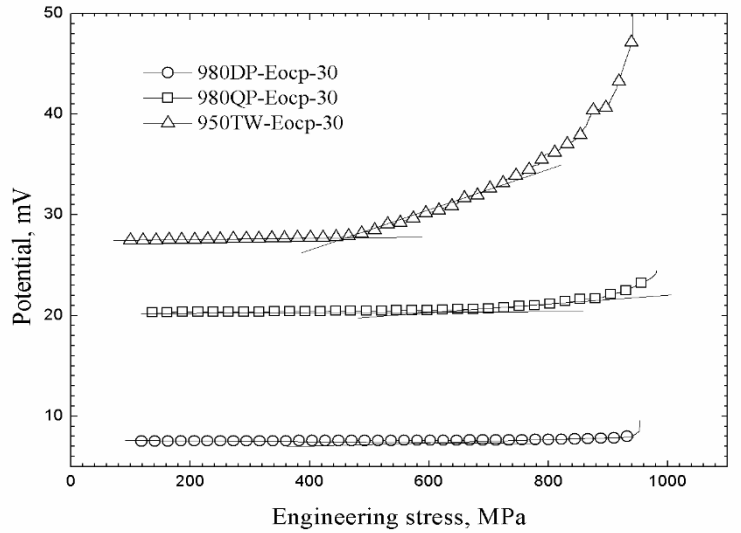

Fig. 2. Typical plots of potential drop vs. engineering stress for DP, Q&P and TWIP steels tested at the free corrosion potential in a 3% NaCl solution.

The fracture stress could be determined by using Eq. (1) with values of the original cross section area, A, and the distance, d_f, at fracture.

The yield stress for specimens tested in air (or under non-cracking conditions), σ_y, or the threshold stress for the initiation of subcritical cracking for specimens tested under cracking conditions, σ_{th}, could be measured by a direct current potential drop (DCPD) method, which plotted the potential drop versus the applied stress. Fig. 2 illustrates typical potential drop curves for typical DP, Q&P and TWIP steels. The significant change in the slope of the plots corresponded to the σ_{th} or σ_y. Fractography was subsequently used to identify that this stress corresponded to the yield stress in each case in this present work; there was no subcritical crack growth.

The extent of the hydrogen influence was quantified using the hydrogen embrittlement index (E_I), given by:

$$EI = \frac{R_{A,air} - R_{A,H}}{R_{A,air}} \times 100\% \quad (2)$$

where $R_{A,air}$ is the reduction in area tested in air, and $R_{A,H}$ is the reduction in area under hydrogen charging conditions. The values of E_I range from 0 to 100%, with E_I = 0 indicating no HE susceptibility, and E_I=100% indicating no reduction in area under hydrogen charging conditions.

LIST has been utilized to study HE and stress corrosion cracking (SCC) of metals such as medium-strength steels [17, 18] and high-strength steels [19, 33, 40-44]. LIST was used to study the HE of some DP, Q&P and TWIP steels, with cathodic hydrogen charging in a 0.1 M NaOH solution, in our previous study [35].

2.3. LIST using 3 wt% NaCl solution

LIST specimens were cut from the steel sheets into a dog-bone shape, with dimensions as described in our previous study [35]. The LIST specimens were subjected to various testing environments. Corrosion in 3 wt% NaCl solution with pH 7.3 at the free corrosion potential, E_{corr}, was used in this work as the environment for LIST tests to simulate the most severe corrosion that could occur in actual auto service, and so would represent the highest amount of hydrogen to be picked up by the steel from corrosion in service. Some hydrogen was picked up by the specimen corroding in 3 wt% NaCl at the free corrosion potential, E_{corr}, simulating corrosion of bare steel. A greater amount of hydrogen was picked up by a specimen immersed in 3 wt% NaCl and maintained electrochemically at a potential more negative than the free corrosion potential, E_{corr}. The greatest amount of hydrogen is expected for the steel immersed in 3 wt% NaCl and under cathodic polarization to the zinc potential, E_{Zn}, in order to simulate galvanized steel. A 24 h pre-charging was conducted at these two potentials with a static stress of 20% yield strength applied to the specimen. Thereafter, the tests were commenced at motor speeds of 30 and 3 revolutions per hour (rph) to introduce various applied stress rates to the specimens. The actual stress rates could be calculated based on Eq. (1). For example, for 980QP, the applied stress rates corresponding to 30 and 3 rph were 0.084 and 0.0084 MPa s^{-1}, respectively. For each test, the applied stress was provided along with the results.

The experiments at the zinc potential used a three-electrode system, with the specimen as the working electrode, an Ag/AgCl (saturated KCl) electrode as the reference electrode, and a graphite rod as the counter electrode. The value of the applied zinc potential was –0.950 $V_{Ag/AgCl}$, which was the measured open circuit potential of the zinc coating in a 3 wt% NaCl solution. This potential simulated the maximum amount of hydrogen produced for the steels protected by a zinc coating applied by galvanization.

LIST experiments at all the potentials and stress rates were carried out on 980DP, 980QP and 950TW, whereas only the LIST at the zinc potential and with 3 rph motor was conducted on the other stronger DP steels (980DP-650YS, 980DP-700YS and1200DP), with the expectation to observe the greatest hydrogen influence, since our previous study [35] showed that the hydrogen influence increased with increasing steel strength, increasing hydrogen fugacity and decreasing stress rate.

2.4. Considerable loading rate tests

In order to a simulate crash situation, tensile tests with considerable loading rates were conducted as per ASTM standard E8/E8M [45], using a 4505 Instron universal testing machine (UTM) at a strain rate of 0.015 min^{-1}. This strain rate corresponded to a stress rate of 50 MPa s^{-1} in the initial elastic region of the LIST, and was at least sixty times higher than that produced by LIST at 300 rph.

The specimen had the same dimensions as for the LIST experiments. The specimen was subjected to a 24 h pre-charging at –1.700 $V_{Hg/HgO}$ in 0.1 M NaOH (pH 12.6) at a stress equal to 20% of the yield strength. For the first experiments, pre-charging was carried out in the LIST apparatus, and the test was subsequently carried out in the Instron UTM. The charging was executed using a three-electrode system. The reference electrode was an Hg/HgO, KOH (20%) electrode and the counter electrode was a graphite rod, because our previous research has shown that a Pt counter electrode should not be used in such tests [33]. After pre-charging for 24 h in the LIST apparatus, the specimen was dismounted, rinsed with ethanol, dried, and tested in the 4505 Instron UTM in air. There was an inevitable time interval of about 10 min between the end of hydrogen pre-charging in the LIST apparatus, and the start of tensile testing in the Intron UTM. Therefore, the influence of the time interval on HE susceptibility was also studied. The applied time intervals were 0, 10 min and 24 h. Time interval 0 indicated that the 24 h of hydrogen pre-charging was carried out in the Instron UTM, so that the test was started with 0 min interval between pre-charging and tensile testing; and the in situ hydrogen charging continued until fracture of the specimen.

LIST experiments at 300 and 30 rph with the same procedures as mentioned above were also carried out for comparisons. In these tests, there were also 0 min, 10 min and 24 h between the end of the pre-charging, and the start of the LIST. For tests using the UTM and the LIST apparatus, 980DP, 980QP and 950TW were used. 980DP was the least susceptible to HE among the four DP steels based on our previous work [35]. Thus, the other three DP steels were not studied, since they were also expected to experience hydrogen influence if HE occurred to 980DP under the same testing conditions.

2.5. Specimen designations

For Table 2 for LIST testing, the specimen designations were as follows: 'steel type-testing environment-test speed'. 'A' was used to designate the air-testing environment. For testing in 3 wt% NaCl, 'Ecorr' and 'Ezn' were used to indicate the free corrosion potential and the zinc potential, respectively. L0.054 and L0.0054 indicate tests carried out in the LIST at an initial applied stress rates of 0.054 MPa s^{-1} and 0.0054 MPa s^{-1}, respectively. Typical examples were (i) '980DP-A-L0.054', which was the designation for 980DP, tested in air, using LIST with an applied stress rate of 0.054 MPa s^{-1}, corresponding to a motor speed of 30 rph (revolutions per hour), and (ii) '980DP-650YS-Ezn-L0.0100', which indicated 980DP-650YS tested at E_{Zn} in 3 wt% NaCl using LIST with a stress rate of 0.0100 MPa s^{-1}, corresponding to a motor speed of 3 rph.

For Table 3, the pre-charging condition was specified as "S (NaOH)" for specimens pre-charged in 0.1M NaOH at –1.700 $V_{Hg/HgO}$; the testing condition was specified as "S (NaOH)" for specimens charged during testing in 0.1M NaOH at –1.700 $V_{Hg/HgO}$; the testing condition was specified as "air" for tests in air; and the designation "Air, air" indicated tests with no pre-charging and testing in air. The specimen designation was as follows: 'steel designation-environment designation-test speed'. The steel designation was as in Table 1. The environment designations were as follows: A = test in air; 0min indicates tests for specimens pre-charged in 0.1M NaOH at –1.700 $V_{Hg/HgO}$ and charged during testing in 0.1M NaOH at –1.700 $V_{Hg/HgO}$; and 10min and 24 h indicates tests for specimens pre-charged in 0.1M NaOH at –1.700 $V_{Hg/HgO}$ and tested in air. I50 indicates a test carried out in the Instron UTM at an initial applied stress rate of 50 MPa s^{-1}; and similarly, L0.84 and L0.084 indicate tests carried out in the LIST at an initial applied stress rates of 0.84 MPa s^{-1} and 0.084 MPa s^{-1}, respectively.

Typical examples were (i) '980QP-0min-L0.84' indicated 980QP, tested in LIST at a stress rate of 0.84 MPa s^{-1}, corresponded to a motor speed of 300 rph with simultaneous in

situ hydrogen charging in 0.1 M NaOH until fracture, and (ii) '950TW-10min-I50' indicated that there was a 10 min time interval between the end of 24 h pre-charging in 0.1 M NaOH and the start of UTM testing for 950TW in air.

2.6. XRD

The X-ray diffraction (XRD), with Cu K_α radiation, was used to qualitatively determine the constituent phases, such as the existence of any type of martensite in 950TW steels before and after mechanical tests with or without hydrogen charging. XRD was carried out on 950TW steels that were (i) as received (uncharged and without deformation), (ii) fractured in air using LIST at 30 rph (at an applied stress rate of 0.072 MPa s^{-1}), and (iii) fractured by testing in LIST at 30 rph (at an applied stress rate of 0.072 MPa s^{-1}) with simultaneous in situ charging at –1.700 $V_{Hg/HgO}$ in 0.1 M NaOH.

3. Results

3.1. DP in 3 wt% NaCl solution

Table 2 presents LIST results for all the DP, Q&P and TWIP steels tested in air and in 3 wt% NaCl at the free corrosion potential and at the zinc potential. For tests in air, the yield stress, σ_y, fracture stress, UTS, σ_f, and fractography were all comparable with those from our previous study [35], and with the mechanical properties provided by the steel supplier. For the tests with simulated service corrosions, DP, Q&P and TWIP steels exhibited different HE susceptibility as presented in the following sections.

For 980DP and 1200DP, the remarks in the Table 2 under the column headed fractography indicated ductile cup and cone features at all the potentials and stress rates. The values of reduction in area, R_A, for those tested at the free corrosion potential and the zinc potential in 3 wt% NaCl were comparable to their counterparts tested in air. The highest R_A of 78% was for 980DP-Ecorr-L0.054 (at the free corrosion potential and at 30 rph corresponded to an applied stress rate of 0.054 MPa s^{-1}), which was essentially the same as that tested in air. The lowest R_A was 72%, for 980DP-Ezn-L0.0054 tested at the zinc potential at 3 rph (at an applied stress rate of 0.0054 MPa s^{-1}), giving a hydrogen embrittlement index, E_I, of 9%, whilst 1200DP tested at the same conditions exhibited a 11% E_I. The values of fracture stress, UTS, σ_f, and yield stress, σ_y, were similar for tests in solution and in air. The fractography indicated no subcritical crack growth, so that the quantity measured by the change in potential drop slope was the yield stress, in all cases.

Table 2 Results from LIST experiments in air and in a 3 wt% NaCl solution. σ_{th}, apparent threshold stress. σ_y, yield stress. σ_f , fracture stress, UTS. R_A, reduction in area. E_I, hydrogen embrittlement index. E_{corr}, free corrosion potential. The fractography indicated no subcritical crack growth, so that the quantity measured by the change in potential drop slope was the yield stress. The specimen designation is as follows: "steel designation"-"Environment designation"-"test speed". The steel designation was as in Table 1. The environment designations were as follows: A = test in air; Ecorr = test in 3 wt% NaCl solution at the free corrosion potential, and Ezn = test in 3 wt% NaCl solution at the Zn potential.

Specimen designation	Environment	Potential ($V_{Ag/AgCl}$)	Applied stress rate (MPa s^{-1})	σ_y ±5 (MPa)	σ_f ±2 (MPa)	R_A (%)	E_I (%)	Fractography
980DP-A-L0.054	Air	n/a	0.054	603	949	79		cup and cone, necking
980DP-A-L0.0054	Air	n/a	0.0054	592	975	78		cup and cone, necking
980DP-Ecorr-L0.054	S (NaCl)	E_{corr}	0.054	594	950	78	1	cup and cone, necking
980DP-Ecorr-L0.0054	S (NaCl)	E_{corr}	0.0054	591	934	75	5	cup and cone, necking
980DP-Ezn-L0.054	S (NaCl)	-0.950	0.054	591	961	73	8	cup and cone, necking
980DP-Ezn-L0.0054	S (NaCl)	-0.950	0.0054	589	962	72	9	cup and cone, necking
1200DP-A- L0.0072	Air	n/a	0.0072	880	1150	70		cup and cone, necking
1200DP -Ezn-L0.0072	S (NaCl)	-0.950	0.0072	866	1159	62	11	cup and cone, necking
980DP-650YS-A- L0.0100	Air	n/a	0.0100	655	1073	63		cup and cone, necking
980DP-650YS-Ezn-L0.0100	S (NaCl)	-0.950	0.0100	632	1054	28	56	similar to cup and cone, necking present
980DP-700YS-A- L0.0107	Air	n/a	0.0107	680	1003	62		cup and cone, necking
980DP-700YS-Ezn-L0.0107	S (NaCl)	-0.950	0.0107	651	980	30	52	similar to cup and cone, necking present
980QP-A-L0.084	Air	n/a	0.084	677	1025	63		cup and cone, necking
980QP-A-L0.0084	Air	n/a	0.0084	687	1029	63		cup and cone, necking
980QP-Ecorr-L0.084	S (NaCl)	E_{corr}	0.084	617	984	28	56	shearing, necking present
980QP-Ecorr-L0.0084	S (NaCl)	E_{corr}	0.0084	616	976	27	57	shearing, necking present
980QP-Ezn-L0.084	S (NaCl)	-0.950	0.084	618	1002	23	63	shearing, necking present
980QP-Ezn-L0.0084	S (NaCl)	-0.950	0.0084	602	957	17	73	shearing, necking present
950TW-A-L0.72	Air	n/a	0.72	513	1023	65		cup and cone, necking
950TW-A-L0.072	Air	n/a	0.072	479	1012	59	10	shearing, necking
950TW-A-L0.0072	Air	n/a	0.0072	478	1015	56	14	shearing, necking
950TW-Ecorr-L0.072	S (NaCl)	E_{corr}	0.072	461	937	54	17	shearing, necking visible
950TW-Ecorr-L0.0072	S (NaCl)	E_{corr}	0.0072	466	946	51	21	shearing, necking visible
950TW- Ezn-L0.072	S (NaCl)	-0.950	0.072	460	982	53	18	shearing, necking visible
950TW- Ezn-L0.0072	S (NaCl)	-0.950	0.0072	460	991	49	25	shearing, necking visible

980DP-650YS and 980DP-700YS, on the other hand, showed a significant decrease in the R_A when tested at zinc potential and at 3 rph (at applied stress rates of 0.0100 MPa s^{-1} and 0.0107 MPa s^{-1}). The respective R_A value for 980DP-650YS and 980DP-700YS was 28% and 30%. These values were close to each other and resulted in corresponded hydrogen embrittlement index values, E_I, of 56% and 52%, which indicated some hydrogen influence on these two DP steels. Moreover, the values of σ_f and σ_y slightly decreased by 4% and 2%, respectively, compared with those in air.

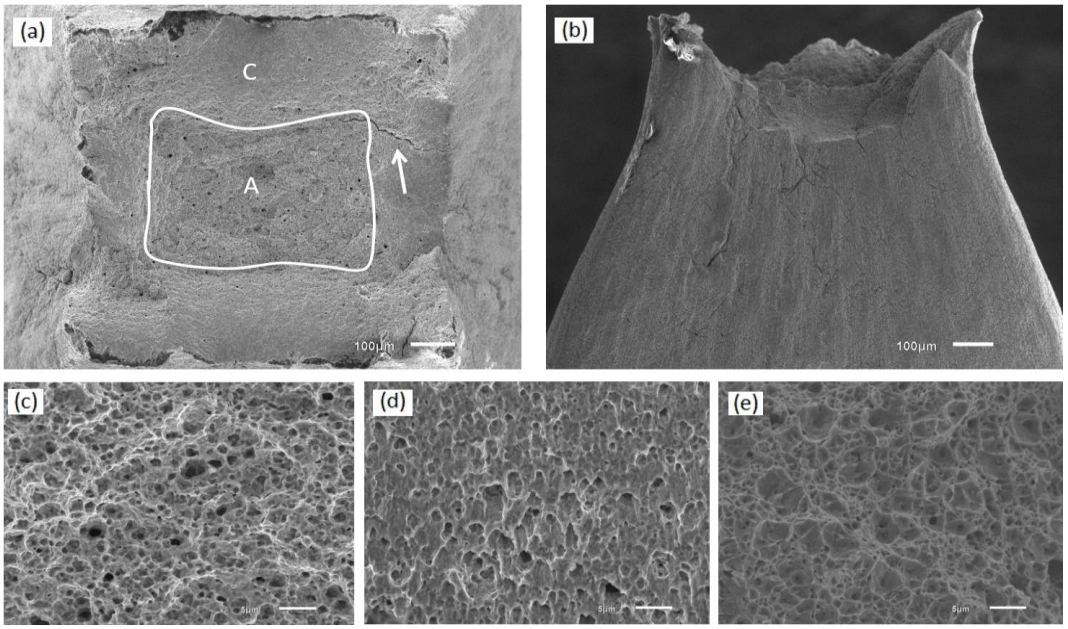

Fig. 3. Micrographs of 980DP-Ecorr-L0.0054 showing typical cup and cone features for 980DP tested in 3% NaCl: (a) the top view, (b) the transverse side view, (c) the centre dimples in region A, and (d) surrounding shear dimples in region C. For comparison, (e) presents the centre dimples for 980DP-A-L0.0054.

Fig. 3 presents the fracture surface of 980DP-Ecorr-L0.0054. Figs. 3(a) and (b) indicate a typical cup and cone fracture mode, with ductile necking. There was a secondary crack in the shear lip region among the shear dimples on the fracture surface, as pointed out by an arrow in Fig. 3(a). Such secondary cracks occasionally occurred for 980DP and 1200DP. There were no horizontal surface cracks in the necked region or in the part away from the necked region, as shown in Fig. 3(b). The cup and cone fracture contained (i) a centre cone part A and (ii) its adjacent shear lip regions C. Figs. 3(c) and (d) demonstrate the magnified views of the centre cone part and the surrounding shear lips, respectively. Due to micro-void coalescence (MVC), there were dimples in both of the centre cone part and the surrounding shear lip regions. The dimples were round in the centre cone part, indicating ductile fracture, whilst those in the surrounding shear lips were parabolic, attributed to shearing during final fracture. Such cup and cone fracture was obtained for 980DP and 1200 DP tested at all the potentials and stress rates, and was similar to that in air. The dimple

details, in the centre cone part and in the shear lips for 980DP and 1200DP steels were similar for tests under corrosion conditions and in air. For example, Figs. 3(c) and (e) compare the micro-void coalescence dimples in the centre region for 980DP-Ecorr-L0.0054 and 980DP-A-L0.0054. The dimples for 980DP-Ecorr-L0.0054, as in Fig. 3(c), were round and were essentially similar to those for 980DP-A-L0.0054 in Fig. 3(e).

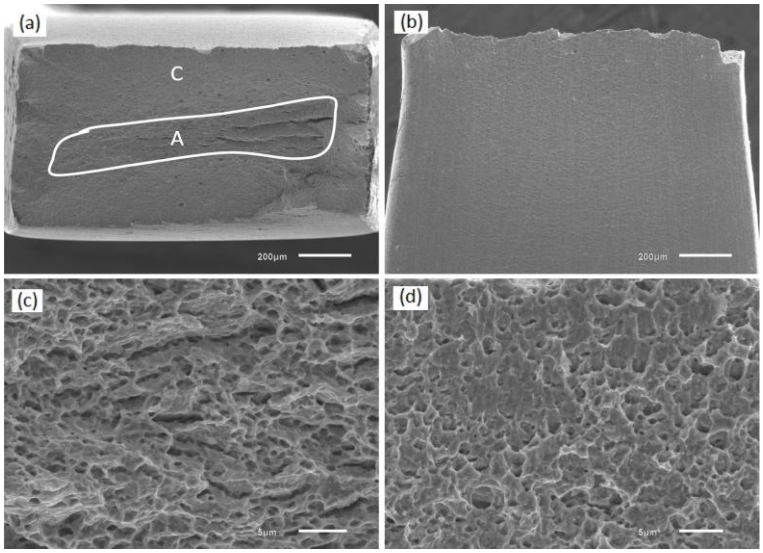

Fig. 4. SEM images of 980DP-650YS-Ezn-L0.0100 showing cup-cone like features: (a) the top view, (b) the transverse side view, (c) the centre dimples in region A and (d) the surrounding shear dimples in region C.

Fig. 4 shows SEM images of the fractured specimen 980DP-650YS-Ezn-L0.0100 tested at the zinc potential at 3 rph (at an applied stress rate of 0.0100 MPa s^{-1}). Fig. 4(a) and (b) indicate a fracture mode similar to the ductile cup and cone fracture, supported by (i) the centre region A, (ii) the surrounding shearing lips C and (iii) the ductile necking as shown in Fig. 4(b). Fig. 4(c) and (d) show the magnified image of centre region A and its surrounding region C, respectively. The centre dimples were shallow, making the features seem to be flat. There were also many of small secondary cracks in this region. 980DP-700YS also produced a similar change in dimple features.

3.2. QP in 3 wt% NaCl solution

Table 2 also presents the LIST results for 980QP. The values of reduction in area, R_A, for 980QP tested in 3 wt% NaCl, were significantly lower than their counterparts tested in air. For 980QP-Ecorr-L0.084, R_A was 28%, resulting in an E_I value of 56%, which indicated significant hydrogen influence. A lower stress rate and the charging potential changed to the zinc potential, caused a further decrease in the value of R_A and concomitantly the E_I value increased. The severest situation occurred for 980QP-Ezn-L0.0084 (tested at the zinc potential and at 3 rph corresponded to an applied stress rate of 0.0084 MPa s^{-1}), which

exhibited an R_A of 17% and an E_I of 73%. The values of fracture stress, UTS, σ_f, and yield stress, σ_y, for tests in solution also slightly decreased, compared with those in air. The highest extent of the decrease in σ_f and σ_y was 7% and 10%, respectively, and was for 980QP-Ezn-L0.0084, which showed the highest hydrogen embrittlement index, E_I. As for 980DP, the fractography for 980QP indicated no subcritical crack growth, so that the quantity measured by the change in potential drop slope was the yield stress, in all cases.

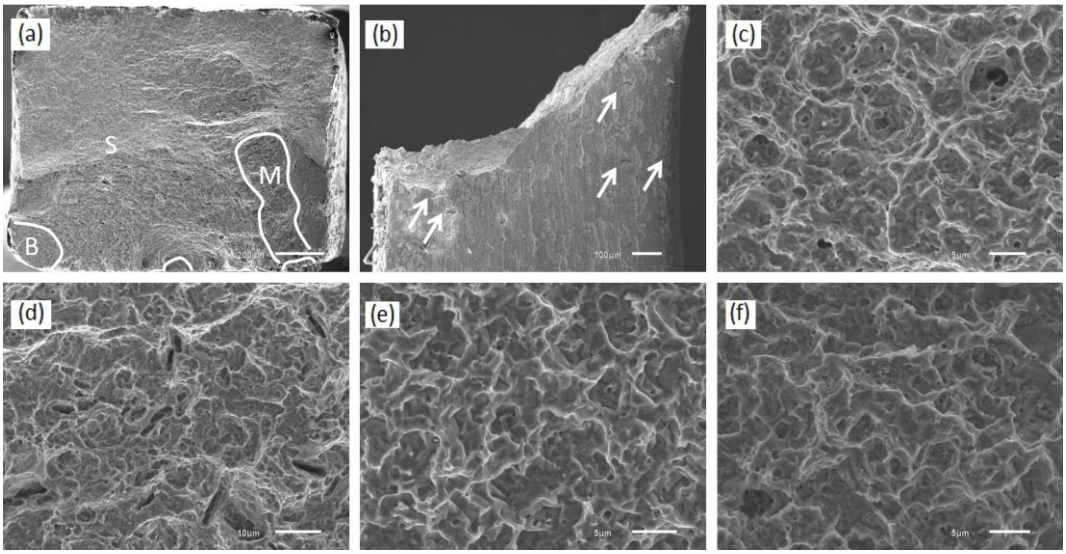

Fig. 5. SEM images of 980QP-Ecorr-L0.084 showing shear fracture surface: (a) the top view, (b) the transverse side view, (c) the dimple features in region S, (d) the mixed features in region M, and (e) the brittle features in region B. For comparison, (f) presents the brittle features for 980QP-Ezn-L0.0084.

Fig. 5 shows the fracture surface features of 980QP-Ecorr-L0.084 as an example of all the 980QP tested in solution. Figs. 5(a) and (b) present the top and transverse side view of the specimen, respectively. The top view in Fig. 5(a) indicates three distinctive regions: (i) region S with shear dimples, (ii) region M with mixed features, and (iii) brittle region B near the surface. The fracture initiated from the edge, forming a brittle region B, propagated to form a region M, and then grew in a shear manner until rupture. The side view in Fig. 5(b) indicates a typical shear fracture and obvious necking. The relatively flat surface edge from the transverse side corresponded to brittle region B. There were also some small horizontal surface cracks near the flat edge of the fracture surface and near the necking on the transverse side, as pointed by the arrows in Fig. 5(b). Figs. 5(c), (d) and (e) show the magnified features in regions S, M and B, respectively. The dimples in Fig. 5(c) were quite shallow. The mixed features in Fig. 5(d) contained dispersed small secondary cracks, flat areas and shallow dimples similar to those in Fig. 5(c). The brittle features in Fig. 5(e) were transgranular quasi-cleavage. There were similar features for 980QP tested at all the potentials and stress rates. The details of the brittle features in Figs. 5(e) for 980QP-Ecorr-L0.0084 were essentially the

same as in Fig. 5(f) for 980QP-Ezn-L0.0084. However, there was a slight increase in the area of the brittle regions, especially the mixed region M, which correlated with the increase in the hydrogen embrittlement index, E_I.

3.3. TWIP in 3 wt% NaCl solution

Table 2 also documents the LIST results for 950TW. For tests in air at 30 (at an applied stress rate of 0.072 MPa s^{-1}) and 3 rph (at an applied stress rate of 0.0072 MPa s^{-1}), 950TW experienced some influence of hydrogen, manifested by (i) a small decreases in σ_f, σ_y and R_A, and (ii) shear fracture as indicated by the remarks under the heading fractography, compared with those tested in air at 300 rph (at an applied stress rate of 0.72 MPa s^{-1}), which fractured in a ductile manner, similar to the cup and cone mode. This HE was consistent with our previous research [35], where there was no influence of hydrogen at 300 rph in air and some hydrogen influence at 30 and 3 rph in air, attributed to a combined effect of the slower stress rate and some residual hydrogen. Thus, here in this work, the values of σ_f, σ_y and R_A for the hydrogen-immune 950TW-A-L0.72 were adopted as references to evaluate the HE of 950TW tested under other conditions, thereby giving a respective hydrogen embrittlement index value of 10% and 14% for 950TW-A-L0.072 and 950TW-A-L0.0072. For 950TW tested in 3 wt% NaCl, the values of σ_f, σ_y and R_A decreased slightly further, and the hydrogen embrittlement index, E_I, increased concomitantly. The highest E_I of 25% was for 950TW-Ezn-L0.0072, increased from 14% for 950TW-A-L0.0072.

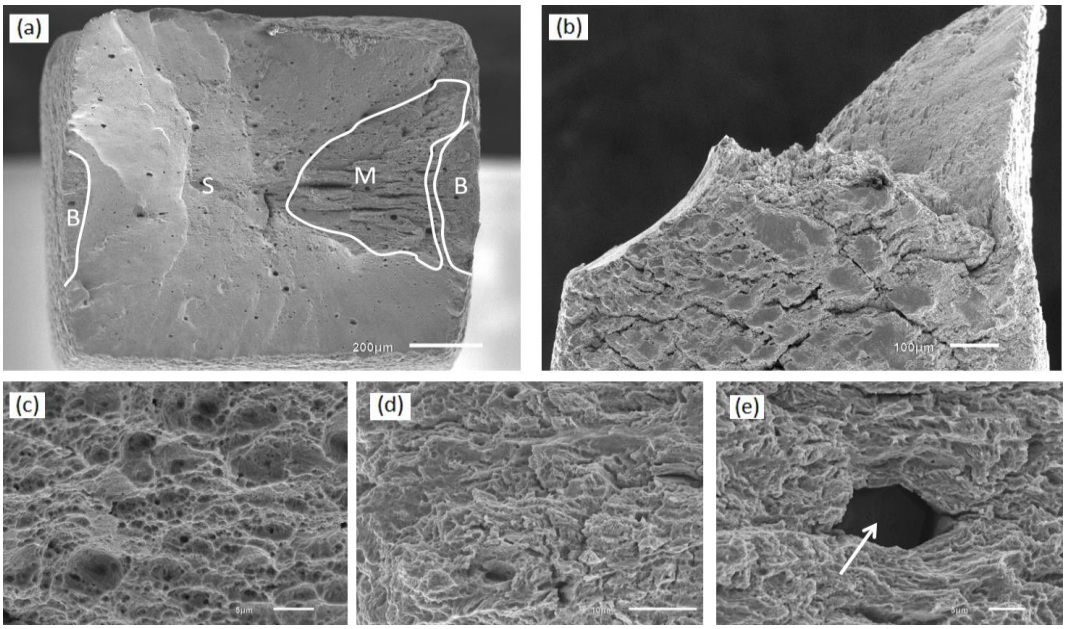

Fig. 6. Fractographic images of 950TW-Ecorr-L0.072 showing typical shear fracture surface: (a) the top view, (b) the transverse side view, (c) shear dimples in region S, (d) brittle features and (e) an inclusion in region B.

Fig. 6 shows typical fracture surface for specimen 950TW-Ecorr-L0.072 tested in 3 wt% NaCl. Fig. 6(a) indicates three regions of the fracture surface, (i) region S with shear dimples, (ii) region M with mixed features of shear dimples and small brittle areas, and (iii) brittle regions B with transgranular quasi-cleavage features. The fracture initiated from both of the short transverse surfaces, grew towards each other in a shear manner until final rupture. Fig. 6(b) presents the transverse side view of 950TW-Ecorr-L0.0072. There was clear shearing and necking, together with some horizontal surface cracks in the necked region. Figs. 6(c) and (d) show the magnified view of the shear dimples in regions S and transgranular quasi-cleavage features in region B. AlN inclusions were also occasionally among the brittle features in region B, such as the one indicated by an arrow in Fig. 6(e). These regions and feature details were essentially similar to those in 950TW in our previous study [35]. Among the testing conditions in this work, there was essentially no significant change in the area of brittle regions for 950TW.

3.4. Faster loading with hydrogen charging

Table 3 presents the data for 980DP, 980QP and 950TW tested at the stated applied stress rates using LIST and a universal tensile machine (UTM), in air and with simultaneous in situ hydrogen charging at –1.700 $V_{Hg/HgO}$ in a 0.1 M NaOH solution (0 time interval). The aim of these experiments was to study the hydrogen influence at substantial loading rates.

The first three rows for each steel in Table 3 presented the results for tests in air using the universal tensile machine and using LIST at 300 and 30 rph; the values of fracture stress, σ_f, the yield stress, σ_y, and the reduction in area, R_A, for uncharged 980DP, 980QP and 950TW were similar at each applied stress rate, except for 950TW-A-L0.072, which showed some hydrogen influence and some decrease in mechanical properties, attributed to the residual hydrogen and the slower stress rate, as mentioned above in section 3.3. The comparable results of the mechanical properties measured using LIST and UTM tests, indicated that the LIST machine was well calibrated and was able to provide accurate results.

The rows four to six present the results for the tests with simultaneous in situ hydrogen charging at –1.700 $V_{Hg/HgO}$ in the 0.1 M NaOH solution; all the steels, 980DP, 980QP and 950TW were subjected to some hydrogen influence and all showed some decrease in mechanical properties.

Table 3 shows that both 980DP-0min-I50 and 980DP-0min-L0.54 exhibited a hydrogen embrittlement index (E_I) of 34%, indicating similar hydrogen influence on these two specimens, whereas 980DP-0min-L0.054 experienced an increased E_I of 51%, and a

decrease in σ_f and σ_y by 2% and 10%, respectively. Fig. 7 presents the fracture surface of 980DP-0min-I50, which was a typical shear fracture. The top view in Fig. 7(a) indicated some small brittle regions B along the edges of the specimen surface. The rest of the surface, region S, possessed mainly shear dimples with some fisheyes randomly dispersed. Fig. 7(b) shows the transverse side view. There was clear shearing and necking. There were also some surface cracks parallel or at 45 degree to the rolling direction, in the necked region. Examinations of the brittle features revealed transverse quasi-cleavage features, as presented in Fig. 7(c). Figs. 7(d) and (e) show two typical types of fisheyes found in region S. The fisheye was initiated from an elongated hole or a TiN inclusion, and then radiated from this centre core to a diameter of about 20 μm. 980DP-0min-L0.54 and 980DP-0min-L0.054 presented similar fracture features, consisting of brittle regions B near the edges and shear region S on the remaining part of the surface, as shown in Figs. 8(a) and (b). There was a slight increase in the area of region B for 980DP-0min-L0.054, compared with 980DP-0min-L0.54. The transverse side view of 980DP-0min-L0.054, shown in Fig. 8(c), also indicated shearing, necking and surface cracks. 980DP-0min-L0.54 and 980DP-0min-L0.054 also contained transverse quasi-cleavage brittle features, as exampled in Fig. 8(d), and these features were essentially similar to those for 980DP-0min-I50, as compared with Fig. 7(c).

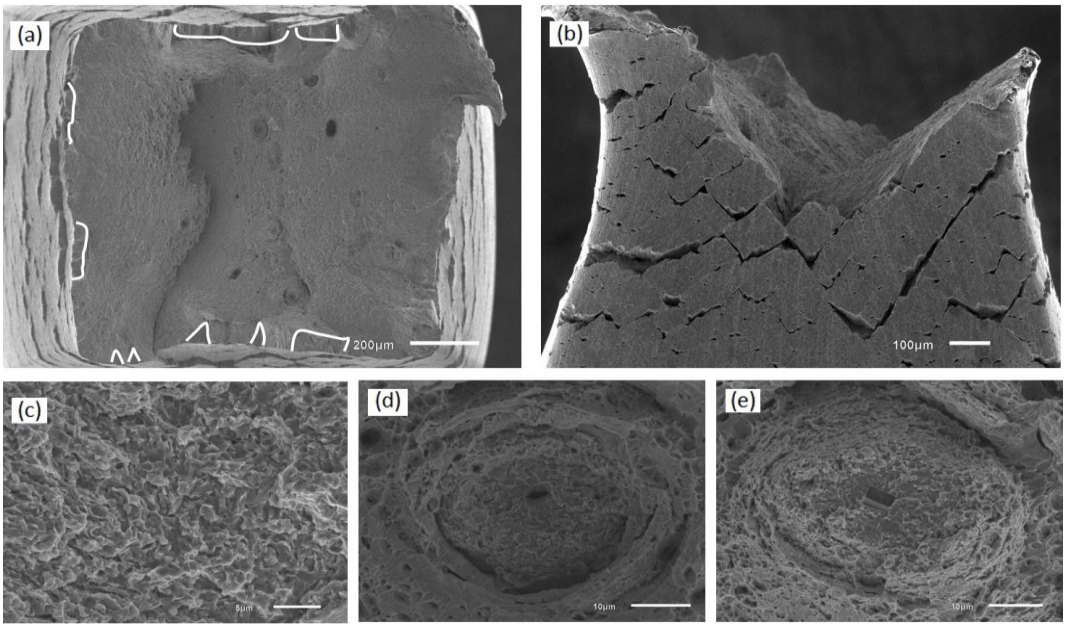

Fig. 7. SEM images of 980DP-0min-I50 showing shear fracture: (a) the top view, (b) the transverse side view, (c) brittle features in region B, and typical fisheyes initiated from (d) an elongated hole and from (e) a TiN inclusion.

Table 3 Results for 980DP, 980QP and 950TW tested using LIST and UTM for various conditions of hydrogen precharging and testing. σ_{th}, apparent threshold stress. σ_y, yield stress. σ_f , fracture stress, UTS. R_A, reduction in area. E_I, hydrogen embrittlement index. The fractography indicated no subcritical crack growth, so that the quantity measured by the change in potential drop slope was the yield stress.
The pre-charging condition was specified as "S (NaOH)" for specimens precharged in 0.1M NaOH at -1.700 $V_{Ag/AgCl}$; the testing condition was specified as "S (NaOH)" for specimens charged during testing in 0.1M NaOH at -1.700 $V_{Ag/AgCl}$; the testing condition was specified as "air" for tests in air; and the designation "Air, air" indicates test with no pre-charging and testing in air.
The specimen designation is as follows: "steel designation"-"Environment designation"-"test speed. The steel designation was as in Table 1. The environment designations were as follows: A = test in air; 0min indicates tests for specimens pre-charged in 0.1M NaOH at -1.700 $V_{Ag/AgCl}$ and charged during testing in 0.1M NaOH at -1.700 $V_{Ag/AgCl}$; and 10min and 24 h indicates tests for specimens pre-charged in 0.1M NaOH at -1.700 $V_{Ag/AgCl}$ and tested in air. I50 indicates a test carried out in the Instron UTM at an initial applied stress rate of 50 MPa s^{-1}; and L0.54 and L0.054 indicate tests carried out in the LIST at an initial applied stress rates of 0.054 MPa s^{-1} and 0.054 MPa s^{-1}, respectively.

Specimen designation	Pre-charging condition, testing condition	Potential ($V_{Ag/AgCl}$)	Applied stress rate (MPa s^{-1})	σ_y ±5 (MPa)	σ_f ±2 (MPa)	R_A (%)	E_I (%)	Fractography
980DP-A-I50	Air, air	n/a	50	627	994	78		cup and cone, necking
980DP-A-L0.54	Air, air	n/a	0.54	605	988	79		cup and cone, necking
980DP-A-L0.054	Air, air	n/a	0.054	603	949	79		cup and cone, necking
980DP-0min-I50	S (NaOH), S (NaOH)	-1.700	50	573	1007	52	34	shearing, necking
980DP-0min-L0.54	S (NaOH), S (NaOH)	-1.700	0.54	554	967	52	34	shearing, necking
980DP-0min-L0.054	S (NaOH), S (NaOH)	-1.700	0.054	540	932	39	51	shearing, necking
980DP-10min-I50	S (NaOH), air	-1.700	50	623	987	74	6	cup and cone, necking
980DP-10min-L0.54	S (NaOH), air	-1.700	0.54	591	987	76	4	cup and cone, necking
980DP-10min-L0.054	S (NaOH), air	-1.700	0.054	583	934	76	4	cup and cone, necking
980DP-24h-I50	S (NaOH), air	-1.700	50	628	996	77	2	cup and cone, necking
980DP-24h-L0.54	S (NaOH), air	-1.700	0.54	583	970	79	0	cup and cone, necking
980DP-24h-L0.054	S (NaOH), air	-1.700	0.054	587	932	78	1	cup and cone, necking
980QP-A-I50	Air, air	n/a	50	698	1090	62		cup and cone, necking
980QP-A-L0.84	Air, air	n/a	0.84	683	1074	62		cup and cone, necking
980QP-A-L0.084	Air, air	n/a	0.084	677	1025	63		cup and cone, necking
980QP-0min-I50	S (NaOH), S (NaOH)	-1.700	50	644	1075	30	52	shearing, necking
980QP-0min-L0.84	S (NaOH), S (NaOH)	-1.700	0.84	635	1053	32	49	shearing, necking
980QP-0min-L0.084	S (NaOH), S (NaOH)	-1.700	0.084	620	933	13	79	shearing, necking
980QP-10min-I50	S (NaOH), air	-1.700	50	659	1093	39	38	shearing, necking
980QP-10min-L0.84	S (NaOH), air	-1.700	0.54	652	1046	42	33	shearing, necking
980QP-10min-L0.084	S (NaOH), air	-1.700	0.054	662	1006	56	11	cup and cone, necking
980QP-24h-I50	S (NaOH), air	-1.700	50	674	1084	52	17	shearing, necking
980QP-24h-L0.84	S (NaOH), air	-1.700	0.54	661	1038	58	8	cup and cone, necking
980QP-24h-L0.084	S (NaOH), air	-1.700	0.054	673	1003	61	3	cup and cone, necking
950TW-A-I50	Air, air	n/a	50	530	1041	63		cup and cone, necking

950TW-A-L0.72	Air, air	n/a	0.72	513	1023	65		cup and cone, necking
950TW-A-L0.072	Air, air	n/a	0.072	479	1012	59	10	shearing, necking
950TW -0min-I50	S (NaOH), S (NaOH)	-1.700	50	493	1010	42	35	shearing, necking
950TW -0min-L0.72	S (NaOH), S (NaOH)	-1.700	0.72	474	952	43	34	shearing, necking
950TW -0min-L0.072	S (NaOH), S (NaOH)	-1.700	0.072	457	955	39	40	shearing, necking
950TW-10min- I50	S (NaOH), air	-1.700	50	524	1037	59	9	shearing, necking
950TW-10min- L0.72	S (NaOH), air	-1.700	0.72	493	996	62	5	shearing, necking
950TW-10min-L0.072	S (NaOH), air	-1.700	0.072	467	972	58	11	shearing, necking
950TW-24h- I50	S (NaOH), air	-1.700	50	526	1061	53	18	shearing, necking
950TW-24h- L0.72	S (NaOH), air	-1.700	0.72	489	991	58	11	shearing, necking
950TW-24h- L0.072	S (NaOH), air	-1.700	0.072	466	966	57	12	shearing, necking

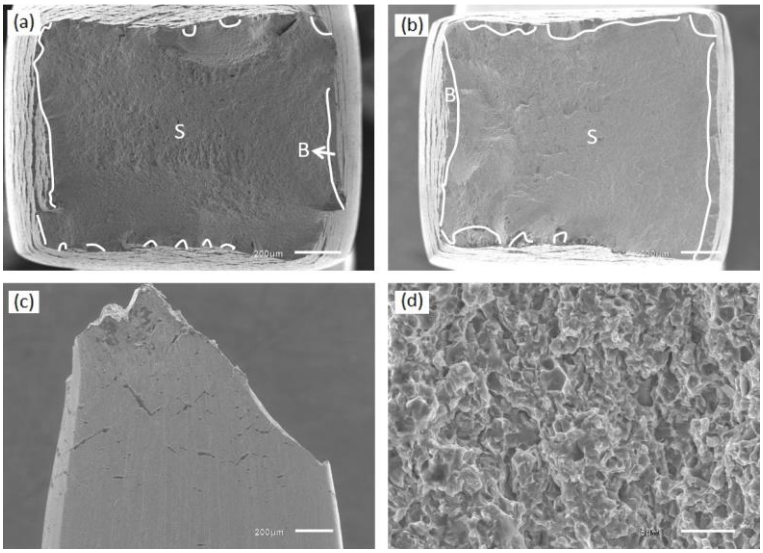

Fig. 8. Fracture surface images showing (a) top views of 980DP-0min-L0.54 and (b) 980DP-0min-L0.054, (c) transverse side view of 980DP-1.7-L0.054, and the (d) magnified brittle features of region B in (b).

Table 3 shows that the E_I values for 980QP-0min-I50, 980QP-0min-L0.84 and 980QP-0min-L0.084 were 52%, 49% and 79%, respectively. The mechanical properties were also decreased compared with their counterparts in air. For example, for 980QP-0min-I50, σ_f and σ_y decreased by 2% and 8%, respectively. Examinations of the fractured surfaces also illustrated (i) region S with shear dimples, (ii) region M with mixed features of shear dimples and small brittle facets, and (iii) brittle region B, as illustrated in Figs. 9(a) and (d). There were fisheyes occasionally in the mixed and brittle regions for 980QP-0min-L0.84 and 980QP-0min-L0.084, such as the one marked in the white circle in Fig. 9(d). There was also shearing, necking and surface cracks as evident from the transverse side view in Figs. 9(b) and (e). All the three specimens possessed similar transgranular quasi-cleavage brittle features, as was evidenced by comparison of Figs. 9(c) and (f).

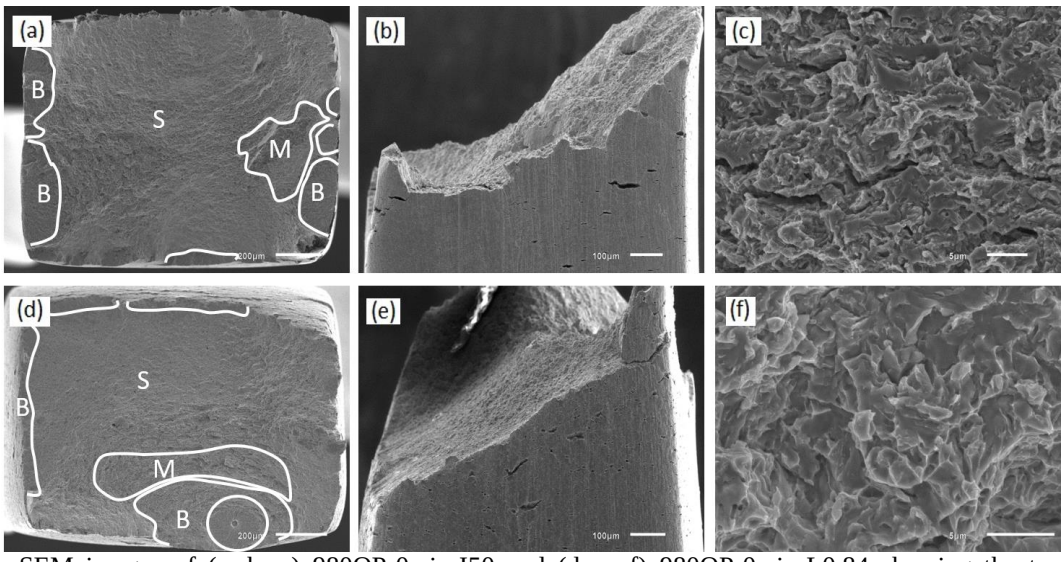

Fig. 9. SEM images of (a, b, c) 980QP-0min-I50 and (d, e, f) 980QP-0min-L0.84 showing the top view, transverse side view and details of brittle features.

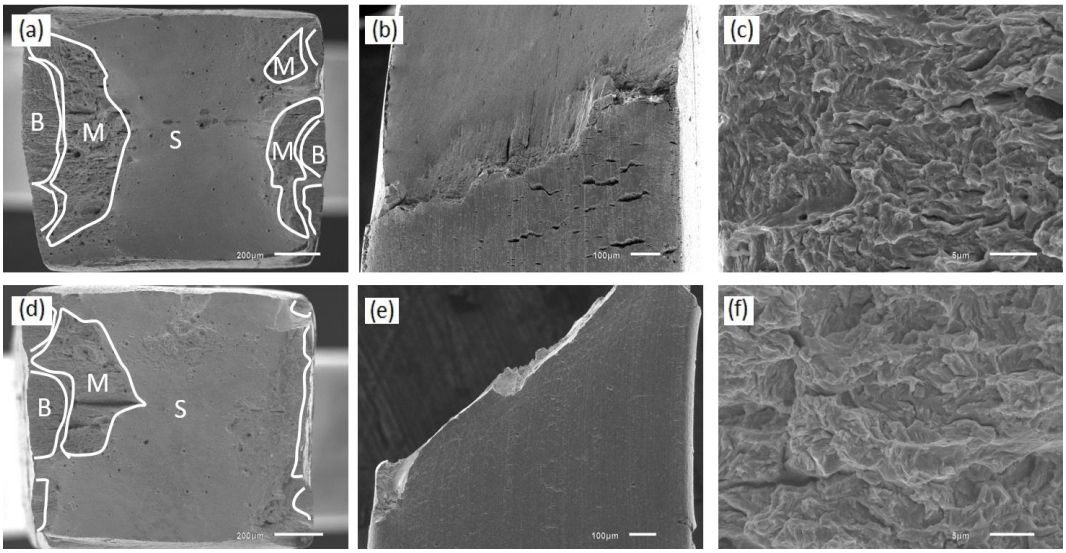

Fig. 10. SEM images of (a, b, c) 950TW-0min-I50 and (d, e, f) 950TW-0min-L0.72 showing the top view, transverse side view and details of brittle features of the fracture surface.

Table 3 also indicates that 950TW steels showed an increased hydrogen influence when tested in 0.1 M NaOH using LIST and UTM, manifested by an increased E_I and decreased σ_f and σ_y. For example, the E_I value for 950TW-0min-I50 was 35%, whilst σ_f and σ_y decreased by 3% and 5%, respectively. The extent of such changes slightly increased for 950TW-0min-L0.072, resulting in a 40% E_I. Fractography observations in Fig. 10 also indicated that the fracture features were similar for all steels tested in LIST and UTM, and were similar to those under simulated corrosion (e.g. compared with Fig. 6) and under cathodic charging in our previous study [35]. There were three distinctive regions, as shown in Figs. 10(a) and (d), revealing the same manner of fracturing as from the edges of both transverse sides towards the inner part of specimen. Figs. 10(b) and (e) also present the shearing mode viewed from the transverse side, accompanied by some necking and surface horizontal cracks. Figs. 10(c) and (f) show similar details of quasi-cleavage brittle features.

3.5. Time intervals

The last six rows for each steel in Table 3 present the values of the fracture stress, σ_f, the yield stress, σ_y, reduction in area, R_A, and hydrogen embrittlement index, E_I, for 980DP, 980QP and 950TW with time intervals of 10 min and 24 h between the end of hydrogen pre-charging and the start of testing using UTM and LIST in air. Fig. 11 presents the values of R_A for the different testing conditions.

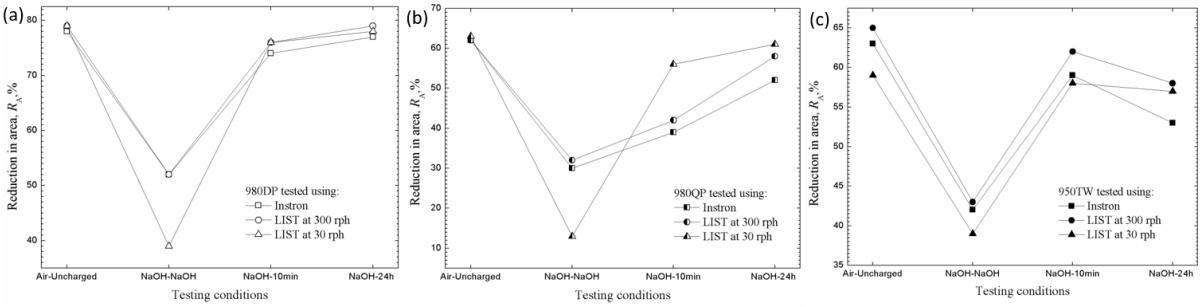

Fig.11. Plots showing the reduction in area, R_A, for the different testing conditions using theInstron and LIST for (a) 980DP, (b) 980QP and (c) 950TW. 'Air-Uncharged' refers to uncharged specimens tested in air. 'NaOH-NaOH' indicates 24 h pre-charging in NaOH and continued hydrogen charging during testing until fracture. 'NaOH-10min' and 'NaOH-24h' present respectively a time interval of 10 min and 24 h between the end of 24 h pre-charging in NaOH and the start of testing in air.

Table 3 and Fig. 11 indicate that for 980DP steel, the values of σ_f, σ_y, and R_A were all close to their uncharged counterparts tested in air for the tests with time intervals of 10 min and 24 h between the end of hydrogen pre-charging and the start of testing using UTM and LIST, e.g. compare 980DP-10min-L0.54 with 980DP-A-L0.54. Concomitantly, the values for hydrogen embrittlement index, E_I, were all small, with the highest one of 6% for 980DP-10min-I50. Examinations of the fracture surface for all the steels with different time intervals indicated cup and cone fracture mode, similar to that for the uncharged fractures. For example, Fig. 12 compares the fractured features of 980DP-10min-I50 and 980DP-A-I50. For both cases, there were distinctive cup and cone features, accompanied by extensive necking, as shown in Figs. 12(a) and (d). Moreover, Figs. 12(b) and (e), 12(c) and (f), indicate no discernible difference of the centre dimples and shear dimples for these two specimens. However, there was a fisheye in the fracture surface of 980DP-10min-I50, contributing to the highest E_I of 6%. There was no such a fisheye in the other 980DP specimens.

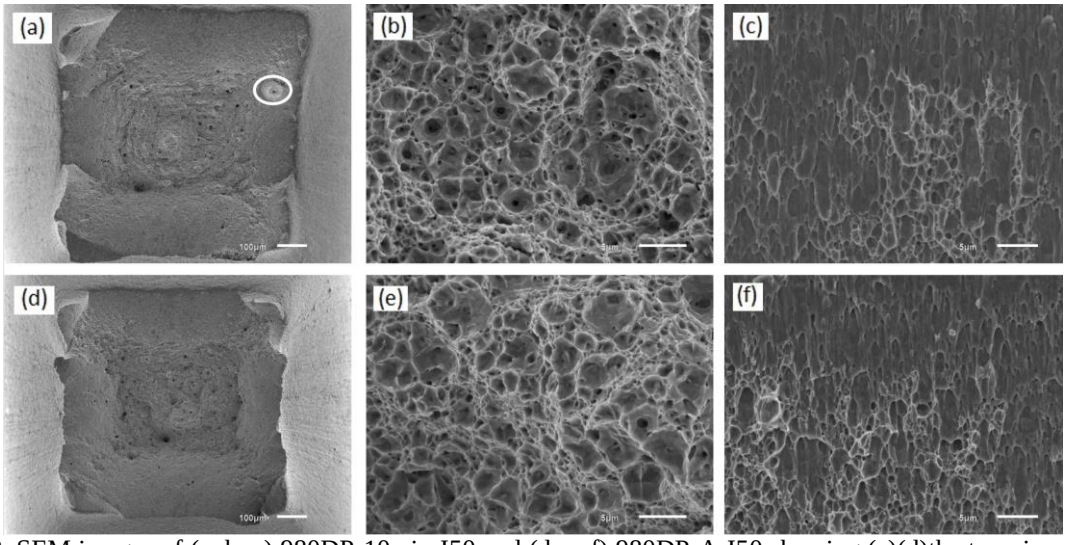

Fig.12. SEM images of (a, b, c) 980DP-10min-I50 and (d, e, f) 980DP-A-I50 showing (a)(d)the top view, (b)(e) details of the dimples in the centre and (c)(f)in the surrounding shear lips.

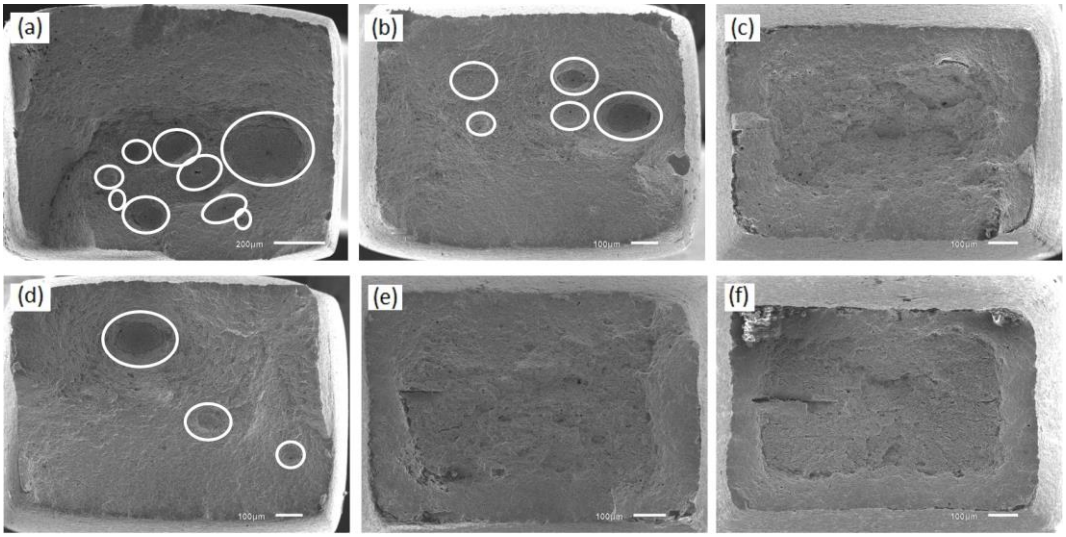

Fig.13. SEM images comparing the fracture surface of (a) 980QP-10min-I50, (b) 980QP-10min-L0.84, (c) 980QP-10min-L0.084 (d) 980QP-24h-I50 (e) 980QP-24h-L0.84 and (f) 980QP-24h-L0.084.

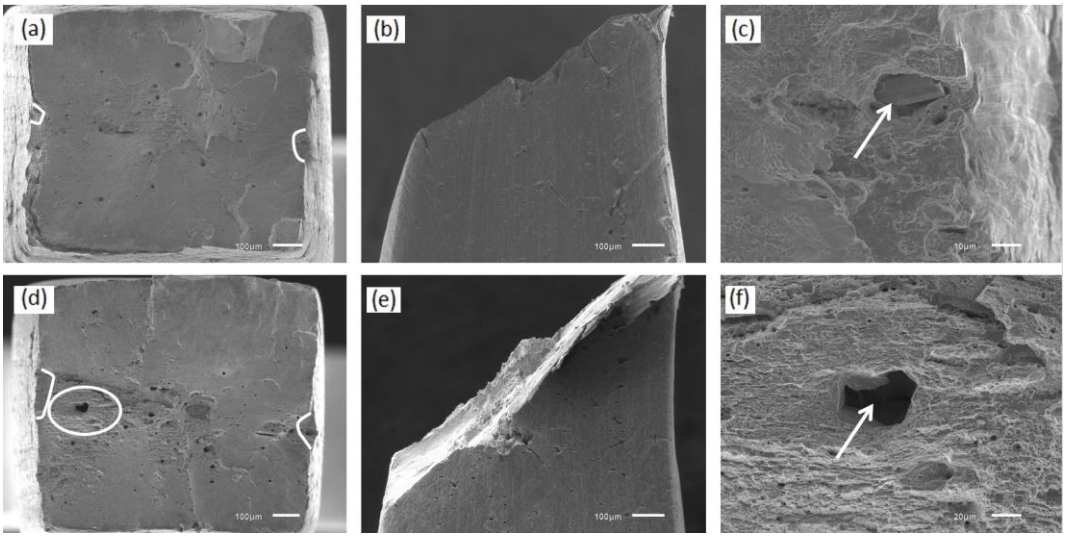

Fig.14. SEM images of (a, b, c) 950TW-10min-L0.72 and (d, e, f) 950TW-24h-I50 showing the top view, transverse side view and details of brittle features of the fracture surface.

980QP exhibited various fracture behaviours depending on the stress rate and time interval. This was different to 980DP, which displayed ductile cup and cone fracture under all the testing conditions. Table 3 and Fig. 11, indicated that the mechanical properties of 980QP-10min-L0.084, 980QP-24h-L0.84, and 980QP-24h-L0.084 recovered to similar values to those uncharged in air, whereas the values for the other specimens (980QP-10min-I50, 980QP-10min-L0.84, and 980QP-24h-I50) were still lower than their uncharged counterparts. The R_A value for steels tested with both 10 min and 24 h time intervals increased in following order: 980QP-10min (24 h)-I50, 980QP-10min (24 h)-L0.84 and 980QP-10min (24 h)-L0.084, leading to E_I decreasing accordingly. For instance, the R_A value was 39%, 42% and 56% for 980QP-10min-I50, 980QP-10min-L0.84 and 980QP-10min-L0.084, respectively. Moreover, Fig. 11 also illustrates that the degree of R_A recovery

increased as the time interval extended from 10 min to 24 h, resulting in the highest R_A of 61% for 980QP-24h-L0.084. Correspondingly, the fracture surface features presented two distinctive modes: (i) cup and cone fracture and (ii) shear fracture, as shown in Fig. 13. There was cup and cone fracture for 980QP-10min-L0.084, 980QP-24h-L0.84, and 980QP-24h-L0.084, as shown in Figs. 13(c) (e) and (f), respectively. This cup and cone fracture was essentially similar to that for uncharged specimens in air. The fact that there was cup and cone fracture for these three specimens was consistent with that they exhibited higher values of strengths and reduction in area, indicating that hydrogen influence on these three steels was reduced further towards insignificance, as for their uncharged counterparts. This indicates that the hydrogen influence was fully reversible. On the other hand, shear fracture occurred to the other three steels (980QP-10min-I50, 980QP-10min-L0.84, and 980QP-24h-I50). There were no quasi-cleavage brittle features as those in Figs. 6 and 9, yet, there were some fisheyes accompanying the shear dimples, as marked by circles in Figs. 13(a) (b) and (d). The fisheyes were mainly near the centre part of the surface. The size and amount of fisheyes increased from 980QP-24h-I50, 980QP-10min-L0.84, to 980QP-10min-I50, corresponded to the trend of mechanical property decreases and E_I increase for these steels. The centre nucleus of the fisheyes corresponded to an oval hole, an elongated hole, or brittle phases. There were no alien inclusions in the fisheyes or among the shear dimples.

Table 3 and Fig. 11 indicated that 950TW also showed a reduced hydrogen influence when subjected to LIST and UTM at all the stress rates and time intervals after pre-charging, as was evidenced by comparing the values of σ_f, σ_y, R_A and E_I. σ_f, σ_y and R_A increased and E_I thereby decreased in comparison with their counterparts for 950TW with 0 time interval (simultaneous in situ hydrogen charging). Furthermore, the decrease in hydrogen influence was somewhat slightly more significant with 10 min time interval than that with 24 h time interval, as indicated in Fig. 11. The lowest E_I was for 950TW-10min-L0.72, whereas the highest was for 950TW-24h-I50. However, the difference in σ_f, σ_y and R_A were not large. The fracture surfaces for all these specimens were also similar to each other and to that for tests with simultaneous hydrogen charging. Fig. 14 compares the fractography of 950TW-10min-L0.72 with the lowest E_I and 950TW-24h-I50 with the highest E_I. There were small brittle regions originated from two short transverse edges for both steels, as shown in Figs. 14(a) and (d). Figs. 14(b) and (e) present shear fractures accompanied by obvious necking. There were AlN inclusions in the brittle regions, e.g. in Fig. 14(c), or near the brittle region causing fisheyes, as shown in Figs. 14(d) and (f). There was no clear trend of the change in area of the brittle regions for all these specimens.

3.6. XRD analysis

950TW steels were subjected to hydrogen influence in this study and in our previous work [35], accompanied by transgranular quasi-cleavage brittle features. In order to identify microstructures associated with these brittle features, XRD analysis was conducted considering there might be some phase transformation caused by straining during the LIST and UTM tests.

XRD was carried out on (i) 950TW-AR, as received without hydrogen charging and without deformation, (ii) 950TW-A-L0.072, fractured by LIST in air at 30 rph (at an applied stress rate of 0.072 MPa s^{-1}), and (iii) 950TW-0min-L0.072, fractured by LIST at 30 rph (at an applied stress rate of 0.072 MPa s^{-1}) with simultaneous in situ hydrogen charging at – 1.700 $V_{Hg/HgO}$ in 0.1 M NaOH.

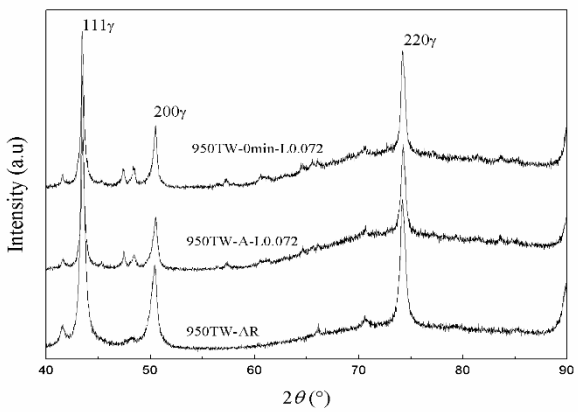

Fig.15. XRD profiles of 950TW specimens. 950TW-AR refers to specimen tested in as received condition, without hydrogen charging and straining. 950TW-A-L0.072 refers to specimen tested after fracture by LIST in air at an applied stress rate of 0.072 MPa s^{-1}. 950TW-0min-L0.072 refers to specimen tested after fracture by LIST at an applied stress rate of 0.072 MPa s^{-1} with simultaneous in situ hydrogen charging at – 1.700 $V_{Hg/HgO}$.

Fig. 15 shows the XRD profiles. The plots were separated by displacement vertically for the ease of distinction. The results were analysed based on the powder diffraction file (PDF) No. 01-074-5520. This indicated that, within the limits of detection, there was full austenite (γ-Fe). No deformation induced phase transformation, such as martensitic transformation occurred in the specimens that were undeformed and were fractured by LIST in the different environments. This absence of deformation induced phase transformation was consistent with that documented in other work [27].

4. Discussion

4.1. Tests in air

Mechanical tests were conducted on DP, Q&P and TWIP steels at The University of Queensland using UTM and LIST apparatus under various stress rates in air. Tables 2 and 3 include the results for these tests. The obtained mechanical properties were essentially similar to those presented in Table 1, which were measured and provided by the steel supplier using another tensile machine. Correspondingly, nearly all the fractured steels in this work exhibited ductile features accompanied by extensive necking. However, there were minor exceptions in this study. 950TW tested in air using LIST at stress rates corresponded to motor speeds of 30 (at an applied stress rate of 0.072 MPa s^{-1}) and 3 rph (at an applied stress rate of 0.0072 MPa s^{-1}), showed some brittle features along with significant necking, due to a combined effect of the slower stress rate and some residual hydrogen, as was elucidated in section 3 and in our previous study [35].

The DP, Q&P and TWIP steel sheets were from commercial production and it was indicated that they were the same as those supplied to the auto industry. These steels might contain some hydrogen introduced during production. For the tests in air, the steels were tested in as-received condition, without any hydrogen charging. The results that all the tested steels (excepted for 950TW-A-L0.072 and 950TW-A- L0.0072) displayed ductile fracture indicated essentially no hydrogen influence on the as-received steels. This is consistent with our previous results that there was less than 0.002 μg g^{-1} of diffusible hydrogen in the as-received DP and Q&P steels [36]. The 950TW specimens may contain a higher amount of hydrogen, introduced in during steel production, attributed to a greater hydrogen solubility in the fcc austenite [21]. A 0.7 wtppm of residual hydrogen in the as-received TWIP steels after processing was documented in other research [27]. Such residual hydrogen may be detrimental in combination with an applied stress, especially under slower stress/strain rates, which could enhance the diffusion of dislocation-carried hydrogen and thereby increase the sensitivity to hydrogen [27, 46, 47]. Moreover, the fact that there were AlN inclusions among the brittle features in 950TW (e.g. see Figs. 6 and 14) indicated that these inclusions may play a role as traps for the residual hydrogen, and further influence HE susceptibility of the steels. Inclusions associated with hydrogen embrittlement were presented in previous studies [18, 20].

4.2. LISTs in 3 wt% NaCl

4.2.1. Hydrogen concentrations

Hydrogen was absorbed by the LIST tests which were carried out using steel specimens immersed in 3 wt% NaCl at (i) the free corrosion potential, E_{corr}, and at (ii) the zinc potential, E_{Zn}. The tests at the free corrosion potential, E_{corr}, were carried out to simulate the largest amount of hydrogen absorbed during corrosion of bare steels. The tests at the zinc potential, E_{Zn}, were carried out to simulate the largest amount of hydrogen absorbed because of cathodic polarization of a galvanized steel with a zinc coating for corrosion protection. Such hydrogen charging conditions for immersion in 3 wt% NaCl solution were significantly more severe than those would occur to the auto components during actual service, and thus represent two extreme cases of service corrosion situations. Therefore, understanding the HE susceptibility of the steels under these extreme situations provides indications for steels under the milder conditions of actual service.

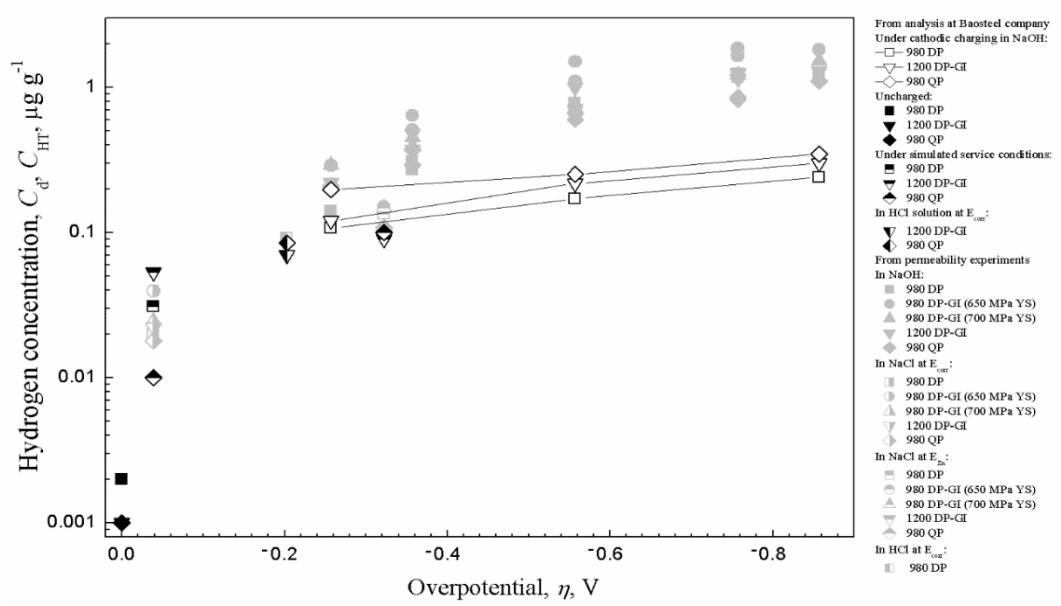

Fig. 16. The measured diffusible hydrogen concentration, C_d, using the BRUKER G4 PHOENIX DH analyser in comparison with the prior measurements of the hydrogen concentration, C_{HT}, which are represented by the grey symbols [36].

Fig. 16, from our previous research [36] under the same corrosion condition in 3 wt% NaCl showed that hydrogen was introduced in the steels by the hydrogen reduction partial reaction, even though the oxygen reduction reaction is the main cathodic partial reaction during corrosion the steel in these conditions. Cathodic polarisation at the zinc potential increased the hydrogen evolution reaction, resulting in more hydrogen introduced into the steel specimen. The amount of diffusible hydrogen for DP steels, at E_{corr} and E_{Zn} in 3 wt%

NaCl, increased in the following order: 980DP, 1200DP, 980DP-700YS, and 980DP-650YS. 980QP, at E_{corr} and E_{Zn}, possessed similar amounts of diffusible hydrogen to 980DP. For all the DP and Q&P steels, polarisation at E_{Zn} introduced more hydrogen than that at E_{corr}, at least by a factor of four. For 950TW steels, measurements of the hydrogen content under these corrosion conditions are yet to be conducted.

Our previous works [33, 35] developed a model to estimate the time needed for the hydrogen concentration inside the specimen to reach the same concentration as that at the surface, with electrochemical charging at a constant cathodic potential. This time period depends on the sample thickness and the hydrogen diffusion coefficient in the sample. This model, applied to the steels immersed in 3 wt% NaCl in this study, and based on the values of the hydrogen diffusion coefficient measured in our previous work [35], indicated that after 24 h of pre-charging at E_{Zn}, the hydrogen content at the centre of specimen reached to more than 99% of that at the specimen surface for all the DP and Q&P steels. Thus, there was essentially an uniform hydrogen concentration throughout the specimen. The same hydrogen concentration was obtained at a distance ~30 µm from the surface for a 950TW specimen after 24 h of pre-charging at E_{Zn}. At E_{corr}, the hydrogen diffusion coefficient is expected to be somewhat lower because of trapping, and thus, for the same distance inside specimen, the hydrogen concentration is expected to be somewhat lower than that at E_{Zn}. Nevertheless, this estimate shows that after 24-precharging at both E_{corr} and E_{Zn}, the hydrogen concentration (i) at the centre of all the DP and Q&P steel specimens was essentially the same as the hydrogen concentration that at the surface; and (ii) at a distance of about 30 µm inside of 950TW steels, the hydrogen content was substantial compared with that at the surface.

4.2.2. 980DP and 1200DP

Table 2 indicates that each 980DP and 1200DP specimen, subjected to LIST whilst immersed in 3wt% NaCl at both potentials, exhibited a ductile cup and cone fracture mode. The fracture initiated from the centre of the specimen due to plastic deformation, and then propagated towards the surface. The specimen became unstable at the ultimate tensile stress, necked, and fractured in a shearing manner. Details of the dimple features indicated no discernible difference among all the specimens, whereas the small reduction in the value R_A and the consequent values of E_I of less than 11% implied a small hydrogen influence. This small decrease in the value R_A could be ascribed to the occurrence of secondary cracks. There were secondary cracks for 980DP and 1200DP tested at all conditions (except for 980DP-Ecorr-L0.054), corresponding to E_I values ranging from 5% to 11%. These secondary cracks

had lengths exceeding 100 µm and normally occurred in the shear lip regions among the shear dimples, indicating that they initiated and grew during the final stage of the ductile fracture, when there was intensive stress and the specimen was mechanically unstable. The occurrence of secondary cracks could be attributed to hydrogen interacting with minor metallurgical heterogeneities [33]. However, such hydrogen influence was small and the overall fracture process was ductile cup and cone, accompanied by extensive necking. Since the occurrence of a significant hydrogen influence requires a critical concentration of hydrogen, the minimal hydrogen influence on these two steels could be associated with their relatively low hydrogen contents, as was evidenced by our previous study on hydrogen concentration under the same corrosion conditions in 3 wt% NaCl solution [36]. Within this concept of critical hydrogen content for HE, the facts that (i) hydrogen influence occurred to 980DP and 1200DP under cathodic charging conditions in 0.1 M NaOH, even under the least negative charging potential of –1.100 $V_{Hg/HgO}$ [35], and (ii) such influence was absent for these two steels tested at simulated corrosion conditions (E_{corr} and E_{Zn}) in 3 wt% NaCl at the same applied stress rates using LIST, indicate that the critical hydrogen concentration for HE in 980DP and 1200DP lies between the hydrogen concentration corresponded to charging at E_{Zn} of –0.950 $V_{Ag/AgCl}$ (–0.752 V_{SHE}) in 3 wt% NaCl and that to charging at –1.100 $V_{Hg/HgO}$ (–1.002 V_{SHE}) in 0.1 M NaOH.

4.2.3. 980DP-650YS and 980DP-700YS

Table 2 indicates that 980DP-650YS and 980DP-700YS tested at E_{Zn} using the 3 rph motor (specimens 980DP-650YS-Ezn-L0.0100 and 980DP-700YS-Ezn-L0.0107) showed a more significant hydrogen influence, manifested by (i) a decrease in R_A and concomitantly an E_I value higher than 50%, and (ii) slightly decreased σ_f and σ_y values. The fracture surface resembled cup and cone fracture, yet, had some differences in that (i) the centre cone part was not as distinctive, (ii) the centre dimples were shallower than the counterparts in air, and (iii) there was a considerable amount of secondary cracks throughout the fracture surface, as shown in Fig. 4. There was also substantial necking and no subcritical crack growth. The depth of dimples indicate the ductility, thus shallower dimples implied reduced ductility. It was considered that the fracture nucleated at the centre of the specimen due to plastic deformation and grew towards the specimen surface, however, the micro-void coalescence process was influenced by the presented hydrogen under intensive stress, causing shallower dimples and fast propagation to form the shearing lips. When the specimen became mechanically unstable during the last stage of ductile fracture, secondary cracks occurred.

Thus, this fracture is considered semi-ductile and semi-brittle under the influence of hydrogen. This process is somewhat similar to the hydrogen-enhanced local plasticity (HELP) mechanism of sub-critical crack growth, which involves localized plastic deformation and macroscopic brittle failure. Moreover, section 4.2.1 indicated that 24 h pre-charging at E_{Zn} caused a uniform hydrogen concentration throughout the specimen. This indicates that hydrogen influenced the micro-void coalescence process at the centre of the specimen. Furthermore, as already mentioned in section 4.2.1, our previous work [36] indicated that 980DP-650YS and 980DP-700YS possessed concentrations of diffusible hydrogen higher than those of 980DP and 1200DP tested under similar corrosion conditions. The more significant hydrogen influence of these 980DP-650YS and 980DP-700YS steels is attributed to these higher hydrogen concentrations. In addition, there could also be contributions from the grain size [48], alloying elements [48] and thickness of the specimens [35].

4.2.4. 980QP

Table 2 indicates that all 980QP specimens were subjected to significant hydrogen influence at E_{corr} and E_{Zn} at both applied stress rates. All specimens experienced decreases in σ_f, σ_y and R_A, compared with their counterparts tested in air, and thereby gave E_I values ranging from 56% to 73%. The decrease in mechanical properties and the increase in the hydrogen embrittlement index were greater when the charging potential was changed from E_{corr} to E_{Zn}, and when the applied stress rate was decreased from an applied stress rate of 0.084 MPa s^{-1} to an applied stress rate of 0.0084 MPa s^{-1}. The highest hydrogen influence occurred for 980QP-Ezn-L0.0084, with an E_I value of 73% and reduced σ_f and σ_y by 7% and 12%, respectively. Compared with that at E_{corr}, the hydrogen uptake is enhanced at E_{Zn}, attributed to the cathodic-polarisation facilitating the hydrogen evolution reaction [49]. Our previous research [36] indicated that hydrogen content at E_{Zn}, was higher by a factor of six, than that at E_{corr} for 980QP. A greater hydrogen concentration thereby increased the hydrogen influence. This is consistent with the fact that Scharf et al. [50] found that zinc-galvanized high-strength steels possessed higher hydrogen concentrations and consequently lower resistance to hydrogen induced delayed fracture when immersed in a NaCl solution. Moreover, the increased hydrogen influence with a lower applied stress rate or strain rate, as occurred to 980QP in this work, is also consistent with the findings of other works [19, 28, 33, 35, 51], and is attributed to (i) a longer time for hydrogen to diffuse to the critically stressed regions at a lower stress or strain rate [28, 51], and (ii) more hydrogen being supplied to the newly formed dislocations, which are essentially free of hydrogen and can facilitate hydrogen

transportation [52-54] and can cause hydrogen assisted micro-fracture events. Examinations of the fracture surface supported the more profound hydrogen influence in that the area of mixed region M slightly increased as the hydrogen embrittlement index, E_I, increased (see section 3.1). All the 980QP exhibited shear fracture, accompanied by significant necking, indicating that the fracture occurred at the ultimate tensile stress when the specimen became mechanically unstable, rather than caused by subcritical crack growth at the threshold stress. The fracture initiated from the brittle regions at the edges of the surface, and then propagated towards the inner part of the specimen in a shear manner, consequently the mixed and shear regions were formed. The findings that the brittle regions were small, the shear dimples were shallow, and the mixed region area were increased with an higher hydrogen embrittlement index, indicated (i) hydrogen content was not sufficient to cause an extended area of transgranular brittle region B, and (ii) the hydrogen influenced the micro-void coalescence process during shearing in a manner somewhat similar to HELP, as mentioned above in section 4.2.3. Furthermore, the fracture initiation in the brittle regions could occur by a mechanism similar to the hydrogen-enhanced decohesion (HEDE) mechanism for sub-critical crack growth, associated with hydrogen-enriched martensite or retained austenite/martensite interface, as was elucidated in [35]. In any case, it is worth stressing that the critical influence of hydrogen was (i) in causing some solid solution softening, attributed to hydrogen facilitated macroscopic movement of significant dislocation masses, which can be named hydrogen enhanced macroscopic plasticity (HEMP), and (ii) in modifying the micro-fracture events during the final specimen fracture when the specimen was mechanically unstable and was undergoing relatively fast fracture, with considerable ductility, which can be designated as hydrogen assisted micro-fracture (HAM).

4.2.5. 950TW

Table 2 indicates that 950TW specimens experienced an influence of (residual) hydrogen when subjected to LIST in air at an applied stress rate of 0.072 MPa s^{-1} and an applied stress rate of 0.0072 MPa s^{-1}. Their susceptibility to HE increased when tested at E_{corr} and E_{Zn}, at these applied stress rates, leading to slightly lower mechanical properties and a slightly increased hydrogen embrittlement index, E_I, as evidenced by comparisons of 950TW-Ezn-L0.0072 and 950TW-A-L0.0072. This is within expectation, since both E_{corr} and E_{Zn} produced more hydrogen and increased hydrogen concentration in the steels, particularly, the introduction of hydrogen was enhanced by the movement of hydrogen-carrying dislocations during the test with in situ charging. There was also the trend that hydrogen

influence slightly increased with higher charging potential at E_{Zn}, and with a slower applied stress rate, similar to that which occurred to 980QP, however, due to relatively low hydrogen diffusion coefficient in the fully austenitic microstructure [16], the increment was small, which was also supported by no discernible change in brittle region area of the steels tested in each simulated corrosion condition. The fractographic images indicated similar shearing fracture as that under cathodic charging in NaOH in our previous work [35], yet, with a smaller brittle area, consistent with a lower hydrogen content under simulated corrosion conditions than under cathodic charging conditions. The characters of transgranular features were essentially similar for all cases. Thus, the fracture initiation and propagation are also considered to be associated with a mechanism similar to the HEDE mechanism associated with twin boundaries [25, 27], twin-twin intersections within a grain [25, 27], or interface of austenite and deformation induced martensite [24, 27, 55].

4.3. Substantial loading rates

4.3.1. Simultaneous charging

Table 3 and Figs. 7-11 present the data for simultaneous in situ hydrogen charging at –1.700 $V_{Hg/HgO}$ in 0.1 M NaOH applied to 980DP, 980QP and 950TW specimens subjected to (i) a substantial stress rate in the UTM, (ii) a motor speed of 300 rph in the LIST, and (iii) a motor speed of 30 rph in the LIST. Table 3 and Figs. 7-11 indicate that all the steels under these conditions were significantly influenced by hydrogen, manifested by decreased mechanical properties and the presence of brittle fracture features. In addition, 980DP, 980QP and 950TW, which were subjected to hydrogen influence when tested by UTM with in situ hydrogen charging, also showed transgranular quasi-cleavage brittle features, essentially similar to those in LIST. Depover et al. [28] studied the hydrogen influence on DP steels using tensile tests at crosshead displacement speeds of 0.083 mm s^{-1} and 0.00083 mm s^{-1} (corresponding to respective initial strain rates of $3.7 \times 10^{-3} s^{-1}$ and 3.7×10^{-5} s^{-1}), with in situ cathodic hydrogen charging at a current density of 2.65 mA cm^{-2} in a 0.5 M H_2SO_4 solution with 1 g L^{-1} thiourea. Their DP steels possessed yield and tensile strengths of around 300 and 600 MPa, respectively, and exhibited significant a hydrogen influence with ductility reduced by more than 50% and with transgranular cleavage brittle features. They further found the hydrogen influence increased as the loading rate became slower. Zhu et al. [21] investigated the hydrogen influence on Q&P 980 steels using a UTM with an initial strain rate of 10^{-5} s^{-1}, tested after hydrogen pre-charging at a current density of 30 mA cm^{-2} for

various times in a 0.5 M H_2SO_4 solution with 1 g L^{-1} thiourea. The Q&P 980 steels were essentially similar to those used in this work, and were also subjected to a significant hydrogen influence, evidenced by loss of ductility as high as 87% and fracture surfaces consisting of a mixture of dimples, quasi-cleavage regions and intergranular facets. Dieudonné et al. [27] studied the HE susceptibility of TWIP steels with various chemical compositions, but all with slightly higher tensile and yield strengths than the 950TW of this study. The experimental details in their work were somewhat similar to those in this work. Tensile tests were conducted at an initial strain rate of 10^{-4} s^{-1}, with in situ cathodic hydrogen charging at a current density of 10 mA cm^{-2} in a 0.1 M NaOH solution. Their TWIP steels demonstrated significant HE susceptibility, with ductility loss ranging from 3% to 54%. Furthermore, they also observed similar fracture surfaces, containing three distinctive regions: (i) intergranular brittle region near the edge, (ii) transition region with large dimples or transgranular decohesion, and (iii) ductile region with fine dimples.

Moreover, the extent of hydrogen influence was similar for steels tested by UTM and by LIST at 300 rph, whereas it increased for steels tested in the LIST at 30 rph. This indicates that (i) the LIST and the UTM can provide comparable results and are both capable of studying the hydrogen influence on 980DP, 980QP and 950TW steels, consistent with that addressed in other research [39], and (ii) the increase in hydrogen influence becomes more profound when the stress rate decreases to a certain level. The trend of increased HE with reduced stress rates is also stated in other works [19, 28, 33] and in our previous study on these steels [35]. Winzer et al. [39] studied stress corrosion cracking by both LIST and UTM under comparable loading rates, and obtained comparable results, and the same trend of more profound influence with lower strain rates. They further addressed that there might be potential mechanistic differences that the local stress intensity at the crack tip was relatively constant in LIST, whereas it reduced in the UTM, leading to a decreased driving force for hydrogen diffusing to the crack tip and thereby hindered HE process under UTM. However, such mechanistic differences were not observed in this work, since the hydrogen influence was similar using both LIST and UTM.

4.3.2. Hydrogen egress with time

For 980DP, 980QP and 950TW steels that were tested in air with the UTM and the LIST, after 24 h pre-charging with hydrogen, there was an inevitable time interval between hydrogen pre-charging and mechanical testing. The small hydrogen atoms that have been introduced in the specimen can relatively easily diffuse within and egress from the steel. Thus,

during the time interval between hydrogen pre-charging and tensile tests, some hydrogen egresses from the specimen, affecting HE susceptibility of the steel. Venezuela et al. [33] studied the influence of different holding times between hydrogen pre-charging and testing on the HE susceptibility. They found that the martensitic high strength steels essentially experienced no hydrogen influence after an egress time of around 10 min, when the surface concentration had decreased, but the bulk of the specimen essentially still retained a high hydrogen concentration.

They proposed a diffusion model to estimate the fraction of remaining hydrogen as a function of time, based on solving Fick's diffusion equations with the following boundary conditions [33]:

$t = 0$, $C = C_0$ for $0 < x < L$ (3)

$t > 0$, $C = 0$ for $x = 0$ and $x = L$ (4)

Their model was that there was initially constant hydrogen content throughout a thin plate specimen with a thickness of L, and that hydrogen egressed equally from both sides of the specimen. The normalised hydrogen concentration is given by [33, 56]:

$$\frac{C}{C_0} = \frac{4}{\pi}\sum_{n=0}^{\infty}\frac{1}{2n+1}\exp\left\{\frac{(2n+1)^2\,D\,\pi^2\,t}{L^2}\right\}\sin\frac{(2n+1)\pi\,x}{L} \quad (5)$$

where D is the hydrogen diffusion coefficient, C/C_0 is the proportion of remaining hydrogen at a location, x, inside the specimen after a desorption time, t. Eq. (5) provides a profile of the remained hydrogen throughout the specimen thickness after different desorption times.

Fig. 17(a) illustrates such profiles of remaining hydrogen throughout the specimen thickness after different desorption time for 980DP as an example. The hydrogen content was constant at the beginning throughout the whole specimen, and the proportion of remaining hydrogen was 1.0. Hydrogen then started desorbing from both sides, and the profile of remaining hydrogen proportion decreased. Such a decrease was further enhanced with prolonged desorption time, and eventually reached zero, indicating that all the hydrogen had effused out of the specimen. An integration of the plot yields the amount of remaining hydrogen in the whole specimen. Fig. 17(b) presents the plots of normalized concentration of remaining hydrogen in the whole specimen, versus desorption time, t, for 980DP, 980QP and 950TW steels. The hydrogen diffusion coefficient, D, was from our previous measurements [37] on 980DP and 980QP, and from other work [25] for 950TW. The thickness, L, was from the average thickness for specimens used in this study.

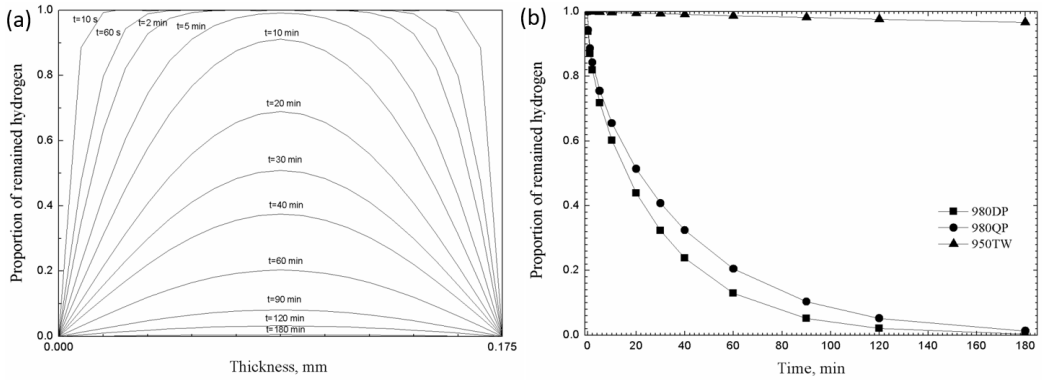

Fig. 17. (a) Profiles of the remained hydrogen proportion throughout the specimen thickness for 980DP, and (b) proportion of remained hydrogen as a function of desorption time for 980DP, 980QP and 950TW steels.

Fig. 17(b) indicates that after 10 min, the proportion of remaining hydrogen in 980DP, 980QP and 950TW steels was 60%, 66% and 99.8%, respectively, whilst the value after 30 min was 32%, 41% and 99.3%. The remaining hydrogen decreased more slowly for 980QP than 980DP, attributed to the intrinsic difference in microstructure, such as the presence of retained austenite in 980QP. In addition, the remaining hydrogen was less than 2% after 3 h in the pre-charged 980DP and 980QP steels, and was about 97% in 950TW. This indicates that hydrogen outgassing from 980DP and 980QP was rather fast, whereas the desorption of hydrogen from 950TW is a relatively slow process, due to the low diffusion coefficient and the high solubility of hydrogen in austenitic TWIP steels [25]. In the study of Venezuela et al. [33], the proportion of hydrogen remaining in the hydrogen-charged martensitic advanced high-strength steels was 75% and 30% after 30 min and 4 h, respectively, and was higher than that for DP and Q&P steels within the same amount of time. This is within expectations, since martensite is considered to possess more hydrogen traps, resulting in a lower hydrogen diffusion coefficient. Moreover, the specimen thickness also plays a role in affecting hydrogen outgassing rate, as was also shown in Eq. (5). For the time interval of 24 h, minimal amount of hydrogen was considered to remained in 980DP and 980QP, whereas for 950TW, after 24 h, the proportion of remaining hydrogen was calculated to be 86% using Eq. (5), indicating that after 24 h between pre-charging and tensile testing, there was still substantial hydrogen remaining, and a hydrogen influence still would be expected for the steel.

4.3.3. Time after H charging for 980DP

A time interval of 10 min and 24 h between the end of the 24 h hydrogen pre-charging and the start of testing in air using UTM and LIST was used in this work. Figs. 11-14 indicate that the hydrogen influence on all the steels declined after a time interval of 10 min and 24 h,

accompanied by mechanical properties reverting towards those for their uncharged counterparts and by the decrease in brittle features.

Table 3 and Figs. 11 and 12 indicate that 980DP experienced minimal hydrogen influence after a time interval of 10 min and 24 h, manifested by the recovered mechanical properties and ductile cup and cone fracture surface. The proportion of remaining hydrogen became minimal after 3 h for pre-charged 980DP steels. This implies that there was essentially no hydrogen remaining in the specimen after a time interval of 24 h and this explains why the 980DP steel had mechanical properties that reverted to those of their uncharged counterparts. One the other hand, after 10 min, there was still 60% of the introduced hydrogen remaining in the specimen. The duration for 980DP subjected to tensile test (980DP-10min-I50), LIST at 300 rph (980DP-10min-L0.54) and LIST at 30 rph (980DP-10min-L0.054) was about 2 min, 30 min and 4 h, respectively. Thus, the total time (time interval and time for testing) corresponding to 980DP-10min-I50, 980DP-10min-L0.54 and 980DP-10min-L0.054 was around 12 min, 40 min and 250 min, respectively. The highest proportion of remaining hydrogen among these three testing conditions was expected to be in 980DP-10min-I50, and was estimated to be around 50% by Eq. (5). This implies that the amount of 50% of the introduced hydrogen was below the level of critical hydrogen content and consequently, all the steels with time interval of 10 min and 24 h subject to tensile test and LIST exhibit minimal hydrogen influence. Moreover, the results that (i) hydrogen influence was significant for tests with simultaneous charging and (ii) was absent with time intervals of 10 min and 24 h, indicates the simultaneous charging could influence HE susceptibility of 980DP. Koyama et al. [11] adopted a time interval of 240 h between hydrogen pre-charging and tensile testing, which allowed most of the introduced hydrogen to desorb out, and found a partial recovery of the DP steel compared with the test conducted shortly after charging. This was out of expectations, since after 240 h exposure to air there was little hydrogen remaining. They further explained that for this specimen, pre-charging was carried out with a 6% engineering strain, which was almost at the same level as the local plastic strain. At this point, martensite cracking had already been initiated and thereafter contributed to finally failure.

4.3.4. Time after H charging for 980QP

980QP showed various extent of recovery depending on the time interval and testing loading rates. A fast loading rate provides a rapid test. Thus, the difference in recovery extent for 980QP can be interpreted in terms of total time (time interval and time for testing)

exposed to air after hydrogen pre-charging. The total time for 980QP-10min-I50, 980QP-10min-L0.84 and 980QP-10min-L0.084 was around 12 min, 30 min and 3 h, respectively, and that for tests with a time interval of 24 h was obviously higher than 24 h. As aforementioned, there was less than 2% of introduced hydrogen remaining after 3 h. Therefore, 980QP-10min-L0.084 (a total time of 3 h) and all the others with a time interval of 24 h, were anticipated to exhibit minimal hydrogen. Indeed, as presented in Fig. 13, all these steels fractured in a ductile cup and cone manner, except for 980QP-24h-I50, which showed three fisheyes. The fact that 980QP-24h-I50 exhibited fisheyes is a sign of embrittlement, and is attributed to (i) the release of hydrogen during transformation from retained austenite to martensite under straining, due to higher solubility of hydrogen in austenite [21] and lower inclination of the solute hydrogen to egress freely out of the specimen without deformation, and (ii) that the duration of tensile tests is relatively too short (2 min) to permit substantial desorption of this released hydrogen. For 980QP-10min-I50 and 980QP-10min-L0.84, there was about 60% and 40% charged hydrogen remaining, and these hydrogen concentration were high enough to cause HE, and the extent of such HE increased with increased remaining hydrogen content, as evidenced by more fisheyes in 980QP-10min-I50 than in 980QP-10min-L0.84. Nevertheless, there was partial recovery for these specimens, as evidenced by improved mechanical properties and change in brittle features from transgranular quasi-cleavage to fisheyes, for example comparing 980QP-0min-I50 with 980QP-10min-I50. This also indicates that simultaneous charging could influence HE susceptibility of 980QP. Similarly, Duprez et al. [57] found essentially full recovery with a time interval of 7 days between the end of hydrogen charging and start of tensile tests.

4.3.5. Time after H charging for 950TW

950TW also showed partial recovery with a time interval of 10 min and 24 h, evidenced by the increased mechanical properties and decreased brittle regions, as was presented in Table 3 and Figs. 11 and 14. However, there was not a clear trend of the recovery regarding the total time (time interval and time for testing). For example, the most profound hydrogen influence was for 950TW-24h-I50, which had a total time of more than 24 h, whereas the least one was for 950TW-10min-L0.72, with a total time of 30 min. The proportion of remained hydrogen was around 86% and 99% after 24 h and 30 min, respectively. This implies that the remaining hydrogen in both cases (after 24 h and 30 min) were still significantly high enough to cause some hydrogen influence. In other words, the outgassing of 1% or 14% of introduced hydrogen did not lead to distinctive difference in

hydrogen influence. Compared with the counterparts with simultaneous in situ hydrogen charging, it was addressed again that simultaneous charging influenced the HE susceptibility of 950TW. Furthermore, the uncharged specimen, 950TW-A-L0.072, also presented some hydrogen influence with an E_I value of 10%, whereas its counterparts, 950TW-10min-L0.072 and 950TW-24h-L0.072 showed respective E_I values of 11% and 12%, showing similar HE susceptibility. This comparison indicates that (i) the HE susceptibility of charged 950TW after just 10 min returned to the same level as the one for uncharged specimen, and (ii) the amount of charged hydrogen was not sufficient to cause significant difference in hydrogen influence, since 950TW-10min-L0.072 contained charged hydrogen and residual hydrogen, whereas 950TW-A-L0.072 only contained residual hydrogen, indirectly supporting that simultaneous charging enhanced hydrogen influence on 950TW. The larger extent of hydrogen influence and thereby brittle regions were also observed in other work [27] for TWIP steels tested with in situ charging in contrast with pre-charging and testing in air. Hydrogen has a relatively low diffusion coefficient in austenitic steels at room temperature [25], thus hydrogen absorption in the specimen is influenced by its interactions at the moving crack tip and such process is enhanced by the motion of newly formed dislocations, which can carry hydrogen and are free of hydrogen [27]. Therefore, this explains the more profound hydrogen influence with simultaneous in situ hydrogen charging.

4.4. Microstructures associated with HE of 950TW

DP, Q&P and TWIP steels were subjected to HE under simulated service conditions and cathodic charging conditions, as presented in this work and in the previous research [35]. Moreover, our previous study [35] elucidated that HE of DP and Q&P steels were associated with the presence of martensite, due to its high susceptibility [58]. Thus, there is a concern that martensite is transformed from austenite in the 950TW steels during LIST or tensile tests, and thereafter contributed to the hydrogen influence on these steels, such as causing crack initiation and propagation through the martensite or at martensite/austenite interfaces. There are studies documenting such martensitic transformation from austenite in TWIP steels and its detrimental influence on HE resistance of these steels [15, 24, 59]. Ryu et al. [24] found that some ε-martensite was formed in hydrogen pre-charged TWIP steels subjected to tensile tests, as detected by XRD, and this ε-martensite was associated with transgranular brittle features. They further found that the occurrence of this martensitic transformation did not result from hydrogen charging, as the case in austenitic stainless steels [60], rather it was induced by deformation during straining.

However, Fig. 15 indicates that all the 950TW steels, tested by XRD in this work, possessed fcc austenite (γ-Fe), and there was not any type of martensite formed. This result (i) supports that 950TW was fully austenitic in the as-received and uncharged state, and (ii) indicates that hydrogen influence on 950TW was not associated with any martensite. The absence of martensitic transformation during straining is consistent with the literature [24, 27, 55, 59]. Mechanical twins are formed during straining in a LIST or in a tensile machine, and hydrogen atoms transport from the lattice, dislocations and grain boundaries to such mechanical twins, leading to the accumulation of hydrogen and fracture initiation at the mechanical twins [59]. Koyama et al. [61] also observed transgranular fracture occurring parallel to the primary and secondary deformation twin boundaries.

4.5. Indications for service

HE was absent for 980DP and 1200DP, and was present for 980DP-650YS, 980DP-700YS, 980QP and 950TW, tested at E_{corr} and E_{zn} in a 3 wt% NaCl solution, simulating corrosion situations in actual service. Such corrosion conditions by immersing steels directly in a 3 wt% NaCl solution are the most extreme corrosion situation that can occur in actual service, as was also mentioned in section 4.2.1. In reality, there are occasions where the auto components are exposed to high salt environments, such as de-icing salts and marine atmosphere, yet, these environments are much milder than the simulated corrosion conditions in this work. Ootsuka et al. studied in situ hydrogen adsorption into cold-rolled steel, and found hydrogen entered the steel only during corrosion, and that such process was enhanced by spraying a 0.5% NaCl on the steel surface. However, even with the acceleration of salt spray, the amount of absorbed hydrogen was an order of magnitude lower than those measured previously in our steels under simulated service corrosions [36]. A lower hydrogen content decreases the likelihood of HE occurrence. Therefore, this work indicates that 980DP and 1200DP would experience minimal HE, whereas the other steels are under concern of HE during actual auto service.

In addition, HE was slightly more significant at E_{zn} than that at E_{corr}. This is consistent with the higher hydrogen content being introduced into the specimen at E_{zn}, as measured in our previous study [36]. It indicates that galvanization could protect the substrate steel from corrosion, however, once the galvanized steel was subjected to corrosion environment, more hydrogen could be absorbed into the specimen, leading to a greater chance of HE occurrence.

The test with simultaneous in situ charging at fast loading rates simulated a crash situation in actual service with the presence of hydrogen in the steel. However, the amount of

hydrogen introduced by electrochemical charging at –1.700 $V_{Hg/HgO}$ in 0.1 M NaOH, was significantly higher than that would be introduced in actual service. Thus, the occurrence of HE to the steels under this simulated condition does not mean that the steels would also be subjected to HE during a crash in service. In some cases [19, 54], HE was absent with stress or strain rate higher than a critical value, and with hydrogen content lower than a critical level.

Furthermore, the results that steels were fully or partially recovered after exposing to air for a brief amount of time, indicate the influence of a simultaneous hydrogen source on HE during loading. Therefore, one would expect that in actual service, if the hydrogen source was deprived (e. g. corrosion ceased), and the steel was exposed to non-hydrogen source (e.g. ambient air), the hydrogen-influenced steel would experience recovery from HE depending on the steel type and exposing time.

The influence of hydrogen was manifest as some decrease in the yield stress (by solid solution softening by hydrogen) and decreased ductility caused by hydrogen charging the micromechanics of fracture. There was no sub-critical cracking.

4.6. Hydrogen embrittlement mechanisms

The influence of hydrogen on the steels studied in this work is similar to that studied in prior research [5, 17, 18, 19, 28, 33, 35, 36, 51], but there was no subcritical crack growth. It is worth emphasising that the current mechanisms of hydrogen embrittlement pertain to subcritical crack growth. These mechanism are Hydrogen Enhanced Localized Plasticity (HELP), Hydrogen Enhanced Decohesion (HEDE) and Adsorption-induced dislocation emission (AIDE) [5].

Since there was no subcritical crack growth in the present work and related work, it is worthwhile critically considering the hydrogen influence observed, and to critically address the mechanisms.

The critical influence of hydrogen was (i) in causing some solid solution softening, attributed to hydrogen facilitated macroscopic movement of significant dislocation masses, which can be named hydrogen enhanced macroscopic plasticity (HEMP), and (ii) in modifying the micro-fracture events during the final specimen fracture when the specimen was mechanically unstable and was undergoing relatively fast fracture, with considerable ductility, which can be designated as hydrogen assisted micro-fracture (HAM).

5. Conclusions

The influence of hydrogen on some DP, Q&P and TWIP grades of advanced high-strength steels under simulated service conditions was studied using the linearly increasing stress test (LIST) and a universal tensile machine. The following conclusions have been drawn:

1. The hydrogen influence was minimal for 980DP and 1200DP, whereas there was significant influence for 980DP-650YS, 980DP-700YS, 980QP and 950TW tested by LIST in 3% wt% NaCl.
2. There was more hydrogen influence at the zinc potential than that at free corrosion for 980DP, 980QP and 950TW steels subjected to 3% wt% NaCl in LIST.
3. There was significant hydrogen influence on 980DP, 980QP and 950TW steels with simultaneous in situ hydrogen charging at fast loading rates, manifested by decreased strengths and ductility, and by the presence of brittle features.
4. The influence of hydrogen was manifest as some decrease in the yield stress (by solid solution softening by hydrogen) and decreased ductility caused by hydrogen changing the micromechanics of fracture. There was no sub-critical cracking.
5. There was full or partial recovery of the hydrogen-influenced 980DP, 980QP and 950TW steels after exposing to air for up to 24 h.
6. The transgranular quasi-cleavage brittle features for 950TW were associated with mechanical twinning rather than martensitic transformation.
7. The critical influence of hydrogen was (i) in causing some solid solution softening, attributed to hydrogen facilitated macroscopic movement of significant dislocation masses, which can be named hydrogen enhanced macroscopic plasticity (HEMP), and (ii) in modifying the micro-fracture events during the final specimen fracture when the specimen was mechanically unstable and was undergoing relatively fast fracture, with considerable ductility, which can be designated as hydrogen assisted micro-fracture (HAM).

Acknowledgements

This research was supported by the Baosteel-Australia Joint Research & Development Centre (BAJC) Grant, BA13037, with linkage to Baoshan Iron and Steel Co., Ltd of China. The

authors also wish to thank the staff at the Centre for Microscopy and Microanalysis at the University of Queensland for their assistance.

References

[1] J Galán, L Samek, P Verleysen, K Verbeken and Y Houbaert, Advanced high strength steels for automotive industry, Rev Metal Madrid. 48 (2012) 118-131.
[2] D Bhattacharya, Developments in Advanced High Strength Steels, Proceedings of Proceedings of the Joint International Conference of HSLA Steels, Sanya, 2005, 70-73.
[3] BC De Cooman, L Chen, HS Kim, Y Estrin, SK Kim and H Voswinckel, State-of-the-science of high manganese TWIP steels for automotive applications, microstructure and texture in steels, Charpter 10, p. 165-183, Springer, London, 2009.
[4] X Zhu, Z Ma and L Wang, Current status of advanced high strength steel for auto-making and its development in Baosteel, Rep Baosteel Research Institute. 201900 (2007) 1-8.
[5] Q Liu, Q Zhou, J Venezuela, M Zhang, J Wang and A Atrens, A review of the influence of hydrogen on the mechanical properties of DP, TRIP, and TWIP advanced high-strength steels for auto construction, Corros Rev. 34 (2016) 127-152.
[6] WorldAutoSteel, Advanced high-strength steels application guidelines version 5.0, Available from http://www.worldautosteel.org/, Access on 2014.
[7] R Kuziak, R Kawalla and S Waengler, Advanced high strength steels for automotive industry, Archives of civil and mechanical engineering. 8 (2008) 103-117.
[8] Baosteel, Baosteel automotive advanced high strength steels, Available from http://www.baosteel.com/, Access on 2013.
[9] AutoSteel, ULSAB-AVC (Advacend Vehicle Concetp) overview report, Available from http://www.autosteel.org/ Access on 2002.
[10] M Loidl, O Kolk, S Veith and T Göbel, Characterization of hydrogen embrittlement in automotive advanced high strength steels, Materialwiss Werkstofftech. 42 (2011) 1105-1110.
[11] M Koyama, CC Tasan, E Akiyama, K Tsuzaki and D Raabe, Hydrogen-assisted decohesion and localized plasticity in dual-phase steel, Acta Mater. 70 (2014) 174-187.
[12] R Davies, Hydrogen embrittlement of dual-phase steels, Metall Trans A. 12 (1981) 1667-1672.
[13] G Lovicu, M Bottazzi, F D'Aiuto, M De Sanctis, A Dimatteo, C Santus and R Valentini, Hydrogen embrittlement of automotive advanced high-strength steels, Metall Mater Trans A. 43 (2012) 4075-4087.

[14] J Ronevich, S Kim, J Speer and D Matlock, Hydrogen effects on cathodically charged twinning-induced plasticity steel, Scripta Mater. 66 (2012) 956-959.
[15] M Koyama, E Akiyama and K Tsuzaki, Hydrogen embrittlement in a Fe–Mn–C ternary twinning-induced plasticity steel, Corros Sci. 54 (2012) 1-4.
[16] G Lovicu, M Barloscio, M De Sanctis, A Dimatteo, C Santus, R Valentini, M Bottazzi, F D'Aiuto, C Federici and S Maggi, Hydrogen embrittlement of advanced high strength steels for automotive use, Proceedings of 2nd International Conference ''Super High Strength Steels'', Italie, 2010,
[17] Q Liu, B Irwanto and A Atrens, The influence of hydrogen on 3.5NiCrMoV steel studied using the linearly increasing stress test, Corros Sci. 67 (2013) 193-203.
[18] Q Liu, B Irwanto and A Atrens, Influence of hydrogen on the mechanical properties of some medium-strength Ni–Cr–Mo steels, Mater Sci Eng A. 617 (2014) 200-210.
[19] J Venezuela, Q Liu, M Zhang, Q Zhou and A Atrens, The influence of hydrogen on the mechanical and fracture properties of some martensitic advanced high strength steels studied using the linearly increasing stress test, Corros Sci. 99 (2015) 98-117.
[20] G Lovicu, EP Bagliani, M De Sanctis, A Dimatteo, R Ishak and R Valentini, Hydrogen embrittlement of a medium carbon Q&P steel, Metallurgical Italiana. 6 (2013) 3-10.
[21] X Zhu, W Li, H Zhao, L Wang and X Jin, Hydrogen trapping sites and hydrogen-induced cracking in high strength quenching & partitioning (Q&P) treated steel, Int J Hydrogen Energy. 39 (2014) 13031-13040.
[22] X Zhu, K Zhang, W Li and X Jin, Effect of retained austenite stability and morphology on the hydrogen embrittlement susceptibility in quenching and partitioning treated steels, Mater Sci Eng A. 658 (2016) 400-408.
[23] J Yang, F Huang, Z Guo, Y Rong and N Chen, Effect of retained austenite on the hydrogen embrittlement of a medium carbon quenching and partitioning steel with refined microstructure, Mater Sci Eng A. 665 (2016) 76-85.
[24] JH Ryu, SK Kim, CS Lee, D-W Suh and H Bhadeshia, Effect of aluminium on hydrogen-induced fracture behaviour in austenitic Fe–Mn–C steel, Proc R Soc A. 469 (2013) 20120458.
[25] M Koyama, E Akiyama, K Tsuzaki and D Raabe, Hydrogen-assisted failure in a twinning-induced plasticity steel studied under in situ hydrogen charging by electron channeling contrast imaging, Acta Mater. 61 (2013) 4607-4618.
[26] M Koyama, E Akiyama and K Tsuzaki, Effect of hydrogen content on the embrittlement in a Fe–Mn–C twinning-induced plasticity steel, Corros Sci. 59 (2012) 277-281.

[27] T Dieudonné, L Marchetti, M Wery, J Chêne, C Allely, P Cugy and C Scott, Role of copper and aluminum additions on the hydrogen embrittlement susceptibility of austenitic Fe–Mn–C TWIP steels, Corros Sci. 82 (2014) 218-226.
[28] T Depover, D Pérez Escobar, E Wallaert, Z Zermout and K Verbeken, Effect of hydrogen charging on the mechanical properties of advanced high strength steels, Int J Hydrogen Energy. 39 (2014) 4647-4656.
[29] E Hamzah and M Kanniah, Corrosion Behavior of low carbon steel sheets for car bodies, Jurnal Mekanikal. 19 (2005) 57-70.
[30] N LeBozec, N Blandin and D Thierry, Accelerated corrosion tests in the automotive industry: a comparison of the performance towards cosmetic corrosion, Materials and corrosion. 59 (2008) 889-894.
[31] E Akiyama, K Matsukado, M Wang and K Tsuzaki, Evaluation of hydrogen entry into high strength steel under atmospheric corrosion, Corros Sci. 52 (2010) 2758-2765.
[32] S Ootsuka, S Fujita, E Tada, A Nishikata and T Tsuru, Evaluation of hydrogen absorption into steel in automobile moving environments, Corros Sci. 98 (2015) 430-437.
[33] J Venezuela, Q Zhou, Q Liu, M Zhang and A Atrens, Influence of hydrogen on the mechanical and fracture properties of some martensitic advanced high strength steels in simulated service conditions, Corros Sci. 111 (2016) 602-624.
[34] QJ Zhou, L Wang and JX Li, Experimental study on delayed fracture of TS 980MPa grade steels for automotive applications, Proceedings of Steely Hydrogen Conference, Ghent, Belgium, 2014, 35-44.
[35] Q Liu, Q Zhou, J Venezuela, M Zhang and A Atrens, Hydrogen influence on some advanced high strength steels, submitted to Corros Sci.
[36] Q Liu, Q Zhou, J Venezuela, M Zhang and A Atrens, Hydrogen concentration in Dual-Phase (DP) and Quenched and Partitioned (Q&P) advanced high-strength steels (AHSS) under simulated service conditions compared with cathodic charging conditions, Adv Eng Mater. 18 (2016) 1588-1599.
[37] Q Liu, J Venezuela, M Zhang, Q Zhou and A Atrens, Hydrogen trapping in some advanced high strength steels, Corros Sci. 111 (2016) 770-785.
[38] A Atrens, CC Brosnan, S Ramamurthy, A Oehlert and IO Smith, Linearly increasing stress test (LIST) for SCC research, Meas Sci Technol. 4 (1993) 1281.
[39] N Winzer, A Atrens, W Dietzel, G Song and KU Kainer, Comparison of the linearly increasing stress test and the constant extension rate test in the evaluation of transgranular stress corrosion cracking of magnesium, Mater Sci Eng A. 472 (2008) 97-106.

[40] S Ramamurthy and A Atrens, Stress corrosion cracking of high-strength steels, Corros Rev. 31 (2013) 1-31.
[41] S Ramamurthy, W Lau and A Atrens, Influence of the applied stress rate on the stress corrosion cracking of 4340 and 3.5 NiCrMoV steels under conditions of cathodic hydrogen charging, Corros Sci. 53 (2011) 2419-2429.
[42] E Villalba and A Atrens, Hydrogen embrittlement and rock bolt stress corrosion cracking, Eng Fail Anal. 16 (2009) 164-175.
[43] E Villalba and A Atrens, Metallurgical aspects of rock bolt stress corrosion cracking, Mater Sci Eng A. 491 (2008) 8-18.
[44] E Gamboa and A Atrens, Material influence on the stress corrosion cracking of rock bolts, Eng Fail Anal. 12 (2005) 201-235.
[45]E8/E8M-16a, Standard test methods for tension testing of metallic materials, 2016.
[46] YS Chun, K-T Park and CS Lee, Delayed static failure of twinning-induced plasticity steels, Scripta Mater. 66 (2012) 960-965.
[47] J Tien, AW Thompson, IM Bernstein and RJ Richards, Hydrogen transport by dislocations, Metall Trans A. 7 (1976) 821-829.
[48] R Davies, Influence of martensite content on the hydrogen embrittlement of dual-phase steels, Scripta metallurgica. 17 (1983) 889-892.
[49] S Hans-Henning, Fundamentals of Corrosion, Corrosion Mechanisms in Theory and Practice, Third Edition, Charpter p. 1-104, CRC Press, 2011.
[50] R Scharf, A Muhr, KH Stellnberger, J Faderl, C Holzer and G Mori, Hydrogen embrittlement of high strength steel under in situ corrosive charging conditions and tensile load, Materials and Corrosion. 68 (2017) 95-104.
[51] T Depover, E Wallaert and K Verbeken, Fractographic analysis of the role of hydrogen diffusion on the hydrogen embrittlement susceptibility of DP steel, Mater Sci Eng A. 649 (2016) 201-208.
[52] GM Pressouyre, Trap theory of Hydrogen embrittlement, Acta Metall. 28 (1980) 895-911.
[53] GM Pressouyre and IM Bernstein, An example of the effect of hydrogen trapping on hydrogen embrittlement, Metall Trans A. 12 (1981) 835-844.
[54] M Hashimoto and RM Latanision, The role of dislocations during transport of hydrogen in hydrogen embrittlement of iron, Metall Trans A. 19 (1988) 2799-2803.

[55] KH So, JS Kim, YS Chun, K-T Park, Y-K Lee and CS Lee, Hydrogen delayed fracture properties and internal hydrogen behavior of a Fe-18Mn-1.5 Al-0.6 C TWIP steel, ISIJ Int. 49 (2009) 1952-1959.
[56] RW Balluffi, S Allen and WC Carter, Kinetics of materials, John Wiley & Sons, 2005.
[57] L Duprez, K Verbeken and M Verhaege, Effect of hydrogen on the mechanical properties of multiphase high strength steels, Proceedings of the 2008 International Hydrogen Conference (2009) 62-69.
[58] J Hirth, Effects of hydrogen on the properties of iron and steel, Metall Trans A. 11 (1980) 861-890.
[59] S-M Lee, I-J Park, J-G Jung and Y-K Lee, The effect of Si on hydrogen embrittlement of Fe-18Mn-0.6C-xSi twinning-induced plasticity steels, Acta Mater. 103 (2016) 264-272.
[60] AE Pontini and JD Hermida, X-ray diffraction measurement of the stacking fault energy reduction induced by hydrogen in an AISI 304 steel, Scripta Mater. 37 (1997) 1831-1837.
[61] M Koyama, E Akiyama, T Sawaguchi, D Raabe and K Tsuzaki, Hydrogen-induced cracking at grain and twin boundaries in an Fe–Mn–C austenitic steel, Scripta Mater. 66 (2012) 459-462.

Chapter 4

Hydrogen trapping in some advanced high strength steels

(published in *Corrosion Science*)

In the previous Chapters 2 and 3, the key DP, Q&P and TWIP steels in this research were found to be subjected to hydrogen influence under cathodic charging condition and simulated crash situation, whilst 980DP and 1200DP experienced minimal hydrogen influence, and other DP, Q&P and TWIP steels exhibited some hydrogen influence, under simulated service corrosion condition.

In order to better understand the hydrogen influence, studies on hydrogen behaviours should be conducted. The following Chapter 4 presents the permeability experiments analysing the hydrogen diffusion and trapping in DP and Q&P steels. The expected results would contribute to the understanding of the hydrogen transportation and interaction within the steels, and the different hydrogen influence behaviours on the same type of steels (e.g. the four DP steels).

Hydrogen trapping in some advanced high strength steels

Qinglong Liu[1], Jeffrey Venezuela, Mingxing Zhang[1], Qingjun Zhou[2], Andrej Atrens[1,*]

[1] The University of Queensland, Division of Materials, School of Mining and Mechanical Engineering, St. Lucia, 4072 Australia

[*] Corresponding author, andrejs.atrens@uq.edu.au, +61 7 3365 3748

[2] Baoshan Iron & Steel Co., Ltd, Research Institute, Shanghai, 201900, China

Abstract

Permeability experiments were used to study hydrogen diffusion and trapping in dual phase (DP), and quenched and portioned (Q&P), advanced high strength steels. The measured reversible hydrogen trap densities indicated that (i) trapping was less significant at a more negative potential, and (ii) the lattice diffusion coefficient of hydrogen could be measured from the partial transients at the most negative potentials. The densities of reversible hydrogen traps evaluated from complete decays from -1.700 $V_{Hg/HgO}$ were ~ 2×10^{18} sites cm^{-2}, and were a factor of two higher than those from partial decay transients between -1.700 $V_{Hg/HgO}$ and -1.100 $V_{Hg/HgO}$.

Keywords: A. Steel, B. Potentiostatic, C. Hydrogen permeation

1. Introduction

1.1 Advanced high strength steels (AHSS)

Advanced high strength steels (AHSS) were developed, and have been adopted, for auto components to reduce vehicle weight and to increase vehicle safety [1-4]. This paper characterises hydrogen trapping in some AHSS and thereby adds to the knowledge base regarding AHSS.

The AHSS include Dual Phase (DP) steels, Complex-Phase (CP) steels, Ferritic-Bainitic (FB) steels, Martensitic (MS) steels, Transformation-Induced Plasticity (TRIP) steels, Hot-Formed (HF) steels, and Twinning-Induced Plasticity (TWIP) steels [3].

DP steels have a microstructure of ferrite and martensite. The soft, continuous, ferrite matrix produces good formability. The hard martensitic phase is dispersed in the ferrite matrix and contributes to the high strength, and high strain hardening. As a result, vehicle

components made from DP steels have a high capacity to absorb energy [5]. DP steel components may be galvanised for corrosion protection in service.

Transformation induced plasticity (TRIP) steels have a microstructure of a ferrite matrix, islands of retained austenite, and dispersed bainite. Martensite is also commonly present. Transformation of retained austenite to martensite causes the transformation induced plasticity, and also causes an increased strain hardening rate at higher strain levels [6]. TRIP steel components also have a good ability to absorb energy [5].

Quenching and partitioning (Q&P) is a new heat treatment to produce TRIP steel. The microstructure [7] contains more retained austenite at room temperature [8, 9], resulting in a greater TRIP effect. As a result, their ductility, formability and strain-hardening rate are greater than other steels with comparable strength. Q&P steels are thus third generation AHSS with high strength and high-ductility [10].

1.2 Hydrogen sources in service

Hydrogen embrittlement (HE) can occur in AHSS [11, 12]. The hydrogen can be liberated by corrosion of the steel of the car body in service. In neutral and alkaline solutions, the hydrogen evolution occurs by the following cathodic partial reaction [13]:

$$H_2O + M + e \rightarrow MH_{ads} + OH^- \quad (1)$$

where M represents the metal surface and MH_{ads} represents hydrogen adsorbed on the metal surface. The atomic hydrogen may be desorbed by the desorption reaction given by Eq. (2), through which two adsorbed hydrogen atoms combine to a molecule of hydrogen that leaves the metal surface, or by the electrochemical desorption reaction given by Eq. (3).

$$2MH_{ads} \leftrightarrow H_2 + 2M \quad (2)$$

$$MH_{ads} + H_2O + e \rightarrow H_2 + OH^- + M \quad (3)$$

Some of the adsorbed hydrogen enters the metal, MH_{abs}, by the following equilibrium reaction:

$$MH_{ads} \leftrightarrow MH_{abs} \quad (4)$$

The hydrogen in the steel, in combination with an applied stress, can cause hydrogen embrittlement (HE), which is of particular concern for high-strength steels [14], such as the AHSS.

1.3 Hydrogen trapping

Hydrogen diffusion is often studied using the permeation technique of Devanathan and Stachurski [15]. This permeation method can provide quantitative information, such as the effective hydrogen diffusion coefficient, D_{eff}, the hydrogen concentration, C_H, and the hydrogen trapping site density. This permeation technique was used in the present research to study hydrogen diffusion and trapping in DP and Q&P AHSS.

Hydrogen atoms are located in interstitial sites and are trapped by microstructure features such as voids, dislocations, grain boundaries, carbide interfaces, and impurities [16-18]. These hydrogen traps play an important role in the transportation and distribution of hydrogen in the steel [18]. Hydrogen traps are characterized as irreversible traps and reversible traps [19-21]. Irreversible traps are sites with a high trap activation energy, and thus the trapped hydrogen is considered as non-diffusible. Examples of irreversible traps are carbide interfaces, incoherent precipitates, and high-angle grain boundaries. In contrast, hydrogen de-trapping is easier from trap sites with lower activation energy. These sites are characterized as reversible traps. Examples are dislocations, low-angle grain boundaries, coherent precipitates and twin boundaries. Hydrogen trapped in reversible hydrogen trap sites is diffusible. These reversible hydrogen traps influence hydrogen diffusion and have an influence on the hydrogen embrittlement of the steel [22].

Hydrogen trapping can be characterised by the parameters: the hydrogen-trap binding energy, E_b, and the density of trap sites, N_t. Hydrogen trapping was incorporated into a kinetic diffusion model by McNabb and Foster [23]. This model was reformulated by Oriani [24] using the assumption that there is a local equilibrium between trapped hydrogen atoms and mobile hydrogen. Based on the Oriani [24] model, Dong et al. [25] proposed that the number of hydrogen-trap sites per unit volume, N_t, could be evaluated from:

$$\ln\left(\frac{D_L}{D_{eff}} - 1\right) = \ln\frac{N_t}{N_L} + \frac{E_b}{RT} \quad (5)$$

where, D_L is the lattice diffusion coefficient for hydrogen, D_{eff} is the effective diffusion coefficient for hydrogen in the presence of traps, N_L is the density of the interstitial sites in the steel, E_b is the hydrogen-trap binding energy, R is the gas constant, and T is the absolute temperature. This model is designated as the Oriani-Dong model in this paper.

Hydrogen trapping can be minimized by successive partial permeation rise transients after which the following permeation rise transients are controlled by lattice diffusion, because all the hydrogen traps are full [26, 27].

Permeation decay transients, in contrast, are sensitive to the de-trapping of hydrogen, and can be used to evaluate the amount of reversibly trapped hydrogen [27-29], as illustrated in Fig. 1, adapted from Liu and Atrens [29]. The area under the experimental desorption permeation curve corresponds to the total amount of diffusible and trapped hydrogen. The area under the corresponding theoretical permeation decay curve, evaluated using the lattice diffusion coefficient, D_L, corresponds to the amount of diffusible hydrogen. By subtraction, the area difference between the two curves, as illustrated by the shaded part in Fig. 1, represents the amount of reversible trapped hydrogen. This method is called the permeation curve method herein.

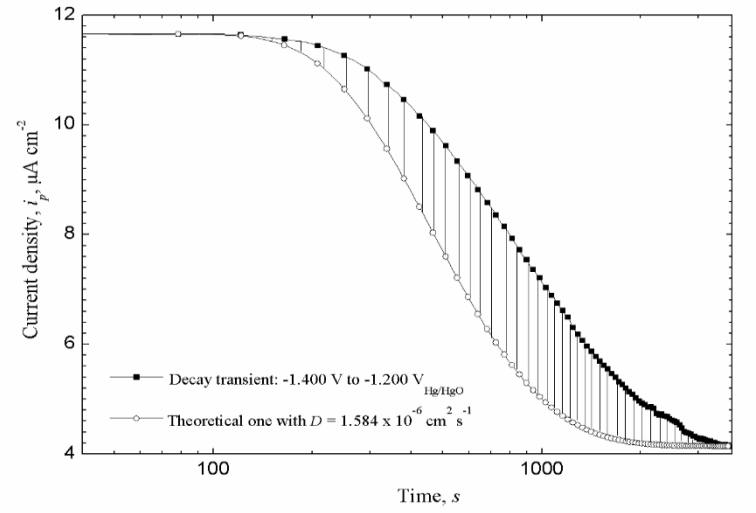

Fig. 1. The typical area difference (shaded part) between the integration of the permeation curve and the theoretical one for a decay transient from a 980 DP-GI (650 MPa YS) steel in 0.1 M NaOH solution.

The permeation curve method indicates that the density of reversible hydrogen traps, designated as N_t^*, is given by [27, 29]:

$$N_t^* = \frac{12.5 \times 10^{18}\ s}{L} \tag{6}$$

where s is the difference in area between the experimental decay curve and the theoretical decay curve evaluated using the lattice diffusion coefficient, D_L, and L is the thickness of the specimen. Eq. (6) assumes that there is only one type of reversible trap for hydrogen, and that each trap holds one hydrogen atom.

The concentration of the trapped hydrogen is given by [29]:

$$C_T^* = \frac{N_t^*}{N_A} \tag{7}$$

where N_A is the Avogadro constant with value of 6.02×10^{23} mol^{-1}.

This permeation curve method was applied by Zakroczymski [27] to Armco iron. Complete decay transients, where complete discharge was allowed, indicated that the reversibly trapped hydrogen corresponded to 98% of the total amount of absorbed hydrogen. This method was also used to measure the density of reversible hydrogen traps influencing hydrogen diffusion between cathodic charging potentials of $-1.700\ V_{Ag/AgCl}$ and $-1.100\ V_{Ag/AgCl}$ for a 3.5NiCrMoV medium strength steel [29]. The density of reversible traps was $\sim 10^{18}$ sites cm^{-3}. In this case the total amount of trapped hydrogen was not measured.

These techniques have not been applied to advanced high strength steels (AHSS) to measure the density of hydrogen traps.

1.4 Scope of current research

The current work (i) studies hydrogen diffusion in DP and Q&P grades of AHSS using permeability experiments, (ii) evaluates the density of reversible hydrogen traps that influence the hydrogen diffusion under these charging conditions using (a) the Oriani-Dong model and (b) the permeation curve method, and (iii) evaluates the total density of reversible hydrogen trap sites from complete permeation decay curves.

2. Experimental Methods

2.1 Materials

The DP and Q&P steels were commercial steels, supplied as rolled sheets, and were designated as follows: 980 DP, 980 DP-GI (650 MPa YS), 980 DP-GI (700 MPa YS), 1200 DP-GI, and 980 QP. The average sheet thicknesses were 1.35 mm for 980 DP and 1200 DP-GI, 0.95mm for 980 DP-GI (650 MPa YS), 0.99 mm for 980 DP-GI (700 MPa YS), and 1.93 mm for 980 QP. Table 1 presents the chemical composition and mechanical properties as provided by the steel supplier.

The microstructures of the DP and Q&P steels were examined using a light microscope (LM), and using a scanning electron microscope (SEM), after metallographic polishing to 1 μm and etching with a nital solution. The volume fraction of each phase was evaluated using the point counting method, as described in ASTM E562 [30]. The grain size were estimated by the linear intercept method [31, 32] for DP steels, and using the microscope calibration bar for Q&P steels.

Table 1 Chemical composition (in wt %) and mechanical properties of the DP and QP steels.

Steel designation	C	Si	Mn	Al	Nb	Ti	Cr	Yield stress, MPa	Tensile stress, MPa	Elongation at fracture, e_f, %
980 DP	0.09	0.28	2.26	0.03	0.004	0.02	0.54	590	930	8
980 DP-GI (650MPa YS)	0.09	0.29	2.19	0.03	0.04	0.03	0.43	650	1060	8
980 DP-GI (700MPa YS)	0.08	0.41	2.18	0.03	0.04	0.05	0.02	700	1040	7
1200 DP-GI	0.12	0.24	2.43	0.03	0.02	0.03	0.56	900	1200	5
980 QP	0.20	1.39	1.88	0.04	0.03	0.006	0.03	680	1020	11

Table 2 Quantitative metallography results for the DP and QP steels.

Steel Designation	Ferrite		Martensite		Bainite		Retained austenite	
	Relative amount %	Grain size μm	Relative amount %	Grain size μm	Relative amount %	Grain size μm	Relative amount %	Grain size μm
980 DP	40%	6.8	60%	5.5	0	-	0	-
980 DP (650 MPa YS)	37%	2.1	63%	1.5	0	-	0	-
980 DP (700 MPa YS)	36%	1.1	64%	1.4	0	-	0	-
1200 DP-GI	26%	5.0	74%	4.8	0	-	0	-
980 QP	39%	9.8	0	0	53%	9.4	8%	1.3

2.2 Permeability experiments

Fig. 2 presents the double cell, permeability apparatus, which was based on that of Devanathan and Stachurski [27], and was similar to that of Liu and Atrens [29]. The two cells were separated by the test specimen in the form of a flat sheet, which was the working electrode for each cell. Each cell also contained a 0.1 M NaOH solution, a Pt wire as the counter electrode, and a Luggin capillary connected to an Hg/HgO, KOH (20%) reference electrode, the potential of which is +0.098 V_{SHE}. Experiments were carried out at room temperature of 23 ± 2 ℃.

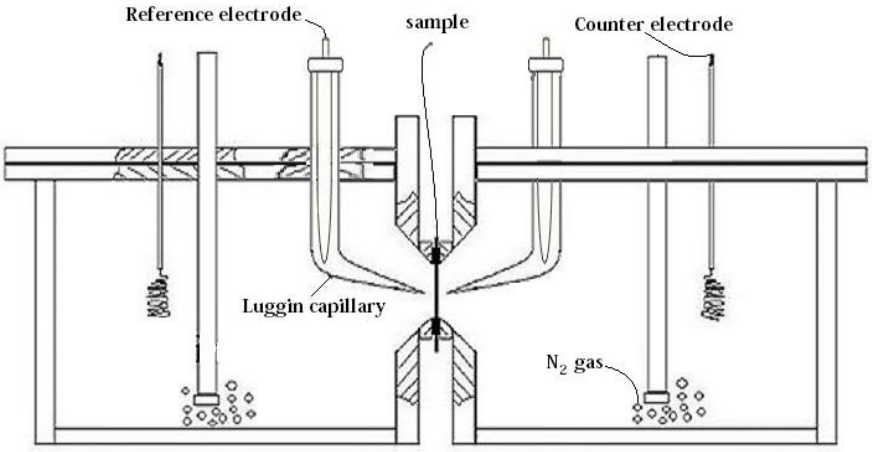

Fig. 2. Schematic of permeability cell.

The specimen side exposed to left-hand-side cell was polished to 3 μm. The left-hand-side cell was the hydrogen entry side. Hydrogen was liberated on the left-hand-side surface of the specimen by a negative potential applied using a MP 81 potentiostat.

The right-hand side was the hydrogen exit side. The 0.1 M NaOH solution was deaerated on this side to ensure a low background current density. N_2 was bubbled throughout the whole experiment to remove oxygen, which would contribute to the oxidation current density. The exit side background current density was lower than 0.2 μA cm^{-2} before cathodic charging commenced on the hydrogen entry side. On the right hand side, a PARSTAT 2273 potentiostat maintained a potential of +300 $mV_{Hg/HgO}$ to oxidise the emerging hydrogen, and the corresponding current measured the amount of permeated hydrogen.

The hydrogen exit side of the specimen was plated with palladium to prevent oxidation of the steel. The processes for palladium (Pd) plating was as follows: the specimen was ground to 1200 grit SiC paper on the side to be Pd coated; cleaned for 15 min at 80 ℃ in

an oil-removal aqueous solution, containing NaOH 16 g L^{-1}, Na_2CO_3 15 g L^{-1}, $Na_3PO_4 \cdot 12H_2O$ 15 g L^{-1} and detergent 2 ml L^{-1}; washed with distilled water, dried with flowing air, and weighed. The non-palladium-plating side was masked with an adhesive sticker and a conductive wire was attached to the edge of the specimen. The specimen was pickled in 32% HCl solution for 5 s and thoroughly washed with distilled water; electroplated in a solution consisting of 5 g $PdCl_2$ in 1 L of 25 wt% ammonia, at a current density of 2-3 mA cm^{-2} for 5 min with stirring during the whole plating time; rinsed immediately with ethanol, dried with flowing air and weighed. The increase in weight was used to calculate the thickness of the Pd coating, which was typically about 0.5 µm.

A long-time uninterrupted cathodic pre-charging was found by Zakroczymski [27, 33, 34] to stabilize the metal surface and minimized the surface effect. A similarly long-time pre-charging was used in this study. Pre-charging, at –1.600 $V_{Hg/HgO}$, was (i) for 48 hour for 980 DP-GI (650 MPa YS) and 980 DP-GI (700 MPa YS), and (ii) for 60 hour for 980 DP, 1200 DP-GI and 980 QP.

After the cathodic pre-charging, successive transients were measured, such as those from – 1.600 $V_{Hg/HgO}$ to – 1.700 $V_{Hg/HgO}$, as well as a transient loop from – 1.700 $V_{Hg/HgO}$ to – 1.100 $V_{Hg/HgO}$ and back to – 1.700 $V_{Hg/HgO}$. The potentials for the transient loop were: – 1.700 $V_{Hg/HgO}$, – 1.600 $V_{Hg/HgO}$, – 1.400 $V_{Hg/HgO}$, – 1.200 $V_{Hg/HgO}$, – 1.100 $V_{Hg/HgO}$, and similarly back to – 1.700 $V_{Hg/HgO}$.

After the permeation current density achieved steady state at – 1.700 $V_{Hg/HgO}$, the charging potential at the entry side was set to the open circuit potential (ocp) so that there was no hydrogen produced on the entry side, and a complete decay transient was measured.

The same experimental sequence was carried out for each steel.

The permeation transients have the following form [27, 35]

$$i_n = \frac{i_p - i_p^0}{i_p^\infty - i_p^0} = \frac{2L}{\sqrt{\pi Dt}} \sum_{n=0}^{\infty} \exp\left(-\frac{(2n+1)^2 L^2}{4Dt}\right) \qquad \text{(Rise transients)} \qquad (8)$$

$$i_n = \frac{i_p - i_p^\infty}{i_p^0 - i_p^\infty} = 1 - \frac{2L}{\sqrt{\pi Dt}} \sum_{n=0}^{\infty} \exp\left(-\frac{(2n+1)^2 L^2}{4Dt}\right) \qquad \text{(Decay transients)} \qquad (9)$$

where i_n is the normalized current, which increases from 0 to 1 for a rise transient, i_p is the measured permeation current density at time t, i_p^0 is the initial steady-state permeation rate at time t = 0, i_p^∞ is the new steady-state permeation current density, and L is the thickness of the steel sheet. For the first charging, $i_p^0 = 0$, and for the complete decay $i_p^\infty = 0$. The experimental permeation curves were fitted to Eq. (8) or (9), to determine the diffusion coefficient, D.

During the first few transients, there were empty traps, which would retard hydrogen diffusion, so that the fitted D values were considered as the effective diffusion coefficient, D_{eff}. For subsequent transients, most of the traps were filled, and the evaluated D values were similar to each other and were close to the lattice value, especially for transients at more negative potentials with less trapping effect, and the lattice diffusion coefficient, D_L, could be determined [26, 29].

The lattice hydrogen concentration, C_L, at the sub-surface on the cathodic side, was calculated from:

$$C_L = \frac{i_p^{\infty} L}{F D_L} \tag{10}$$

and the total hydrogen concentration, C_T, was evaluated from

$$C_T = \frac{i_p^{\infty} L}{F D_{eff}} \tag{11}$$

where F is the Faraday constant, L is the thickness of the membrane, i_p^{∞} is the steady-state permeation rate, D_L is the lattice diffusion coefficient of hydrogen in the specimen material, and D_{eff} is the measured effective diffusion coefficient of hydrogen in the specimen material. The hydrogen concentration, C, was expressed in units of mol m^{-3}, and was also converted to µg g^{-1}, which represented the weight of hydrogen per gram of the steel.

The density of reversible traps was evaluated using (i) the Oriani-Dong model and (ii) the permeation curve method, as outlined in the Introduction.

3. Results

3.1 Microstructure

Fig. 3(a) presents a SEM image of the typical DP steel microstructure, which consisted of the ferrite matrix, marked ‘F’, and martensite islands (M) embedded along ferrite grain boundaries. The martensite, as revealed by the nital etchant, consisted of a needle-like structure and appeared embossed. The ferrite appeared dark and smooth, and not as embossed as the martensite. Table 2 presents the relative amounts and grain sizes of the constituent phases in each steel. There was a decreasing amount of ferrite and an increasing amount of martensite for the DP steels in the following order 980 DP, 980 DP-GI (650 MPa YS), 980 DP-GI (700 MPa YS) and 1200DP-GI. This correlated with the increasing yield strength. The ferrite and martensite grain sizes were comparable.

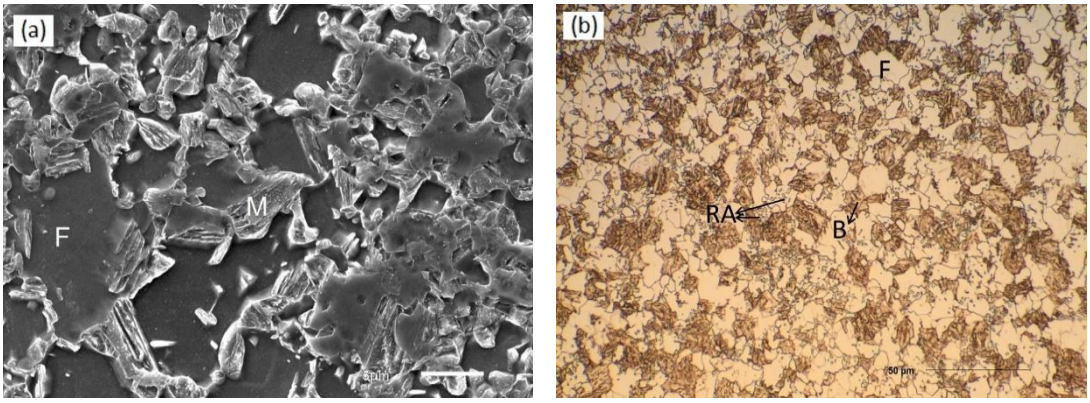

Fig. 3. Microstructures of (a) 980 DP steel observed under SEM and (b) 980 QP steel viewed with light microscope. M stands for martensite, F is for ferrite, B is for bainite and RA refers to retained austenite.

Fig. 3(b) presents a typical microstructure of the 980 QP steel viewed with a light microscope. The microstructure consisted of ferrite, bainite and retained austenite. The ferrite appeared yellow. The bainite appeared brown. The retained austenite appeared as the small white blocks dispersed in the ferrite and the bainite. Table 2 indicates that the volume fraction of ferrite, bainite and retained austenite was 39%, 53% and 8%, respectively. The grain sizes of ferrite and martensite were similar and were significantly larger than that of the retained austenite.

3.2 Cathodic pre-charging

Fig. 4 presents the hydrogen permeation current density versus time for the four DP steels and the Q&P steel during long-time pre-charging in the 0.1 M NaOH solution at –1.600 $V_{Hg/HgO}$, which was started after the background current density in the right hand cell decreased to less than 0.2 μA cm^{-2}. The breakthrough time was about 315 s, 1235 s, 1503 s, 1184 s and 810 s for 980 DP, 980 DP-GI (650 MPa YS), 980 DP-GI (700 MPa YS), 1200 DP-GI, and 980 QP, respectively. Thereafter, the current density increased significantly, reached a maximum for 980 DP-GI (650 MPa YS) and 980 DP-GI (700 MPa YS) and decreased somewhat for these steels. The significant increase in permeation current density with cathodic pre-charging time was consistent with the literature [33, 34], and is attributed to a stabilisation of the steel surface due to (i) the reduction of some of the air-formed oxide, which increased the surface coverage of hydrogen, and (ii) the weakening of the bonding force between the adsorbed hydrogen and the steel, which facilitated hydrogen absorption by reaction (4). The subsequent decrease of the permeation current density at longer charging times is attributed to the formation of surface products such as iron oxy-hydroxide, which provide some hindrance of the entry of adsorbed hydrogen into the steel.

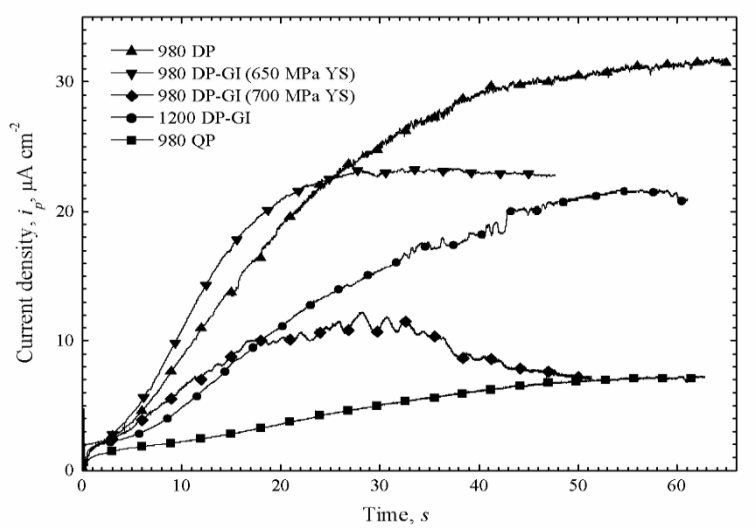

Fig. 4. Hydrogen permeation current density vs. time for the steels during long time pre-charging in 0.1 M NaOH solution at –1.600 $V_{Hg/HgO}$.

The maximum current density indicated approximately steady-state hydrogen charging conditions. These conditions were reached for 980 DP-GI (650 MPa YS) and 980 DP-GI (700 MPa YS) in about 33 hour, at which time the steady-state current density was 23 μA cm^{-2} and 13 μA cm^{-2}, respectively. For 980 DP, 1200 DP-GI and 980 QP steels, reaching steady state required about 60 hour, at which time the steady-state current density was 32 μA cm^{-2}, 21 μA cm^{-2} and 7 μA cm^{-2}, respectively.

Pre-charging was carried out for the subsequent experiments for 48 hour for the 980 DP-GI (650 MPa YS) and 980 DP-GI (700 MPa YS) steels, and 60 hour for the other steels, so that there would be a similar surface state.

3.3 Permeation Transients

Fig. 5(a) presents two typical subsequent partial rise transients. These were identical, indicating that the long-time pre-charging had filled the reversible traps. Fig. 5(b) shows corresponding decay transients. The second decay transient was slower, indicating that it took longer time for the hydrogen to permeate through the steel sheet specimen to reach steady state, due to the retardation of hydrogen diffusion by trapping.

Table 3 presents values of the diffusion coefficient, evaluated by fitting Eq. (8) and (9) by Matlab to each experimental permeation transient, obtained from successive transients and from the transient loop. The values of diffusion coefficient were similar for the first two rise transients from –1.600 $V_{Hg/HgO}$ and – 1.700 $V_{Hg/HgO}$ after long time pre-charging, and these values of the diffusion coefficient are identified as the lattice diffusion coefficient, D_L. The diffusion coefficients measured for the subsequent decay transients gave decreasing values of

D_{eff}. Thereafter the partial rise transients gave values of the effective diffusion coefficient, D_{eff}, that increased towards the value for the lattice diffusion coefficient.

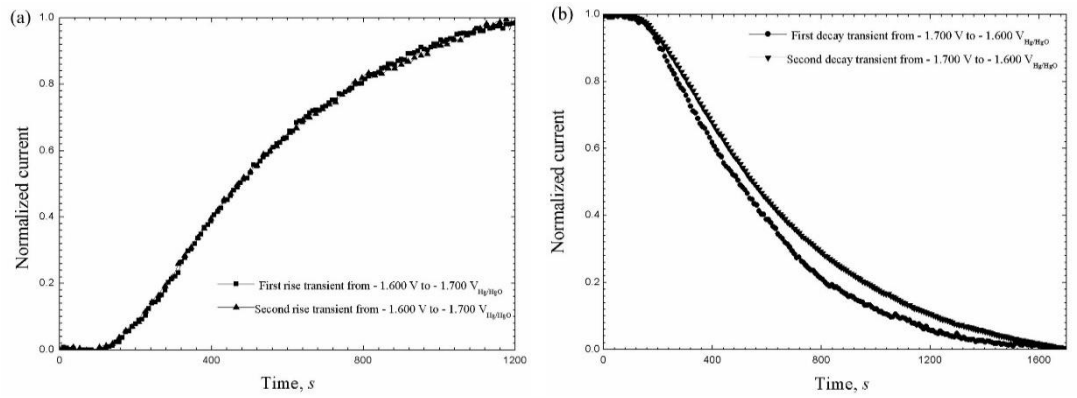

Fig. 5. The normalized current (as defined by Eq. (8) and (9)) of two sequential (a) rise and (b) decay transients between –1.700 $V_{Hg/HgO}$ and –1.600 $V_{Hg/HgO}$ for 980 DP-GI (645 MPa YS) in 0.1 M NaOH solution. For a rise transient, the normalised current is equal to (the measured current minus the initial current) divided by (the difference between the final current and the initial current). For a decay transient, the normalised current is equal to (the initial current minus the measured current) divided by (the difference between the initial current and the final current). The normalized current is identical to the normalized current density.

Fig. 6 presents the fitting of rise and decay transients to the theoretical curves for 980 DP-GI (650 MPa YS) steel. Fig. 6(a) shows the normalized experimental rise transient from – 1.600 $V_{Hg/HgO}$ and – 1.700 $V_{Hg/HgO}$, which was well fitted by the theoretical curve. This indicated that when the cathodic potential decreased to the more negative value, the hydrogen concentration at the subsurface immediately changed to the new constant value, the hydrogen diffusion was controlled by lattice diffusion, and that trapping was negligible. The fitted value of 1.58×10^{-6} cm^2 s^{-1} was identified as the hydrogen lattice diffusion coefficient, D_L, for 980 DP-GI (650 MPa YS) steel. In contrast, for the decay transients, as shown in Fig. 6(b), the fitting was not as good as those for rise transients, attributed to the influence of trapping.

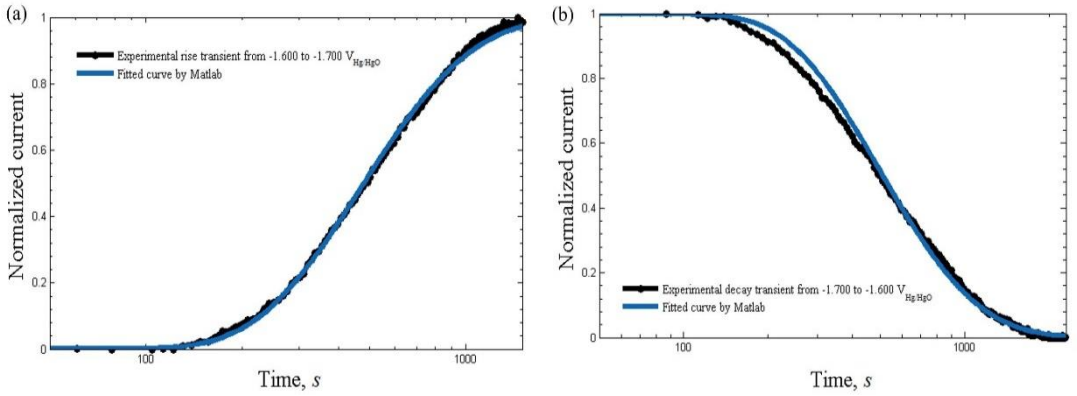

Fig. 6. Fitted curves (a) for a rise transient from – 1.600 $V_{Hg/HgO}$ to – 1.700 $V_{Hg/HgO}$ by Matlab and (b) for a decay transient from – 1.700 $V_{Hg/HgO}$ to – 1.600 $V_{Hg/HgO}$ for 980 DP-GI (650 MPa YS) specimen in 0.1 M NaOH solution. For a rise transient, the normalised current is equal to (the measured current minus the initial current) divided by (the difference between the final current and the initial current). For a decay transient, the normalised current is equal to (the initial current minus the measured current) divided by (the difference between the initial current and the final current).

There was the same trend for each steel. This allowed determination of the hydrogen lattice diffusion coefficient, D_L, for each steel: 2.07×10^{-6} cm^2 s^{-1}, 0.76×10^{-6} cm^2 s^{-1}, 1.27×10^{-6} cm^2 s^{-1} and 0.68×10^{-6} cm^2 s^{-1} for 980 DP, 980 DP-GI (700 MPa YS), 1200 DP-GI and 980 QP steels, respectively.

Fig. 7 presents a transient loop from – 1.700 $V_{Hg/HgO}$ to – 1.100 $V_{Hg/HgO}$ and back to – 1.700 $V_{Hg/HgO}$ in the 0.1 M NaOH solution for 980 DP-GI (650 MPa YS) steel. Each transient was a partial transient, which meant that there was always a significant charging potential applied to the specimen, and the specimen was not allowed to completely discharge all hydrogen. Similar transient loops were also carried out for other DP and Q&P steel grades. Each experimental transient was fitted by Matlab to Eq. (8) or Eq. (9) to determine the hydrogen diffusion coefficient values.

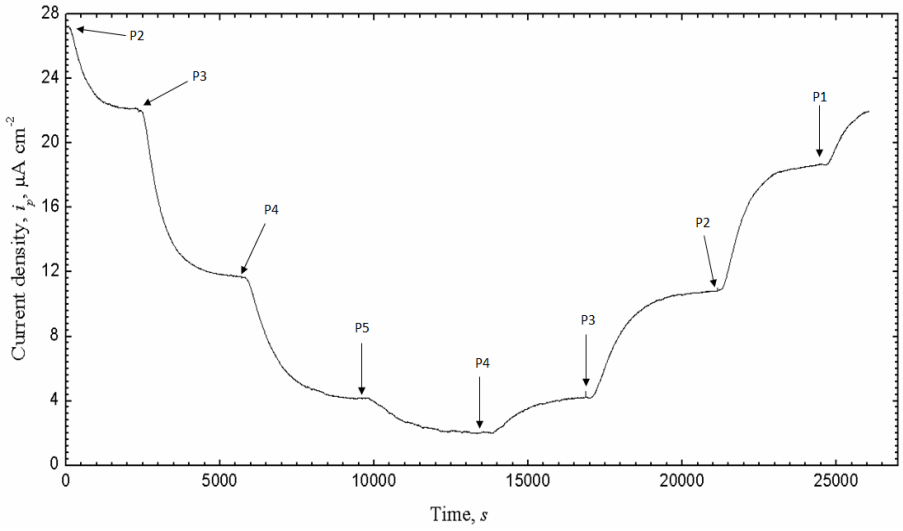

Fig. 7. Hydrogen permeation transients at different cathodic potentials at the input side of the 980 DP-GI (650 MPa YS) steel after 48 h pre-charging at – 1.600 $V_{Hg/HgO}$ in 0.1 M NaOH solution (P1: – 1.700 $V_{Hg/HgO}$, P2: – 1.600 $V_{Hg/HgO}$, P3: – 1.400 $V_{Hg/HgO}$, p4: – 1.200 $V_{Hg/HgO}$ and P5: – 1.100 $V_{Hg/HgO}$).

Table 3 presents the values of hydrogen diffusion coefficient, the steady-state current density and the hydrogen concentration, evaluated using Eq.(10). Fig. 7 and Table 3 indicate that as the charging potential was changed from – 1.700 $V_{Hg/HgO}$ to – 1.100 $V_{Hg/HgO}$ the steady-state current density and the hydrogen concentration at each potential decreased, indicating less hydrogen entered and permeated through the steel at a less negative charging potential. When the charging potential was increased from – 1.100 $V_{Hg/HgO}$ to – 1.700 $V_{Hg/HgO}$, there was more hydrogen entering and permeating through the specimen, providing a higher steady-state current density and hydrogen concentration. Venezuela et al. [36] stated that during cathodic charging in the 0.1M NaOH solution, an increasingly negative charging potential lead to an increased hydrogen fugacity, as also found by Liu et al. [33], and thus an

increased hydrogen concentration in the steel. They further found that this increased hydrogen concentration increased the susceptibility of martensitic advanced high strength steels to hydrogen embrittlement. The steady-state current density at – 1.700 $V_{Hg/HgO}$ at the end of the loop was somewhat lower than that at – 1.700 $V_{Hg/HgO}$ at the beginning of the loop, attributed to a slight change of the surface during the transients. This is consistent with the decrease of the permeation current density after peaking, as shown in Fig. 4.

4.0 Trap density evaluations

4.1 Oriani-Dong model

Table 4 presents the values of the density of reversible hydrogen trap sites, N_t, evaluated from the successive partial decay transients from the transient loop, evaluated using the Oriani-Dong model using Eq. (5) with (i) the hydrogen lattice diffusion coefficient as presented in part 3.3, (ii) $N_L = 7.2 \times 10^{22}$ cm^{-3} [25], (iii) $E_b = 28.9$ kJ mol^{-1} [16], and (iv) values of D_{eff} as listed in Table 3 for each transient. This particular value of binding energy was chosen because it is in the middle of the range of binding energies for reversible traps, and was the value used in our prior study [29].

Table 4 indicates that the trap density increased as the charging potential became less negative. For example, for 980 DP-GI (650 MPa YS), for the decay transient from the most negative charging condition from –1.700 $V_{Hg/HgO}$ to –1.600 $V_{Hg/HgO}$, the N_t value of 0.39×10^{17} sites cm^{-3} was the smallest. In contrast, the N_t value of 6.82×10^{17} sites cm^{-3} was the largest for decay transient that involved the least negative charging conditions (i.e. from –1.200 $V_{Hg/HgO}$ to –1.100 $V_{Hg/HgO}$). Similarly, for 980 QP, the minimum N_t value of 0.81×10^{17} sites cm^{-3} was evaluated for the transient from –1.700 $V_{Hg/HgO}$ to –1.600 $V_{Hg/HgO}$, whereas the maximum value of 5.40×10^{17} sites cm^{-3} was evaluated for the decay transient from –1.200 $V_{Hg/HgO}$ to –1.100 $V_{Hg/HgO}$. There was the same trend for each steel.

The hydrogen trap site density decreased with more negative charging during decay transients. This was attributed to the fact that the reversible traps in each steel were emptied step by step during successive each decay transient. At a less negative potential, more of the filled traps were emptied, leading to more interactions between the traps and diffused hydrogen, and thus there was a higher value for the trap site density. The trend that the hydrogen trap site density decreased with more negative charging potentials, resulting in a less potent trapping effect, was also consistent with the results that the hydrogen diffusion coefficient, D_{eff}, increased with more negative charging potential.

Table 3. Permeability parameter values for the DP and QP steels obtained from experimental transients cathodically charged in 0.1 M NaOH solution.

Steel designation	Thickness (L, cm)	Working area (S, cm^2)	Starting and finishing potential for transient, ($V_{Hg/HgO}$)	i_∞ ($\mu A\ cm^{-2}$)	$i_\infty \times L$ ($\mu A\ cm^{-1}$)	D_{eff} ($cm^2\ s^{-1}$)	C_L ($mol\ m^{-3}$)	C_L ($\mu g\ g^{-1}$)
980 DP	0.053	3.394	-1.600 to -1.700	39.99	2.12	2.07×10^{-6}	10.6	1.41
			-1.600 to -1.700	39.96	2.12	2.07×10^{-6}	10.6	1.41
			-1.700 to -1.600	32.33	1.71	2.00×10^{-6}	8.55	1.14
			-1.700 to -1.600	32.02	1.70	1.88×10^{-6}	8.51	1.13
			-1.600 to -1.400	15.04	0.80	1.61×10^{-6}	4.01	0.54
			-1.400 to -1.200	4.50	0.24	1.21×10^{-6}	1.20	0.16
			-1.200 to -1.100	2.14	0.11	1.06×10^{-6}	0.55	0.07
			-1.100 to -1.200	4.32	0.23	0.99×10^{-6}	1.15	0.15
			-1.200 to -1.400	12.37	0.66	1.16×10^{-6}	3.30	0.44
			-1.400 to -1.600	24.29	1.29	1.52×10^{-6}	6.45	0.86
			-1.600 to -1.700	29.51	1.56	1.77×10^{-6}	7.81	1.04
					Average:	$1.58 \pm 0.4 \times 10^{-6}$		
980 DP-GI (650 MPa YS)	0.075	3.308	-1.600 to -1.700	27.32	2.05	1.58×10^{-6}	13.4	1.94
			-1.600 to -1.700	27.08	2.03	1.56×10^{-6}	13.3	1.92
			-1.700 to -1.600	22.34	1.68	1.55×10^{-6}	11.0	1.59
			-1.700 to -1.600	22.06	1.65	1.49×10^{-6}	10.8	1.56
			-1.600 to -1.400	11.76	0.88	1.19×10^{-6}	5.77	0.83
			-1.400 to -1.200	4.06	0.30	0.86×10^{-6}	1.97	0.28
			-1.200 to -1.100	1.96	0.15	0.76×10^{-6}	0.98	0.14
			-1.100 to -1.200	4.10	0.31	0.72×10^{-6}	2.03	0.29
			-1.200 to -1.400	10.63	0.80	0.80×10^{-6}	5.25	0.76
			-1.400 to -1.600	18.20	1.37	1.11×10^{-6}	8.99	1.30
			-1.600 to -1.700	22.07	1.66	1.36×10^{-6}	10.9	1.57
					Average:	$1.18 \pm 0.3 \times 10^{-6}$		
980 DP-GI (700 MPa YS)	0.080	3.133	-1.600 to -1.700	10.55	0.84	0.75×10^{-6}	11.5	1.46
			-1.600 to -1.700	10.21	0.82	0.76×10^{-6}	11.2	1.42
			-1.700 to -1.600	8.27	0.66	0.71×10^{-6}	9.00	1.14
			-1.700 to -1.600	7.91	0.63	0.68×10^{-6}	8.59	1.09
			-1.600 to -1.400	4.13	0.33	0.60×10^{-6}	4.50	0.57
			-1.400 to -1.200	1.94	0.16	0.54×10^{-6}	2.18	0.28
			-1.200 to -1.100	1.36	0.11	0.49×10^{-6}	1.50	0.19

			-1.100 to -1.200	1.95	0.16	0.47×10^{-6}	2.18	0.28
			-1.200 to -1.400	3.80	0.30	0.51×10^{-6}	4.09	0.52
			-1.400 to -1.600	6.34	0.51	0.55×10^{-6}	6.95	0.88
			-1.600 to -1.700	9.20	0.74	0.64×10^{-6}	10.1	1.28
					Average:	$0.61 \pm 0.1 \times 10^{-6}$		
1200 DP-GI	0.070	2.997	-1.600 to -1.700	24.74	1.73	1.26×10^{-6}	14.1	1.37
			-1.600 to -1.700	23.97	1.68	1.27×10^{-6}	13.7	1.33
			-1.700 to -1.600	20.14	1.41	1.14×10^{-6}	11.5	1.12
			-1.700 to -1.600	19.61	1.37	1.21×10^{-6}	11.2	1.09
			-1.600 to -1.400	11.59	0.81	1.14×10^{-6}	6.61	0.64
			-1.400 to -1.200	4.91	0.34	0.93×10^{-6}	2.77	0.27
			-1.200 to -1.100	2.55	0.18	0.79×10^{-6}	1.47	0.14
			-1.100 to -1.200	5.14	0.36	0.77×10^{-6}	2.94	0.29
			-1.200 to -1.400	11.95	0.84	0.85×10^{-6}	6.86	0.67
			-1.400 to -1.600	18.54	1.30	1.05×10^{-6}	10.6	1.03
			-1.600 to -1.700	21.95	1.54	1.20×10^{-6}	12.6	1.22
					Average:	$1.05 \pm 0.2 \times 10^{-6}$		
980 QP	0.048	2.930	-1.600 to -1.700	10.00	0.48	0.66×10^{-6}	7.32	1.05
			-1.600 to -1.700	9.47	0.46	0.68×10^{-6}	7.01	1.01
			-1.700 to -1.600	7.85	0.38	0.63×10^{-6}	5.79	0.83
			-1.700 to -1.600	7.38	0.35	0.61×10^{-6}	5.33	0.77
			-1.600 to -1.400	4.15	0.20	0.50×10^{-6}	3.05	0.44
			-1.400 to -1.200	1.69	0.08	0.42×10^{-6}	1.22	0.18
			-1.200 to -1.100	0.93	0.05	0.36×10^{-6}	0.76	0.11
			-1.100 to -1.200	1.74	0.08	0.33×10^{-6}	1.22	0.18
			-1.200 to -1.400	3.69	0.18	0.40×10^{-6}	2.74	0.39
			-1.400 to -1.600	5.53	0.27	0.49×10^{-6}	4.12	0.59
			-1.600 to -1.700	8.66	0.42	0.57×10^{-6}	6.40	0.92
					Average:	$0.51 \pm 0.1 \times 10^{-6}$		

Table 4. The density of reversible hydrogen trap sites in the DP and Q&P steels for the successive partial decay transients from -1.700 $V_{Hg/HgO}$ to -1.100 $V_{Hg/HgO}$. N_T was evaluated using the Oriani-Dong model. N_T^* was evaluated using the permeation curve method.

Steel designation	Starting and finishing potential for transient, ($V_{Hg/HgO}$)	η, V, (at start of transient)	i_x, ($\mu A\ cm^{-2}$), (at end of transient)	D_{eff}, ($cm^2\ s^{-1}$), (average for transient)	N_t, (sites cm^{-3}), (at start of transient)	C_t, (mol m^{-3}), (at start of transient)	C_t, ($\mu g\ g^{-1}$), (at start of transient)	C_L, (mol m^{-3}), (at start of transient)	C_L, ($\mu g\ g^{-1}$), (at start of transient)	C_T, ($\mu g\ g^{-1}$), (at start of transient)	C_t / (C_t + C_L), (%)	N_t^*, (sites cm^{-3}), (average for transient)	C_t^*, (mol m^{-3}), (average for transient)	C_t^*, ($\mu g\ g^{-1}$), (average for transient)	C_L^*, (mol m^{-3}) , (at start of transient)	C_L^*, ($\mu g\ g^{-1}$) , (at start of transient)	C_t^* / (C_t^* + C_L^*), (%)
980 DP-GI	-1.700 to -1.600	-0.857	32.02	1.88×10^{-6}	0.65×10^{17}	0.11	0.015	10.6	1.410	1.556	1	0.69×10^{17}	0.11	0.015	11.1	1.476	1
	-1.600 to -1.400	-0.757	15.04	1.61×10^{-6}	1.82×10^{17}	0.30	0.040	8.51	1.130	1.447	3	2.91×10^{17}	0.48	0.064	8.76	1.168	5
	-1.400 to -1.200	-0.557	4.50	1.21×10^{-6}	4.42×10^{17}	0.73	0.097	4.01	0.535	0.911	15	5.15×10^{17}	0.85	0.113	5.13	0.684	14
	-1.200 to -1.100	-0.357	2.14	1.06×10^{-6}	5.93×10^{17}	0.99	0.132	1.20	0.160	0.311	45	1.31×10^{17}	0.22	0.029	1.05	0.140	17
				sum	12.8×10^{17}							10.1×10^{17}					
980 DP-GI (650 MPa YS)	-1.700 to -1.600	-0.857	22.06	1.49×10^{-6}	0.39×10^{17}	0.06	0.009	13.3	1.920	2.035	0.5	0.50×10^{17}	0.08	0.012	14.3	2.060	0.6
	-1.600 to -1.400	-0.757	11.76	1.19×10^{-6}	2.05×10^{17}	0.34	0.049	10.8	1.560	2.080	3	3.26×10^{17}	0.53	0.077	12.6	1.817	4
	-1.400 to -1.200	-0.557	4.06	0.86×10^{-6}	5.19×10^{17}	0.86	0.124	5.77	0.833	1.530	13	5.68×10^{17}	0.94	0.136	5.50	0.794	15
	-1.200 to -1.100	-0.357	1.96	0.76×10^{-6}	6.82×10^{17}	1.13	0.163	1.97	0.284	0.598	37	1.88×10^{17}	0.36	0.052	1.69	0.244	18
				sum	14.4×10^{17}							11.1×10^{17}					
980 DP-GI (700 MPa YS)	-1.700 to -1.600	-0.857	7.91	0.68×10^{-6}	0.70×10^{17}	0.12	0.015	11.2	1.420	1.572	1	0.95×10^{17}	0.16	0.020	13.1	1.658	1
	-1.600 to -1.400	-0.757	4.13	0.60×10^{-6}	1.67×10^{17}	0.28	0.036	8.59	1.090	1.383	3	1.87×10^{17}	0.31	0.039	7.27	0.922	4
	-1.400 to -1.200	-0.557	1.94	0.54×10^{-6}	2.61×10^{17}	0.43	0.055	4.50	0.571	0.804	9	2.40×10^{17}	0.40	0.051	6.25	0.793	6
	-1.200 to -1.100	-0.357	1.36	0.49×10^{-6}	3.44×10^{17}	0.57	0.072	2.18	0.276	0.415	21	1.02×10^{17}	0.17	0.022	1.60	0.203	10
				sum	8.42×10^{17}							6.24×10^{17}					
1200 DP-GI	-1.700 to -1.600	-0.857	19.61	1.21×10^{-6}	0.27×10^{17}	0.04	0.004	13.7	1.330	1.398	0.3	0.22×10^{17}	0.04	0.004	13.7	1.330	0.3
	-1.600 to -1.400	-0.757	11.59	1.14×10^{-6}	0.67×10^{17}	0.11	0.011	11.2	1.090	1.216	1	0.77×10^{17}	0.13	0.013	9.04	0.877	1
	-1.400 to -1.200	-0.557	4.91	0.93×10^{-6}	2.27×10^{17}	0.38	0.037	6.61	0.641	0.877	6	2.62×10^{17}	0.43	0.042	6.00	0.582	7
	-1.200 to -1.100	-0.357	2.55	0.79×10^{-6}	3.83×10^{17}	0.64	0.062	2.77	0.269	0.438	19	1.47×10^{17}	0.24	0.023	2.42	0.235	9
				sum	7.04×10^{17}							5.08×10^{17}					
980 QP	-1.700 to -1.600	-0.857	7.38	0.61×10^{-6}	0.81×10^{17}	0.13	0.019	7.01	1.010	1.112	2	0.71×10^{17}	0.12	0.017	12.5	1.796	1
	-1.600 to -1.400	-0.757	4.15	0.50×10^{-6}	2.21×10^{17}	0.37	0.053	5.33	0.767	1.056	7	1.01×10^{17}	0.17	0.024	7.97	1.147	2
	-1.400 to -1.200	-0.557	1.69	0.42×10^{-6}	3.97×10^{17}	0.66	0.095	3.05	0.439	0.708	18	8.51×10^{16}	0.14	0.020	3.11	0.448	5
	-1.200 to -1.100	-0.357	0.93	0.36×10^{-6}	5.40×10^{17}	0.90	0.130	1.22	0.176	0.338	42	5.51×10^{16}	0.09	0.013	1.30	0.187	7
				sum	12.4×10^{17}							3.12×10^{17}					

The density of the emptied reversible trap sites provided the amount of reversible trapped hydrogen for a particular condition, if it is assumed that there was only one hydrogen atom trapped at each reversible trap. For example, for 980 DP-GI (650 MPa YS) steel, when the charging potential was decreased from –1.700 $V_{Hg/HgO}$ to –1.600 $V_{Hg/HgO}$, the N_t value was 0.39×10^{17} sites cm^{-3}, indicating that 0.39×10^{17} sites cm^{-3} were emptied under this charging condition, and the trapped hydrogen concentration C_t was ~ 0.06 mol m^{-3} at –1.700 $V_{Hg/HgO}$. For comparison, the lattice hydrogen concentration, C_L, was calculated from Eq. (10), which at –1.700 $V_{Hg/HgO}$ was calculated to be 13.3 mol m^{-3}. Thus, the reversibly trapped hydrogen accounted for 0.5 % of the total absorbed hydrogen, which was the sum of trapped and lattice hydrogen.

Using this approach, for 980 DP-GI (650 MPa YS) steel, the amount of reversibly trapped hydrogen was equal to 3 %, 13 % and 37 % of the total absorbed hydrogen for the decay transient from –1.600 $V_{Hg/HgO}$ to –1.400 $V_{Hg/HgO}$, from –1.400 $V_{Hg/HgO}$ to –1.200 $V_{Hg/HgO}$, and from –1.200 $V_{Hg/HgO}$ to –1.100 $V_{Hg/HgO}$, respectively. The increasing portion of trapped hydrogen was consistent with the fact that the hydrogen trapping effect was more significant at a less negative charging potential.

Similarly, the percentage of trapped hydrogen at each charging potential from –1.700 $V_{Hg/HgO}$ to –1.600 $V_{Hg/HgO}$, from –1.600 $V_{Hg/HgO}$ to –1.400 $V_{Hg/HgO}$, from –1.400 $V_{Hg/HgO}$ to –1.200 $V_{Hg/HgO}$, and from –1.200 $V_{Hg/HgO}$ to –1.100 $V_{Hg/HgO}$, was 1 %, 3 %, 15 % and 45 %, respectively, for 980 DP steel, and the corresponding percentage at each charging potential was 1 %, 3 %, 9 % and 21 % for 980 DP-GI (700 MPa YS) steel, 0.3 %, 1 %, 6 % and 19 % for 1200DP-GI steel and 2 %, 7 %, 18 % and 42 % for 980 QP steel.

It is assumed that the reversible hydrogen traps were emptied step by step during the partial transients. The total density of the emptied traps could be considered as the sum of traps evaluated from each transient. Thus, the density of hydrogen trap sites for the decay transients from –1.700 $V_{Hg/HgO}$ to –1.100 $V_{Hg/HgO}$ was 12.8×10^{17} sites cm^{-3} for 980 DP, 14.4×10^{17} sites cm^{-3} for 980 DP-GI (650 MPa YS), 8.42×10^{17} sites cm^{-3} for 980 DP-GI (700 MPa YS), 7.04×10^{17} sites cm^{-3} for 1200 DP-GI and 12.4×10^{17} sites cm^{-3} for 980 QP steel.

Table 4 also includes values of the total hydrogen concentration, C_T, evaluated using Eq.(11). This value of total trapped hydrogen was in good agreement with the value of trapped hydrogen evaluated as the sum of trapped hydrogen concentration, C_t, and the lattice hydrogen concentration, C_L.

4.2 Permeation curves

Fig. 8(a) presents the decay transients obtained at various applied potentials and the theoretical curve calculated with a D_L value of 1.58×10^{-6} cm^2 s^{-1} for 980 DP-GI (650 MPa YS). Fig. 8(b) presents the corresponding normalised curves. The area difference, between each decay transient curve and the theoretical curve, is shown shaded in Fig. 8(a). This area increased with less negative applied potential and then decreased for the transient from –1.200 $V_{Hg/HgO}$ to –1.100 $V_{Hg/HgO}$. As stated above in the Introduction, the area difference between the experimental curve and the theoretical curve provided a measurement of the amount of trapped hydrogen. Thus, the general increased area difference indicated that there was more hydrogen trapped at a less negative potential, consistent with a more potent trapping effect at a less negative potential. This same trend also occurred for each DP and Q&P steel, indicating that a more potent trapping effect at a less negative potential for each steel.

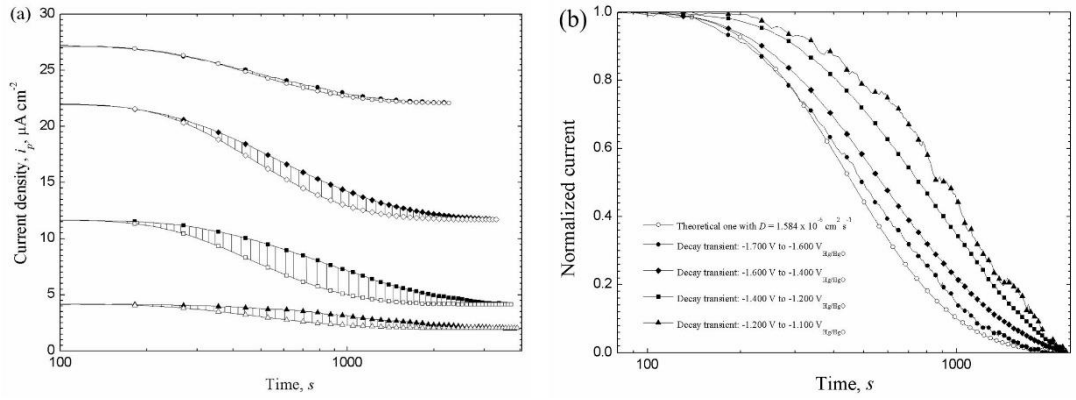

Fig. 8. (a) The area difference between the experimental permeation curves (full symbols) and the theoretical curve (open symbols) for decay transients for 980 DP-GI (650 MPa YS) in 0.1 M NaOH solution: (1) circles – experimental decay transient from –1.700 $V_{Hg/HgO}$ to –1.600 $V_{Hg/HgO}$, theoretical curve with D = 1.584×10^{-6} cm^2 s^{-1}; (2) diamonds – experimental decay transient from –1.600 $V_{Hg/HgO}$ to –1.400 $V_{Hg/HgO}$, theoretical curve with D = 1.584×10^{-6} cm^2 s^{-1}; (3) squares – experimental decay transient from –1.400 $V_{Hg/HgO}$ to -1.200 $V_{Hg/HgO}$, theoretical curve with D = 1.584×10^{-6} cm^2 s^{-1}; (4) triangles – experimental decay transient from –1.200 $V_{Hg/HgO}$ to –1.100 $V_{Hg/HgO}$, theoretical curve with D = 1.584×10^{-6} cm^2 s^{-1} and (b) the normalized experimental decay transients and the corresponded theoretical curve calculated with D value of 1.584×10^{-6} cm^2 s^{-1}. For a decay transient, the normalised current is equal to (the initial current minus the measured current) divided by (the difference between the initial current and the final current).

Table 4 presents the values for the density of reversibly trapped hydrogen, N_t^*, evaluated from the difference between the experimental permeation curve and the theoretical curve as illustrated in Fig. 8(a), and Eq. (6). Table 4 also presents the concentration of the trapped hydrogen, C_t^*, and the concentration of lattice hydrogen, C_L^*, which was evaluated based on the proportion of the shaded area to the area below the theoretical curve. Due to different values of i_0 and i_∞, the area below the theoretical curve was different for each partial

decay transient, resulting in changed values of C_L^*. From –1.700 $V_{Hg/HgO}$ to –1.100 $V_{Hg/HgO}$ for the 980 DP-GI (650 MPa YS) steel, the trap site density, N_t^*, was 0.50 × 10^{17} sites cm^{-3}, 3.26 × 10^{17} sites cm^{-3}, 5.68 × 10^{17} sites cm^{-3}, 1.88 × 10^{17} sites cm^{-3} for each successive decay transient. The trap site density value, N_t^*, from –1.700 $V_{Hg/HgO}$ to –1.600 $V_{Hg/HgO}$ was comparable to that, N_t, obtained using Oriani-Dong model, for 980 DP-GI (650 MPa YS) and also for each steel. In general, the trap site density was higher at a less negative potential for each steels evaluated using this permeation curve method.

For the 980 DP-GI (650 MPa YS) steel, the concentration of trapped hydrogen for the decay transient from –1.400 $V_{Hg/HgO}$ to –1.200 $V_{Hg/HgO}$, as shown in Fig. 8(a), was calculated to be ~ 0.94 mol m^{-3}. Based on the area below the theoretical curve, the corresponding lattice hydrogen concentration at –1.400 $V_{Hg/HgO}$ was calculated to be ~ 5.50 mol m^{-3}. The trapped hydrogen corresponded to 15 % of the total amount of hydrogen from –1.400 $V_{Hg/HgO}$ to –1.200 $V_{Hg/HgO}$. Correspondingly, the reversibly trapped hydrogen from –1.700 $V_{Hg/HgO}$ to –1.600 $V_{Hg/HgO}$, from –1.600 $V_{Hg/HgO}$ to –1.400 $V_{Hg/HgO}$, from –1.400 $V_{Hg/HgO}$ to –1.200 $V_{Hg/HgO}$, and from –1.200 $V_{Hg/HgO}$ to –1.100 $V_{Hg/HgO}$, accounted for 0.6 %, 4 %, 15% and 18 % of the total absorbed hydrogen, respectively. The portion of trapped hydrogen also increased with less negative potential, consistent with the results from Oriani-Dong model.

Table 4 also presents the calculated N_t^*, C_t^* and C_L^* values for all the other steels. In all cases the percentage of trapped hydrogen increased from –1.700 $V_{Hg/HgO}$ to –1.100 $V_{Hg/HgO}$. The percentage of trapped hydrogen was 1 %, 5 %, 14 % and 17%, respectively for 980 DP steel; 1 %, 4 %, 6 % and 10 % for 980 DP-GI (700 MPa YS) steel; 0.3 %, 1 %, 7 % and 9 % for 1200 DP-GI steel, and 1 %, 2 %, 5 % and 7 % for 980 QP steel.

The total density of reversibly trapped hydrogen was the sum of the density from each transient. The total trap site density influencing the hydrogen diffusion between –1.700 $V_{Hg/HgO}$ to –1.100 $V_{Hg/HgO}$ was 10.1 × 10^{17} sites cm^{-3} for 980 DP, 11.1 × 10^{17} sites cm^{-3} for 980 DP-GI (650 MPa YS), 6.24 × 10^{17} sites cm^{-3} for 980 DP-GI (700 MPa YS), 5.08 × 10^{17} sites cm^{-3} for 1200 DP-GI and 3.12 × 10^{17} sites cm^{-3} for 980 QP. The trap density values, N_t^*, for all the DP steels were between 20 ~ 30 % lower than those evaluated from Oriani-Dong model for the same steels. Similarly, the N_t^* value was 3.12 × 10^{17} sites cm^{-3} from the permeation curve method, about a quarter of the value obtained from Oriani-Dong model.

4.3 Complete decay transients

Fig. 9 presents the area difference between the experimental complete decay curve and the theoretical curve for 980 DP-GI (650 MPa YS) steel and 980 QP steel. The complete

decay transient curve was obtained by discharging on the hydrogen entry side, meaning the charging potential was changed to the open circuit potential (ocp) from –1.700 $V_{Hg/HgO}$, so that there was no hydrogen being introduced into the specimen. According to the permeation curve method, the area of the shaded parts in Fig. 9(a) and (b) reflect the total amount of reversible hydrogen trap sites that were emptied from –1.700 $V_{Hg/HgO}$ to 0 V_{SHE}, and the area below the theoretical curve provided the amount of lattice diffused hydrogen at –1.700 $V_{Hg/HgO}$. This area difference between the experimental complete decay curve and the theoretical one was obtained for all the steels. Table 5 presents the values of the trap site density N_t^*, the trapped hydrogen concentration C_t^*, the concentration of lattice diffused hydrogen C_L^* and the percentage of trapped hydrogen.

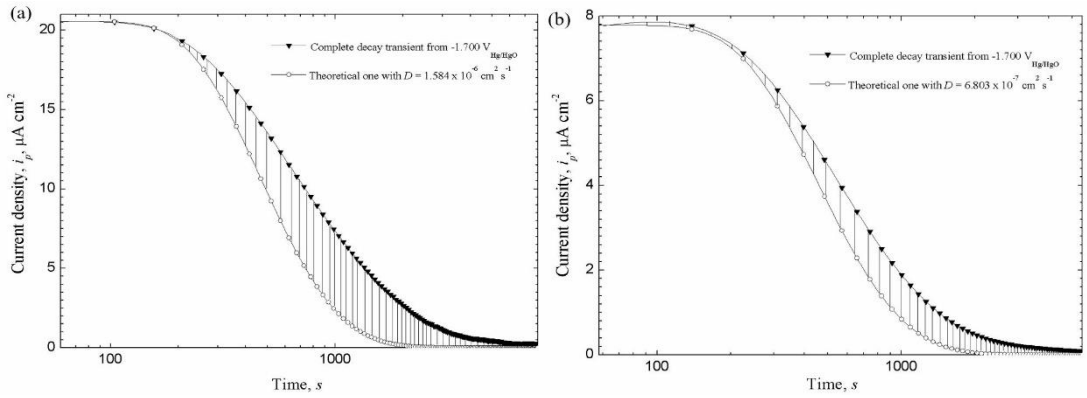

Fig. 9. The typical area difference between the experimental complete decay curve and the theoretical one for (a) 980 DP-GI (650 MPa YS) and (b) 980 QP steels in 0.1 M NaOH solution.

Table 5 indicated that, for 980 DP-GI (650 MPa YS) steel, the trap site density N_t^* from –1.700 $V_{Hg/HgO}$ to 0 V_{SHE} was 2.42 × 10^{18} sites cm^{-3}. Assuming one hydrogen atom occupied one trap site, the corresponding trapped hydrogen concentration was 4.02 mol m^{-3}, equivalent to 58 % of the total absorbed hydrogen.

For the three 980 DP steels, 980 DP, 980 DP-GI (650 MPa YS) and 980 DP-GI (700 MPa YS) steel, with increasing yield strength and decreasing grain size, the calculated reversible hydrogen trap site density increased from 1.88 × 10^{18} sites cm^{-3} to 2.42 × 10^{18} sites cm^{-3} and to 3.30 × 10^{18} sites cm^{-3}, and the corresponding percentage of trapped hydrogen in total absorbed hydrogen also increased from 54 % to 58 % and to 64 %. This was consistent with the results of the decreased diffusion coefficients for these three steel grades, caused by more hydrogen traps with finer grain sizes.

For 980 DP and 1200 DP-GI, which had similar grain sizes, the trap site density for 1200 DP-GI was 2.26 × 10^{18} sites cm^{-3}, 20 % higher than that of 1.88 × 10^{18} sites cm^{-3} for 980 DP steel, attributed to the higher martensite content that provided more trap sites in 1200 DP-GI.

The density of reversible hydrogen trap sites for 980 QP steel was 5.91×10^{17} sites cm^{-3} and was significantly lower, by a factor of 3 to 4, than that for the 980 DP steels. This was considered to result from the presence of retained austenite, acting as more potent hydrogen traps, and that the hydrogen trapped in austenite was not emptied during the complete decay transients. Sojka et al. [37] found that TRIP 800 steel absorbed much more hydrogen than other AHSS due to the higher retained austenite content. Zhu et al. [38], observed the hydrogen trap sites in Q&P steels directly using three-dimensional atom probe tomography (3DAPT). They found that austenite contained three times more hydrogen than martensite and the hydrogen trapping in ferrite was low due to the small solubility and fast diffusivity of hydrogen in the bcc iron structure. They further claimed that this retained austenite with high concentration of hydrogen could be detrimental source when the martensite transformation occurred, leading to susceptibility of the steels to hydrogen embrittlement, as also stated in other studies [39, 40]. Therefore, the stability of retained austenite was important to reduce the martensite transformation so that the high concentration of hydrogen in austenite would not assist the HE of the steel [41-43]. In addition, the size and morphology of the retained austenite were also stated to be decisive in terms of the resistance to HE [37, 44]. However, the stability and morphology of retained austenite are beyond the scope of this study.

5. Discussion

5.1 Charging conditions

In this study, the purpose of the pre-charging was (i) to condition the surface to a relatively stable state, which minimized the surface effect to allow reproducible permeation transients; and (ii) to fill all the irreversible and reversible hydrogen traps. During the pre-charging, it is considered that all traps were filled at random, but that the hydrogen in irreversible traps cannot escape. Thus, with sufficient pre-charging time, all the irreversible traps are filled and reversible traps are in equilibrium with the diffusible hydrogen. In subsequent permeation transients, only reversible traps are evaluated.

The successive partial transients did not allow complete dehydrogenation, and thus the irreversible traps remained saturated during the transients. The charging conditions for partial transients in this study correspond to the charging conditions for hydrogen embrittlement tests, and the evaluated density of reversible hydrogen trap sites correspond to each charging condition.

The complete decay transients, in contrast, allowed dehydrogenation on the hydrogen entry side. However, due to the high binding energy of irreversible hydrogen traps, ~ 56 kJ mol^{-1} [45], the irreversible hydrogen traps were unlikely to be emptied at a temperature of 25 ± 2 ℃. Thus, the trap site density evaluated from the complete decay in this study was also the density of reversible hydrogen trap sites.

5.2 Diffusion coefficients

Fig. 10 presents the measured diffusion coefficient for each steel at the different applied potentials from the transient loop. The error bars in Fig. 10 depict the standard deviation for the measured D_{eff} values. Fig. 10 and Table 3 indicate that, for the DP steels studied in this research, the values for effective diffusion coefficient were in the range of 0.5 × 10^{-6} cm^2 s^{-1} ~ 2.1 × 10^{-6} cm^2 s^{-1}, consistent with those from literature [46-49]. For 980 QP steel, the effective diffusion coefficient varied from 3 × 10^{-7} cm^2 s^{-1} to 7 × 10^{-7} cm^2 s^{-1}, in agreement with the range of 0.3 × 10^{-7} cm^2 s^{-1} to 6 × 10^{-7} cm^2 s^{-1} from other studies [41, 44, 47], despite the fact that different methods were used to determine the diffusion coefficient, which would lead to a variance of the values. For instance, Yang et al. [41] used two methods, the time lag method and the breakthrough method, to determine the hydrogen diffusion coefficient of their Q&P steels. The results obtained from both methods had a difference of least a factor of 2.

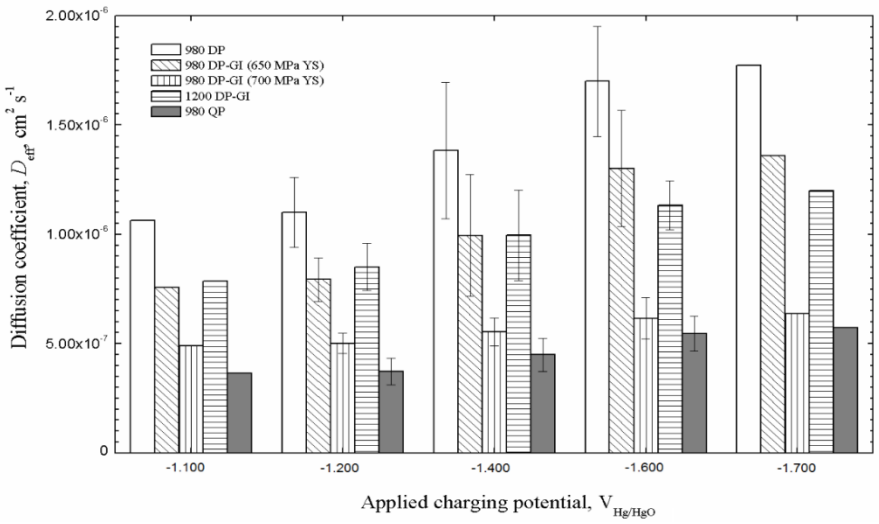

Fig. 10. Hydrogen diffusion coefficient values of the studied DP and Q&P steels during the transient loop from –1.700 $V_{Hg/HgO}$ to –1.100 $V_{Hg/HgO}$ and back to –1.700 $V_{Hg/HgO}$ in 0.1 M NaOH solution.

Fig. 10 and Table 3 further indicate that, for each steel, the diffusion coefficient increased with increasingly negative potential from – 1.100 $V_{Hg/HgO}$ to – 1.700 $V_{Hg/HgO}$ for

both the rise and decay transients. For example, at – 1.100 $V_{Hg/HgO}$, the value of hydrogen diffusion coefficient for 980 DP-GI (650 MPa YS) was 0.76×10^{-6} cm^2 s^{-1}, whilst at – 1.700 $V_{Hg/HgO}$, the D_{eff} value was 1.36×10^{-6} cm^2 s^{-1}. There was a similar trend for each steel. This trend was attributed to more potent trapping at a less negative charging potential. At a less negative potential, less hydrogen was produced and entered into the specimen, fewer traps were full, more traps were filled during the transient, and consequently the diffusion coefficient was lower. In comparison, there was a larger amount of generated hydrogen at more negative potentials, more hydrogen traps were full, and the empty traps had less influence on hydrogen diffusion coefficient.

5.3 Trap site densities

Table 4 indicates that that, for each of the DP and Q&P steels, with increasingly negative charging potential, from -1.100 $V_{Hg/HgO}$ to -1.700 $V_{Hg/HgO}$, the corresponding reversible hydrogen trap site density decreased. The increase in the effective diffusion coefficient with increasingly negative potential is attributed to a less potent trapping effect at a more negative potential. From -1.700 $V_{Hg/HgO}$ to -1.600 $V_{Hg/HgO}$, the trapped hydrogen corresponded to 1 % or less of the total absorbed hydrogen, and thus, the repeated transient from -1.600 $V_{Hg/HgO}$ to -1.700 $V_{Hg/HgO}$ could be used to determine the lattice diffusion coefficient. Furthermore, the effective diffusion coefficient decreased from the value of the lattice diffusion coefficient as the trap effect became greater.

Tables 3 and 4 indicate that, for the three 980 DP steel grades, with increasing yield strength and decreasing grain size, the values of the lattice diffusion coefficient and the values of the effective diffusion coefficient decreased slightly, but the hydrogen trap density increased from 980 DP to 980 DP-GI (650 MPa YS) and then decreased to 980 DP-GI (700 MPa YS). Thus the decrease in effective diffusion coefficient in this series is attributed to a combination of the decrease in lattice diffusion coefficient and the increase in trapping effect.

The values of the diffusion coefficient of 1200 DP-GI steel were somewhat lower than that of the 980 DP steel. The lower lattice diffusion coefficient of 1200 DP-GI is attributed to the lower ferrite content. The small decrease with decreasingly negative potential is attributed to a slightly increased trapping effect; the trap density for 1200 DP-GI is similar to that of 980 DP-GI (700 MPa YS).

The lattice and effective diffusion coefficients for 980 QP steel were similar to those of 980 DP-GI (700 MPa YS). The lower lattice diffusion coefficient is attributed to the higher

carbon content of the 980 QP steel. The similar decrease of effective diffusion coefficient with decreasingly negative potential is attributed to a similar trap effect.

In summary, the values of the effective diffusion coefficient for each steel could be explained in terms of a trapping effect.

5.3.1 Partial decay transients

The density of reversible hydrogen trap site was evaluated using the two methods: (i) the Oriani-Dong model [25], and the permeation curve method [27], Table 4. The values were comparable, however the values of total trap density evaluated by the permeation curve method were somewhat smaller than those evaluated using Oriani-Dong model. This may be attributed to the followed reasons:

(i) N_L. This study, due to the lack of available data for DP and Q&P steels, used the value of 7.2×10^{22} sites cm^{-3}, adopted from the reported value for α-Fe [16]. Since N_t is directly proportional to N_L, an error in N_L directly causes a similar error in the density of trap sites.

(ii) E_b. The trap binding energy characterises the trap type. Each trap has a different binding energy. In this study one type of reversible trap was assumed. A value of 28.9 kJ mol^{-1} was assumed for E_b. However, more than one type of reversible trap was expected in the DP and Q&P steels, especially the Q&P steel because of the retained austenite. Thus, using a single value of E_b would also lead to the different calculated values.

Nevertheless, the results from both methods showed good consistency: (i) the densities of reversible hydrogen trap sites, N_t and N_t^*, exhibited the same trend that the values were lower at a more negative potential, (ii) the trapped hydrogen was a lower percentage of the total absorbed hydrogen at a more negative potential, and (iii) the reversible hydrogen trap density values evaluated between -1.700 $V_{Hg/HgO}$ to -1.100 $V_{Hg/HgO}$ using these two methods were similar in magnitude of ~10^{18} sites cm^{-3} for all the steels, although there was a difference of three times for 980 QP steel. Such a difference was not higher than that from the literature [29].

5.3.2 Complete decay transients

Tables 4 and 5 present values of the reversible hydrogen trap site density, evaluated using the permeation curve method, (i) for partial decay transients between -1.700 $V_{Hg/HgO}$ to

-1.100 $V_{Hg/HgO}$, and (ii) for complete decay transients from -1.700 $V_{Hg/HgO}$ to the open circuit potential (ocp).

The trap site density from complete decay was significantly higher than that from partial decay transients for each of the studied steels. For example, for 980 DP-GI (650 MPa YS) steel, N_t^* was 11.1 × 10^{17} sites cm^{-3} between -1.700 $V_{Hg/HgO}$ to -1.100 $V_{Hg/HgO}$, whereas N_t^* was 24.2 × 10^{17} sites cm^{-3}, more than 100 % higher, from the complete decay. Correspondingly, the trapped hydrogen, evaluated from the complete decay, accounted for 58 % of the total absorbed hydrogen, whilst from partial decay transients, the percentage was significantly lower. Especially for the most negative charging conditions, from -1.700 $V_{Hg/HgO}$ to -1.600 $V_{Hg/HgO}$, the trapped hydrogen was 0.5 % of the total amount of hydrogen. This was attributed to the less significant trapping effect at more negative charging potentials, as was also found by Liu and Atrens [29].

Reversible traps have a significant influence on hydrogen diffusion and on hydrogen embrittlement susceptibility. The permeation curve method is a useful way of estimation the reversible trap site density. However, when using this method, the evaluated value from a complete decay involves all the reversible traps and is higher than that evaluated from partial decay transients, which only involved the reversible traps under the particular charging conditions. Thus, for understanding the reversible hydrogen traps that influence the hydrogen diffusion behaviour under particular charging conditions, the Oriani-Dong model and permeation curve method are both useful.

5.4 Comparison with literature

Table 6 shows the values of reversible hydrogen trap density determined through permeability experiments from the literature [25, 27-29, 44, 45, 47, 50], where t_L is the lattice breakthrough time and t_L* is the lattice time lag, both related to the lattice diffusion coefficient, D_L, t_T is the breakthrough time with trapping and t_T* is time lag in the presence of trapping, C_a is the average hydrogen concentration at steady state, and the other symbols have the same meaning as in this paper.

The magnitude of reversible hydrogen trap densities ranged from 10^{12} sites cm^{-3} to 10^{26} sites cm^{-3} for different steels and using various mathematic models. The values measured herein are in the middle of this range.

Liu and Atrens [29] used an approach similar to that used herein, and evaluated similar trap densities to those estimated herein. Fallahmohammadi et al. [28] and Frappart et al. [45] used similar models, both adopted from Kumnick and Johnson [51] and related to

time lag or breakthrough time, to calculate the trap site density in their steels. Both studies estimates similar values of 10^{19} sites cm^{-3}, and similar values were obtained by [24, 52, 53], and were somewhat higher than the values estimated herein. This difference in values may be attributed to the intrinsic difference of the materials used in these studies and difference in methods for calculating the trap site density.

Zhu et al. [44] determined the density of hydrogen traps in quenching and partitioning (Q&P) steels with different heat treatments. The densities for all their steels were of similar magnitude of 10^{21} sites cm^{-3}. However, the model they used to calculate hydrogen trap density did not involve the trap binding energy, E_b, and was also different from the Oriani-Dong model [25] as used herein this paper.

Zakroczymski [27] determined the mount of trapped hydrogen using complete permeation decay curve and obtained around 10^{-7} mol cm^{-2} of trapped hydrogen from the hydrogen detection side. By using Eq. (6) and (7) in this paper, we converted the amount of hydrogen to trap site density and obtained an estimation of around 10^{13} sites cm^{-3}, as shown in Table 6. This value was lower than those in our study by a few orders of magnitude. This is within expectation, since a much lower hydrogen trap density is expected in the Armco iron used in the study of Zakroczymski [27].

In other research [25, 29, 47, 50] using similar model as the Oriani-Dong model [25] as in this paper, the reversible hydrogen trap density values ranged from 10^{12} sites cm^{-3} to 10^{26} sites cm^{-3}. Table 6 documents that different values have been assigned to the parameters in this model. For example, Liu et al. [29] used the value for N_L obtained from a quenched and tempered martensitic steel, whereas other researchers [25, 47, 50] used the N_L values for α-Fe or the tetrahedral site density in bcc Fe at room temperature. The value of N_L for α-Fe was also used in this study. Araújo et al. [16] asserted that the value for N_L depended on the type of metal being analysed. As a consequent, different values were assigned to this parameter and contributed to the variation of the calculated trap site density. The same would happen when different values were assigned to D_L or E_b, as also mentioned above in section 5. In addition, the Oriani-Dong model [25] also involved the effective diffusion coefficient. The diffusion coefficient was influenced by the sub-surface hydrogen concentration and thus by the charging condition [29, 45].

Nevertheless, the values of trap site density obtained using the two methods in this study were comparable and were around 10^{18} sites cm^{-3}, were consistent with the results of Liu et al. [29] and were within the range of the values from the literature [24, 25, 27-29, 44, 45, 47, 50, 52, 53].

Table 5 The total density of reversible hydrogen trap sites in the DP and Q&P steels for the complete decay transients started at -1.700 $V_{Hg/HgO}$ evaluated using the permeation curve method. The final potential was the open circuit potential (ocp).

Steel designation	Starting and finishing potential for transient, ($V_{Hg/HgO}$)	η, V, (at start of transient)	i_∞, ($\mu A\ cm^{-2}$), (at start of transient)	D_{eff}, ($cm^2\ s^{-1}$), (average for transient)	C_T, ($\mu g\ g^{-1}$), (at start of transient)	N_t^*, (sites cm^{-3}), (average for transient)	C_t^*, ($mol\ m^{-3}$), (average for transient)	C_t^*, ($\mu g\ g^{-1}$), (average for transient)	C_L^*, ($mol\ m^{-3}$), (at start of transient)	C_L^*, ($\mu g\ g^{-1}$), (at start of transient)	Percentage of trapped hydrogen, (%),
980 DP-GI	-1.700 to ocp	-0.857	28.95	1.25×10^{-6}	1.689	18.8×10^{17}	3.12	0.416	2.65	0.353	54
980 DP-GI (650 MPa YS)	-1.700 to ocp	-0.857	20.48	0.98×10^{-6}	2.223	24.2×10^{17}	4.02	0.581	2.92	0.422	58
980 DP-GI (700 MPa YS)	-1.700 to ocp	-0.857	8.44	0.51×10^{-6}	1.737	33.0×10^{17}	5.48	0.695	3.11	0.394	64
1200 DP-GI	-1.700 to ocp	-0.857	21.61	0.88×10^{-6}	1.728	22.6×10^{17}	3.75	0.364	4.13	0.400	48
980 QP	-1.700 to ocp	-0.857	7.80	0.42×10^{-6}	1.331	5.91×10^{17}	0.98	0.141	1.90	0.273	34

Table 6. The values of reversible hydrogen trap density from the literature.

Authors	Material	Mathematic model	Assigned value to parameters	Charging conditions	Trap site density (sites cm^{-3})
Liu and Atrens [29]	3.5NiCrMoV medium strength steel	$N_t = N_L \times \left(\frac{D_L}{D_{eff}} - 1\right) \exp(-\frac{E_b}{RT})$	$D_L = 1.29 \times 10^{-6}\ cm^2\ s^{-1}$ $N_L = 1.45 \times 10^{23}$ sites cm^{-3} $E_b = 29\ kJ\ mol^{-1}$	Between -1.700 $V_{Ag/AgCl}$ and -1.100 $V_{Ag/AgCl}$ in 0.1 M NaOH	~ 10^{18}
Fallahmohammadi et al. [28]	X65 and F22 pipeline steel	$\frac{t_T^*}{t_L^*} - 1 = \frac{3N_t}{C_a}$	$t_L^* = L^2/6D_L$	Constant cathodic current density of 0.5 mA cm^{-2} in 0.2 mol L^{-1} CH_3COOH + 0.4 mol L^{-1} CH_3COONa	~ 10^{19}
Frappart et al. [45]	Quenched and tempered martensitic steel	$\frac{t_T}{t_L} - 1 = \frac{3N_t}{C_a}$	$t_L = L^2/15.3D_L$	Constant cathodic current density of 5-200 mA cm^{-2} in 1 M H_2SO_4	~ 10^{19}
Zhu et al. [44]	Quenching and partitioning steels	$N_t = \frac{N_A \times C_T}{3}\left(\frac{D_L}{D_{eff}} - 1\right)$	$D_L = 1.28 \times 10^{-4}\ cm^2\ s^{-1}$ $N_A = 6.02 \times 10^{23}\ mol^{-1}$	Constant cathodic current density of 7.64 mA cm^{-2} in 0.2 M NaOH + 3 g L^{-1} NH_4SCN	~ 10^{21}
Zakroczymski [27]	Armco iron	Permeation curve method	-	Complete decay from a current density of 10mA cm^{-2} in 0.1M NaOH	~ 10^{13}
Haq et al. [50]	X70 pipeline steel	$N_t = N_L \times \left(\frac{D_L}{D_{eff}} - 1\right) \exp(-\frac{E_b}{RT})$	$D_L = 7.20 \times 10^{-5}\ cm^2\ s^{-1}$ $N_L = 7.52 \times 10^{22}$ sites cm^{-3} $E_b = 0.3$ eV	Constant cathodic current density of 3.52 mA cm^{-2} in 0.1 N NaOH + 10 g L^{-1} $Na_2S \cdot 9H_2O$	~ 10^{12}
Dong et al. [25]	X100 pipeline steel	$N_t = N_L \times \left(\frac{D_L}{D_{eff}} - 1\right) \exp(-\frac{E_b}{RT})$	$D_L = 1.28 \times 10^{-4}\ cm^2\ s^{-1}$ $N_L = 7.52 \times 10^{22}$ sites cm^{-3} $E_b = 0.3$ eV	Constant cathodic current density of 10 mA cm^{-2} in 0.2 M H_2SO_4 + 0.25 g L^{-1} As_2O_3	~ 10^{26}
Begić Hadžipašić et al. [47]	DP and TRIP steel	$N_t = N_L \times \left(\frac{D_L}{D_{eff}} - 1\right) \exp(-\frac{E_b}{RT})$	$D_L = 1.28 \times 10^{-4}\ cm^2\ s^{-1}$ $N_L = 7.52 \times 10^{22}$ sites cm^{-3} $E_b = 0.3$ eV	Open circuit potential (ocp) in 2 mol L^{-1} H_2SO_4	~ 10^{25}

5.5 Microstructure

Table 1 and Fig. 3 indicate that the microstructure of the DP steels consisted mainly of ferrite and martensite whereas the microstructure of the Q&P steel consisted of ferrite, bainite and retained austenite.

Table 1 and 2 indicate that, for the three 980 DP grades of steels, from 980 DP to 980 DP-GI (650 MPa YS) and to 980 DP-GI (700 MPa YS), the yield strength increased, the relative amount of ferrite decreased, and the grain size decreased. The decreasing grain size can be related to grain refinement by the increasing Ti alloying content, and is consistent with the increasing yield strength.

1200 DP-GI and 980 DP steels had similar grain sizes. The higher strength of the 1200 DP steel was attributed to (i) the higher amount of martensite, which was 74% compared with 60% for 980 DP steel and thus the lower volume fraction of ferrite, and (ii) the slightly higher carbon concentration, which is expected to produce a stronger martensite.

980 QP steels had 39% of soft ferrite and 53% of hard bainite and 8% of retained austenite, which had a hydrogen diffusion coefficient much lower than that of ferrite, and a solubility of hydrogen higher than ferrite and martensite [47, 54].

During pre-charging, it took the hydrogen about 315 s, 1235 s, 1503 s, 1184 s and 810 s to breakthrough to the other side of the specimen of 980 DP, 980 DP-GI (650 MPa YS), 980 DP-GI (700 MPa YS), 1200 DP-GI, and 980 QP, respectively. Increased breakthrough time indicates a lower effective diffusion coefficient, which could be caused by a larger trapping effect, or there could be also a contribution from the lattice diffusion coefficient. The breakthrough times roughly correlate with the total density of trap sites as evaluated in Table 5, except that the trap densities are not sufficiently high for 980 QP, in which case there is assumed to be a significant influence from the low lattice diffusion coefficient for 980 QP, see Table 3. Fig. 4 shows that it took a shorter time of peaking for the 980 DP-GI (650 MPa YS) and 980 DP-GI (700 MPa YS). This is attributed to the surface of these steel samples, which had been galvanized and the galvanizing was removed by grinding and polishing. The reason for the different times to reach steady-state current density of the different steels was attributed to the differences in the way the surfaces reacted to the cathodic charging. The values of the steady-state current density of different steels correspond to the values of i_∞ at the end of transient from -1.700 $V_{Hg/HgO}$ to -1.600 $V_{Hg/HgO}$ in Table 4, which provides corresponding values for C_T and C_L.

Tables 1, 2 and 3 indicate that, for the three 980 DP steel grades, with increasing yield strength, decreasing ferrite content, and decreasing grain size, the values of the lattice diffusion coefficient decreased slightly from 2.07×10^{-6} cm^2 s^{-1} to 1.58×10^{-6} cm^2 s^{-1} to 0.75×10^{-6} cm^2 s^{-1}. This decrease in the lattice diffusion coefficient is attributed to the decreasing fraction of ferrite in the microstructure. It is expected that the diffusion coefficient of the ferrite dominates the diffusion coefficient of the steel, because the diffusion coefficient of the martensite is much lower due to its highly distorted lattice.

The value of the diffusion coefficient of 1200 DP-GI steel was somewhat lower than that of the 980 DP steel. The lower lattice diffusion coefficient of 1200 DP-GI is attributed to the lower ferrite content.

The lattice diffusion coefficient values for 980 QP steel was lower than that of 980 DP-GI (700 MPa YS) attributed to the higher carbon content of the 980 QP steel.

6. Conclusions

1. The values of reversible hydrogen trap site density and the proportion of the reversibly trapped hydrogen for the DP and Q&P steels indicated that (i) the trapping effect was less significant at a more negative potential, and (ii) the lattice diffusion coefficient of hydrogen could be measured from the partial transients at the most negative potentials.
2. The values of the effective diffusion coefficient measured in this work were consistent with literature values.
3. The densities of reversible hydrogen trap sites from complete decays were ~ 2×10^{18} sites cm^{-2} and were a factor of two higher than those from partial decay transients between -1.700 $V_{Hg/HgO}$ and -1.100 $V_{Hg/HgO}$.
4. The densities of reversible hydrogen trap sites estimated in this work were consistent with literature values.
5. The values of hydrogen lattice diffusion coefficient and values of the reversible trap site density were within fairly narrow ranges for the steels studied, reflecting the fact that the steels were quite similar.

Acknowledgements

This research is supported by the Baosteel-Australia Joint Research & Development Centre (BAJC) Grant, BA13037, with linkage to Baoshan Iron and Steel Co., Ltd of China.

References

[1] D Bhattacharya, Developments in advanced high strength steels, Proceedings of Proceedings of the Joint International Conference of HSLA Steels, Sanya, 2005, 70-73.

[2] X Zhu, Z Ma and L Wang, Current status of advanced high strength steel for auto-making and its development in Baosteel, Avaliable from www.baosteel.com, Access on November 26, 2014.

[3] WorldAutoSteel, Advanced high-strength steels application guidelines version 5.0, Available from http://www.worldautosteel.org/, Access on 2014.

[4] BC De Cooman, L Chen, HS Kim, Y Estrin, SK Kim and H Voswinckel, State-of-the-Science of High Manganese TWIP Steels for Automotive Applications, Microstructure and Texture in Steels, Charpter 10, p. 165-183, Springer, London, 2009.

[5] BaoSteel, BaoSteel automotive advanced high strength steels, Avaliable from www.baosteel.com, Access on November 12, 2014 (2013).

[6] VF Zackay, ER Parker, D Fahr and R Busch, The enhancement of ductility in high-strength steels, ASM Trans Quart. 60 (1967) 252-259.

[7] M Chen, R Wu, H Liu, L Wang, J Shi, H Dong and X Jin, An ultrahigh strength steel produced through deformation-induced ferrite transformation and Q&P process, Sci China Technol Sci. 55 (2012) 1827-1832.

[8] DV Edmonds, K He, FC Rizzo, BC De Cooman, DK Matlock and JG Speer, Quenching and partitioning martensite—A novel steel heat treatment, Mater Sci Eng A. 438-440 (2006) 25-34.

[9] MJ Santofimia, L Zhao and J Sietsma, Overview of Mechanisms Involved During the Quenching and Partitioning Process in Steels, Metall Mater Trans A. 42 (2011) 3620-3626.

[10] DK Matlock and JG Speer, Third Generation of AHSS: Microstructure Design Concepts, Microstructure and Texture in Steels, Charpter 11, p. 185-205, Springer London, 2009.

[11] G Lovicu, M Bottazzi, F D'Aiuto, M De Sanctis, A Dimatteo, C Santus and R Valentini, Hydrogen Embrittlement of Automotive Advanced High-Strength Steels, Metall Mater Trans A. 43 (2012) 4075-4087.

[12] M Robinson and P Kilgallon, Hydrogen embrittlement of cathodically protected high-strength, low-alloy steels exposed to sulfate-reducing bacteria, Corrosion. 50 (1994) 626-635.

[13] A Lasia and D Grégoire, General model of electrochemical hydrogen absorption into metals, J Electrochem Soc. 142 (1995) 3393-3399.

[14] D Hardie, EA Charles and AH Lopez, Hydrogen embrittlement of high strength pipeline steels, Corros Sci. 48 (2006) 4378-4385.

[15] M Devanathan and Z Stachurski, The adsorption and diffusion of electrolytic hydrogen in palladium, Proceedings of the Royal Society of London. Series A. Mathematical and Physical Sciences. 270 (1962) 90-102.

[16] DF Araújo, EO Vilar and J Palma Carrasco, A critical review of mathematical models used to determine the density of hydrogen trapping sites in steels and alloys, Int J Hydrogen Energy. 39 (2014) 12194-12200.

[17] J Lee and S Lee, Hydrogen trapping phenomena in metals with BCC and FCC crystals structures by the desorption thermal analysis technique, Surf Coat Technol. 28 (1986) 301-314.

[18] P Castaño Rivera, VP Ramunni and P Bruzzoni, Hydrogen trapping in an API 5L X60 steel, Corros Sci. 54 (2012) 106-118.

[19] AH Krom and A Bakker, Hydrogen trapping models in steel, Metall Mater Trans. 31 (2000) 1475-1482.

[20] M Luppo and J Ovejero-Garcia, The influence of microstructure on the trapping and diffusion of hydrogen in a low carbon steel, Corros Sci. 32 (1991) 1125-1136.

[21] J Rehrl, K Mraczek, A Pichler and E Werner, The Impact of Nb, Ti, Zr, B, V, and Mo on the Hydrogen Diffusion in Four Different AHSS/UHSS Microstructures, steel research international. 85 (2014) 336-346.

[22] J Hirth, Effects of hydrogen on the properties of iron and steel, Metall Trans A. 11 (1980) 861-890.

[23] A McNabb and P Foster, A new analysis of the diffusion of hydrogen in iron and ferritic steels, Trans. Aime. 227 (1963) 618.

[24] RA Oriani, The diffusion and trapping of hydrogen in steel, Acta Metall. 18 (1970) 147-157.

[25] CF Dong, ZY Liu, XG Li and YF Cheng, Effects of hydrogen-charging on the susceptibility of X100 pipeline steel to hydrogen-induced cracking, Int J Hydrogen Energy. 34 (2009) 9879-9884.

[26] A Atrens, D Mezzanotte, N Fiore and M Genshaw, Electrochemical studies of hydrogen diffusion and permeability in Ni, Corros Sci. 20 (1980) 673-684.

[27] T Zakroczymski, Adaptation of the electrochemical permeation technique for studying entry, transport and trapping of hydrogen in metals, Electrochim Acta. 51 (2006) 2261-2266.

[28] E Fallahmohammadi, F Bolzoni and L Lazzari, Measurement of lattice and apparent diffusion coefficient of hydrogen in X65 and F22 pipeline steels, Int J Hydrogen Energy. 38 (2013) 2531-2543.

[29] Q Liu and A Atrens, Reversible hydrogen trapping in a 3.5NiCrMoV medium strength steel, Corros Sci. 96 (2015) 112-120.

[30] E562-08, Standard Test Method for Determining Volume Fraction by Systematic Manual Point Count, 2008.

[31] E-112, Standard test methods for determining average grain size, 2010.

[32] GF Vander Voort, Metallography, principles and practice, ASM International, 1984.

[33] Q Liu, AD Atrens, Z Shi, K Verbeken and A Atrens, Determination of the hydrogen fugacity during electrolytic charging of steel, Corros Sci. 87 (2014) 239-258.

[34] J Flis, T Zakroczymski, V Kleshnya, T Kobiela and R Duś, Changes in hydrogen entry rate and in surface of iron during cathodic polarisation in alkaline solutions, Electrochim Acta. 44 (1999) 3989-3997.

[35] J McBreen, L Nonis and W Beck, A method for determination of the permeation rate of hydrogen through metal membranes, J Electrochem Soc. 113 (1966) 1218-1222.

[36] J Venezuela, Q Liu, M Zhang, Q Zhou and A Atrens, The influence of hydrogen on the mechanical and fracture properties of some martensitic advanced high strength steels studied using the linearly increasing stress test, Corros Sci. 99 (2015) 98-117.

[37] J Sojka, V Vodárek, I Schindler, C Ly, M Jérôme, P Váňová, N Ruscassier and A Wenglorzová, Effect of hydrogen on the properties and fracture characteristics of TRIP 800 steels, Corros Sci. 53 (2011) 2575-2581.

[38] X Zhu, W Li, H Zhao, L Wang and X Jin, Hydrogen trapping sites and hydrogen-induced cracking in high strength quenching & partitioning (Q&P) treated steel, Int J Hydrogen Energy. 39 (2014) 13031-13040.

[39] J Ronevich, B De Cooman, J Speer, E De Moor and D Matlock, Hydrogen effects in prestrained transformation induced plasticity steel, Metall Mater Trans A. 43 (2012) 2293-2301.

[40] JH Ryu, YS Chun, CS Lee, HKDH Bhadeshia and DW Suh, Effect of deformation on hydrogen trapping and effusion in TRIP-assisted steel, Acta Mater. 60 (2012) 4085-4092.

[41] J Yang, F Huang, Z Guo, Y Rong and N Chen, Effect of retained austenite on the hydrogen embrittlement of a medium carbon quenching and partitioning steel with refined microstructure, Mater Sci Eng A. 665 (2016) 76-85.

[42] T Hojo, J Kobayashi, T Kajiyama and K Sugimoto, Effects of Alloying Elements on Impact Properties of Ultra High-Strength TRIP-Aided Bainitic Ferrite Steels, Res Rep Tsuyama Technical College. 52 (2010) 9-16.

[43] X Zhu, W Li, H Zhao and X Jin, Effects of cryogenic and tempered treatment on the hydrogen embrittlement susceptibility of TRIP-780 steels, Int J Hydrogen Energy. 38 (2013) 10694-10703.

[44] X Zhu, K Zhang, W Li and X Jin, Effect of retained austenite stability and morphology on the hydrogen embrittlement susceptibility in quenching and partitioning treated steels, Mater Sci Eng A. 658 (2016) 400-408.

[45] S Frappart, X Feaugas, J Creus, F Thebault, L Delattre and H Marchebois, Study of the hydrogen diffusion and segregation into Fe–C–Mo martensitic HSLA steel using electrochemical permeation test, Journal of Physics and Chemistry of Solids. 71 (2010) 1467-1479.

[46] J Malina, A Begić Hadžipašić and Š Nižnik, Electrochemical corrosion and hydrogen diffusivity in dual-phase steel, Proceedings of 2nd International Conference Corrosion and Material Protection, EFC Event, 2010,

[47] A Begić Hadžipašić, J Malina and M Malina, The influence of microstructure on hydrogen diffusion and embrittlement of multiphase fine-grained steels with increased plasticity and strength, Chem Biochem Eng Q. 25 (2011) 159-169.

[48] T Depover, E Wallaert and K Verbeken, Fractographic analysis of the role of hydrogen diffusion on the hydrogen embrittlement susceptibility of DP steel, Mater Sci Eng A. 649 (2016) 201-208.

[49] M Koyama, CC Tasan, E Akiyama, K Tsuzaki and D Raabe, Hydrogen-assisted decohesion and localized plasticity in dual-phase steel, Acta Mater. 70 (2014) 174-187.

[50] AJ Haq, K Muzaka, DP Dunne, A Calka and EV Pereloma, Effect of microstructure and composition on hydrogen permeation in X70 pipeline steels, Int J Hydrogen Energy. 38 (2013) 2544-2556.

[51] A Kumnick and H Johnson, Deep trapping states for hydrogen in deformed iron, Acta Metall. 28 (1980) 33-39.

[52] A Turnbull, M Carroll and D Ferriss, Analysis of hydrogen diffusion and trapping in a 13% chromium martensitic stainless steel, Acta Metall. 37 (1989) 2039-2046.

[53] A Perujo, E Serra, S Alberici, S Tominetti and J Camposilvan, Hydrogen in the martensitic DIN 1.4914: a review, Journal of alloys and compounds. 253 (1997) 152-155.

[54] M Koyama, E Akiyama and K Tsuzaki, Hydrogen embrittlement in a Fe–Mn–C ternary twinning-induced plasticity steel, Corros Sci. 54 (2012) 1-4.

Chapter 5

Hydrogen concentration in dual phase (DP) and quenched and partitioned (Q&P) advanced high strength steels (AHSS) under simulated service conditions compared with cathodic charging conditions

(published in *Advanced Engineering Materials*)

The previous Chapter 4 presents the hydrogen diffusion and trapping behaviours in the key DP and Q&P steels. The following Chapter 5 continues to study the hydrogen behaviours to understand the hydrogen influence.

The Chapter 5 compares the results of hydrogen concentration, from the permeability experiments and the hot extraction analysis, under simulated service corrosion condition and with those under cathodic charging condition, regarding to the different hydrogen influence on the same steel under these two conditions. For example, there was minimal hydrogen influence on 980DP under simulated service corrosion condition whereas there was significant hydrogen influence on the same steel under cathodic charging condition. Moreover, by comparing the expected results, the different extent of the hydrogen influence on the four DP steels may also be explained.

Hydrogen concentration in dual phase (DP) and quenched and partitioned (Q&P) advanced high strength steels (AHSS) under simulated service conditions compared with cathodic charging conditions

Qinglong Liu[a], Qingjun Zhou[b,*], Jeffrey Venezuela[a], Mingxing Zhang[a], Andrej Atrens[a,*]

[a] The University of Queensland, Division of Materials, School of Mining and Mechanical Engineering, St. Lucia, 4072 Australia

[*] Corresponding author, andrejs.atrens@uq.edu.au, +61 7 3365 3748,

zhouqingjun@baosteel.com, +86 21 26641807

[b] Baoshan Iron & Steel Co., Ltd, Research Institute, Shanghai, 201900, China

Abstract

The hydrogen permeation through dual phase (DP) and quenched and partitioned (Q&P) advanced high strength steels (AHSS) was investigated under simulated auto service conditions. The hydrogen concentration in the steels under simulated auto service corrosion in 3wt% NaCl solution (either at the free corrosion potential or if polarised to the potential of a galvanised steel surface) was lower than that at the least negative cathodic charging potential of –1.100 $V_{Hg/HgO}$ in 0.1M NaOH. Crevice corrosion introduced 3 times more hydrogen than the corrosion at the free corrosion potential.

Key words: steel; hydrogen permeation; advanced high strength steel

1. Introduction

1.1 Hydrogen concentration in service

Hydrogen can be introduced into the steel of a car body during auto service, by general corrosion of the steel of the car body, and by crevice corrosion [1-4]. Such hydrogen in the steel, in combination with an applied stress, could cause hydrogen embrittlement (HE), which is of concern for high strength steels [1, 5] such as the advanced high strength steels (AHSS). Thus it is important to understand how much hydrogen can enter the AHSS in auto service. This research is part of a wider research program that seeks to understand the influence of hydrogen on the mechanical behaviour of AHSS, and to provide information for their applications in auto service. The program seeks to build on existing research that has

studied hydrogen embrittlement (HE) of AHSS under increasingly severe hydrogen charging conditions [1, 6-10], from inert, moderate, to severe. Our prior study [11] investigated hydrogen trapping in these DP and Q&P steels.

The cathodic reaction during corrosion of steel in auto service in neutral and alkaline solutions is mostly oxygen reduction. Nevertheless, some hydrogen could be evolved during corrosion by the following cathodic partial reactions:

$$H_3O^+ + M + e \rightarrow MH_{ads} + H_2O \quad \text{(acid)} \quad (1)$$

$$H_2O + M + e \rightarrow MH_{ads} + OH^- \quad \text{(neutral, alkaline)} \quad (2)$$

where M represents the metal surface, and MH_{ads} represents the adsorbed hydrogen on the metal surface. Two adsorbed hydrogen atoms can combine to form a molecule of hydrogen that leaves the metal surface, by the following reaction:

$$2MH_{ads} \rightarrow H_2 + 2M \quad (3)$$

In addition, during cathodic hydrogen charging at a substantial overpotential, hydrogen can be desorbed by the following electrochemical reactions:

$$MH_{ads} + H_3O^+ + e \rightarrow H_2 + H_2O + M \quad \text{(acid)} \quad (4)$$

$$MH_{ads} + H_2O + e \rightarrow H_2 + OH^- + M \quad \text{(neutral, alkaline)} \quad (5)$$

The adsorbed hydrogen is in equilibrium with the hydrogen absorbed into the metal, MH_{abs}, through the equilibrium reaction:

$$MH_{ads} \leftrightarrow MH_{abs} \quad (6)$$

1.2 Steel metallurgy

Dual phase (DP) and transformation induced plasticity (TRIP) advanced high strength steels (AHSS) have been used for components in automobile construction for weight reduction and improved safety [12-17]. DP steels [18] have a microstructure of a soft, continuous, ferrite matrix, with hard martensite islands dispersed along the ferrite grain boundaries. TRIP steels have a microstructure of a ferrite matrix, with islands of retained austenite, some bainite, and typically some martensite [18]. Deformation of a TRIP steel causes the retained austenite to transform to martensite, which is transformation induced plasticity (TRIP) [19]. TRIP steels can also be produced by a quenching and partitioning (Q&P) heat treatment [20]. The steel is quenched from an elevated temperature (at which the

steel has an austenitic microstructure) to below the martensite start temperature, and above the martensite finish temperature, to form a controlled amount of martensite and some retained austenite. The subsequent partitioning treatment heats the steel typically to a temperature higher than the initial quenching temperature to complete the enrichment of carbon from the martensite to the retained austenite, which stabilizes the retained austenite [21, 22]. Thus, the Q&P steel contains more retained austenite, and has a greater TRIP effect.

1.3 Hydrogen characterisation

The diffusible hydrogen concentration produced by corrosion in auto service, or by cathodic hydrogen charging, can be characterised using hot extraction, with an instrument such as the BRUKER G4 PHOENIX DH carrier gas hot extraction analyser. Such an instrument was used by Zhou et al. [23] in their study of the delayed fracture of MS 980 MPa grade automotive steels.

The hydrogen concentration can also be characterised using the permeation technique of Devanathan and Stachurski [24], and the theoretical development by Atrens et al. [25], based on Bockris et al. [26, 27], and further developed by Liu et al. [28]. Hydrogen is typically charged into the left hand side of a steel membrane, see Fig. 1, and the amount of hydrogen exiting the right hand side of the steel membrane is measured as a current density. The permeation transients have the following general form [28-30]:

$$\frac{i_p - i_p^0}{i_p^\infty - i_p^0} = \frac{2L}{\sqrt{\pi Dt}} \sum_{n=0}^{\infty} \exp\left(-\frac{(2n+1)^2 L^2}{4Dt}\right) \qquad \text{(Rise transients)} \qquad (7)$$

$$\frac{i_p - i_p^\infty}{i_p^0 - i_p^\infty} = 1 - \frac{2L}{\sqrt{\pi Dt}} \sum_{n=0}^{\infty} \exp\left(-\frac{(2n+1)^2 L^2}{4Dt}\right) \qquad \text{(Decay transients)} \qquad (8)$$

where i_p is the measured permeation current density at time t, i_p^0 is the initial steady-state permeation rate at time t = 0, i_p^∞ is the new steady-state permeation current density, L is the thickness of the steel sheet, and D is the diffusion coefficient. For an uncharged steel, $i_p^0 = 0$, and for the complete decay transient $i_p^\infty = 0$. A measured permeation transient can be fitted to these equations to determine the effective diffusion coefficient. It is assumed that the steel can be modelled as a homogeneous single-phase material.

These equations are appropriate for experiments with successive hydrogen permeation transients where each transient proceeds to steady state, and each permeation transient is followed by a subsequent permeation transient with either a higher or lower input hydrogen fugacity. These equations are also applicable to the case where the input hydrogen fugacity is

established by corrosion on the input side of the permeation cell, either by general corrosion or by crevice corrosion.

Liu et al. [31] applied the method of successive transients, with increasing hydrogen fugacity produced by cathodic charging, to a 3.5NiCrMoV martensitic steel. They found that the first permeation transients had low values of the effective diffusion coefficient, D_{eff}, because there were empty hydrogen traps that retarded hydrogen permeation through the steel. In subsequent permeation transients, with increasing hydrogen fugacity, the traps were successively filled, until the latice diffusion coefficient was measured when all the traps were filled.

The hydrogen concentration dissolved in the steel lattice at the input side of the steel membrane, C_{HL}, can be evaluated, using this hydrogen permeation technique, from:

$$C_{HL} = \frac{i_p^{\infty} L}{F D_L} \tag{9}$$

where, F is the Faraday constant (96 485 C mol^{-1}), L is the thickness of the steel membrane in the permeability experiment, i_p^{∞} is the steady-state permeation current density, and D_L is the lattice diffusion coefficient. This requires measurement of a permeation transient under conditions such that lattice diffusion of hydrogen is the dominant transport mechanism of hydrogen through the steel membrane. This condition can be met using successive permeation transients with increasing input fugacities until all the hydrogen traps in the steel are filled, and there is only lattice diffusion [28].

The total hydrogen concentration in the steel at the input side of the steel membrane, C_{HT}, can also be evaluated using the hydrogen permeation technique, provided that there are only reversible traps [32]. Under these conditions, the total hydrogen concentration, C_{HT}, can be evaluated from [32]:

$$C_{HT} = \frac{i_p^{\infty} L}{F D_{eff}} \tag{10}$$

where D_{eff} is the effective diffusion coefficient, i.e. the diffusion coefficient measured in the presence of traps. The total hydrogen concentration, C_{HT}, is the sum of the hydrogen dissolved in the steel lattice, C_{HL}, plus the hydrogen concentration associated with hydrogen traps, C_{Ht}.

Turnbull [32] also considered the case of a two-phase steel like a duplex stainless steel which consists of two phases that have markedly different hydrogen diffusivities. In that case, hydrogen diffusion occurs largely through the alpha phase, which has the much higher

hydrogen diffusivity. The hydrogen concentration in the ferrite at the input side of the steel membrane, C_{Ha}, (per unit volume of steel) is given by:

$$C_{Ha} = \frac{i_p^{\infty} L}{F w D_{La}} \quad (11)$$

where and D_{La} is the lattice diffusion coefficient in the ferrite, and w is the tortuosity factor which relates to the longer diffusion path for the hydrogen. The concentration of hydrogen in the ferrite is obtained by dividing C_{Ha} by the volume fraction of ferrite. Eq. (11) is equivalent to Eq. (10) with:

$$D_{eff} = wD_{La} \quad (12)$$

and the hydrogen in the ferrite can be evaluated using Eq. (10). This approach can also be used for DP and Q&P steels. In DP and Q&P steels, it is expected that the ferrite has a lattice diffusivity higher than that of the martensite, because of the distorted nature of the martensite lattice.

1.4 Service hydrogen

Similarly, the hydrogen concentration produced by corrosion in simulated service can be determined by the hot extraction method or by the permeation technique.

In the permeation technique, the simulated service corrosion conditions are established on the left side of the steel membrane, the corresponding permeation current density can be measured on the right hand side of the steel membrane, and the hydrogen concentration at the input side of the steel membrane can be evaluated using Eq. (10).

A greater concentration of hydrogen could potentially enter the steel if there is a scratched galvanised layer, because the steel is cathodically polarised and protected by the sacrificial corrosion of the zinc. The scratched galvanized steel sample exhibits a mixed potential; the potential is between the free corrosion potential of the steel and the free corrosion potential of the zinc. The more negative applied potential means that more hydrogen is evolved at the surface of the steel, and more hydrogen can enter the steel. The maximum amount of hydrogen that can enter the steel is that corresponding to a steel sample polarised to the free corrosion potential of zinc. This is a quantity that this study aims to measure.

1.5 Research approach

The present study measured the maximum hydrogen concentration in DP and Q&P

steels associated with simulated auto service and compared these hydrogen concentrations with those produced by cathodic hydrogen charging in a 0.1M NaOH solution. The auto service corrosion was simulated by (i) continuous free corrosion in 3wt% NaCl solution, simulating continuous free corrosion of the steel of the car body in auto service, (ii) cathodic polarisation of the steel to the zinc potential in 3wt% NaCl to simulate the maximum amount of hydrogen produced for the steels protected by a zinc coating applied by galvanisation, and (iii) simulated crevice corrosion in 3wt% NaCl solution.

The amount of hydrogen was also measured for free corrosion in 0.1M HCl. The 0.1M HCl solution is much more severe than any environment encountered in auto service, but this solution has been used to study the apparent influence of hydrogen on AHSS [33, 34].

2. Experimental Methods

2.1 Materials

The DP and Q&P steels were commercial steels, and were designated as 980 DP, 980 DP-GI (650 MPa YS), 980 DP-GI (700 MPa YS), 1200 DP-GI and 980 QP. The "GI" indicates that the steel sheet had been galvanised, by an in-line hot-dip process. The galvanising zinc layer was removed by grinding and etching. The steels were supplied from commercial production as rolled sheets of the following thicknesses: 1.35 mm for 980 DP, 0.95mm for 980 DP-GI (650 MPa YS), 0.99 mm for 980 DP-GI (700 MPa YS), 1.93 mm for 980 QP, and 1.35 mm for 1200 DP-GI. Table 1 presents the chemical composition and mechanical properties as provided by the steel supplier. Table 1 also includes the relevant microstructure parameters. These microstructures were typical of DP and Q&P steels.

Table 1 Chemical composition (in wt %), mechanical properties, and microstructures of the DP and Q&P steels. The microstructure of each steel was ferrite plus martensite or bainite. 980 QP contained bainite. All other steels contained martensite.

Steel designation	C	Si	Mn	Al	Nb	Ti	yield stress, MPa	tensile stress, MPa	elongation at fracture, e_f, %	ferrite %	martensite %	retained austenite %
980 DP	0.09	0.30	2.4	<0.03	<0.04	<0.02	592	930	8.3	40%	60%	0%
980 DP-GI (650 MPa YS)	0.09	0.30	2.4	<0.03	<0.04	<0.03	645	1057	7.9	37%	63%	0%
980 DP-GI (700 MPa YS)	0.08	0.40	2.4	<0.03	<0.04	<0.05	697	1039	6.9	36%	64%	0%
1200 DP-GI	0.12	0.30	2.4	<0.03	<0.04	<0.03	896	1198	4.7	26%	74%	0%
980 QP	0.20	1.50	2.0	<0.03	<0.04	<0.01	682	1020	11.3	39%	53%	8%

2.2 Diffusible hydrogen concentration

The diffusible hydrogen concentration was measured using a BRUKER G4 PHOENIX DH carrier gas hot extraction analyser for 980 DP, 1200 DP-GI and 980 QP steels. The sample dimensions were 10 mm × 50 mm with thicknesses equivalent to the thickness of the as-received steel sheet. All sample surfaces were ground to 1200 grit using SiC paper.

After hydrogen charging, the sample was cleaned with distilled water and ethanol, dried with blowing air, weighed, inserted in the quartz extraction tube in the temperature-programmable infrared heated furnace, and the furnace was heated by the instrument to 400 °C. The diffusible hydrogen was released into the carrier gas flow of pure nitrogen, and the amount of hydrogen was determined from the increase in thermal conductivity of the carrier gas. There was a constant time interval of 3 min between the end of hydrogen charging and the beginning of the hydrogen measurement.

The temperature of 400 °C was used because it was expected that all diffusible hydrogen would be released but that irreversibly bound hydrogen would not be released.

The diffusible hydrogen concentration was measured as described above for unchanged 980 DP, 1200 DP-GI, and 980 QP steels, and for these steels for (i) hydrogen chathodic charging in 0.1M NaOH solution at 23 ± 2 °C at over potential values of –0.257 V, –0.557 V and –0.857 V, (ii) free corrosion in 3wt% NaCl solution, simulating free corrosion of the steel of the car body in service, (iii) cathodic polarisation of the steel to the zinc potential in 3wt% NaCl to simulate the maximum amount of hydrogen produced for the steels protected by a zinc coating applied by galvanisation, and (iv) free corrosion potential in 0.1M HCl, all for 24 h. The details of the exposures were as presented below.

2.3 Cathodic charging

Fig. 1 shows the Devanathan and Stachurski [24] type permeation cell, which was the same as that of Liu and Atrens [31]. The steel sheet sample, 30 mm × 30 mm, was the working electrode for the electrochemical cells on both sides of the steel sheet. Each counter electrode was a Pt wire, and each reference electrode was an Hg/HgO, 20% KOH reference electrode, the potential of which is + 0.098 V_{SHE}. Each cell contained 0.1M NaOH solution. All experiments were carried out at room temperature of 23 ± 2 ℃.

The 980 DP, 980 DP-GI (650 MPa YS), 980 DP-GI (700 MPa YS), 1200 DP-GI and 980 QP specimens were ground to: 0.53, 0.75, 0.80, 0.70 and 0.48 mm, respectively. The area exposed to the solution on the hydrogen-exit side was slightly different in each case, as this

area was determined by the clamping force holding the two parts of the permeability cell together. This area was measured in each case after the permeability experiments. For the case of cathodic hydrogen charging, these areas were 3.394, 3.308, 3.133, 2.997 and 2.9296 cm^2, respectively.

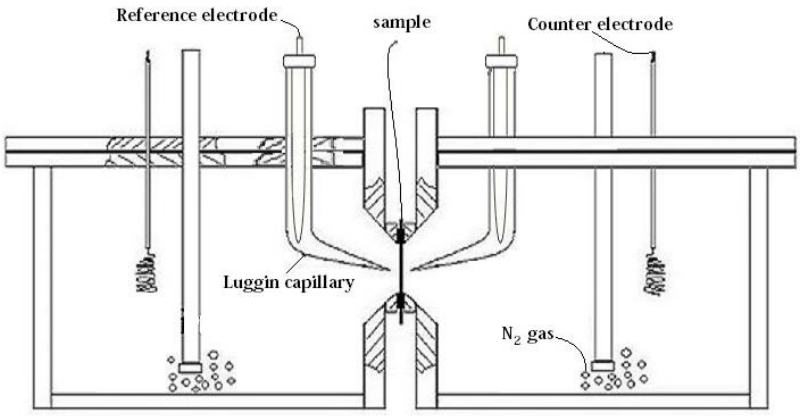

Fig. 1. Schematic of a cross-section through the permeability cell.

The specimen surface in the left hand cell was polished to 3 μm. Hydrogen was produced by a negative potential applied with a MP 81 potentiostat. The input specimen surface was pre-charged in order to stabilise the surface, as was done by Zakroczymski et al. [30, 35] and Qian et al. [28, 31]. During precharging there was typically a steady increase in permeation current density until a steady state permeation current density was reached. The precharging conditions were at – 1.600 $V_{Hg/HgO}$, for (i) 48 hour for 980 DP-GI (650 MPa YS) and 980 DP-GI (700 MPa YS) steels, and (ii) 60 hour for 980 DP, 1200 DP-GI and 980 QP steels.

The right hand side was the hydrogen exit side. The specimen was plated with palladium to prevent oxidation of the steel. To remove oxygen from this solution, N_2 gas was bubbled through the solution until the exit side background current density was less than 0.2 μA cm^{-2} before hydrogen charging was commenced. This background current was subtracted from the permeation current. A potential of + 300 $mV_{Hg/HgO}$ was maintained using a PARSTAT 2273 to oxidise the emerging hydrogen atoms.

Successive permeation transients were measured, such as those with input charging potential values from – 1.600 $V_{Hg/HgO}$ to – 1.700 $V_{Hg/HgO}$, as well as a permeation transient loop from – 1.700 $V_{Hg/HgO}$ to – 1.100 $V_{Hg/HgO}$ and back to – 1.700 $V_{Hg/HgO}$. The potentials for the transient loop were: – 1.700 $V_{Hg/HgO}$, – 1.600 $V_{Hg/HgO}$, – 1.400 $V_{Hg/HgO}$, – 1.200 $V_{Hg/HgO}$, – 1.100 $V_{Hg/HgO}$, and similarly back to – 1.700 $V_{Hg/HgO}$. These measured permeation transients

were fitted to Eq. (7) or (8) to determine the effective diffusion coefficient, D_{eff}, and the corresponding total hydrogen concentration was determined using Eq.(10).

The overpotential of the hydrogen evolution reaction at each applied potential was determined by [28]:

$$\eta = E_a - E_H^0 \quad (13)$$

where E_a is the applied potential, and E_H^0 is the equilibrium potential of the hydrogen evolution reaction at the steel surface at a fugacity of one atmosphere pressure, which was calculated using the Nernst equation [36]:

$$E_H^0 = -0.0591\ pH \quad (14)$$

2.4 Simulated service corrosion

The left hand permeability cell contained either (i) 3wt% NaCl solution with pH 7.3 with the steel at the free corrosion potential, (ii) 3wt% NaCl solution with pH 7.3 with the steel surface polarised to the free corrosion potential of zinc, in order to simulate the maximum hydrogen concentration for steel corroding in contact with a galvanised layer, and (iii) crevice corrosion conditions in 3wt% NaCl solution.

For the experiments at the free potential in 3wt% NaCl solution, the 980 DP, 980 DP-GI (650 MPa YS), 980 DP-GI (700 MPa YS), 1200 DP-GI and 980 QP specimens were ground to 0.71, 0.69, 0.97, 0.86 and 0.47 mm, respectively. The area exposed to the solution in the hydrogen-exit-side cell was 3.309, 3.056, 3.226, 3.423 and 2.588 cm^2, respectively. The open circuit potential was measured to be –0.668 $V_{Ag/AgCl}$ for the steels freely corroded in the 3wt% NaCl solution. The free corrosion potential was constant and did not change significantly with time.

The experiments at the Zn potential in 3wt% NaCl solution used an applied potential of –0.950 $V_{Ag/AgCl}$, which was the measured open circuit potential of the Zn coating in 3% NaCl solution. The reference electrode was Ag/AgCl, KCl (saturated) and the counter electrode was a Pt wire. The 980 DP, 980 DP-GI (650 MPa YS), 980 DP-GI (700 MPa YS), 1200 DP-GI and 980 QP specimens were ground to 0.56, 0.83, 0.70, 0.90 and 0.55 mm, respectively, and exposed an area of 2.608, 2.983, 2.635, 2.912 and 3.243 cm^2, respectively, to the deaerated 0.1 M NaOH solution.

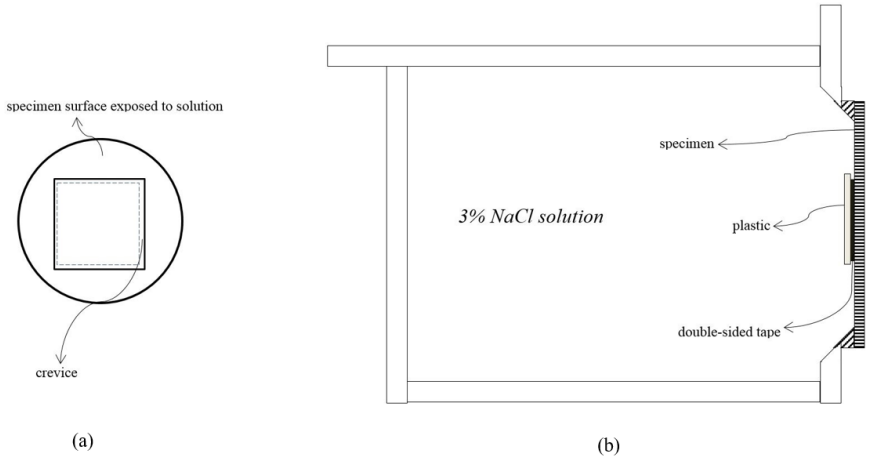

Fig. 2. Schematics of the experimental arrangement for simulating crevice corrosion in the cathodic-side permeation cell viewed from (a) the front and (b) the side.

Fig. 2 presents the arrangement for simulating crevice corrosion in the hydrogen-entry-side of the permeation cell. The 980 DP steel specimen was ground to 0.66 mm, polished to a 3 μm surface finish, and an area of 3.213 cm^2 was exposed to the deaerated 0.1 M NaOH solution in the hydrogen-exit-side cell. A plastic sheet, with dimensions 10 × 10 × 0.8 mm, was glued to the steel surface using a doubled-sided tape with dimensions of about 9 × 9 × 0.5 mm. Thus, a crevice of about 10 × 0.5 × 0.5 mm was created between the plastic sheet and metal sheet, along the four sides of the plastic sheet. The specimen was immersed in 3 wt% NaCl solution at the free corrosion potential.

2.5. 0.1M HCl

Experiments at the free potential in 0.1M HCl solution were carried out using 980 DP steel. The 0.1M HCl solution is much more severe than any environment encountered in auto service. These experiments were carried out because this solution has been used to study the influence of hydrogen on AHSS [33, 34]. The specimen was ground to 0.91 mm with a 3 μm surface finish, and exposed area of 2.608 cm^2 in the hydrogen-exit-side cell. The open circuit potential was measured to be –0.476 $V_{Ag/AgCl}$.

3. Results

3.1. Cathodic charging

Fig. 3(a) presents a typical normalized permeation rise transient for 980 DP, fitted to Eq. (7). There was good agreement between the measured permeation rise transient and the theoretical curve. Fig. 3(b) presents a typical decay transient for 980 DP, and the fit to Eq. (8).

The fitting was not as good for the decay transient indicating that there was more of a trapping effect.

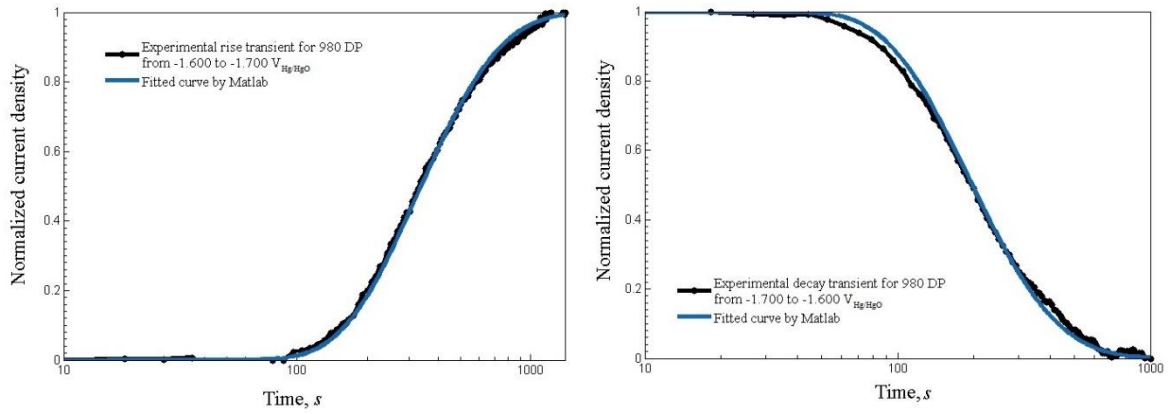

Fig. 3. Fitted curves (a) for a permeation rise transient from – 1.600 $V_{Hg/HgO}$ to – 1.700 $V_{Hg/HgO}$ by Matlab and (b) for a permeation decay transient from – 1.700 $V_{Hg/HgO}$ to – 1.600 $V_{Hg/HgO}$ for 980 DP specimen in 0.1 M NaOH solution.

Fig. 4 shows a typical transient loop with input charging potentials values from – 1.700 $V_{Hg/HgO}$ to – 1.100 $V_{Hg/HgO}$ and back to – 1.700 $V_{Hg/HgO}$ in the 0.1 M NaOH solution for 980 DP. Fitting such transients to Eqs. (7) and (8) allowed determination of the values of the effective diffusion coefficient, D_{eff}, and the corresponding total hydrogen concentrations, C_{HT}, at the input side of the steel specimens using Eq. (10).

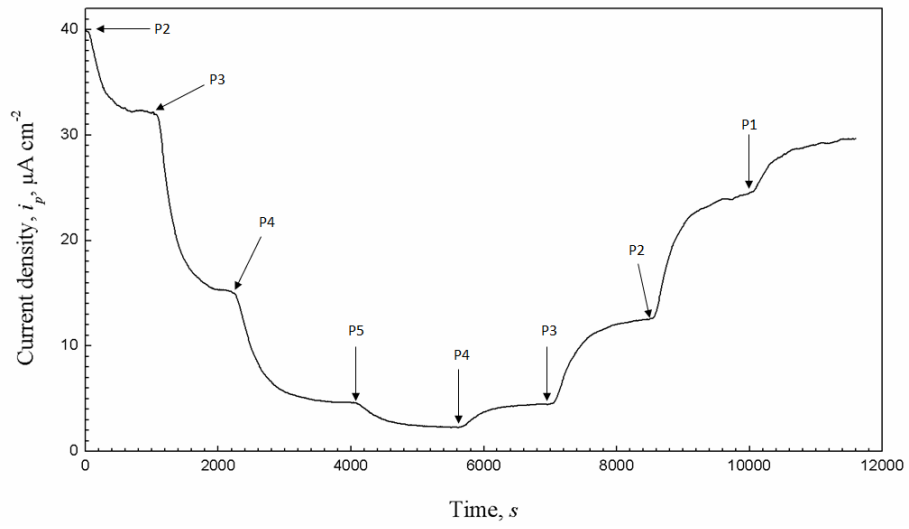

Fig. 4. Hydrogen permeation transients at different cathodic potentials at the input side of the 980 DP steel after 60 h pre-charging at – 1.600 $V_{Hg/HgO}$ in 0.1 M NaOH solution (P1: – 1.700 $V_{Hg/HgO}$, P2: – 1.600 $V_{Hg/HgO}$, P3: – 1.400 $V_{Hg/HgO}$, p4: – 1.200 $V_{Hg/HgO}$ and P5: – 1.100 $V_{Hg/HgO}$).

Fig. 5 presents, as the open symbols, the experimentally determined relationship between the total hydrogen concentration at the input side of the permeation specimen, C_{HT}, and the overpotential, η, for all the steels with cathodic hydrogen charging in the 0.1M NaOH

solution. For clarity, fitting lines are shown only for 980 DP-GI (650 MPa YS) and 980 QP. There was a turning point for each steel at an overpotential of 0.5 V. The relationship between ln C_{HT} and η was linear both below and above the turning point.

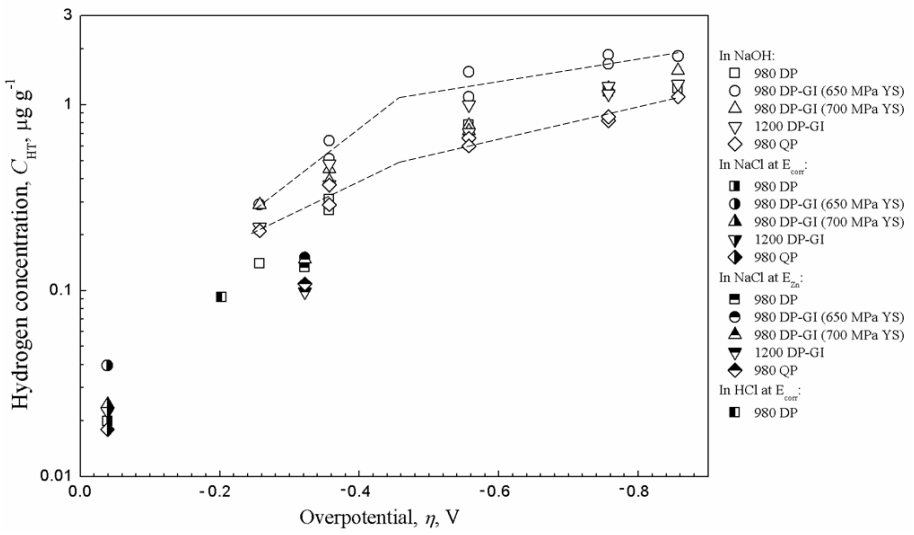

Fig. 5. The hydrogen concentration, C_{HT} vs. the overpotential, η for all the studied steels (i) under simulated service corrosion in 3wt% NaCl solution, (ii) under cathodic charging in 0.1M NaOH at various potential as shown in Fig. 4, and (iii) at free corrosion in 0.1 M HCl solution. For clarity, fitting lines are shown only for 980 DP-GI (650 MPa YS) and 980 QP.

3.2. Simulated service corrosion

Fig. 6 presents the hydrogen permeation current density versus time for all the steels under simulated auto service conditions in 3wt% NaCl solutions at E_{corr} and E_{Zn}. These are not permeation transients, as is apparent by a comparison with Fig. 4. The current density changed slowly with time, attributed to the slow conditioning of the input surface to a steady state. Fig. 6(a) shows that for the steels charged at E_{Zn}, the curve consisted of three periods: a fast rising stage, a declining stage and a slowly rising stage, especially for the curves of 980 DP-GI (700 MPa YS), 1200 DP-GI and 980 QP. During the first few hours, the permeation current density increased rapidly. In the next couple of hours, the permeation current density decreased somewhat. This decrease was attributed to the formation of an oxide film on the cathodic polarized surface. Thereafter, there was a slowly increasing current density and a few tiny corrosion pits on the surface. The permeation current density reached a steady state after about 60-hour charging. The steady-state permeation current density could be higher than the maximum value during the fast rising stage.

Fig. 6(b) presents the magnified view of the permeation current density, to present the curves at E_{corr}. These curves all exhibited two stages: a rising stage and a steady state stage. The time to steady state was much longer than the time for a permeation transient [11] see

Fig. 4. The increase in the permeation current density over this long time is attributed to changes at the ingress side of the specimen. During the rising stage, the hydrogen permeation current density increased with time, resulting from an increased amount of hydrogen atoms that formed and permeated through the steel during the corrosion reaction. The increased amount of hydrogen formed on the surface is attributed to a reduction of the surface oxide film formed during specimen preparation [11]. The hydrogen permeation current density reached a steady state when the ingress surface conditions had reached steady state [11]. After about 60 hour at E_{corr} in 3wt% NaCl solution, most of the surface area of the studied steels was covered by a brown corrosion layer, which easily chipped off after removal of the specimen from the cell, revealing a black layer underneath. This black layer has been identified as magnetite [37].

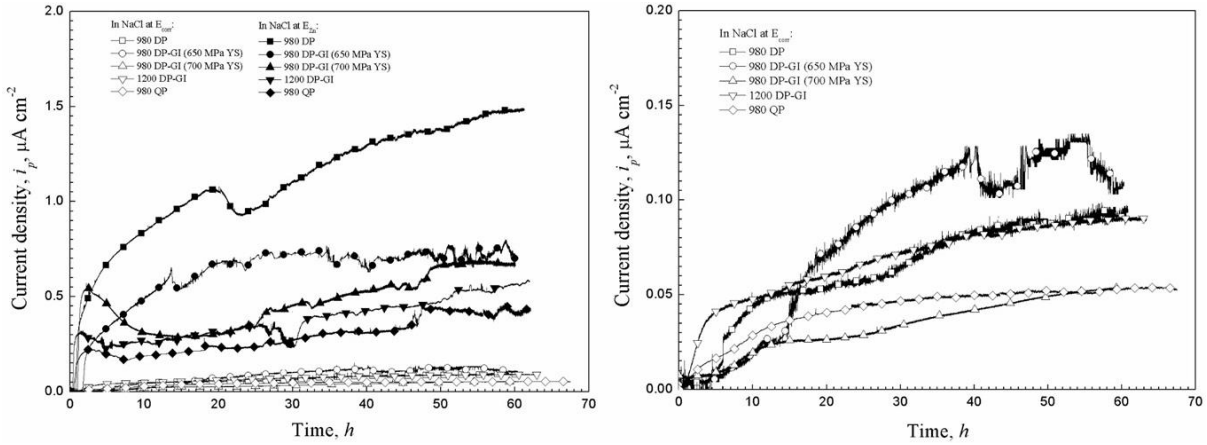

Fig. 6. Hydrogen permeation current density versus time for the steels in (a) 3wt% NaCl at E_{corr} and E_{Zn}, and (b) magnified view showing the hydrogen permeation current density versus time curves in 3wt% NaCl at E_{corr}.

Fig. 5 includes the corresponding values of the total hydrogen concentration, C_{HT}, determined from the stead-state permeation current density from Fig. 6, the effective hydrogen diffusivity, D_{eff}, determined from permeation transients like those in Fig. 4, and by using Eq. (10). At E_{corr} in 3wt% NaCl solution, the values C_{HT}, for 980 DP, 980 DP-GI (650 MPa YS), 980 DP-GI (700 MPa YS), 1200 DP-GI and 980 QP steels, were 0.020 μg g^{-1}, 0.040 μg g^{-1}, 0.024 μg g^{-1}, 0.022 μg g^{-1}, and 0.018 μg g^{-1}, respectively. The highest amount of hydrogen and the highest permeation rate were for 980 DP-GI (650 MPa YS). For the steels hydrogen charged at E_{Zn} in 3wt% NaCl solution, the values C_{HT} were 0.133 μg g^{-1}, 0.150 μg g^{-1}, 0.147 μg g^{-1}, 0.098 μg g^{-1}, and 0.109 μg g^{-1}, respectively, for each steel. The highest amount of hydrogen was in 980 DP-GI (650 MPa YS) steel, and the highest permeation rate was for 980 DP steel.

The hydrogen concentration, C_{HT}, was significantly higher when hydrogen was charged at E_{Zn} than for those at E_{corr} for each steel in the 3wt% NaCl solution. For example, the values of C_H for 980 DP steel were 0.020 μg g^{-1} at E_{corr}, and 0.133 μg g^{-1} at E_{Zn}, increased by about 7 times.

3.3. Crevice corrosion

Fig. 7 presents the hydrogen permeation current density versus time curves for 980 DP steel under the simulated crevice corrosion in 3wt% NaCl solution and compares these data with those measured previously under simulated auto service corrosion conditions in 3wt% NaCl solutions at E_{corr}, Fig. 6(b). Fig. 7 shows that the permeation current density versus time curve for the simulated crevice corrosion almost overlapped the curve at E_{corr} in NaCl solution.

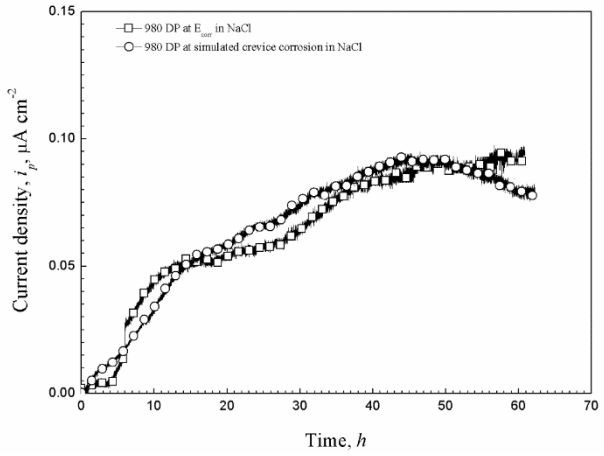

Fig. 7. Hydrogen permeation current density versus time curves for 980 DP steel under the simulated crevice corrosion in 3wt% NaCl solution and compares these data with those measured previously under simulated auto service corrosion conditions in 3wt% NaCl solutions at E_{corr}.

Fig. 7 indicates that the values of steady state permeation current density and the calculated hydrogen concentration for simulated crevice corrosion and auto service corrosion conditions were 0.092 μA cm^{-2} and 0.095 μA cm^{-2}, and 0.019 μg g^{-1} and 0.020 μg g^{-1}, respectively. The values were essentially the same. However, the corroded areas were significantly different.

For the simulated crevice corrosion condition, corrosion occurred (i) in the area associated with the crevice and also (ii) on the open surface outside of the crevice. The corroded area in the crevice was 0.398 cm^2 and the open surface area was 0.871 cm^2. Assuming the permeation current density related to the corrosion on the open surface of the steel under simulated crevice corrosion was the same as that at E_{corr} in the 3wt% NaCl

solution, since the permeation current density and permeation rate were essentially the same for both conditions, the following equation could be derived:

$$i_o\ s_o + i_c\ s_c = i_o\ s_e \quad (15)$$

where i_o is the permeation current density related to the corrosion on the open surface of the steel, i_c is the permeation current density related to the corrosion associated with the crevice, s_o is the corroded area of the open surface, s_c is the corroded area in the crevice, and s_e is the corroded area on the surface of the steel at E_{corr} in the 3wt% NaCl solution. The values of s_o, s_c and s_e were measured to be 0.871 cm^2, 0.398 cm^2 and 2.014 cm^2.

Thus, i_c was calculated to be 3 times as high as i_o, meaning crevice corrosion could provide 3 times more hydrogen permeated through the specimen than did corrosion on the open surface.

3.4. 0.1M HCl

Fig. 8 presents the permeation current density versus time curves for 980 DP steel in the 0.1M HCl solution at E_{corr} and compares these data with those measured previously under simulated auto service corrosion in 3wt% NaCl solutions at E_{corr} and E_{Zn}.

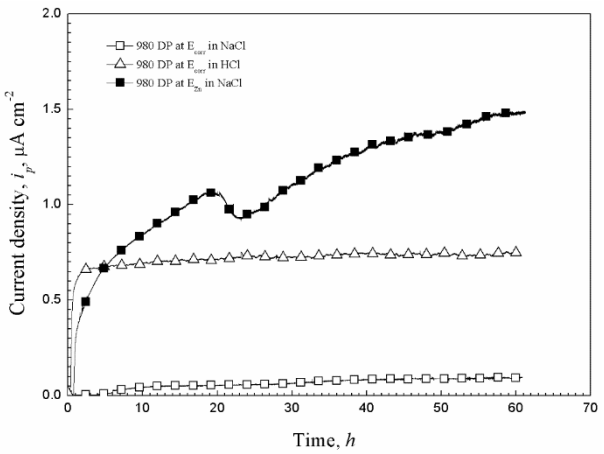

Fig. 8. Hydrogen permeation current density versus time curves for 980 DP steel in the 0.1 M HCl solution at E_{corr} compared with the data measured previously under simulated auto service corrosion conditions in 3wt% NaCl solutions at E_{corr} and E_{Zn}.

The hydrogen permeation current density, in the 0.1 M HCl solution at E_{corr}, increased to a nearly steady-state after about 5 hour and remained steady thereafter, whereas Fig. 7 indicates that it took about 60 hour for hydrogen permeation current density to reach a steady-state in the 3wt% NaCl solution at E_{corr}. The steady-state permeation rate and hydrogen concentration were 0.748 μA cm^{-2} and 0.129 μg g^{-1} and were significantly higher in

the 0.1M HCl solution than in the 3 wt% NaCl solution. The steel surface was observed to be fully covered by corrosion products in the 0.1M HCl solution. The corroded area was measured to be 3.002 cm^2 and 2.014 cm^2 for the steel at E_{corr} in 0.1M HCl and in the 3wt% NaCl solution, respectively.

3.5. Diffusible hydrogen content

Fig. 9 presents the diffusible hydrogen concentration, C_d, for 980 DP, 1200 DP-GI, and 980 QP steels for (i) hydrogen cathodic charging in 0.1M NaOH solution at 23 ± 2 °C at over potential values of –0.257 V, –0.557 V and –0.857 V, (ii) free corrosion in 3wt% NaCl solution, simulating free corrosion of the steel of the car body in service, (iii) cathodic polarisation of the steel to the zinc potential in 3wt% NaCl to simulate the maximum amount of hydrogen produced for the steels protected by a zinc coating applied by galvanisation, (iv) free corrosion in 0.1M HCl, and (v) uncharged.

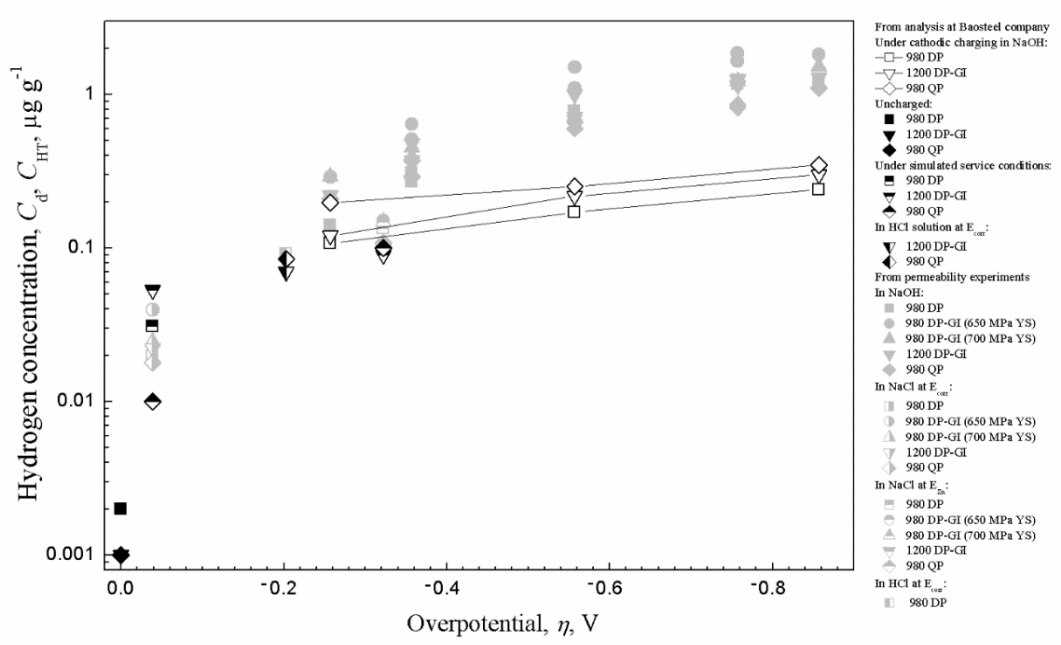

Fig. 9. The measured diffusible hydrogen concentration, C_d, using the BRUKER G4 PHOENIX DH analyser in comparison with the prior measurements of the hydrogen concentration, C_{HT}, which are represented by the grey symbols.

Fig. 9 shows that, at E_{corr} in 3% NaCl solution, the diffusible hydrogen concentration was 0.031 μg g^{-1}, 0.053 μg g^{-1} and 0.010 μg g^{-1} for 980 DP, 1200 DP-GI and 980 QP, respectively, at least 10 times higher than the values of uncharged samples, which were 0.002 μg g^{-1}, 0.001 μg g^{-1} and 0.001 μg g^{-1}. For the steels hydrogen charged at E_{Zn} in 3wt% NaCl solution for 24 h, the diffusible hydrogen concentration was 0.090 μg g^{-1} for 1200 DP-GI and 0.100 μg g^{-1} for 980 QP, higher than the corresponded values at free corrosion. The hydrogen

concentration at the free corrosion in 0.1M HCl solution was 0.070 μg g^{-1} for 1200 DP-GI and 0.085 μg g^{-1} for 980 QP, higher than that for samples freely corroded in NaCl solution. For those under cathodic charging conditions in NaOH solution, the hydrogen concentration was 0.107 μg g^{-1}, 0.171 μg g^{-1} and 0.240 μg g^{-1} for 980 DP steel charged at over potential of –0.257, –0.557 and –0.857 V, respectively. For 1200 DP-GI and 980 QP steels charged at the corresponding overpotentials, the hydrogen concentration was 0.120 μg g^{-1}, 0.218 μg g^{-1} and 0.300 μg g^{-1}, and 0.197 μg g^{-1}, 0.252 μg g^{-1} and 0.347 μg g^{-1}, respectively. The diffusible hydrogen concentration increased with more negative charging potential for each of the steel grades. This trend was consistent with our previous results, as shown in Fig. 5.

Fig. 9 also presents the measured diffusible hydrogen concentration in comparison with the prior measurements of the hydrogen concentration (as presented in Fig. 5). At E_{corr} in 3% NaCl solution, the diffusible hydrogen concentrations, at E_{corr} and at E_{Zn} in 3% NaCl solution, were similar to the values of total hydrogen concentration determined by the permeability experiments. This was also the case for that cathodically charged at overpotential of –0.257 V. However, at more negative charging overpotentials of –0.557 and –0.857 V, the diffusible hydrogen concentrations were lower than the total hydrogen concentration values obtained from our permeability experiments.

4. Discussion

4.1. Diffusible and total hydrogen content

Fig. 9 allows a comparison between the measured amount of diffusible hydrogen, C_d as measured by hot extraction, and the total amount of hydrogen, C_{HT}, as measured by the permeation technique.

The amount of diffusible hydrogen in the as-received steels was low, indicating that either there was little hydrogen in the steels due to steel production, or that the hydrogen had effused out of the steels by the time that these steel samples were tested in this work.

Fig. 9 shows that there was good agreement between the measured amount of diffusible hydrogen, C_d as measured by hot extraction, and the total amount of hydrogen, C_{HT}, as measured by the permeation technique, for the conditions of (i) continuous free corrosion in 3wt% NaCl solution, (ii) free corrosion in 0.1M HCl, (iii) cathodic polarisation of the steel to the zinc potential in 3wt% NaCl, and (iv) cathodic polarisation at the lowest overpotential value in the 0.1M NaOH solution. This good agreement provides validation of the analysis of

the permeation curves by Eqs. (7) and (8), and the estimation of the total hydrogen concentration, C_{HT}, by Eq.(10).

Fig. 9 shows that, at the larger values of overpotential for cathodic hydrogen charging, the measured amount of diffusible hydrogen, C_d, was somewhat less than the total amount of hydrogen, C_{HT}. This is attributed to the loss of some diffusible hydrogen between the end of the cathodic charging and the measurement of the amount of diffusible hydrogen. There was an inevitable delay between the end of cathodic changing and the commencement of the hydrogen content measurement because the specimen needed to be washed, dried, inserted into the measurement apparatus and the commencement of heating for hydrogen extraction. The loss of diffusible hydrogen by diffusion out of the sample is related to the amount of diffusible hydrogen and was thus much larger at the higher hydrogen concentrations. In addition, the effective diffusion coefficient tends to be larger at the higher concentrations because of less trapping, and consequently the diffusion loss is greater at the higher hydrogen concentrations. In contrast, the total amount of hydrogen, C_{HT}, was measured by the permeation technique under steady state conditions, and thus represented the total hydrogen in the specimen.

4.2. Service versus cathodic charging

Fig. 5 presents the experimentally determined relationship between the total hydrogen concentration at the input side of the steel specimen, C_{HT}, and the overpotential, η, for all the steels under simulated service conditions, and for cathodic charging in the 0.1M NaOH solution. This allows a direct comparison between the hydrogen concentration produced under service conditions with that under cathodic charging conditions.

There was a turning point at a overpotential of –0.5 V for each steel for cathodic charging in the relationship between C_{HT} and η. Similarly, a turning point was also reported by Bockris et al. [26] and Liu et al. [28]. The turning point was attributed to the change of hydrogen evolution mechanisms from coupled discharge-recombination mechanism at lower overpotentials (i.e. a combination of Eq.(2) plus Eq.(3)) to a slow discharge-fast electrochemical mechanism at higher overpotentials; that is electrochemical dischange of adsorbed hydrogen becomes increasingly probable by Eq.(5).

Fig. 5 shows that, for each steel, the hydrogen concentration at the input side of the steel, C_{HT}, was significantly lower under simulated auto service conditions in 3wt% NaCl or in 0.1M HCl solution than that under cathodic charging in 0.1M NaOH solution, even lower than that at the least negative charging potential of –1.100 $V_{Hg/HgO}$. For example, for 980 DP steel, the overpotential at the free corrosion in NaCl solution, at the free corrosion in 0.1M

HCl solution and at the zinc potential in NaCl solution was –0.039 V, –0.203 V and –0.322 V, respectively, and the experimentally determined hydrogen concentration, C_{HT}, was 0.020 μg g^{-1}, 0.129 μg g^{-1} and 0.133 μg g^{-1}, respectively, whereas, the value of C_{HT} was 0.14 μg g^{-1} at the least negative charging potential, –1.100 $V_{Hg/HgO}$ with an overpotential of –0.257 V in the 0.1M NaOH solution. The C_{HT} value, at the least negative charging potential in the 0.1M NaOH solution, was higher than those under the simulated service corrosion conditions. Furthermore, extrapolating the experimental data obtained in the 0.1M NaOH solution, the C_H value for 980 DP steel in the 0.1M NaOH solution, at each overpotential corresponding to that under simulated auto service corrosion conditions, was calculated to be 0.036 μg g^{-1}, 0.131 μg $g^{-1}$and 0.225 μg g^{-1}, respectively, and was higher than that experimentally determined under simulated auto service conditions.

Similarly, at overpotential values of –0.039 V and –0.322 V, the extrapolated hydrogen concentration, C_{HT} in the 0.1M NaOH solution, was 0.066 μg g^{-1} and 0.451 μg g^{-1} for 980 DP-GI (650 MPa YS), 0.131 μg g^{-1} and 0.370 μg g^{-1} for 980 DP-GI (700 MPa YS), 0.054 μg g^{-1} and 0.333 μg g^{-1} for 1200 DP-GI, and 0.080 μg g^{-1} and 0.282 μg g^{-1} for 980 QP. At the same overpotential, the hydrogen concentration was significantly higher in the 0.1M NaOH solution than those in the 3wt% NaCl solution, indicating that at the same overpotential, more hydrogen entered in and permeated through the steel specimen in the 0.1M NaOH solution than that in the 3wt% NaCl solution.

4.3. Hydrogen evolution

In the 0.1M HCl solution, where the pH is low, hydrogen is evolved through the reduction of hydronium ions, as in Eq. (1). When the pH is neutral and alkaline, such as in 3wt% NaCl and 0.1M NaOH solutions, the transport of H_3O^+ to the steel surface becomes rate limited, so that instead of the reduction of hydronium ions, hydrogen is produced by water decomposition [38-40]. Therefore, the mechanism of hydrogen evolution, as in Eq. (2), is different from that in acid solutions.

In all the solutions, either under cathodic polarization or at the free corrosion potential, the hydrogen evolution reaction acts as part of the cathodic partial reaction, which balances the anodic reaction. For the tests under cathodic polarization in 0.1 M NaOH and 3wt% NaCl solutions, the electrons for hydrogen reduction reaction were provided by the external potentiostat, whereas for those at free potential in 0.1M HCl and 3wt% NaCl solutions, the electrons for hydrogen evolution reaction came from the anodic reaction:

$$Fe \rightarrow Fe^{2+} + 2e \quad (16)$$

The cathodic partial reaction as in Eq. (2) and the oxygen partial reduction reaction balance the anodic partial reaction as in Eq. (16) in the 3wt% NaCl solution. A change of either reaction rate causes an adjustment to minimize the effect of this change. Cathodic polarization causes increased hydrogen evolution by Eq. (2) and decreased corrosion rate by the rate of Eq. (16). This explains why the amount of corrosion for steels cathodically polarized at E_{Zn} is significantly less than that at E_{corr} in 3wt% NaCl solution. During cathodic polarization in the 0.1M NaOH solution, hydrogen is produced due to the continuously provided electrons. A more negative overpotential increased the current of the hydrogen evolution reaction [41]. Thus, the rate of Eq. (2) was accelerated and more hydrogen was produced.

Liu et al. [28] stated that after long time pre-charging, surface oxides would be expected to be reduced to a stable state, and thus it would be expected that there was equilibrium between the adsorbed hydrogen on the steel surface and the hydrogen dissolved into the steel. In the cathodic charging experiments, prolonged charging was conducted for permeation experiments in the 0.1M NaOH solution. Thus, equilibrium was expected for our study in the 0.1M NaOH solution. In the 3wt% NaCl and 0.1M HCl solutions, it was also expected that there was equilibrium between the released hydrogen on the steel surface and the absorbed hydrogen, since water molecule or hydronium ion diffused through gaps in the oxide film to the steel surface and was reduced, releasing hydrogen adsorbed on the steel surface and then introducing the adsorbed hydrogen into the specimen.

Therefore, both of cathodic charging and corrosion conditions in this study provided hydrogen evolution. Equilibrium between the adsorbed hydrogen on the steel surface and the hydrogen dissolved into the steel was satisfied, so that the produced hydrogen could be absorbed into the steel, permeate through and be oxidized by the applied potential on the other side.

4.4. Hydrogen permeation current density

In the 0.1M NaOH solution, the permeation rate, i_∞, increased with a more negative potential, due to the higher rate of hydrogen reduction reaction, Eq. (2) and a less potent trapping effect. This result is consistent with that from prior studies [26, 28], where a more negative charging potential increased the hydrogen fugacity, and also the trapping effect decreased because of the higher hydrogen concentration.

For each of the steels in the 3wt% NaCl solution, the hydrogen concentration was higher at E_{Zn} than that at E_{corr}. When applying E_{Zn} to the steel immersed in the 3wt% NaCl solution, cathodic polarization increased the hydrogen reduction reaction, Eq. (2), and decreased the corrosion of the steel, Eq. (16), the same as applied in cathodic protection [42, 43]. Thus, this explains the results that, for the same steel at E_{Zn} compared with that at E_{corr}, more hydrogen entered and permeated into the steel.

4.5. Steel metallurgy

Table 1 indicates that the metallurgy of the steels ~40% ferrite, with the remainder largely martensite. For the first four steels in Table 1, the ferrite content decreased, and the martensite content increased and caused the yield strength to increase. Nevertheless, the total hydrogen content was $C_{HT} = 0.13 \pm 0.2$ μg g^{-1} for immersion in 3wt% NaCl at E_{Zn}. Moreover, the 980 Q&P steel had a total hydrogen concentration within this range.

This indicates that these steels were similar in metallurgy with relatively small differences in steel metallurgy and strength and were associated with similar hydrogen concentrations caused by service corrosion and by hydrogen charging.

4.6. Simulated service conditions

In order to simulate auto service corrosion conditions, the following experimental conditions were studied using 980 DP steels: (i) free corrosion at E_{corr} in 3wt% NaCl solution, (ii) crevice corrosion in the 3wt% NaCl solution, (iii) cathodic polarization at E_{Zn} in the 3% NaCl solution, and (iv) free corrosion at E_{corr} in the 0.1 M HCl solution. The experimental results showed that the permeation rate and the hydrogen concentration decreased in the following order (i) E_{Zn} in the 3wt% NaCl solution, (ii) free corrosion at E_{corr} in the 0.1M HCl solution, (iii) simulated crevice corrosion in the 3% NaCl solution, and (iv) free corrosion at E_{corr} in the 3wt% NaCl solution.

In an alkaline solution, a thin protective oxide or hydroxide layer is formed and tends to passivate the steel. In contrast, in the 3wt% NaCl and 0.1M HCl solutions, the adsorption of aggressive ions such as Cl^- on the surface metal increases the corrosion current density, i.e. increases the corrosion rate [44]. Thus corrosion occurred in the 3wt% NaCl solution and the 0.1M HCl solution at the free potential in this study. Furthermore, iron dissolution depends on H^+ ion concentration more than on the Cl^- ion concentration [45]. Starkey et al. [46] indicated that the pK_a values for water and hydronium ions are 15.73 and –1.74, respectively. The lower pK_a value for hydronium ions results in preferable hydrogen evolution from these

hydronium ions. Therefore, in this study at the free corrosion, the corrosion rate in the 0.1M HCl solution was higher, reflected by the steeper initial slope of the permeation current density in Fig. 8, and produced more hydrogen than that in the 3wt% NaCl solution. More hydrogen entered into and diffused through the specimen, resulting in higher permeation rates and higher hydrogen concentrations at the free corrosion in 0.1 M HCl solution than in 3wt% NaCl solution, as presented in Fig. 5.

Under simulated crevice corrosion condition, corrosion occurred both on the open surface area, and the area within the crevice. The total corroded area was significantly smaller than that at E_{corr} in the 3wt% NaCl solution, yet the permeation current rates were essentially the same for the simulated crevice corrosion and for the free corrosion on the open surface. By assuming the permeation current density related to the surface area under simulated crevice corrosion was the same as that at E_{corr} in 3wt% NaCl solution, the permeation rate related to crevice corrosion was calculated, using Eq. (15), to be 3 times higher than that related to corrosion on the open surface.

The crevice corrosion is reported to initiate due to the depletion of oxygen inside the crevice, resulting in rapid dissolution of the metal and reduced pH in the crevice [47]. Thus, more hydrogen is evolved in the crevice. The set-up in this study could satisfy the conditions for the initiation of crevice corrosion, and corrosion was also observed inside the crevice area in addition to that in the un-creviced area. Furthermore, the oxygen content outside of the crevice was considered not to be influenced when simulating the crevice corrosion, so that the assumption of the unchanged corrosion rate on the open surface for the simulated crevice corrosion and for the free corrosion in 3wt% NaCl solution, was considered appropriate. Therefore, Eq. (15) could be proposed, yielding the result that the amount of hydrogen introduced into and permeated through the steel caused by crevice corrosion was 3 times higher than that for the corrosion on the open surface. Details for the standard test methods for crevice corrosion resistance could be referred as per [48].

For the experiments at E_{Zn} in the 3wt% NaCl solution, the cathodic polarization increased the hydrogen reduction reaction, Eq. (2), and decreased the corrosion of the steel, Eq. (16), as stated above. This explained the highest permeation rate and hydrogen concentration at E_{Zn} in 3wt% NaCl solution, compared with the other conditions simulated auto service.

During actual auto service, the steel could be corroded, introducing hydrogen, and influencing the steel properties, so the permeation experiments at E_{corr} and under simulated crevice corrosion in 3% NaCl solution indicated how much hydrogen had permeated under

these conditions. These experiments indicated that crevice corrosion would introduce 3 times more hydrogen into and permeate through the steel than that at the open corrosion potential. In addition, in order to prevent the steel from corrosion, steel can be galvanized, by applying a Zn coating on the steel surface. The permeation experiments at E_{Zn} in the 3wt% NaCl solution indicated that this Zn coating could significantly reduce the corrosion of the steel, but more hydrogen could be introduced into the steel in addition to the hydrogen from the corrosion on the open surface of the steel. Thus, more hydrogen would be introduced into and permeate through the galvanized steel if there is access of the steel surface to the corroding solution.

Ootsuka et al. [49] recently measured the amount of hydrogen absorbed into a 270 MPa cold rolled steel in an automobile moving environment. They found that (i) hydrogen entered the steel only during corrosion, and that (ii) 0.5% NaCl sprayed on the surface enhanced the hydrogen absorption into the steel. Nevertheless, the hydrogen concentrations were an order of magnitude lower than those measured herein, and moreover, the hydrogen was desorbed within hours of the cessation of corrosion. Their work indicated that one mol of hydrogen was absorbed for every 1000 mol of steel corroded, indicating that the hydrogen evolution reaction compromised 0.1% of the cathodic reaction.

5. Conclusions

1. The hydrogen concentrations and permeation rates for simulated auto service conditions were significantly lower than the values at the least negative cathodic charging potential of –1.100 $V_{Hg/HgO}$ in 0.1M NaOH solution.
2. The amount of hydrogen introduced by crevice corrosion in 3wt% NaCl solution into the steel was 3 times larger than that introduced by the corrosion on the open circuit potential of the steel.
3. The Zn coating on the steels could protect the substrate steel from corrosion, however, once the Zn coating was corroded under actual service condition, more hydrogen could enter and permeate through the steel.

Acknowledgements

This research is supported by the Baosteel-Australia Joint Research & Development Centre (BAJC) Grant, BA13037, with linkage to Baoshan Iron and Steel Co., Ltd of China.

References

[1] G Lovicu, M Bottazzi, F D'Aiuto, M De Sanctis, A Dimatteo, C Santus and R Valentini, Hydrogen embrittlement of automotive advanced high-strength steels, Metall Mater Trans A. 43 (2012) 4075-4087.

[2] M Robinson and P Kilgallon, Hydrogen embrittlement of cathodically protected high-strength, low-alloy steels exposed to sulfate-reducing bacteria, Corrosion. 50 (1994) 626-635.

[3] E Hamzah and M Kanniah, Corrosion Behavior of low carbon steel sheets for car bodies, Jurnal Mekanikal. 19 (2005) 57-70.

[4] N LeBozec, N Blandin and D Thierry, Accelerated corrosion tests in the automotive industry: a comparison of the performance towards cosmetic corrosion, Materials and corrosion. 59 (2008) 889-894.

[5] D Hardie, EA Charles and AH Lopez, Hydrogen embrittlement of high strength pipeline steels, Corros Sci. 48 (2006) 4378-4385.

[6] R Davies, Hydrogen embrittlement of dual-phase steels, Metall Trans A. 12 (1981) 1667-1672.

[7] R McCoy and W Gerberich, Hydrogen embrittlement studies of a trip steel, Metall Trans. 4 (1973) 539-547.

[8] J Ronevich, B De Cooman, J Speer, E De Moor and D Matlock, Hydrogen effects in prestrained transformation induced plasticity steel, Metall Mater Trans A. 43 (2012) 2293-2301.

[9] JA Ronevich, JG Speer and DK Matlock, Hydrogen embrittlement of commercially produced advanced high strength sheet steels, SAE Int. J. Mater. Manuf. 3(1) (2010) 255-267.

[10] J Venezuela, Q Liu, M Zhang, Q Zhou and A Atrens, The influence of hydrogen on the mechanical and fracture properties of some martensitic advanced high strength steels studied using the linearly increasing stress test, Corros Sci. 99 (2015) 98-117.

[11] Q Liu, J Venezuela, M Zhang, Q Zhou and A Atrens, Hydrogen diffusion and trapping in dual phase and quenched and partitioned advanced high strength steels, Corros Sci. Avaliable from, Access on (2015).

[12] D Bhattacharya, Developments in Advanced High Strength Steels, Proceedings of Proceedings of the Joint International Conference of HSLA Steels, Sanya, 2005, 70-73.

[13] J Galán, L Samek, P Verleysen, K Verbeken and Y Houbaert, Advanced high strength steels for automotive industry, Rev Metal Madrid. 48 (2012) 118-131.

[14] WorldAutoSteel, Advanced high-strength steels application guidelines version 5.0, Available from http://www.worldautosteel.org/, Access on 2014.

[15] DK Matlock and JG Speer, Third Generation of AHSS: Microstructure Design Concepts, Microstructure and Texture in Steels, Charpter 11, p. 185-205, Springer London, 2009.

[16] DK Matlock, JG Speer, E De Moor and PJ Gibbs, Recent developments in advanced high strength sheet steels for automotive applications: an overview, Jestech. 15 (2012) 1-12.

[17] X Zhu, Z Ma and L Wang, Current status of advanced high strength steel for auto-making and its development in Baosteel, Avaliable from www.baosteel.com, Access on 26.11.2014.

[18] Baosteel, Baosteel automotive advanced high strength steels, Available from http://www.baosteel.com/, Access on 2013.

[19] VF Zackay, ER Parker, D Fahr and R Busch, The enhancement of ductility in high-strength steels, ASM Trans Quart. 60 (1967) 252-259.

[20] M Chen, R Wu, H Liu, L Wang, J Shi, H Dong and X Jin, An ultrahigh strength steel produced through deformation-induced ferrite transformation and Q&P process, Sci China Technol Sci. 55 (2012) 1827-1832.

[21] DV Edmonds, K He, FC Rizzo, BC De Cooman, DK Matlock and JG Speer, Quenching and partitioning martensite—A novel steel heat treatment, Mater Sci Eng A. 438-440 (2006) 25-34.

[22] MJ Santofimia, L Zhao and J Sietsma, Overview of Mechanisms Involved During the Quenching and Partitioning Process in Steels, Metall Mater Trans A. 42 (2011) 3620-3626.

[23] Q J Zhou, L Wang and JX Li, Experimental study on delayed fracture of TS 980MPa grade steels for automotive applications, Proceedings of Steel Hydrogen Conference, Ghent, Belgium, 2014, 35-44.

[24] M Devanathan and Z Stachurski, The adsorption and diffusion of electrolytic hydrogen in palladium, Proceedings of the Royal Society of London. Series A. Mathematical and Physical Sciences. 270 (1962) 90-102.

[25] A Atrens, D Mezzanotte, N Fiore and M Genshaw, Electrochemical studies of hydrogen diffusion and permeability in Ni, Corros Sci. 20 (1980) 673-684.

[26] JM Bockris, J McBreen and L Nanis, The Hydrogen Evolution Kinetics and Hydrogen Entry into [alpha]-Iron, J Electrochem Soc. 112 (1965) 1025-1031.

[27] JM Bockris and P Subramanyan, The equivalent pressure of molecular hydrogen in cavities within metals in terms of the overpotential developed during the evolution of hydrogen, Electrochim Acta. 16 (1971) 2169-2179.

[28] Q Liu, AD Atrens, Z Shi, K Verbeken and A Atrens, Determination of the hydrogen fugacity during electrolytic charging of steel, Corros Sci. 87 (2014) 239-258.

[29] J McBreen, L Nonis and W Beck, A method for determination of the permeation rate of hydrogen through metal membranes, J Electrochem Soc. 113 (1966) 1218-1222.

[30] T Zakroczymski, Adaptation of the electrochemical permeation technique for studying entry, transport and trapping of hydrogen in metals, Electrochim Acta. 51 (2006) 2261-2266.

[31] Q Liu and A Atrens, Reversible hydrogen trapping in a 3.5NiCrMoV medium strength steel, Corros Sci. 96 (2015) 112-120.

[32] A Turnbull, Hydrogen diffusion and trapping in metals, Gaseous Hydrogen Embrittlement of Materials in Energy Technologies, Woodhead Publishing, Oxford, UK. 2 (2012) 89-128.

[33] S Takagi, Y Toji, M Yoshino and K Hasegawa, Hydrogen embrittlement resistance evaluation of ultra high strength steel sheets for automobiles, ISIJ Int. 52 (2012) 316-322.

[34] Y Toji, S Takagi, M Yoshino, K Hasegawa and Y Tanaka, Evaluation of hydrogen embrittlement for high strength steel sheets, Proceedings of Mater Sci Forum, 2010, 3537-3542.

[35] J Flis, T Zakroczymski, V Kleshnya, T Kobiela and R Duś, Changes in hydrogen entry rate and in surface of iron during cathodic polarisation in alkaline solutions, Electrochim Acta. 44 (1999) 3989-3997.

[36] P Delahay, M Pourbaix and P Van Rysselberghe, Potential-pH diagrams, Journal of Chemical Education. 27 (1950) 683.

[37] H Moller, E Boshoff and H Froneman, The corrosion behaviour of a low carbon steel in natural and synthetic seawaters, JOURNAL-SOUTH AFRICAN INSTITUTE OF MINING AND METALLURGY. 106 (2006) 585.

[38] L Nylén and A Cornell, Effects of electrolyte parameters on the iron/steel cathode potential in the chlorate process, Journal of Applied Electrochemistry. 39 (2009) 71-81.

[39] T Hurlen, S Gunvaldsen and F Blaker, Effects of buffers on hydrogen evolution at iron electrodes, Electrochim Acta. 29 (1984) 1163-1164.

[40] M Stern, The electrochemical behavior, including hydrogen overvoltage, of iron in acid environments, J Electrochem Soc. 102 (1955) 609-616.

[41] S Hans-Henning, Fundamentals of Corrosion, Corrosion Mechanisms in Theory and Practice, Third Edition, Charpter p. 1-104, CRC Press, 2011.

[42] PE Francis, Cathodic protection in practise, Avaliable from www.npl.co.uk, Access on 28.09.2015.

[43] T Tezdogan and YK Demirel, An overview of marine corrosion protection with a focus on cathodic protection and coatings, Brodogradnja. 65 (2014) 49-59.

[44] M Sun, K Xiao, C Dong and X Li, Electrochemical corrosion behavior of 300M ultra high strength steel in chloride containing environment, Acta Metall. Sin.(Engl. Lett.). 23 (2010) 301-311.

[45] EA Noor and AH Al-Moubaraki, Corrosion behavior of mild steel in hydrochloric acid solutions, Int. J. Electrochem. Sci. 3 (2008) 806-818.

[46] R Starkey, J Norman and M Hintze, Who knows the Ka values of water and the hydronium ion?, Journal of Chemical Education. 63 (1986) 473.

[47] JW Oldfield, Test techniques for pitting and crevice corrosion resistance of stainless steels and nickel-base alloys in chloride-containing environments, International materials reviews. 32 (1987) 153-172.

[48] ASTM, Standard test methods for pitting and crevice corrosion resistance of stainless steels and related alloys by use of ferric chloride solution, ASTM International. Avaliable from, Access on (2009).

[49] S Ootsuka, S Fujita, E Tada, A Nishikata and T Tsuru, Evaluation of hydrogen absorption into steel in automobile moving environments, Corros Sci. 98 (2015) 430-437.

Chapter 6

Equivalent hydrogen fugacity during electrochemical charging of 980DP steel determined by thermal desorption spectroscopy

(submitted to industrial partner for approval of publication)

This last chapter follows the previous Chapters 4 and 5 in continuing analysing the hydrogen behaviours to contribute to understanding the hydrogen influence.

Chapter 6 incorporates the TDS study on 980DP steel, with the following aims: (i) determination of hydrogen concentration in the steels after charged with various conditions, (ii) establishing the relationship of the hydrogen fugacity during electrochemical charging and the charging overpotential to estimate the severity of the hydrogen environment, and (iii) evaluating the hydrogen trap activation energy and identifying the trap types. The expected results would permit correlating the hydrogen charging condition with the hydrogen fugacity on the steel surface, with the hydrogen concentration introduced into the steel, with the microstructures associated with hydrogen trapping, and further with the influence of this hydrogen on the properties of the key steels.

Equivalent hydrogen fugacity during electrochemical charging of 980DP steel determined by thermal desorption spectroscopy

Qinglong Liu[a], Evan Gray[b], Jeffrey Venezuela[a], Qingjun Zhou[c,*], Clotario Tapia-Bastidas[b,d], Mingxing Zhang[a], Andrej Atrens[a,*]

[a] The University of Queensland, Division of Materials, School of Mining and Mechanical Engineering, St. Lucia, 4072 Australia

[*] Corresponding author, andrejs.atrens@uq.edu.au, +61 7 3365 3748, zhouqingjun@baosteel.com, +86 21 26641807

[b] Queensland Micro- and Nanotechnology Centre, Griffith University, Brisbane 4111, Australia

[c] Baoshan Iron & Steel Co., Ltd, Research Institute, Shanghai, 201900, China

[d] Faculty of Mechanical Engineering and Production Science, Escuela Superior Politécnica del Litoral (ESPOL), Guayaquil, Ecuador

Abstract

Analysis was conducted using a new thermal desorption spectroscopy (TDS) apparatus on 980DP steels after (i) electrochemical hydrogen charging in 0.1 M NaOH and in 3 wt% NaCl, and (ii) gaseous hydrogen charging at various pressures. The hydrogen concentration increased with (i) a more negative charging potential and (ii) an increasing hydrogen gas pressure. The equivalent hydrogen fugacity versus electrochemical hydrogen charging overpotential was evaluated. The de-trapping activation energies were 40.5 kJ mol^{-1} and 50.2 kJ mol^{-1}, indicating hydrogen traps at boundary defects.

Keywords: A. steel, B. TDS, C. hydrogen embrittlement

1. Introduction

Due to their good combination of strength and ductility, good formability, and high energy absorption capability, Dual Phase (DP) steels have demonstrated the capability to fulfil the demands of improved safety and environmental friendliness by light-weighting, and have been widely used in the auto industry, since their first development in the 1980's [1-5]. In addition, the relatively low cost for manufacturing DP steels has also contributed to their increasing proportion in auto construction [1, 6]. DP steels find applications in the crumple zones (e.g. rear shock reinforcements and rear rails), and in the safety cage compartments (e.g. B-pillar and floor panel), of the car body [3, 7].

DP steels are exposed to hydrogen-producing environments during production and application, permitting hydrogen to be absorbed into the steels. This hydrogen, in combination with stress, could cause a deterioration of the steel mechanical properties, especially ductility [8-11]. This phenomenon is called hydrogen embrittlement (HE), and has been widely documented for DP steels [12-18].

Our recent studies [19, 20] indicated a detrimental hydrogen influence on DP steels under various hydrogen environments. We further found [20] that the hydrogen influence was associated with a critical hydrogen concentration, a concept also proposed in other research [10, 21]. Moreover, Pérez Escobar et al. [22] argued that the nature of hydrogen in the steels (e.g. diffusible or trapped hydrogen) was more critical than the amount of hydrogen, in terms of hydrogen influence, provided that there was sufficient hydrogen. Diffusible and reversibly trapped hydrogen are detrimental hydrogen sources for hydrogen embrittlement, whereas irreversible traps always function as hydrogen sinks, preventing hydrogen from moving to flaws, and are beneficial to HE resistance [23, 24]. Microstructure features such as grain boundaries, dislocations, and impurities, can act as different types of hydrogen traps, and thereby have various effects on HE resistance [2]. Therefore, a better understanding of hydrogen influence could be obtained through identifying hydrogen traps, and studying the interactions of hydrogen with such traps.

To study the hydrogen influence on steels, there are two common methods to introduce hydrogen into the specimen: (i) electrochemical hydrogen charging, which involves producing hydrogen by cathodic charging at the surface of a specimen submerged in an electrolyte and the subsequent adsorption of the produced hydrogen into the steel, and (ii) gaseous hydrogen charging, which exposes the steel to a high pressure hydrogen gas. Atrens et al. [25] considered the equivalence between gaseous charging and electrochemical hydrogen charging at a constant potential. Liu et al. [26] established the relationship for the equivalent hydrogen fugacity during electrochemical charging using thermodynamics and permeation experiments for an annealed low interstitial steel. They found that the hydrogen fugacity increased with increasing overpotential, and was higher for charging at the same overpotential in 0.1 M NaOH than in 0.1 M Na_2SO_4. Venezuela et al. [27] critically reviewed the equivalent hydrogen fugacity during electrochemical charging in previous studies, and proposed that the hydrogen fugacity was influenced by the steel type, the electrolyte and the charging potential. They also conducted thermal desorption spectroscopy (TDS) analysis on 3.5NiCrMoV steel [28] and found that the equivalent hydrogen fugacity, during

electrochemical charging at the same overpotential, was higher in 0.1 M Na_2SO_4 than in 0.1 M NaOH.

Significant factors for understanding hydrogen influence on DP steels are (i) the hydrogen concentration, (ii) the hydrogen-trap interactions, and (iii) the equivalent hydrogen fugacity during electrochemical charging. These can all be studied using thermal desorption spectroscopy (TDS). TDS has been widely used to study hydrogen trapping and embrittlement in steels [14, 22, 29-34].

This current work used the TDS apparatus designed by Tapia-Bastidas et al. [35] based on the ultra-high-vacuum (UHV) TDS [36] designed by Smith and Scully [37]. This new TDS can accurately characterise hydrogen at concentrations of 1 μg g^{-1} (wt ppm) [35], and has been used to study medium-strength martensitic steel [28], martensitic advanced high-strength steels [27], and is for the first time hereby being used to study dual phase (DP) advanced high-strength steels.

The current work is complementary to our previous studies on DP steels [19, 20, 38, 39], and aims to (i) evaluate the hydrogen concentration in the DP steels subjected to (a) electrochemical cathodic hydrogen charging in 0.1 M NaOH and in 3 wt% NaCl, and (b) gaseous hydrogen charging, (ii) determine the equivalent hydrogen fugacity during electrochemical charging, and (iii) identify the de-trapping activation energy and the associated hydrogen traps.

2. Experimental section

2.1. Materials and microstructure

A commercial DP steel with tensile strength of 980 MPa, designated as 980DP, was supplied from commercial production for auto construction, as rolled sheets. The TDS specimens were cut from the sheet steel into dimensions of 27 mm × 6 mm, with the as-received thickness. All the surfaces were mechanically ground with SiC papers up to 1200 grit. The specimens were washed, dried and stored in a desiccator. Each specimen was reground with 1200 grit SiC papers using ethanol as a lubricant, just before electrochemical or gaseous hydrogen charging, to remove any surface oxides that could retard hydrogen absorption into the specimen. The average thickness of the specimens after grinding was 1.70 mm.

Table 1 Chemical composition (in wt %), microstructure and mechanical properties of 980DP. Chemical compositions were determined by two independent institutes.

Steel designation	Composition (wt%)							Microstructure		Mechanical properties		
	C	Si	Mn	Al	Nb	Ti	Cr	Martensite (%)	Ferrite (%)	Yield strength (MPa)	Tensile strength (MPa)	Elongation at fracture (e_f, %)
980DP	0.09	0.28	2.26	0.03	<0.01	0.02	0.54	60	40	592	930	8.3
	0.08	0.27	2.31	0.02	0.01	0.03	0.55					

Table 2 The hydrogen concentration for 980DP after various electrochemical or gaseous charging conditions. The measured hydrogen concentration was determined by integration of the whole TDS spectra. The corrected hydrogen concentration was evaluated by correcting for the hydrogen loss prior to analysis for the low temperature peak P1, and adding the hydrogen concentration corresponded to the high temperature peak P2.

Specimen designation	Weight (g)	Environments	Charging potential or charging pressure	Overpotential (η, V)	T_{max}^{P1} (℃)	T_{max}^{P2} (℃)	Measured hydrogen concentration (μg g^{-1})	Corrected hydrogen concentration (μg g^{-1})
980DP-AR	2.524	n/a	n/a	0	81.5	136.9	0.0052	0.0067
980DP-Ecorr	2.505	3 wt% NaCl	E_{corr}	-0.039	84.8	168.5	0.0203	0.0371
980DP-Ezn	2.505	3 wt% NaCl	E_{Zn}, -0.950 $V_{Ag/AgCl}$	-0.322	66.6	148.3	0.0371	0.0651
980DP-1.1V	2.503	0.1 M NaOH	-1.100 $V_{Hg/HgO}$	-0.257	80.1	145.9	0.0784	0.1282
980DP-1.4V	2.516	0.1 M NaOH	-1.400 $V_{Hg/HgO}$	-0.557	79.6	152.8	0.1084	0.1720
980DP-1.7V	2.529	0.1 M NaOH	-1.700 $V_{Hg/HgO}$	-0.857	74.6	153.9	0.1098	0.1800
980DP-2B	2.476	Hydrogen gas	2 bar	n/a	87.5	151.3	0.0322	0.0401
980DP-80B	2.520	Hydrogen gas	80 bar	n/a	84.1	145.2	0.0382	0.0519
980DP-200B	2.497	Hydrogen gas	200 bar	n/a	86.0	145.0	0.0491	0.0764

Table 3 Calculated data for each heating rate using the temperatures for both peaks to evaluate the de-trapping activation energy for each peak.

	Heating rate (℃ min^{-1})	T_{max} (℃)	T_{max} (K)	$1/T_{max}$ (K^{-1})	$\ln(\varphi/T_{max}^2)$	De-trapping activation energy (kJ mol^{-1})
1st peak	2	74.6	347.76	0.00288	-6.92	40.5
	5	103.6	376.76	0.00265	-6.16	
	10	107.1	380.26	0.00263	-5.48	
2nd peak	2	153.9	427.06	0.00234	-7.33	50.2
	5	156.9	430.06	0.00233	-6.42	
	10	190.2	463.36	0.00216	-5.88	

Table 1 presents the chemical composition, microstructure and mechanical properties for 980DP. The chemical composition and mechanical properties in the first line were provided by the steel supplier. The chemical composition in the second line was measured by Spectrometer Service Pty. Ltd, Coburg, Vic. The microstructure, as shown in Table 1, were examined using a scanning electron microscope (SEM), after metallographic polishing to 1 μm and etching with a 2% nital solution. The volume fraction of each phase was evaluated using the point counting method, as per ASTM E562 [40]. 980DP had a dual-phase microstructure consisted of 40% soft ferrite and 60% hard martensite. The microstructure of 980DP was also presented in our previous works [19, 39].

2.2. Thermal desorption spectroscopy (TDS)

Fig. 1 presents the schematic of the TDS apparatus. This TDS apparatus, described in detail by Tapia-Bastidas et al. [35], consisted of three main parts: (i) the analytical chamber (AC), (ii) the calibration rig for calibration with hydrogen gas, and (iii) the loading chamber (LC).

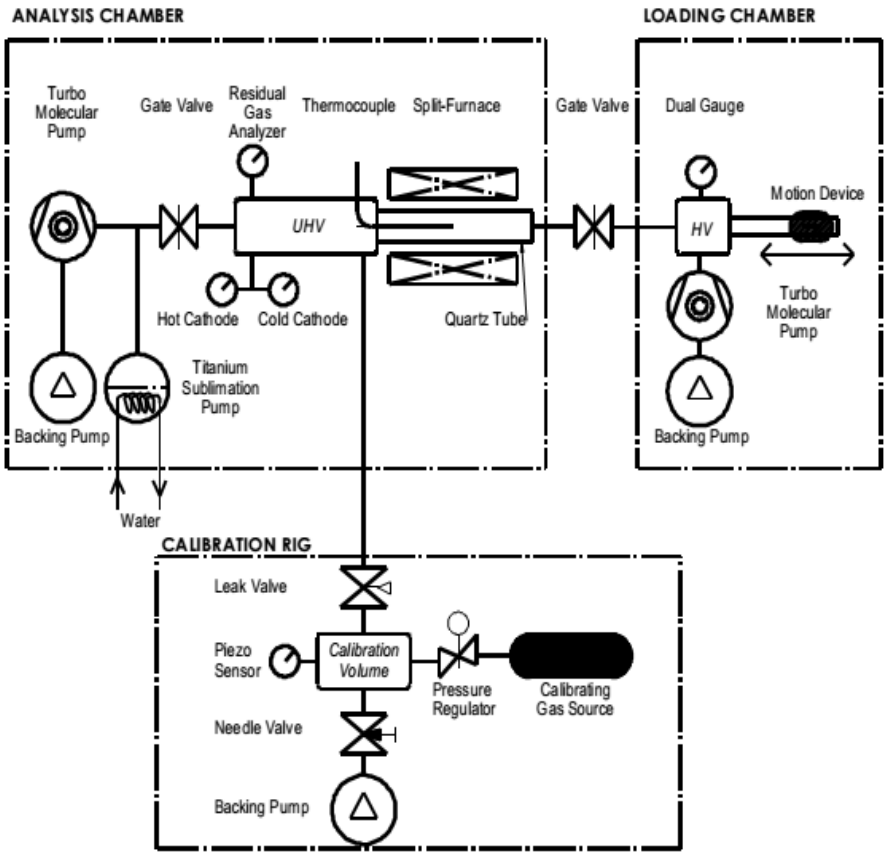

Fig. 1. Schematic of the thermal desorption spectroscopy (TDS) apparatus [35].

The loading and analysis procedures for a TDS specimen were described previously [27, 28] and are summarized as follows.

The loading chamber (LC), initially at 1×10^{-8} mbar, was brought up to atmospheric pressure by turning off the turbo molecular pump (TMP), and by injecting ultra-high purity (UHP) nitrogen. Once atmospheric pressure was reached, the LC was unlocked. The specimen was dismounted from hydrogen charging apparatus, washed, dried with UHP nitrogen, mounted onto the specimen holder and loaded into the loading chamber. The UHP nitrogen stream was maintained throughout the whole process of loading the specimen, to prevent water from the moisture in the air contaminating the LC. The door of LC was closed, and the LC was evacuated by turning on the TMP. The specimen was kept in high-vacuum in the LC for 120 min to minimize the effect of adventitious water, present on the specimen, on the ensuing TDS spectra, as suggested in [35, 41]. At the end of the allotted time, the specimen was introduced into the analytical chamber (AC) by a motion device. After another 12.5 min for stabilizing the AC pressure, the main gate valve was throttled from fully open to 30% open, and after an additional 2.5 min stabilization time following, the analysis was commenced.

For the TDS analysis, the furnace was first turned on. The target temperature was set to 870 ℃ and the temperature was increased from room temperature at a software-controlled temperature ramp of 2 ℃ min^{-1}. At the same time, the residual gas analyser (RGA) was started to record the desorbed gases. The RGA was a mass spectrometer that measured the desorbed species, such as hydrogen, water and carbon dioxide. The furnace was turned off after the target temperature was reached. The main gate valve was throttled back to the fully open position. The specimen was allowed to cool to room temperature in the AC, was retrieved, and weighed. Heating temperature ramps of 2 ℃ min^{-1}, 5 ℃ min^{-1}, and 10 ℃ min^{-1} were used in this work. TDS analyses were conducted at a heating temperature ramp of 2 ℃ min^{-1} for specimens subjected to each of the electrochemical and gaseous hydrogen charging conditions. Heating temperature ramps of 5 ℃ min^{-1} and 10 ℃ min^{-1} were used for specimens electrochemically charged at –1.700 $V_{Hg/HgO}$ in 0.1M NaOH.

2.3. Electrochemical charging

Electrochemical hydrogen charging was carried out in (i) 0.1 M NaOH at –1.100 $V_{Hg/HgO}$ (–1.002 V_{SHE}), –1.400 $V_{Hg/HgO}$ (–1.302 V_{SHE}) and –1.700 $V_{Hg/HgO}$ (–1.602 V_{SHE}), and (ii) in 3 wt% NaCl at the free corrosion potential, E_{corr}, and with polarization to the zinc potential, E_{Zn} (–0.950 $V_{Ag/AgCl}$, –0.752 V_{SHE}), at room temperature for 24 h, to ensure a constant hydrogen content throughout the specimen [10]. A three electrode cell was used for the cathodic charging, with (i) the specimen as the working electrode, (ii) a graphite rod as

the counter electrode, (as suggested by Venezuela et al. [11] to prevent undesired metallic deposition by using a Pt counter electrode at such charging conditions), and (iii) a reference electrode of an Hg/HgO, KOH (20%) reference electrode for charging in 0.1 M NaOH, or an Ag/AgCl (saturated KCl) reference electrode for charging in 3 wt% NaCl. After the hydrogen charging for 24 h, the specimen was dismounted from the charging setup, cleaned with isopropanol, dried with ultra-high purity (UHP) nitrogen, and immediately loaded into the TDS loading chamber.

2.4. Gaseous charging

Gaseous hydrogen charging was conducted with the specimen subjected to hydrogen gas with a pressure of 200 bar for 24 h, and thereafter exposed to the target pressures of 2, 80, and 200 bar for another 24 h. The gaseous hydrogen charging procedure was as follows. The specimen was positioned into a sealed pressure chamber, which was then connected to a fabricated hydrogen charging apparatus. The specimen chamber was evacuated by a vacuum pump for 15-20 min. At the end of the evacuation, hydrogen was injected into the specimen chamber by heating the attached metal-hydride high-purity hydrogen source (multi-substituted AB_5 intermetallic based on mischmetal) with a laboratory heat gun to reach the target pressure. As aforementioned, the specimen was exposed to hydrogen gas with a pressure of 200 bar for 24 h, this procedure was to ensure the hydrogen uptake of the steel. At the end of this procedure, the pressure was changed to the target pressure and maintained for a further 24 h, after which the specimen was removed from the chamber and immediately loaded into the TDS apparatus.

3. Results

3.1. Electrochemical hydrogen charging

Fig. 2 presents the TDS results for all the 980DP specimens tested (i) in the as-received condition (uncharged), (ii) with cathodic hydrogen charging in 0.1 M NaOH at –1.100 $V_{Hg/HgO}$, –1.400 $V_{Hg/HgO}$, and –1.700 $V_{Hg/HgO}$, and (iii) in 3 wt% NaCl at the free corrosion potential, E_{corr}, and the zinc potential, E_{Zn} (–0.950 $V_{Ag/AgCl}$).

There were two peaks for each curve: a low temperature peak (P1) and a high temperature peak (P2). The peak temperature, T_{max}, corresponding to the two peaks, varied for the different testing conditions. Table 2 presents the values of each peak temperature for all the tested conditions, determined by Gaussian fitting. The T_{max} values of low temperature

peak (P1) ranged from 66 ℃ to 85 ℃, whereas those for the high temperature peak P2 ranged from 136 ℃ to 167 ℃.

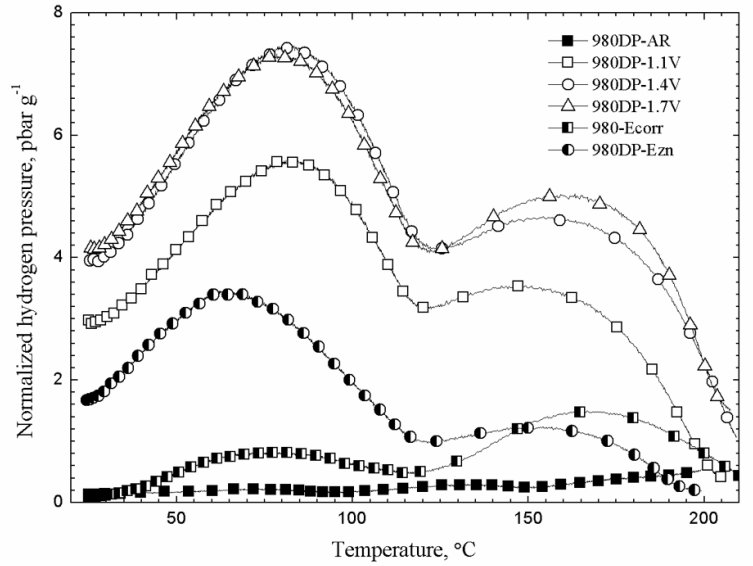

Fig. 2. TDS spectra of 980DP electrochemically charged in (i) 0.1 M NaOH at –1.100 $V_{Hg/HgO}$, –1.400 $V_{Hg/HgO}$, and –1.700 $V_{Hg/HgO}$, and (ii) in 3 wt% NaCl at the free corrosion potential, E_{corr}, and the zinc potential, E_{Zn} (–0.950 $V_{Ag/AgCl}$).

The height of the peaks indicated the amount of desorbed hydrogen during the TDS measurement, and varied for different charging conditions. The lowest peak height was for the as-received (AR) specimen, followed by those for charging in 3 wt% NaCl. The height of low temperature peak (P1) for charging at E_{Zn} was significantly higher than that at E_{corr}, whereas the height of high temperature peak (P2) was slightly higher for charging at E_{corr}. The height of both peaks (P1 and P2) for charging in 0.1 M NaOH was higher than those in 3 wt% NaCl, and increased with increasingly negative charging potential, with the exception that P1 height was slightly lower for charging at –1.700 $V_{Hg/HgO}$ than that at –1.400 $V_{Hg/HgO}$.

The TDS analysis was limited to around 220 ℃. This was consistent with the previous study [27] using this TDS apparatus, and was based on the facts that (i) the height of the peaks at temperatures higher than 200 ℃ was similar to the water peaks from previous measurements for a medium-strength steel using the same TDS apparatus, and (ii) there was no hydrogen peaks for this medium-strength steel after similar charging conditions, as measured by Verbeken using a commercial TDS apparatus at the University of Ghent [28].

3.2. Hydrogen concentration

3.2.1. TDS calibration

Tapia-Bastidas et al. [28] conducted calibration experiments for the TDS apparatus, used in this work. A series of TDS evaluations were performed using commercial certified hydrogen standards (purchased from the LECO Australia Pty Ltd) with various hydrogen contents, which were correlated with the integrated peak area from TDS analysis.

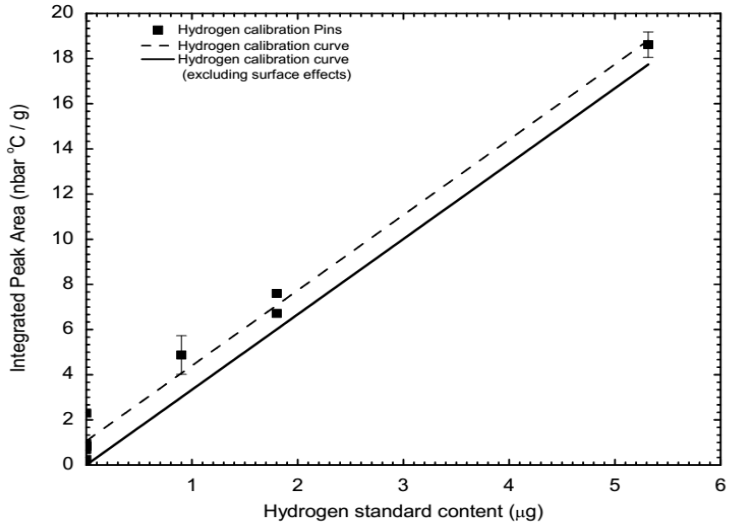

Fig. 3. The amount of hydrogen measured by the TDS plotted against the known amount of hydrogen contained in calibration standards: (i) 1 μg/g, (ii) 5 μg/g and (iii) 2 x 1 μg/g . The dash line represents the uncorrected calibration curve with the effect of adventitious water. The solid line is the corrected calibration curve, excluding the effect of surface-adsorbed water, and is obtained by drawing a line that crosses the origin and parallel to the uncorrected line [28].

Fig. 3 shows the calibration curve (dash line), as obtained using (i) a nominal 1 μg g^{-1} standard (ii) two nominal 1 μg g^{-1} standards, (iii) a nominal 5 μg g^{-1} standard, and (iv) zero hydrogen standard (previously degassed). There was a linear relationship between the hydrogen content and the integrated peak area, with a positive intercept on Y-axis. Tapia-Bastidas et al. [35] ascribed this Y-intercept to the adsorbed water on the surface of the hydrogen standards, as evidenced by the fact that the measurement of the standard with zero hydrogen was consistent with this Y-intercept. They further corrected the calibration line to exclude the effect of adsorbed water, by drawing a parallel line crossing the origin, as the solid line shown in Fig. 3. This corrected calibration line was used to evaluate the hydrogen content in the prior studies [27, 28], and was also used in this work.

3.2.2. Hydrogen loss

Hydrogen introduced into the steel specimen could effuse relatively easily after the completion of hydrogen charging. The hydrogen content evaluated from the calibration line only took into account the desorbed hydrogen during TDS analysis, and excluded the egressed hydrogen during the time period between the end of hydrogen charging and the start of TDS analysis. This time period was 135 min, as described above in section 2.2, and could result in significant hydrogen outgassing [27]. Thus, evaluation of this egressed hydrogen content should be performed to obtain an accurate hydrogen content presented in the specimen at the end of hydrogen charging.

Venezuela et al. [11] proposed a mathematical model to evaluate the amount of egressed hydrogen, based on solving Fick's diffusion equations with the following initial and boundary conditions [11]:

$t = 0, C = C_0$ for $0 < x < L$ (1)

$t > 0, C = 0$ for $x = 0$ and $x = L$ (2)

Their model was that there was initially a constant hydrogen content throughout the thin plate specimen with a thickness of L, and that hydrogen egressed equally from both sides of the specimen. The normalised hydrogen concentration is given by [11, 42]:

$$\frac{C}{C_0} = \frac{4}{\pi}\sum_{n=0}^{\infty}\frac{1}{2n+1}\exp\left\{\frac{(2n+1)^2\,D\,\pi^2\,t}{L^2}\right\}\sin\frac{(2n+1)\pi\,x}{L} \quad (3)$$

where D is the hydrogen diffusion coefficient, C/C_0 is the proportion of remaining hydrogen at a location, x, inside the specimen after a desorption time, t.

This model has been applied to evaluate the hydrogen outgassing between the end of hydrogen charging and the start of mechanical testing for martensitic high-strength steels [11], as well as for DP steels [20]. It was further proposed [27, 28] that two regimes for the model should be considered, with the concept that the hydrogen desorption was more rapid at the beginning, and then slowed down due to hydrogen trapping. Our previous study [39] showed that the hydrogen diffusion coefficient, for the 980DP used in this work, increased with a more negative charging potential, attributed to less a profound trapping effect, and therefore allowing determination of the lattice diffusion coefficient at the most negative charging potential. At the beginning of desorption (e.g. during the first 5 min), hydrogen egress was mainly governed by lattice diffusible hydrogen and was rapid, whereupon trapping became more significant, so that hydrogen egress slowed. Thus, a composite plot including two

regimes was used [27, 28], and was also adopted in this research to evaluate the desorbed hydrogen content. The values of diffusion coefficient, D_{eff}, ranged from 0.99×10^{-6} cm^2 s^{-1} to 2.07×10^{-6} cm^2 s^{-1} for 980DP steels [39]. In the first 5 min, the highest D_{eff} value was used due to fast diffusion, and the lowest D_{eff} value was used for hydrogen egress after 5 min, taking into account trapping. Based on this model, after 135 min (120 min of dwell time in the LC, 12.5 min of stabilization in the AC, and 2.5 min of stabilization after the main gate valve throttled to 30% open), the proportion of remaining hydrogen was calculated to be 51 %. This meant that 49 % of the charged hydrogen had effused out, between the end of hydrogen charging and the start of TDS analysis. This amount of lost hydrogen was used to correct the total hydrogen concentration in the specimens.

3.2.3. Total hydrogen concentration

As mentioned above, (i) the desorbed hydrogen concentration during TDS analysis could be determined by the calibration line and the integrated area of the TDS curve, and (ii) the lost hydrogen between the end of hydrogen charging and the start of TDS analysis could be evaluated by the desorption model. Furthermore, it was considered that the lost hydrogen was highly diffusible or weakly trapped, which was associated with the low temperature peak, as shown in Fig. 2. Thus, the corrected hydrogen concentration was evaluated by adding the amount of lost hydrogen to that corresponding to the low temperature peak P1, and then adding the hydrogen content corresponded to the high temperature peak P2.

Table 2 presents the values of (i) the hydrogen concentration measured from the areas of the two peaks, and (ii) the corrected hydrogen concentration, compensated for the lost hydrogen, for all the specimens charged in 0.1 M NaOH and 3 wt% NaCl. The corrected hydrogen concentration was higher than the as-measured value, by the compensation for the lost hydrogen. The corrected hydrogen concentration represented the actual hydrogen concentration. The as-received steel contained the lowest amount of hydrogen, of 0.0067 μg g^{-1}. The hydrogen concentration increased with increasingly negative charging potential in 0.1 M NaOH. The hydrogen concentration for steel immersed in 3 wt% NaCl at E_{Zn} was higher than that at E_{corr}, yet, was much lower than that with the least negative cathodic charging potential of –1.100 $V_{Hg/HgO}$, as evidenced by the value of 0.0651 μg g^{-1} for charging at E_{Zn} in 3 wt% NaCl and that of 0.1282 μg g^{-1} for charging at –1.100 $V_{Hg/HgO}$ in 0.1 M NaOH. The results were consistent with the peak heights.

3.3. Gaseous hydrogen charging

Fig. 4 shows the TDS spectra of 980DP after gaseous hydrogen charging at 2, 80 and 200 bar. Similar to the curves for electrochemical cathodic charging, there were two distinct desorption peaks, corresponding to a low and a high temperature, respectively. Table 2 includes the values of the two peak temperatures, evaluated by Gaussian fitting of the curves. The T_{max} values for the low temperature peaks ranged from 84 ℃ to 88 ℃, and those for the high temperature peaks ranged from 145 ℃ to 151 ℃. The T_{max} values for the low temperature peaks for gaseous hydrogen charging were somewhat slightly higher than those for electrochemical hydrogen charging, whereas the T_{max} values for the high temperature peaks were comparable for both charging conditions. The height of the peaks increased with increasing charging pressure.

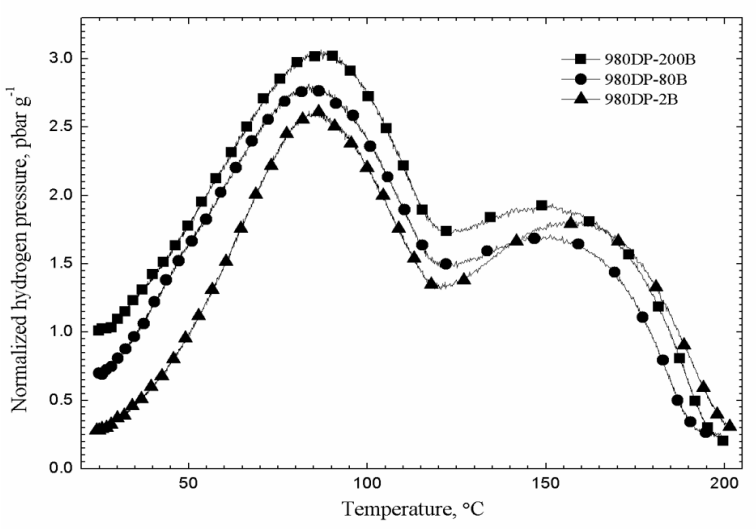

Fig. 4. TDS spectra of 980DP after gaseous charging at 2, 80 and 200 bar.

The hydrogen concentration values for gaseous hydrogen charging were comparable to the values for the electrochemical hydrogen charging in 3 wt% NaCl, and were all lower than those for the electrochemical hydrogen charging in 0.1 M NaOH.

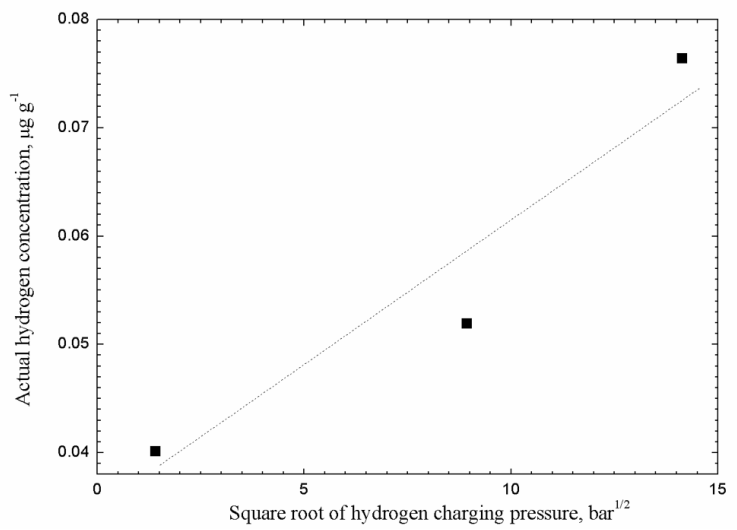

Fig. 5. Plot of hydrogen concentration versus the square root of gaseous hydrogen charging pressure.

Fig. 5 shows the plot of the actual hydrogen concentration versus the square root of the gaseous hydrogen charging pressure. There was good linearity. This was consistent with Sievert's law, which indicates that the hydrogen concentration dissolved in the steel, C_H, is related to the hydrogen partial pressure (fugacity, f_H), by the following equation:

$$C_H = S\sqrt{f_{H_2}} \tag{4}$$

where S is the solubility constant.

3.4. De-trapping activation energy

TDS allows evaluation of the activation energy of the different hydrogen traps in the steel and thereafter to associate the traps with microstructural features of this steel. Lee et al. [32] indicated that the de-trapping activation energy, E_d, was related to the associated peak temperature, T_{max}, and the heating rate of the TDS measurement, φ, by:

$$\frac{d\ln(\frac{\varphi}{T_{max}^2})}{dT_{max}} = -\frac{E_d}{R} \tag{5}$$

where R is the universal gas constant.

Thus, the de-trapping activation energy, E_d, could be evaluated using Eq. (5), and the results from a series of TDS measurements conducted at different heating rates. The heating rates of 2 ℃ min^{-1}, 5 ℃ min^{-1}, and 10 ℃ min^{-1} were used in this work. Fig. 6(a) presents the TDS curves with these heating rates. The curves for 2 ℃ min^{-1} and 5 ℃ min^{-1} had two distinct peaks, similar to those for the electrochemical and gaseous hydrogen charging, whilst, the TDS curve for 10 ℃ min^{-1} only exhibited one peak. Deconvolution of the peak for 10 ℃ min^{-}

[1] was performed to obtain two distinct peaks [22], as was shown in Fig. 6(b). The height of the peaks increased with increasing heating rates.

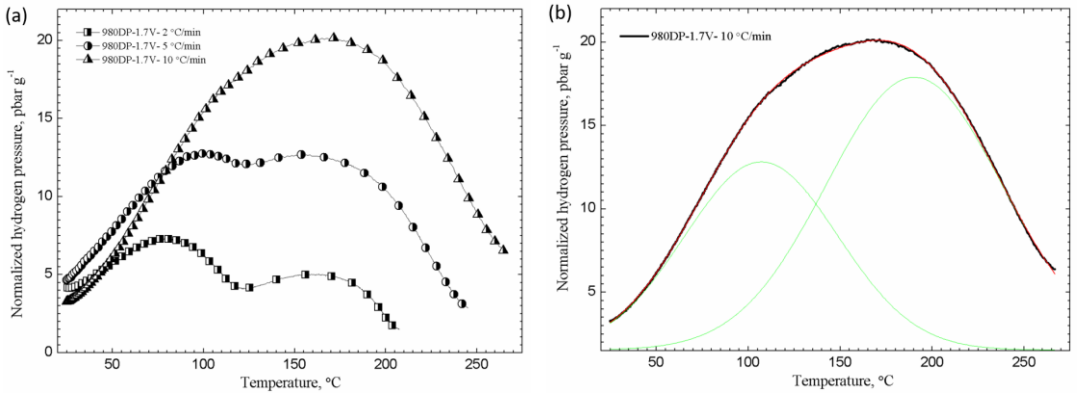

Fig. 6. (a) TDS spectra of 980DP electrochemically charged in 0.1 M NaOH at –1.700 $V_{Hg/HgO}$, and heated in TDS with different rates. (b) Deconvolution of TDS curve for 980DP tested with heating rate of 10 °C/min.

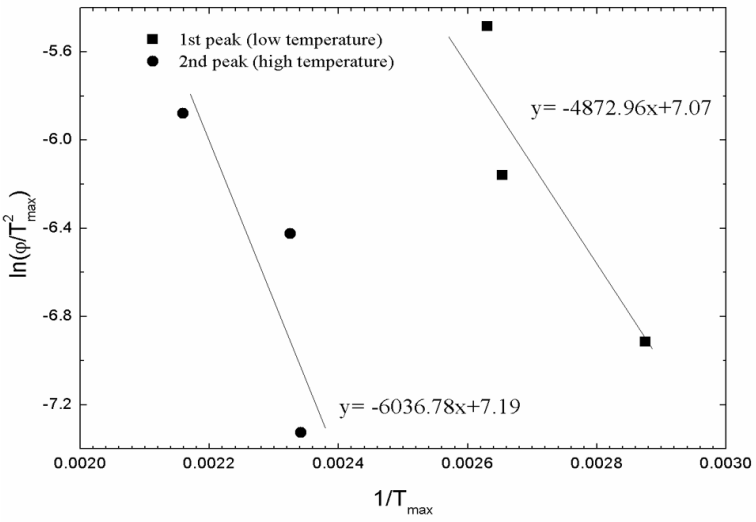

Fig. 7. $\ln(\varphi/T_{max}^2)$ as a function of $(1/T_{max}^2)$ for the two peaks.

Table 3 presents the peak temperature values, determined by Gaussian fitting. The peak temperatures increased with increasing heating rates. Using these peak temperature values, the values of $\ln(\frac{\varphi}{T_{max}^2})$ and $1/T_{max}$ were calculated and were also included in Table 3. The plots of $\ln(\frac{\varphi}{T_{max}^2})$ versus $1/T_{max}$ are presented in Fig. 7. There was a linear fit for each peak. The slopes of these regression lines allowed evaluation of the de-trapping activation energy, E_d, which were 40.5 kJ mol^{-1} and 50.2 kJ mol^{-1} for the low temperature and high temperature peak, respectively, as also shown in Table 3.

4. Discussion

4.1. Peak temperatures

Table 2 lists the values of the peak temperature, T_{max}, for the low temperature and the high temperature peaks, for specimens for all the charging conditions. The T_{max} values of the low temperature peaks for electrochemical charging in 0.1 M NaOH ranged from 75 ℃ to 80 ℃, and were slightly lower than those for the other charging conditions (as received, at E_{corr} in 3 wt% NaCl, and gaseous charging), which ranged from 82 ℃ to 88 ℃, whereas those of the high temperature peak P2 for electrochemical charging in 0.1 M NaOH ranged from 145 ℃ to 154 ℃, comparable with the values for other charging conditions.

The peak temperature, also considered as the hydrogen desorption temperature, provides an indication for the trap activation energy. A higher peak temperature may imply stronger trap(s). The lower peak temperature values for P1 for electrochemical charging in 0.1 M NaOH could be interpreted as containing two sub-peaks with slightly different peak temperatures, and that the hydrogen introduced in the steels by charging in 0.1 M NaOH had a higher potential, had filled all the traps associated with the relatively higher peak temperature and was engaging the traps associated with the relatively lower temperature peak. This interpretation implies that the higher temperature peak had a lower energy. Consistent with this interpretation, the hydrogen with the lower potential, for the other charging conditions, occupied the traps associated with the relatively higher temperature peak. However, an exception was for 980DP charged at E_{Zn} in 3 wt% NaCl, which exhibited a temperature value for peak P1 of 66 ℃. Such a peak temperature value was lower than those for the other charging conditions, yet, did not associate with a high hydrogen potential. Similarly, the temperature values for peak P2 were similar for all the charging conditions, except for as-received 980DP and for charging at E_{corr} in 3 wt% NaCl, which showed a much lower and a higher value, respectively. The peak temperature (desorption temperature) of traps with the same activation energy could also be affected by other factors such as trap density, specimen thickness, heating rates (e.g. see Fig. 6), and hydrogen charging time [43, 44]. Furthermore, Venezuela et al. [27] indicated that the change of temperature range for the same peak could be associated with only one type of trap, but that interacted with hydrogen in differences ways. It is also possible that the differences in peak temperature reflect the experimental accuracy of these measurements.

4.2. Hydrogen concentration

Table 2 presents the values of the actual hydrogen concentration, with correction for the lost hydrogen content, for 980DP (i) in the as-received condition, (ii) with electrochemical hydrogen charging in 0.1 M NaOH and in 3 wt% NaCl, and (iii) with gaseous hydrogen charging at various pressures.

The hydrogen concentration in the as-received specimen was minimal. The hydrogen concentration increased with polarization to the zinc potential in 3 wt% NaCl, and increased with increasingly negative charging potential in 0.1 M NaOH. Moreover, the hydrogen concentration for specimen charged at E_{Zn} in 3 wt% NaCl was significantly lower than the least negative charging potential of –1.100 $V_{Hg/HgO}$ in 0.1 M NaOH. These observations are consistent with the results from our previous research on 980DP [38], and were similar to those in the studies of other steels with the same charging conditions [26-28]. A more negative charging potential increases the equivalent hydrogen fugacity at the specimen surface, and thereby increases the amount of hydrogen introduced into the steel [26].

The hydrogen concentration in 980DP under the same charging conditions, was also evaluated in our previous work [38], by permeability tests and hot extraction analysis. Fig. 8 shows a comparison of the results of the three different analytical methods. The results from this work fall in between those from the previous work, being in good agreement to those from the hot extraction analysis, but being significantly lower than the values from permeability tests at substantial values of over-potential. Such a difference might be attributed to the intrinsic difference in the testing methods, and was also observed by Venezuela et al [27] for martensitic advanced high-strength steels.

The increased hydrogen concentration in the steel enhances the probability of HE occurrence. Thus the hydrogen concentration from this study could be used to correlate with the HE susceptibility of 980DP. Our past mechanical tests [19, 20] studying the hydrogen influence on 980DP under the same hydrogen charging conditions as in this work, showed that (i) there was no hydrogen influence on the as received specimen, (ii) there was HE susceptibility for steels under cathodic charging in 0.1 M NaOH and such susceptibility increased with a more negative charging potential, and (iii) hydrogen had minimal influence on the steels at E_{corr} and E_{Zn} in 3 wt% NaCl. This is consistent with the aforementioned trend of the changes in hydrogen concentrations, and it also indicates that the critical hydrogen concentration for HE occurrence lies between the hydrogen concentration for charging at E_{Zn} in 3 wt% NaCl and that for hydrogen charging at –1.100 $V_{Hg/HgO}$ in 0.1 M NaOH, which were

0.0651 μg g^{-1} and 0.1282 μg g^{-1} respectively, from the TDS results in this study. This critical hydrogen concentration was comparable with that from the work of Loidl et al. [14], where they reported that between 0.14 to 0.41 μg g^{-1} hydrogen could cause a large decease of the ductility of the steels, including DP steels.

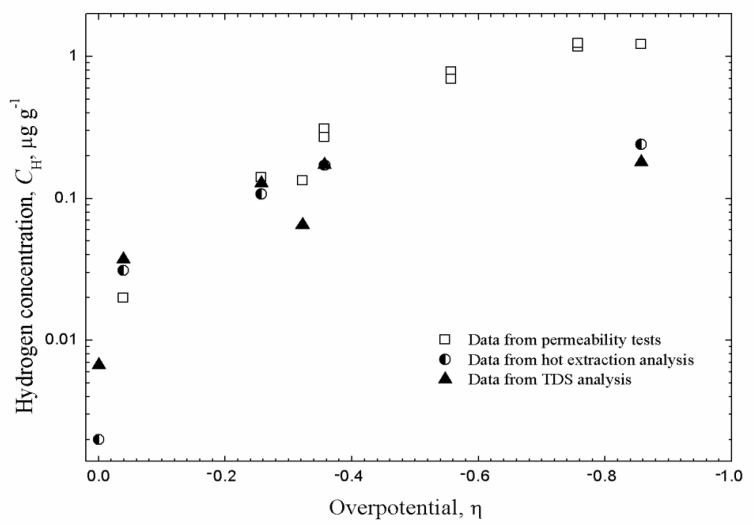

Fig. 8. Plot of the hydrogen concentration versus the electrochemical hydrogen charging overpotential for 980DP, obtained from (i) the permeability experiments [38], (ii) the hot extraction analysis [38], and (iii) the TDS analysis in this work.

Table 2 and Fig. 5 indicate that the hydrogen concentration in the steel specimen increased with the square root of the hydrogen gaseous charging pressure. This was consistent with the Sievert's law as given Eq. (4).

4.3. Equivalent hydrogen fugacity

TDS allows evaluation of the equivalent hydrogen fugacity on the steel surface corresponding to the electrochemical charging potential. This is important for the study of the hydrogen influence on steels during electrochemical charging, in that it permits evaluation of the hydrogen concentration introduced in the specimen, and correlates with the hydrogen influence.

The evaluating procedure for the equivalent hydrogen fugacity is as follows; (i) determination of the linear relationship of hydrogen concentration introduced by the gaseous hydrogen charging and the square root of the charging pressure, Fig. 5, (ii) fitting the hydrogen concentration introduced by the electrochemical hydrogen charging to this linear relationship, and (iii) determination of the equivalent hydrogen fugacity during this electrochemical hydrogen charging. This procedure follows that in previous studies [27, 28].

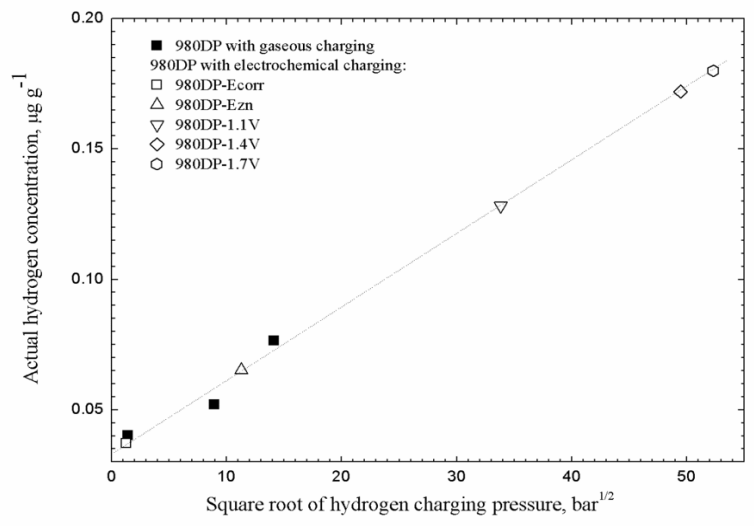

Fig. 9. Plot showing the linear relationship of the hydrogen concentration versus the square root of gaseous hydrogen charging pressure, with the superimposed hydrogen concentrations from the electrochemically hydrogen charged specimens.

Fig. 9 shows the plot of the hydrogen concentration versus the square root of the gaseous hydrogen pressure, with the hydrogen concentration values for electrochemical charging fitted to the linear regression, using the aforementioned procedure. Table 4 presents the results of the equivalent hydrogen fugacity during electrochemical hydrogen charging. The hydrogen fugacity increased from charging at E_{corr} to that at E_{Zn} in 3 wt% NaCl, increased with a more negative charging potential in 0.1 M NaOH, and was significantly lower for specimen charged at E_{Zn} in 3 wt% NaCl than at the least negative charging potential of –1.100 $V_{Hg/HgO}$ in 0.1 M NaOH. This is consistent with the trend of changes in hydrogen concentration in the steels, as mentioned above in section 4.2, and again, it indicates that a more negative charging (over)-potential increases the hydrogen fugacity on the steel surface, increases the amount of hydrogen injected to the steel, and consequently increases the chance of HE occurrence.

Table 4 The equivalent hydrogen fugacity of 980DP during electrochemical hydrogen charging in 0.1 M NaOH and 3 wt% NaCl.

Specimen designation	Electrolytes	Charging potential	Overpotential (η, V)	Equivalent hydrogen fugacity (atm)	Equivalent hydrogen pressure (atm)
980DP-Ecorr	3 wt% NaCl	E_{corr}	-0.039	1.6	1.6
980DP-Ezn	3 wt% NaCl	E_{zn}, -0.950 $V_{Ag/AgCl}$	-0.322	126	118
980DP-1.1V	0.1 M NaOH	-1.100 $V_{Hg/HgO}$	-0.257	1129	737
980DP-1.4V	0.1 M NaOH	-1.400 $V_{Hg/HgO}$	-0.557	2415	1206
980DP-1.7V	0.1 M NaOH	-1.700 $V_{Hg/HgO}$	-0.857	2702	1288

Past studies have determined the equivalent hydrogen fugacity during electrochemical charging. Fig. 10 shows the equivalent hydrogen fugacity versus the electrochemical charging overpotential, to compare the results from this work with those for (i) low interstitial

steels [26], (ii) 3.5NiCrMoV steel [28], and (iii) MS1500 martensitic advanced high-strength steels (AHSS) [27], for charging with similar conditions. The fugacity values for the 3.5NiCrMoV from [28] were the lowest for electrochemical charging in 0.1M NaOH. The fugacity values for the 980DP in this work were comparable to those for the low interstitial steels from [26] and for the MS1500 AHSS [27] at similar charging overpotential values for both 3wt% NaCl and 0.1M NaOH, indicating the possibility of comparable amount of hydrogen being adsorbed into these steels.

However, Venezuela et al. [27] suggested that a surface oxide might influence the hydrogen uptake at the steel surface, and thereby affect the evaluated hydrogen fugacity. Furthermore, Park et al. [45] observed that the aluminum oxide layer formed on the surface of the TWIP AHSS hindered the permeation of the produced hydrogen into the steel and resulted in improved HE resistance. Other factors, such as the composition and microstructures of the steel may also play a role in the evaluated hydrogen fugacity values.

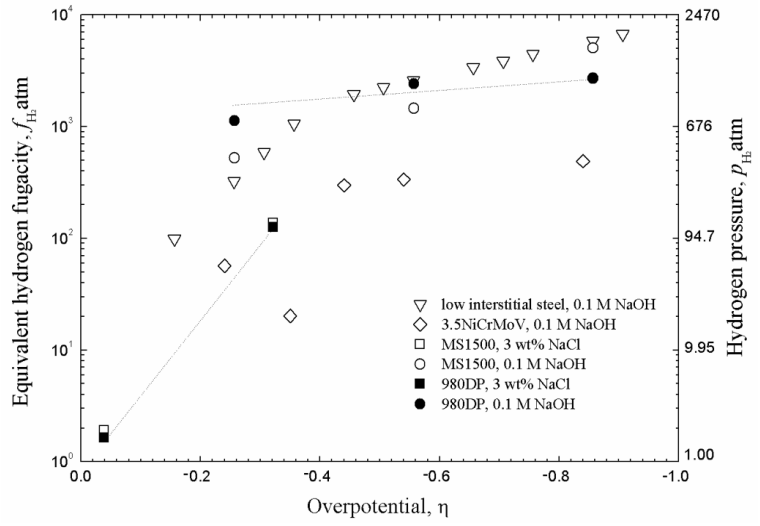

Fig. 10. Equivalent hydrogen fugacity versus the electrochemical charging overpotential for (i) 980DP in this work, (ii) low interstitial steels from [26], (iii) 3.5NiCrMoV from [28], and (iv) MS1500 from [27], with similar charging solutions.

It is recognized that there was significant scatter for the gaseous hydrogen data plotted in Fig. 5, which consequently influences the values of hydrogen fugacity for 980DP plotted in Fig. 10 and evaluated from Fig. 9. In view of this scatter, it is probable that the hydrogen fugacity for hydrogen charging in 3wt% NaCl and 0.1M NaOH was the same for 980DP, MS1500 and low interstitial steel.

4.4. Identification of hydrogen traps

The occurrence of HE requires a critical amount of hydrogen, however, the amount of hydrogen is not the most decisive factor for the hydrogen influence, but it is the nature of the hydrogen (diffusible, reversibly or irreversibly trapped) in the steel that is more important [22], provided that there is sufficient hydrogen. Therefore, besides the evaluation of the hydrogen concentration, the determinations of trap activation energy and the associated trap types are also helpful to gain a deeper understanding of the hydrogen influence on the steels.

Table 3 shows that the values of the de-trapping activation energy, E_d, were 40.5 kJ mol^{-1} and 50.2 kJ mol^{-1}, corresponding to the low temperature and high temperature desorption peak, respectively, for the 980DP in this study, and indicating two traps. For DP steels, a hydrogen trap can be a microstructure defect, such as a micro-void, dislocation, grain boundary, carbide interface, or impurity [2]. The value of the trap activation energy or binding energy could be used to identify the type of traps.

Both of the two traps were reversible traps, since the E_d for reversible traps is normally considered to be less than 60 kJ mol^{-1} [2, 46], however, other values have also been used for this upper limit, such as 65 kJ mol^{-1} [47]. The values of the de-trapping activation energy, E_d, for lath boundaries, phase and grain boundaries spread from 17 to 58 kJ mol^{-1}. [23, 31, 34, 48, 49]. The E_d values evaluated in this work, fall into this range, indicating that the traps may be boundary defects. Pérez Escobar et al. [22] measured de-trapping activation energy values of 35 ± 5 and 38 ± 7 kJ mol^{-1} for DP steels, and associated these values with possible traps at phase and grain boundaries. The activation energy value of 40.5 kJ mol^{-1} measured in this work is close to these two values, thus the trap could also be attributed to phase or grain boundaries, such as the boundaries of ferrite and martensite.

The high temperature peak corresponded to an activation energy value of 50.2 kJ mol^{-1}. The H trap could be associated with the interface of TiN inclusions present in 980DP, as detected in our previous studies [19, 20], based on the facts that (i) the H trap corresponded to a relatively high temperature peak, (ii) the interface of non-metallic inclusions were strong traps with a relatively higher activation energy [31], and (iii) the activation energy values for coherent or semi-coherent TiC ranged from 46 to 59 kJ mol^{-1} [29, 41, 50]. However, there were such TiN inclusions only occasionally in the brittle fracture surface, rather than being widely distributed throughout the specimen, and TiC or other precipitates were not presented according to our previous examinations [19, 20]. Luppo et al. [51] measured an activation energy of 46 kJ mol^{-1} in martensitic steels, and associated it with lath interfaces of martensite,

and prior austenitic grain boundaries. Similarly, Venezuela et al. [27] also identified these boundary defects for hydrogen traps in martensitic high-strength steels with an activation energy value of 66.7 kJ mol^{-1}. Moreover, the activation energy value of 50.2 kJ mol^{-1} is also within the range from 17 to 58 kJ mol^{-1} for boundary defects as above mentioned. Therefore, the type of trap corresponding to this higher activation energy is also considered to be a boundary defect, such as the lath interfaces of martensite.

The hydrogen trapping at these boundary defects is consistent with our previous examinations [19] of the hydrogen induced cracks, which were associated with the martensite phase, and the interfaces of ferrite/martensite, and the transgranular fracture in the 980DP steels.

4.5. Associations with HE

The occurrence of HE requires the interaction of a critical amount of hydrogen with the stressed steel. Moreover, the state of the introduced hydrogen in the steel plays an important role in the hydrogen influence; the irreversibly trapped hydrogen may be largely innocuous to HE, whereas the reversibly trapped hydrogen is detrimental for internal hydrogen embrittlement (IHE).

980DP steels could be subjected to IHE [19, 20], when the hydrogen concentration exceed the critical amount between around 0.0651 and 0.1282 μg g^{-1}. Hydrogen was produced during charging in 0.1 M NaOH and 3 wt% NaCl, which results in the hydrogen being adsorbed into the steel specimen. Some of the introduced hydrogen was diffusible, whereas some other hydrogen was reversibly trapped at boundary defects, such as the interfaces of the lath martensite, and those of ferrite/martensite. This dissolved hydrogen facilitates massed motion of dislocations throughout the gauge volume of the specimen during a LIST or tensile test, causing the decrease of the yield stress, as was described by the mechanism of hydrogen influence, hydrogen enhanced macroscopic plasticity (HEMP) [20]. Moreover, this introduced hydrogen also changes the micro-fracture mode, leading to the change of the macroscopic form of the fracture at the ultimate tensile strength from the ductile cup and cone fracture mode to the macroscopically-brittle transgranular shear fracture mode, by the mechanism of hydrogen-assisted micro-fracture (HAM) [20]. The facilitation of the dislocation motion and the change of the micro-fracture mode are enhanced by more available hydrogen. However, the TDS tests do not involve stressing the specimen, whereas LIST tests apply increasing stress on the specimen at various rates, causing the production of

substantial amount of dislocations, so that the significant interaction of dislocations with the hydrogen was not detected by TDS.

Furthermore, comparisons could be carried out in order to better understand the different hydrogen influence behaviour on different DP steels. For example, our previous research [19, 20, 38, 39] showed that 980DP (i) was less susceptible to HE, (ii) had a lower reversible hydrogen trap site density evaluated from a complete decay transient, and (iii) a lower hydrogen concentration, than the stronger 1200DP, which had a tensile strength of 1200 MPa. Assuming that there were the same boundary-defect type of reversible traps, the higher density of such reversible trap sites leads to more hydrogen trapped at these sites, contributes to higher amount of hydrogen, and causes the easier occurrence of crack initiation and growth, resulting in higher HE susceptibility and similar transgranular fracture. In this manner, the better HE resistance of 980DP compared with 1200DP could be explained.

5. Conclusions

980DP steel was studied using a new TDS apparatus to (i) measure the hydrogen concentration in the DP steel subjected to (a) electrochemical cathodic hydrogen charging in 0.1 M NaOH and in 3 wt% NaCl, and (b) gaseous hydrogen charging, (ii) evaluate the equivalent hydrogen fugacity during electrochemical charging, and (iii) identify the trap activation energy and the associated hydrogen traps. The following conclusions have been drawn:

1. The hydrogen concentration increased with (i) increasingly negative charging potential and (ii) increasing hydrogen gas pressure.
2. The equivalent hydrogen fugacity for electrochemical hydrogen charging was evaluated for 980DP charged in the two solutions.
3. The values of the de-trapping activation energy were 40.5 kJ mol^{-1} and 50.2 kJ mol^{-1} and were attributed to hydrogen traps at boundary defects in DP steels.

Acknowledgements

This research is supported by the Baosteel-Australia Joint Research & Development Centre (BAJC) Grant, BA13037, with linkage to Baoshan Iron and Steel Co., Ltd of China. Atrens wishes to express his thanks to Frédéric Christien, Krzysztof Wolski and David Delafosse for stimulating discussions, and for special studies program support to the Ecole Nationale Supérieure de Mines de Saint-Etienne, Saint-Étienne, France.

References

[1] D Bhattacharya, Developments in advanced high strength steels, Proceedings of Proceedings of the Joint International Conference of HSLA Steels, Sanya, 2005, 70-73.
[2] Q Liu, Q Zhou, J Venezuela, M Zhang, J Wang and A Atrens, A review of the influence of hydrogen on the mechanical properties of DP, TRIP, and TWIP advanced high-strength steels for auto construction, Corros Rev. 34 (2016) 127-152.
[3] WorldAutoSteel, Advanced high-strength steels application guidelines version 5.0, Available from http://www.worldautosteel.org/, Access on 2014.
[4] R Kuziak, R Kawalla and S Waengler, Advanced high strength steels for automotive industry, Archives of civil and mechanical engineering. 8 (2008) 103-117.
[5] J Galán, L Samek, P Verleysen, K Verbeken and Y Houbaert, Advanced high strength steels for automotive industry, Rev Metal Madrid. 48 (2012) 118-131.
[6] X Zhu, Z Ma and L Wang, Current status of advanced high strength steel for auto-making and its development in Baosteel, Rep Baosteel Research Institute. 201900 (2007) 1-8.
[7] Baosteel, Baosteel automotive advanced high strength steels, Available from http://www.baosteel.com/, Access on 2013.
[8] Q Liu, B Irwanto and A Atrens, The influence of hydrogen on 3.5NiCrMoV steel studied using the linearly increasing stress test, Corros Sci. 67 (2013) 193-203.
[9] Q Liu and A Atrens, A critical review of the influence of hydrogen on the mechanical properties of medium-strength steels, Corros Rev. 31 (2013).
[10] J Venezuela, Q Liu, M Zhang, Q Zhou and A Atrens, The influence of hydrogen on the mechanical and fracture properties of some martensitic advanced high strength steels studied using the linearly increasing stress test, Corros Sci. 99 (2015) 98-117.
[11] J Venezuela, Q Zhou, Q Liu, M Zhang and A Atrens, Influence of hydrogen on the mechanical and fracture properties of some martensitic advanced high strength steels in simulated service conditions, Corros Sci. 111 (2016) 602-624.
[12] R Davies, Hydrogen embrittlement of dual-phase steels, Metall Trans A. 12 (1981) 1667-1672.
[13] T Depover, E Wallaert and K Verbeken, Fractographic analysis of the role of hydrogen diffusion on the hydrogen embrittlement susceptibility of DP steel, Mater Sci Eng A. 649 (2016) 201-208.
[14] M Loidl, O Kolk, S Veith and T Göbel, Characterization of hydrogen embrittlement in automotive advanced high strength steels, Materialwiss Werkstofftech. 42 (2011) 1105-1110.

[15] M Koyama, CC Tasan, E Akiyama, K Tsuzaki and D Raabe, Hydrogen-assisted decohesion and localized plasticity in dual-phase steel, Acta Mater. 70 (2014) 174-187.
[16] R Davies, Influence of martensite content on the hydrogen embrittlement of dual-phase steels, Scripta metallurgica. 17 (1983) 889-892.
[17] T Depover, D Pérez Escobar, E Wallaert, Z Zermout and K Verbeken, Effect of hydrogen charging on the mechanical properties of advanced high strength steels, Int J Hydrogen Energy. 39 (2014) 4647-4656.
[18] L Duprez, K Verbeken and M Verhaege, Effect of hydrogen on the mechanical properties of multiphase high strength steels, Proceedings of the 2008 International Hydrogen Conference (2009) 62-69.
[19] Q Liu, Q Zhou, J Venezuela, M Zhang and A Atrens, Hydrogen influence on some advanced high strength steels, submitted to Corros Sci.
[20] Q Liu, Q Zhou, J Venezuela, M Zhang and A Atrens, Influence of hydrogen on some commercial DP, Q&P and TWIP advanced high-strength steels under simulated service conditions, unpublished work.
[21] M Koyama, E Akiyama and K Tsuzaki, Effect of hydrogen content on the embrittlement in a Fe–Mn–C twinning-induced plasticity steel, Corros Sci. 59 (2012) 277-281.
[22] D Pérez Escobar, K Verbeken, L Duprez and M Verhaege, Evaluation of hydrogen trapping in high strength steels by thermal desorption spectroscopy, Mater Sci Eng A. 551 (2012) 50-58.
[23] GM Pressouyre, A classification of hydrogen traps in steel, Metall Trans A. 10 (1979) 1571-1573.
[24] GM Pressouyre and IM Bernstein, An example of the effect of hydrogen trapping on hydrogen embrittlement, Metall Trans A. 12 (1981) 835-844.
[25] A Atrens, D Mezzanotte, N Fiore and M Genshaw, Electrochemical studies of hydrogen diffusion and permeability in Ni, Corros Sci. 20 (1980) 673-684.
[26] Q Liu, AD Atrens, Z Shi, K Verbeken and A Atrens, Determination of the hydrogen fugacity during electrolytic charging of steel, Corros Sci. 87 (2014) 239-258.
[27] J Venezuela, E Gray, Q Liu, Q Zhou, C Tapia-Bastidas, M Zhang and A Atrens, Equivalent hydrogen fugacity during electrochemical charging of some martensitic advanced high-strength steels, unpublished work.
[28] J Venezuela, C Tapia-Bastidas, Q Liu, Q Liu, Q Zhou, K Verbeken, E Gray and A Atrens, Determination of the equivalent hydrogen fugacity during electrochemical charging of 3.5NiCrMoV steel, unpublished work.

[29] T Depover, O Monbaliu, E Wallaert and K Verbeken, Effect of Ti, Mo and Cr based precipitates on the hydrogen trapping and embrittlement of Fe–C–X Q&T alloys, Int J Hydrogen Energy. 40 (2015) 16977-16984.
[30] S Frappart, A Oudriss, X Feaugas, J Creus, J Bouhattate, F Thébault, L Delattre and H Marchebois, Hydrogen trapping in martensitic steel investigated using electrochemical permeation and thermal desorption spectroscopy, Scripta Mater. 65 (2011) 859-862.
[31] WY Choo and J Lee, Thermal analysis of trapped hydrogen in pure iron, Metall Trans A. 13 (1982) 135-140.
[32] J Lee and S Lee, Hydrogen trapping phenomena in metals with BCC and FCC crystals structures by the desorption thermal analysis technique, Surf Coat Technol. 28 (1986) 301-314.
[33] D Pérez Escobar, T Depover, L Duprez, K Verbeken and M Verhaege, Combined thermal desorption spectroscopy, differential scanning calorimetry, scanning electron microscopy and X-ray diffraction study of hydrogen trapping in cold deformed TRIP steel, Acta Mater. 60 (2012) 2593-2605.
[34] D Pérez Escobar, T Depover, E Wallaert, L Duprez, M Verhaege and K Verbeken, Thermal desorption spectroscopy study of the interaction between hydrogen and different microstructural constituents in lab cast Fe–C alloys, Corros Sci. 65 (2012) 199-208.
[35] CV Tapia-Bastidas, A Atrens and EM Gray, CV Tapia-Bastidas, A Atrens, E.MacA. Gray. Thermal desorption spectrometer for measuring wt ppm concentrations of trapped hydrogen. in press., Avaliable from, Access on.
[36] K Bergers, ECd Souza, I Thomas and N Mabho, Determination of Hydrogen in Steel by Thermal Desorption Mass Spectrometry, J. Flock. Steel Research Int. 81 (2010).
[37] S Smith and J Scully, The identification of hydrogen trapping states in an Al-Li-Cu-Zr alloy using thermal desorption spectroscopy, Metall Mater Trans A. 31 (2000) 179-193.
[38] Q Liu, Q Zhou, J Venezuela, M Zhang and A Atrens, Hydrogen Concentration in Dual-Phase (DP) and Quenched and Partitioned (Q&P) Advanced High-Strength Steels (AHSS) under Simulated Service Conditions Compared with Cathodic Charging Conditions, Adv Eng Mater. 18 (2016) 1588-1599.
[39] Q Liu, J Venezuela, M Zhang, Q Zhou and A Atrens, Hydrogen trapping in some advanced high strength steels, Corros Sci. 111 (2016) 770-785.
[40]E562-08, Standard Test Method for Determining Volume Fraction by Systematic Manual Point Count, 2008.

[41] FG Wei and K Tsuzaki, Quantitative analysis on hydrogen trapping of TiC particles in steel, Metall Mater Trans A. 37 (2006) 331-353.
[42] RW Balluffi, S Allen and WC Carter, Kinetics of materials, John Wiley & Sons, 2005.
[43] M Nagumo, M Nakamura and K Takai, Hydrogen thermal desorption relevant to delayed-fracture susceptibility of high-strength steels, Metall. Mater. Trans. A. 32A (Feb 2001) 339.
[44] T Yamaguchi and M Nagumo, Simulation of hydrogen thermal desorption under reversible trapping by lattice defects, ISIJ Int. 43 (2003) 514-519.
[45] I-J Park, K-H Jeong, J-G Jung, CS Lee and Y-K Lee, The mechanism of enhanced resistance to the hydrogen delayed fracture in Al-added Fe–18Mn–0.6 C twinning-induced plasticity steels, Int J Hydrogen Energy. 37 (2012) 9925-9932.
[46] J Venezuela, Q Liu, M Zhang, Q Zhou and A Atrens, A review of hydrogen embrittlement of martensitic advanced high-strength steels, Corros Rev. 34 (2016) 153-186.
[47] P Castaño Rivera, VP Ramunni and P Bruzzoni, Hydrogen trapping in an API 5L X60 steel, Corros Sci. 54 (2012) 106-118.
[48] J Svoboda, G Mori, A Prethaler and FD Fischer, Determination of trapping parameters and the chemical diffusion coefficient from hydrogen permeation experiments, Corros Sci. 82 (2014) 93-100.
[49] D Pérez Escobar, L Duprez, A Atrens and K Verbeken, Thermal desorption spectroscopy study of experimental Ti/S containing steels, Mater Sci Technol. 29 (2013) 261-267.
[50] FG Wei, T Hara and K Tsuzaki, Precise determination of the activation energy for desorption of hydrogen in two Ti-added steels by a single thermal-desorption spectrum, Metall Mater Trans. 35 (2004) 587-597.
[51] M Luppo and J Ovejero-Garcia, The influence of microstructure on the trapping and diffusion of hydrogen in a low carbon steel, Corros Sci. 32 (1991) 1125-1136.

Summary and conclusions

This project aims to study the hydrogen influence on some commercial DP, Q&P and TWIP grades of AHSS for auto construction. The project was advised by Prof. Andrejs Atrens and Prof. Mingxing Zhang from the University of Queensland and by Prof. Evan Gray from Griffith University. The project focused on six steels, including four DP steels, one Q&P steel and one TWIP steel. These steels were supplied from commercial production as rolled sheets, by Baoshan Iron and Steel Co., Ltd of China.

In the first year of the project, plans for experiments were first proposed. Literature review was then commenced to understand (i) the steel, (ii) the hydrogen behaviours, including hydrogen production, adsorption, transportation, interaction in the steel, and hydrogen embrittlement (HE) mechanisms, and (iii) the hydrogen influence on different AHSS. Following that, microstructural studies were conducted on the key steels in as received state to gain a first understanding. Subsequently, with the help of Dr. Qian Liu and Dr. Zhiming Shi, trials of permeability experiments were proceeded. After a large amount of efforts to plate a palladium layer with good quality on the steel surface, reproducible results of permeability experiments were obtained, and this set a good start for the experiments in the next year. By the end of the first year, a literature review manuscript was produced for the confirmation report as well as for a journal paper. The first milestone of my PhD study was accomplished at the end of the first year.

In the second year, following the permeability experiments in the first year, efforts were put to complete all the permeability experiments under cathodic charging and simulated service conditions. With the obtained results, data analysis and paper writing were completed. One more manuscript for journal paper, along with the literature review manuscript from the first year, were submitted for publication. In the second half of the second year, an international conference was attended with the result from the permeability experiments. In addition, one month was spent in the labs of our industrial partner, with the aim to study hydrogen concentration in the steels by conducting experiments using the hot extraction analyser in the labs. The results were helpful and were drafted in another paper along with previous results from the permeability experiments. The second milestone of my PhD study was accomplished on time at the end of the second year.

In the third year, the linearly increasing stress tests (LIST) were conducted to study the hydrogen influence on the key steels, with regards to cathodic hydrogen charging and simulated service conditions. The operation of LIST apparatus was trained by Dr. Zhiming

Shi. Some universal tensile tests were also conducted to study the hydrogen influence. In the meantime, microstructural studies on the features associated with the hydrogen influence were performed using SEM and XRD. TEM examination was also tried with the fractured steels, however, the sample preparation by focused ion beam (FIB) encountered difficulties, and thus awaited for further attempts. The results of LIST and microstructural studies permitted two more papers being drafted and submitted to journal and approval of industrial partner for publication. Those results were also presented in another international conference and during an academic visit to the Ecole Nationale Supérieure de Mines de Saint-Etienne, Saint-Étienne, France. Such experiences allowed meeting with the researchers in the related fields and accessing to the frontier of the research area. In the second half of the third year, the new commercial TDS apparatus was ready in the labs of Prof. Evan Gray from the Griffith University. After the training by Dr. Clotario Tapia-Bastidas, three months were spent conducting TDS tests at Griffith University. The obtained results were incorporated in another manuscript for journal paper and was submitted to the industrial partner for approval of publication. The thesis review meeting was successfully held and the final seminar will be presented after the submission of thesis.

On the whole, in the past three years, the influence of hydrogen on some commercial DP, Q&P and TWIP grades of AHSS for auto construction, has been studied. The following findings have been concluded:

1. Hydrogen influence on mechanical properties

All the DP, Q&P and TWIP steels exhibited some susceptibility to hydrogen influence, resulting in degradation of mechanical properties. Hydrogen had slight influence on the yield and tensile strengths, whereas caused significant loss of ductility of the steels. These results are consistent with other works [1-3] that indicated the hydrogen influence was mainly manifested by the loss of ductility. The change of ductility, measured by the change of reduction in area of the specimen, was therefore adopted to quantify the hydrogen embrittlement susceptibility.

Moreover, hydrogen could cause small decrease in the steel strength. Such reduction in steel strength was due to the hydrogen solid solution softening, associated with the macroscopic movement of significant dislocation masses enhanced by hydrogen.

2. Hydrogen influence on fracture mode

There were two distinguished fracture modes presented in this work: ductile cup and cone fracture and brittle shear fracture.

The ductile cup and cone fracture occurred to steels subjected to minimal hydrogen influence. Two regions, a centre cone part and its adjacent shear lips, were observed in the fracture surface. The centre cone part was relatively flat, normal to the tensile direction, and possessed round ductile dimples due to micro-void coalescence. The shear lips were typically at an angle of 45 degree to the tensile direction and possessed shallower and parabolic dimples, attributed to shearing. The cup and cone fracture indicated that fractures initiated in the centre cone part, attributed to the microvoids nucleation, growth and coalescence, and then propagated to the surrounding shear regions, where the final fracture occurred due to shear stress.

On the other hand, the brittle shear fracture was manifest of hydrogen influence. Two types of fracture regions: a shear fracture region and brittle fracture regions, were identified. Each brittle region was located near the edges of the fracture surface and normally had an arched shape, indicating that these fractures initiated from the edge, and grew towards the inner part of the specimen. The brittle region was relatively flat and contained transgranular and/or intergranular features, whereas the shear fracture region was not flat, had an angle to the tensile direction, and possessed ductile dimples. A transition region was also normally observed between the shear region and brittle region, in the steels especially with significant hydrogen influence. This transition region contained mixed features, such as dimples, brittle features and fisheyes, which were also manifest of hydrogen influence. The brittle fracture initiated from brittle regions and/or the lower edge of a shear region, and then propagated in a shearing manner along single or multiple planes.

In addition, the transverse views showed that necking was present in each case for the hydrogen-influenced steels tested by the LIST and UTM, indicating brittle fracture and ductile fracture occurred competitively. This is also indicated by the fact that the ductile dimple-contained regions occurred along with the brittle regions on the fracture surfaces. Hydrogen needs time to diffuse to the crack tip, contributing to brittle fracture and enhancing crack propagation. Such hydrogen diffusion may take a longer time than crack propagation induced by the applied load, leading to ductile cracking in the remaining surface [4].

Furthermore, there was no subcritical cracking in all the steels subjected to hydrogen influence, indicating that fracture occurred at the onset of necking when the specimen became

mechanically unstable. This observation implied that the apparent threshold stress obtained under hydrogen charging conditions should be considered as yield stress. Moreover, it also raised the consideration and proposition of new mechanisms to explain the hydrogen influence on the steels in this study. The new HE mechanisms will be discussed in a later section.

3. Effect of factors on hydrogen influence

The hydrogen influence increased with increasing steel strength, more negative charging potential, and decreasing stress rate. The more profound hydrogen influence was manifested by the enhanced loss of ductility and a larger area of brittle regions, along with some reduction in necking.

The increased hydrogen influence with increasing steel strength was evidenced, for example, by comparing the HE susceptibility of 980DP and 1200DP. The increased hydrogen influence was related to increased amount and strength of the martensite. The increased martensite strength was due to a higher carbon content. The higher HE susceptibility of 1200DP than 980DP could also be attributed to more reversible hydrogen traps with the increased martensite content. The influence of reversible traps on hydrogen embrittlement is discussed in detail in the following section.

A more negative charging potential causes an increased overpotential, and consequently an exponentially increased hydrogen fugacity, as proposed by Atrens et al. [5] and Liu et al. [6]. A higher hydrogen fugacity therefore results in a higher hydrogen concentration in the steel, leading to a higher propensity for hydrogen influence.

The increased HE sensitivity with decreasing stress rate is attributed to hydrogen diffusion, as hydrogen had more time to diffuse to the critical stressed regions. Moreover, HE dependence on stress rate could also be interpreted by the dynamic trapping effect [7, 8]. During plastic deformation, a great number of dislocations are created. These newly created dislocations are essentially free of hydrogen and therefore obtain hydrogen by diffusion or by interacting with hydrogen enriched reversible traps to meet equilibrium [7, 9]. Thus, if the stress rate is high, the multiplication of dislocations are too high to be supplied with enough hydrogen for cracking, whereas, at a slower stress rate, the diffusion or interaction with reversible traps are sufficient, so that dislocations will be filled with hydrogen and these mobile dislocations can also reach further into the specimen, causing a more profound embrittlement.

4. New HE mechanisms

The DP, Q&P and TWIP steels in this PhD study exhibited some HE sensitivity, however, there was no subcritical crack growth. Cracks occurred after the onset of necking when the steel became menchanically unstable. The current mechanisms of hydrogen embrittlement pertain to subcritical crack growth. These mechanisms are Hydrogen Enhanced Localized Plasticity (HELP), Hydrogen Enhanced Decohesion (HEDE) and Adsorption-induced dislocation emission (AIDE).

Since there was no subcritical crack growth in the present work, it was thus further considered to better address this observation, by proposing two new mechanisms. The hydrogen enhanced macroscopic plasticity (HEMP) mechanism addressed that the critical hydrogen influence was causing some solid solution softening, due to the macroscopic movement of significant dislocation masses enhanced by hydrogen. The hydrogen assisted micro-fracture (HAM) mechanism proposed that hydrogen modified the micro-fracture events during the final specimen fracture, when the specimen was mechanically unstable and was undergoing relatively fast fracture, with considerable ductility.

5. Influence of hydrogen under simulated service corrosion conditions

For 980DP and 1200DP, there was little influence of hydrogen under simulated service corrosion conditions, manifested by the very small decrease in the value of reduction in area and ductile cup and cone features on the fracture surface, similar to their counterparts tested in air. The fracture initiated from the centre of the specimen due to plastic deformation, and then propagated towards the surface. The specimen became unstable at the ultimate tensile stress, necked, and fractured in a ductile shearing manner. The fact that there was minimal hydrogen influence on 980DP and 1200DP, indicates that the hydrogen content introduced into the steels under simulated service corrosion was lower than the critical hydrogen concentration for causing HE.

For the other DP, Q&P and TWIP steels, there was significant hydrogen influence, evidenced by the decreased mechanical properties and changed fracture mode. For example, 980QP exhibited a fracture mode containing brittle region with transgranular features and shear regions containing shear dimples, similar to that of the counterpart tested with cathodic hydrogen charging. This indicates that the hydrogen contents introduced into the steels under simulated service corrosion were enough to cause HE.

The implications of these results from LIST tests under simulated service conditions will be discussed in the following section.

6. Influence of hydrogen under substantial loading rates

The influence of hydrogen at substantial loading rates was studied using a LIST and a UTM under two conditions: (i) with simultaneous in situ cathodic hydrogen charging at the most negative potential in 0.1 M NaOH, and (ii) without simultaneous in situ cathodic hydrogen charging, meaning the specimen was pre-charged in 0.1 M NaOH and then tested in air.

All the steels were subjected hydrogen influence with simultaneous in situ cathodic hydrogen charging at the most negative potential in 0.1 M NaOH, manifested by decreased mechanical properties and the presence of brittle fracture features. Whereas, in the absence of simultaneous in situ hydrogen charging, a period of time (10 min and 24 h) exposing to ambient air after hydrogen charging, would reduce the hydrogen influence on the steels. The mechanical properties and fracture mode would partly or fully revert to those without hydrogen influence, attributed to the egress of internal hydrogen introduced by the pre-charging. For example, after 24 h away from the hydrogen charging source, there was minimal internal hydrogen left in 980DP and 980QP, contributed to the full recover of the steel properties.

The above mentioned results provide indications for the steel applications in service. This will be discussed in the succeeding section.

7. Indications for applications in service

HE was absent for 980DP and 1200DP, and was present for 980DP-650YS, 980DP-700YS, 980QP and 950TW, tested in a 3 wt% NaCl solution, simulating corrosion situations in actual service. Such corrosion conditions by immersing steels directly in a 3 wt% NaCl solution are the most extreme corrosion situation that can occur in actual service. In reality, there are occasions where the auto components are exposed to high salt environments, such as de-icing salts and marine atmosphere, yet, these environments are much milder than the simulated corrosion conditions in this work. Thus, the environments that the auto components can encounter are significantly milder. A lower hydrogen content decreases the likelihood of HE occurrence. Therefore, this work implies that 980DP and 1200DP would experience minimal HE, whereas the other steels might be influenced by hydrogen, during actual auto service.

The tests with simultaneous in situ charging at fast loading rates simulated a crash situation in actual service with the presence of substantial hydrogen in the steel. However, the amount of hydrogen introduced by electrochemical charging at the most negative potential in 0.1 M NaOH, was significantly higher than that would be introduced in actual service. In reality, such abnormally high hydrogen content is rarely encountered for auto components. Thus, the occurrence of HE to the steels under this simulated condition does not mean that the steels would also be subjected to HE during a crash in service. In some cases [8, 10], HE was absent with stress or strain rate higher than a critical value, and with hydrogen content lower than a critical level. Furthermore, the results that steels were fully or partially recovered after exposing to air for a brief amount of time, indicate that in actual service, if the hydrogen source was deprived (e. g. corrosion ceased), and the steel was exposed to non-hydrogen source (e.g. ambient air), the hydrogen-influenced steel would experience recovery from HE depending on the steel type and exposing time. In other words, this also indicates that the steels would exhibited favourable crash performance in the presence of a very low hydrogen content.

8. Microstructures associated with hydrogen influence

SEM examination of the hydrogen induced cracks, on the etched transverse surfaces of DP steels after LIST tests, revealed that the microstructures associated with hydrogen induced fractures were the hard martensite. The fractures were situated inside martensite region or at the interface of martensite and ferrite. These microstructures are preferential hydrogen traps. Thus, hydrogen is considered to diffuse to such sites, reduce cohesive energy and cause fracture initiation upon the stress reaching a critical stress. Moreover, the fractures were also situated in ferrite or transverse martensite. Therefore, it is presumed that fracture initiates in martensite regions and/or at martensite and ferrite interface, thereafter propagates into ferrite due to the hydrogen enhanced dislocation mobility, or transverse martensite, causing transgranular brittle features. This is consistent with other research [1, 11, 12]. This aforementioned information indicates possible methods to improve the HE resistance of DP steels, such as (i) conducting tempering treatments in a temperature range to soften the hard martensite and reduce the propensity of martensite cracking, and (ii) employing compositions that can contribute to a higher strain hardening capability of ferrite to recover its loss in crack-arresting ability.

For Q&P steels, examination of the hydrogen induced small cracks in association with microstructures, demonstrating fractures initiated from somewhere within or near the

martensite, and then propagated into adjacent ferrite or transverse martensite. The presence of lath martensite, accommodated with a high dislocation density, favours high hydrogen concentrations in such martensite. Moreover, during deformation, phase transformation from retained austenite to martensite [13] and concomitant volume expansion occur [14], increasing the local stress intensity in the transformed regions. Thus, hydrogen assembles near the martensite. In addition, the high hydrogen solubility in austenite could enrich the freshly formed martensite with hydrogen [15]. The high hydrogen concentration, in the original or freshly formed martensite, thus results in the reduced cohesive energy, and fracture initiation. Thereafter, fractures transverse martensite or propagate into ferrite. The result that hydrogen influence on Q&P steels was associated with martensite implies that tempering might also be beneficial to reduce HE susceptibility, in a similar way as for DP steels. Moreover, low-temperature tempering could possibly allow precipitation of ε-carbide, which acts as irreversible hydrogen traps in martensite, reduces the amount of diffusible hydrogen, and thus contributed to HE resistance.

XRD analysis in this work suggested that the 950TW steels only possessed fcc austenite (γ-Fe), and ruled out the formation of any type of martensite. This result indicates that hydrogen influence on 950TW was not associated with any martensite. The absence of martensitic transformation during straining is consistent with the literature [16-19]. Instead, the hydrogen influence can be associated with the mechanical twinning. Mechanical twins are formed during straining in a LIST or in a UTM, and hydrogen atoms transport from the lattice, dislocations and grain boundaries to such mechanical twins, leading to the accumulation of hydrogen and fracture initiation at the mechanical twins [17].

Non-metallic inclusions were observed in DP and TWIP steels. These inclusions were associated with brittle features, especially acting as nuclei of brittle fisheyes, contributing to the hydrogen embrittlement fracturing of the steels. It is then logical to consider to eliminate these inclusions in the steels. However, inclusions are inevitable in commercial steels. For example, by adding Al to the TWIP steels, the stability of the austenite and the HE resistance can be both enhanced [20], but Al additions also become the source of the AlN inclusions present in TWIP steels. It was suggested that reducing the inclusion density and/or the size of the inclusion might enhance the HE resistance of the materials [2, 21]. Such a suggestion can also be considered herein to be applied to our hydrogen-influenced DP and TWIP steels, which were associated with non-metallic inclusions, for improving the HE resistance.

9. Hydrogen concentration under various conditions

The hydrogen concentration in the steels, under (i) cathodic charging with increasingly negative potential and (ii) simulated service corrosion conditions, was evaluated by permeability experiments, hot exaction analysis and thermal desorption spectroscopy (TDS), to help understand the hydrogen influence.

The results support that a more negative charging potential leads to a higher hydrogen concentration in the steel, and consequently a more profound hydrogen influence on the steel. Moreover, the hydrogen concentration was found to be significantly higher under cathodic charging in 0.1 M NaOH than under simulated service corrosion conditions. This is also related to the facts that hydrogen influence was minimal or less significant under simulated service corrosion conditions compared with that under cathodic charging conditions. The results from LIST and UTM experiments indicated that hydrogen influence on DP steels increased in the following order, 980DP, 1200DP, 980DP-650YS and 980DP-700YS. However, the hydrogen concentration results did not increase by the same trend, and thus did not provide direct correlation with the hydrogen influence. In fact, there are various factors affecting the hydrogen uptake in the steel, such as the steel surface state and the steel compositions. In addition, comparing 980QP with DP steels also indicates no correlations between hydrogen influence and hydrogen concentration, since 980QP showed lower hydrogen concentration but more profound hydrogen influence than the DP steels. But, it should be addressed that the higher hydrogen influence on 980QP is attributed to the phase transformation from retained austenite to martensite and concomitant release of hydrogen from the transformed retained austenite, and such phase transformation is absent in the permeability test and hot extraction analysis.

10. Hydrogen trapping in the steels

The occurrence of HE requires the interaction of a critical amount of hydrogen with the stressed steel. Moreover, the state of the introduced hydrogen in the steel plays an important role in the hydrogen influence. Therefore, studying the hydrogen trapping behaviour is also important for understanding the hydrogen influence on the steels. The hydrogen trapping characteristics were studied by (i) TDS to determine the de-trapping activation energy and (ii) permeability experiments to evaluate the trap site density.

TDS study on 980DP revealed that the de-trapping activation energies were 40.5 kJ mol^{-1} and 50.2 kJ mol^{-1}, indicating hydrogen traps were reversible and were at boundary defects, such as boundaries of ferrite and martensite and the lath interfaces of martensite. The hydrogen trapping at these boundary defects is consistent with (i) the results of examining the

hydrogen induced cracks, which were associated with the martensite phase and the interfaces of ferrite/martensite, and (ii) the transgranular brittle features in the DP steels.

Permeability experiments indicated that the densities of reversible hydrogen trap sites evaluated from complete decays were ~ 10^{18} sites cm^{-3}. The density for DP steels increased from 980DP, to 1200DP and to 980DP-650YS and 980DP-700YS, consistent with the trend of the increase of hydrogen influence, and consequently correlating the hydrogen influence on DP steels with the reversible hydrogen trap density in the steel.

The above information provides a deeper understanding of the steel fracturing process and a perspective to explain the increased HE susceptibility of different DP steels. Some of the hydrogen introduced in the steel was diffusible, whereas some other hydrogen was reversibly trapped at boundary defects, such as the interfaces of the lath martensite, and those of ferrite/martensite. This dissolved hydrogen facilitates massed motion of dislocations throughout the gauge volume of the specimen during a LIST or tensile test, causing the decrease of the yield stress, as was described by the mechanism of hydrogen influence, hydrogen enhanced macroscopic plasticity (HEMP). Moreover, this introduced hydrogen also changes the micro-fracture mode, leading to the change of the macroscopic form of the fracture at the ultimate tensile strength from the ductile cup and cone fracture mode to the macroscopically-brittle transgranular shear fracture mode, by the mechanism of hydrogen-assisted micro-fracture (HAM). The facilitation of the dislocation motion and the change of the micro-fracture mode are enhanced by more available hydrogen. Therefore, a higher density of the reversible traps at boundary defects in a stronger DP steel permits more available hydrogen and concomitantly a higher HE susceptibility.

Reference

[1] R. Davies, Hydrogen embrittlement of dual-phase steels. Metallurgical Transactions A (1981). 12(9)1667-1672.

[2] Q. Liu, B. Irwanto, and A. Atrens, Influence of hydrogen on the mechanical properties of some medium-strength Ni–Cr–Mo steels. Materials Science and Engineering: A (2014). 617200-210.

[3] M. Loidl, O. Kolk, S. Veith, and T. Göbel, Characterization of hydrogen embrittlement in automotive advanced high strength steels. Materialwissenschaft und Werkstofftechnik (2011). 42(12)1105-1110.

[4] A. Laureys, T. Depover, R. Petrov, and K. Verbeken, Characterization of hydrogen induced cracking in TRIP-assisted steels. International Journal of Hydrogen Energy (2015). 40(47)16901-16912.
[5] A. Atrens, D. Mezzanotte, N. Fiore, and M. Genshaw, Electrochemical studies of hydrogen diffusion and permeability in Ni. Corrosion Science (1980). 20(5)673-684.
[6] Q. Liu, A.D. Atrens, Z. Shi, K. Verbeken, and A. Atrens, Determination of the hydrogen fugacity during electrolytic charging of steel. Corrosion Science (2014). 87239-258.
[7] G.M. Pressouyre, Trap theory of Hydrogen embrittlement. Acta Metallurgica (1980). 28(7)895-911.
[8] M. Hashimoto and R.M. Latanision, The role of dislocations during transport of hydrogen in hydrogen embrittlement of iron. Metallurgical Transactions A (1988). 19(11)2799-2803.
[9] G.M. Pressouyre and I.M. Bernstein, An example of the effect of hydrogen trapping on hydrogen embrittlement. Metallurgical Transactions A (1981). 12(5)835-844.
[10] J. Venezuela, Q. Liu, M. Zhang, Q. Zhou, and A. Atrens, The influence of hydrogen on the mechanical and fracture properties of some martensitic advanced high strength steels studied using the linearly increasing stress test. Corrosion Science (2015). 9998-117.
[11] M. Koyama, C.C. Tasan, E. Akiyama, K. Tsuzaki, and D. Raabe, Hydrogen-assisted decohesion and localized plasticity in dual-phase steel. Acta Materialia (2014). 70174-187.
[12] S. Sun, J. Gu, and N. Chen, The influence of hydrogen on the sub-structure of the martensite and ferrite dual-phase steel. Scripta metallurgica (1989). 23(10)1735-1737.
[13] X. Zhu, K. Zhang, W. Li, and X. Jin, Effect of retained austenite stability and morphology on the hydrogen embrittlement susceptibility in quenching and partitioning treated steels. Materials Science and Engineering: A (2016). 658400-408.
[14] X. Zhu, W. Li, H. Zhao, L. Wang, and X. Jin, Hydrogen trapping sites and hydrogen-induced cracking in high strength quenching & partitioning (Q&P) treated steel. International Journal of Hydrogen Energy (2014). 39(24)13031-13040.
[15] J.H. Ryu, Y.S. Chun, C.S. Lee, H.K.D.H. Bhadeshia, and D.W. Suh, Effect of deformation on hydrogen trapping and effusion in TRIP-assisted steel. Acta Materialia (2012). 60(10)4085-4092.
[16] T. Dieudonné, L. Marchetti, M. Wery, J. Chêne, C. Allely, P. Cugy, and C. Scott, Role of copper and aluminum additions on the hydrogen embrittlement susceptibility of austenitic Fe–Mn–C TWIP steels. Corrosion Science (2014). 82218-226.

[17] S.-M. Lee, I.-J. Park, J.-G. Jung, and Y.-K. Lee, The effect of Si on hydrogen embrittlement of Fe-18Mn-0.6C-xSi twinning-induced plasticity steels. Acta Materialia (2016). 103264-272.
[18] J.H. Ryu, S.K. Kim, C.S. Lee, D.-W. Suh, and H. Bhadeshia, Effect of aluminium on hydrogen-induced fracture behaviour in austenitic Fe–Mn–C steel. Proceedings of the Royal Society A: Mathematical, Physical and Engineering Science (2013). 469(2149)20120458.
[19] K.H. So, J.S. Kim, Y.S. Chun, K.T. Park, Y.K. Lee, and C.S. Lee, Hydrogen delayed fracture properties and internal hydrogen behavior of a Fe-18Mn-1.5 Al-0.6 C TWIP steel. ISIJ international (2009). 49(12)1952-1959.
[20] Q. Liu, Q. Zhou, J. Venezuela, M. Zhang, J. Wang, and A. Atrens, A review of the influence of hydrogen on the mechanical properties of DP, TRIP, and TWIP advanced high-strength steels for auto construction. Corrosion Reviews (2016). 34(3)127-152.
[21] Q. Liu, B. Irwanto, and A. Atrens, The influence of hydrogen on 3.5NiCrMoV steel studied using the linearly increasing stress test. Corrosion Science (2013). 67193-203.

Future work

Based on the work and results from this PhD project, some suggestions can be made for the unsolved issues and further study of the hydrogen influence on DP, Q&P and TWIP grades of AHSS for auto construction:

1. Following the permeability experiments on DP and Q&P steels, it will be beneficial to also conduct some permeability experiments on TWIP steel to contribute to the understanding of hydrogen diffusion and trapping in TWIP steels. Due to the literature-recorded low hydrogen diffusion coefficient in austenitic TWIP steel, either the setup of permeability experiments in this work needs improvements to allow experiments at increased temperatures, or the TWIP steel specimen should be thinned to be feasible for permeability experiments at room temperature.
2. LIST and universal tensile tests were conducted in this PhD project regarding to hydrogen environments similar to the actual service condition. In the actual service, a car component may also be subjected to repeated loading. The presence of hydrogen would reduce the fatigue life of the component, being detrimental to the auto service. Thus, it is also important to conduct fatigue tests to understand the hydrogen influence on the fatigue limit of the key steels.
3. Immersion in a 3 wt% NaCl solution was conducted in this research to simulate the corrosion condition in actual service. However, such experiments represent the extreme hydrogen uptake that could occur in actual service. The normal cases in service for a car component would be much milder than that in this research, and thereby may lead to different hydrogen influence behaviour on the same steel. Thus, it is significant if some in situ tests could be conducted to determine the hydrogen uptake during the service of a car component.
4. Hydrogen influence was examined to be associated with the hard martensite or the interface of martensite/blocky retained austenite in the Q&P steel. Whether the martensite was transformed from the retained austenite during straining was not distinguishable from the SEM observation in this research. Quantitative determination of the evolution of the retained austenite before and after the mechanical tensile testing would provide information illustrating whether the hydrogen influence is associated with the freshly formed martensite. It is beneficial to perform such quantitative measurement.

5. The XRD analysis indicated no martensitic transformation for the TWIP steel during tensile testing in this research, and thus indirectly showing that the hydrogen influence was associated with the mechanical twinning rather than any formed martensite. However, it is significant to obtain direct evidence presenting the correlation of the hydrogen influence on the TWIP steel and the mechanical twining. For example, this could be obtained through TEM examination of the fractured TWIP steel specimen prepared by FIB with the intact fractured surface morphology.
6. Following the TDS tests on 980DP steel, it is necessary to conduct more tests on other DP, Q&P and TWIP steels to gain better understanding of the hydrogen influence on these steels.